Assembly and Test of Prototype 2S Modules for the Phase-2 Upgrade of the CMS Outer Tracker

Von der Fakultät für Mathematik, Informatik und Naturwissenschaften der RWTH Aachen University zur Erlangung des akademischen Grades eines Doktors der Naturwissenschaften genehmigte Dissertation

vorgelegt von

M.Sc. Tim Ziemons
aus
Aachen

Berichter:

apl. Prof. Dr. Oliver Pooth
Prof. Dr. Lutz Feld

Tag der mündlichen Prüfung: 26.08.2022
Diese Dissertation ist auf den Internetseiten der Universitätsbibliothek verfügbar.

Abstract

Within the scope of the High Luminosity LHC upgrade the CMS experiment will be upgraded because due to radiation damage many components cannot be used any longer and higher particle fluxes will raise the technical requirements. In addition to other detector components, the entire silicon strip tracker will be replaced. The new sub-detector will consist of so-called PS and 2S modules with a stacked pair of sensor layers each. This module design will enable the integration of tracking information into the Level-1 trigger of the CMS detector on hardware level.
The Physics Institute IB and the Physics Institute IIIB of RWTH Aachen University committed to assemble and test up to one thousand 2S modules. In the course of this PhD thesis multiple prototype detector modules have been assembled and the assembly procedure has been tested and improved with the focus being placed on the wire bonding step. The bonding quality has been evaluated by analyzing the bond machine data. As a tool for the module series production, a user interface has been developed to identify weak bonds. For the reception test of Kapton strips, which are used as high voltage isolators in the module assembly, a test setup with a dedicated user interface has been created. In addition, the series production was prepared by performing a detailed estimation of the assembly time and the required storage capabilities. Prototype modules were also used to test procedures for identifying and repairing damages.
The properties of close-to-final prototype modules have been measured at the Test Beam Facility DESY with an electron beam. The particle tracks of the beam telescope have been aligned to the hits on the tested modules and the data have been analyzed. The analysis includes a study of the detector's spacial resolution, the assembly precision and a detailed evaluation of the hit and stub efficiency at different locations of the sensors and under different incidence angles. The results of the beam test analysis are furthermore discussed in the context of the detector operation at the High Luminosity LHC.

Zusammenfassung

Das CMS Experiment erfährt im Zuge des High Luminosity Upgrades des LHC ein technisches Upgrade, da durch Strahlenschäden viele Komponenten nicht weiter benutzt werden können und durch höhere Teilchenraten die technischen Anforderungen wachsen werden. Neben anderen Detektorkomponenten wird der Siliziumstreifendetektor für Spurmessungen komplett ausgetauscht. Der neue Subdetektor wird aus sogenannten PS- und 2S-Modulen mit jeweils zwei übereinander verbauten Sensoren bestehen. Dieses Moduldesign wird es ermöglichen, auf Hardwareebene die Spurinformationen für den Level-1 Trigger des CMS Detektors zu nutzen.
Das I. Physikalische Institut B und das III. Physikalische Institut B der RWTH Aachen haben sich zum Bau und dem Test von bis zu eintausend 2S Modulen verpflichtet. Im Zuge dieser Promotion wurden mehrere Prototyp-Detektormodule gebaut und das Modulbauverfahren getestet und weiterentwickelt, wobei der Fokus auf das Drahtbonden gelegt wurde. Die Bondqualität wurde anhand der Daten der Bondmaschine analysiert. Für die Serienfertigung wurde eine Software-Benutzeroberfläche zur Identifizierung schwacher Bondverbindungen entwickelt. Für den Eingangstest der Kaptonstreifen, die im Modulbau als Hochspannungsisolatoren eingesetzt werden, wurde ein Teststand mit dazugehöriger Software aufgebaut. Außerdem wurde als Vorbereitung für die Serienfertigung eine detailierte Abschätzung der Modulbauzeiten und die erforderlichen Lagerflächen durchgeführt. Anhand der Prototypen wurden zudem Verfahren zur Identifizierung und Behebung von Schäden getestet.
Die funktionalen Eigenschaften von fast-finalen Prototypmodulen wurde an der Test Beam Facility DESY mit einem Elektronenstrahl vermessen. Die Spurvorhersage eines Strahlteleskops wurde mit den Teilchentreffern auf den getesteten Modulen aligniert und die gemessenen Daten wurden analysiert. Die Analyse umfasst eine Studie zur Ortsauflösung des Detektormoduls, der Modulbaupräzision und eine detaillierte Auswertung der Nachweiseffizienz von Teilchentreffern an verschiedenen Positionen der Sensoren und unter unterschiedlichen Einfallswinkeln. Die Ergebnisse der Analyse der Teststrahlmessungen werden außerdem im Kontext des Detektorbetriebs am High Luminosity LHC diskutiert.

List of Abbreviations

2K two-component

ADC analog-to-digital-converter

ALICE A Large Ion Collider Experiment

AlCF aluminum carbon fibre

AlN aluminum nitride

APD avalanche photo diode

ATLAS A Toroidal LHC ApparatuS

BF bond force

BPC Bond Process Control

BTL Barrel Timing Layer

BX bunch crossing

CBC CMS Binary Chip

CCD charge coupled device

CERN Conseil européen pour la recherche nucléaire

CFRP carbon fibre reinforced polymer

CIC Concentrator Integrated Circuit

CIS contact image sensors

CMS Compact Muon Solenoid

CSC cathode strip chamber

DAC digital-to-analog-converter

DAQ data acquisition

DOF depth of field

DPI dots per inch

DS downstream

DSM Double-Sided Metrology

DT drift tube

DUT detector under test

ECAL electromagnetic calorimeter

ENIG electroless nickel immersion-gold

ESD electrostatic discharge

ETL Endcap Timing Layer

EYETS extended year-end technical stop

FABEL Framework for Aachen's Beam test studies with Extended Linking

FED front end driver

FEH front-end hybrid

FNAL Fermi National Accelerator Laboratory

FZ float zone

GBL General Broken Lines

GEM gas electron multiplier

GUI graphical user interface

HCAL hadron calorimeter

HEPHY Institute of High Energy Physics

HGCAL high granularity calorimeter

HL High Luminosity

HL-LHC High Luminosity LHC

HLT High-Level Trigger

HB Hadron Barrel Calorimeter

HE Hadron Endcap Calorimeter

HF Hadron Forward Calorimeter

HO Hadron Outer Calorimeter

HV high voltage

IC inner contour

IR infrared

IT Inner Tracker

KIT Karlsruhe Institute of Technology

L1 Level-1

LEIR Low Energy Ion Ring

LGAD low gain avalanche detector

LHC Large Hadron Collider

LHCb Large Hadron Collider beauty

Linac Linear accelerator

lpGBT Low Power Gigabit Transceiver

LS Long Shutdown

LV low voltage

MaPSA Macro-Pixel Sub Assembly

MIP minimum ionizing particle

MMB multi module box

MPA Macro-Pixel ASIC

MTD minimum ionizing particle (MIP) timing detector

OT Outer Tracker

PMT photomultiplier tube

POH power hybrid

PS Proton Synchrotron

PSB PS Booster

QA quality assurance

ROC curve receiver operating characteristic curve

ROH readout hybrid

RPC resistive plate chamber

SCA Slow Control ASIC

SEH service hybrid

SiPM silicon photomultiplier

SM Standard Model

SPS Super Proton Synchrotron

SSA Short Strip ASIC

TBPX Tracker Barrel Pixel Detector

TEPX Tracker Endcap Pixel Detector

TFPX Tracker Forward Pixel Detector

TDC time-to-digital-converter

TD touchdown

TDF touchdown force

TEC tracker endcaps

TIB Tracker Inner Barrel

TID Tracker Inner Disks

TLU Trigger Logic Unit

TOB Tracker Outer Barrel

US ultra-sonic

USG ultra-sonic generator

VPT vacuum photo triode

VTRx+ Versatile TRansceiver plus

Contents

1. Introduction **1**

2. The CMS experiment at the Large Hadron Collider **3**

2.1. The Large Hadron Collider . . . 3

2.2. The CMS experiment . . . 5

3. The CMS Phase-2 upgrade **13**

3.1. HL-LHC . . . 13

3.2. Overview of the CMS Phase-2 Upgrades . . . 14

3.3. Tracker Upgrade . . . 16

3.3.1. Overview . . . 16

3.3.2. The Inner Tracker . . . 18

3.3.3. The Outer Tracker . . . 18

3.3.4. The chronological context . . . 23

4. Wire bonding **27**

5. Assembly of 2S modules **31**

5.1. The assembly procedure at RWTH Aachen University . . . 31

5.1.1. Tools and machines used for module assembly at RWTH Aachen . . . 33

5.1.2. Gluing of Kapton strips and HV pigtail . . . 34

5.1.3. Wire bonding and encapsulation of the HV pigtail . . . 36

5.1.4. Sensor gluing and metrology . . . 37

5.1.5. Hybrid gluing . . . 39

5.1.6. Wire bonding . . . 40

5.1.7. Wire bond encapsulation . . . 42

5.2. Quality assurance for wire bonding process . . . 43

5.2.1. Analysis of machine data . . . 44

5.2.2. Additional wire bonding studies and prototyping experiences . . . 55

5.3. Reception tests of Kapton strips . . . 60

5.3.1. Choice of the scanner . . . 60

5.3.2. Kapton strip specifications . . . 61

5.3.3. Software . . . 63

5.3.4. First tests with a Kapton reception jig . . . 67

5.3.5. Results . . . 67

5.4. Module and sensor lab tests . . . 69
5.4.1. Evaluation of thin sensors for 2S modules . . . 69
5.4.2. Sensor debugging with IR camera / Facing sensor issues . . . 73
5.5. Series production . . . 76
5.5.1. Workflow overview . . . 78
5.5.2. Time estimations . . . 81
5.5.3. Clean room planning . . . 83

6. Beam test **89**
6.1. DESY II Test Beam Facility . . . 90
6.2. Description of the beam test setup . . . 91
6.2.1. The DATURA telescope . . . 91
6.2.2. DAQ . . . 93
6.2.3. DUT mount . . . 96
6.3. The analysis frameworks . . . 97
6.3.1. EUTelescope . . . 97
6.3.2. FABEL . . . 98
6.4. Alignment of runs . . . 104
6.5. Uncertainties . . . 108
6.5.1. Statistical uncertainties . . . 108
6.5.2. Systematic uncertainties . . . 109
6.6. Resolution of the DUT and track uncertainties . . . 110
6.7. Evaluation of module assembly precision . . . 114
6.8. Uniformity of efficiencies . . . 115
6.9. Bias voltage scan . . . 118
6.10. Angle scan measurements . . . 122
6.10.1. Particles with different emulated p_{T} . . . 122
6.10.2. Investigation of the stub-insensitive area . . . 130
6.11. Conclusions for the operation in the Phase-2 CMS OT . . . 133
6.11.1. Stub sensitivity at different positions of the Phase-2 OT . . . 133
6.11.2. The stub mechanism applied on the LHC p_{T} spectrum . . . 135

7. Summary and outlook **141**

Bibliography **143**

List of Figures **153**

List of Tables **161**

A. Detailed tables of assembly time estimation **163**

1. Introduction

One of the largest efforts in the field of particle physics is the construction and operation of the Large Hadron Collider (LHC) at the Conseil européen pour la recherche nucléaire (engl. European Council for Nuclear Research, CERN) and the associated experiments. With the LHC as the world's largest and most powerful particle accelerator, thousands of physicists are trying to determine the correct models to describe particle interactions [1]. The Standard Model (SM) of particle physics, which describes three of the four known fundamental forces in our universe, has been confirmed with extremely good precision. One example is the discovery of the Higgs boson that led to the award of the Nobel Price in physics to Peter Higgs and François Englert for the development of the theory of the Higgs mechanism [2]. However, the SM is not complete. The fourth fundamental force, gravity, is not described and furthermore Dark Matter and the matter anti-matter asymmetry are not included.

The search for answers motivates the ongoing operation of the LHC and the experiments as well as dedicated upgrade projects. The Compact Muon Solenoid (CMS) experiment is one of the four detectors used to observe particle collisions at the LHC. The High Luminosity LHC (HL-LHC) [3] upgrade project will enable to study particle interactions at much higher collision rates. To cope with the increased particle flux in the detectors and the radiation damage after several years of measurements also the experiments will be upgraded in the course of the so-called Phase-2 upgrade. Among other upgrades, the silicon strip tracker, which is a sub-detector used to measure the trajectory of charged particles, will entirely be replaced [4]. The design of the new tracker is driven by the goal to use track information for the first time for the first stage of the experiment's triggering scheme, the Level-1 (L1) trigger. Parts of the new tracker will consist of so-called 2S modules consisting of two stacked silicon strip sensors. The Physics Institutes IB and IIIB have committed themselves to contribute by assembling up to one-thousand 2S modules.

In the course of this PhD thesis several prototype 2S modules have been assembled. Parts of the process and tools of the module assembly have been developed and improved. This thesis focuses especially on the assembly steps involving wire bonding. Wire bonding is a technique to electrically connect two substrates, in the case of the 2S module the sensors and the front-end ASICs, by cold-welding a thin wire from one substrate to the other. Each sensor strip is connected to a readout channel. Therefore, achieving good quality and reliability of the bonding process is crucial for the functionality of the 2S modules. In the framework of this thesis, the mounting of the module in the bonding machine, also referred to as jig, has been improved. Furthermore, a software tool for identification of potentially weak wires based on the analysis of bond machine data has been developed. The high voltage isolation between the sensors and the mounting structure is realized by Polyimide films, which have to be precisely cut. To check their dimensions, a dedicated test setup has been prepared. Also, the workflow of the assembly process has been evaluated with respect to

the series production, which is scheduled to start in April 2024. This is important to be able to prepare sufficient storage capacities and to make sure that enough manpower is available.
The assembled prototype modules have been used to qualify the module design, the ASICs' functionality and the sensor thickness and to develop test procedures in the lab. Experiments have been performed at the Test Beam Facility at DESY [5] with a beam telescope. The spacial detector resolution has been measured and the module assembly precision has been analyzed as a cross check of the metrology measurements performed in the lab in Aachen. Additionally, the hit detection efficiency and the on-module mechanism to select tracks with high transversal momentum p_{T} has been tested as a function of the coordinate on the sensor and at different incidence angles. Furthermore, the charge collection has been studied at different hit detection thresholds and incidence angles. As a last step the beam test results have been discussed in the context of the module operation at the HL-LHC.
A description of the CMS detector at the LHC and the CMS Phase-2 upgrade will be given in Chapters 2 and 3. The process of wire bonding and standard procedures to test the bonding quality are introduced in Chapter 4. The assembly process and its evaluation is discussed in Chapter 5. The description of the beam test and the analysis of the measured data can be found in Chapter 6.

2. The CMS experiment at the Large Hadron Collider

The European research center for particle physics, CERN, located near Geneva at the border between Switzerland and France, has been founded in the year 1954. The most powerful accelerator at CERN, the LHC, is designed to accelerate protons or heavy ions up to an energy of 7 TeV or 2.56 TeV/nucleon, respectively, per beam before they are brought to collision at four locations of the storage ring at which the detectors are located. The LHC is described in more detail in Section 2.1. The four major detectors, ALICE [6], ATLAS [7], CMS [8] and LHCb [9], measure the tracks and properties of particles produced in the collision to reconstruct and analyze the underlying processes. Section 2.2 describes the CMS experiment with its sub-detectors.

2.1. The Large Hadron Collider

The source of the protons that collide within the LHC is a regular hydrogen gas bottle. The hydrogen atoms are negatively ionized and initially accelerated to an energy of 160 MeV by the Linear accelerator 4 (Linac4) [10]. Afterwards, the ions are further accelerated in the PS Booster (PSB) to 2 GeV and stripped off their electrons. Before the protons eventually enter the LHC they are further pre-accelerated by the Proton Synchrotron (PS) and the Super Proton Synchrotron (SPS). Figure 2.1 shows a sketch of the accelerator chain.
Also heavy ion collisions are studied at the LHC. In this case, the lead atoms are stripped off their electrons inside a plasma before the ions are accelerated by Linac3 and injected into the Low Energy Ion Ring (LEIR). After reaching 72 MeV, the ion bunches are guided to the PS to join the same acceleration chain as the protons beams.
The LHC is a storage ring with a circumference of about 27 km. It consists of thousands of superconducting magnets cooled down to -271.3° [1]. Most of these, with a number of 1232, are 15 m long dipole magnets used to bend the particles trajectory. Approximately 400 quadrupole magnets of 5 to 7 m length focus the beams. Additionally, higher order magnets are installed in the region of the collision points. The main dipole magnets generate a magnetic field of 7.74 T [12]. The two proton beams are guided in opposite directions and separate beam lines within ultrahigh vacuum (10^{-10} to 10^{-11} mbar) to avoid collisions with atoms from the atmosphere. The protons traverse the storage ring in bunches each with about 10^{11} particles. The structure of the bunches and their spacing is a direct consequence of the radio frequency cavities used to accelerate them. The bunch spacing is approximately 7.5 m which means that every 25 ns (40 MHz) the bunches are brought to collision. To increase the probability of proton collisions, the bunches are squeezed at the collision points. The variable to quantify the rate of particles colliding and therefore one

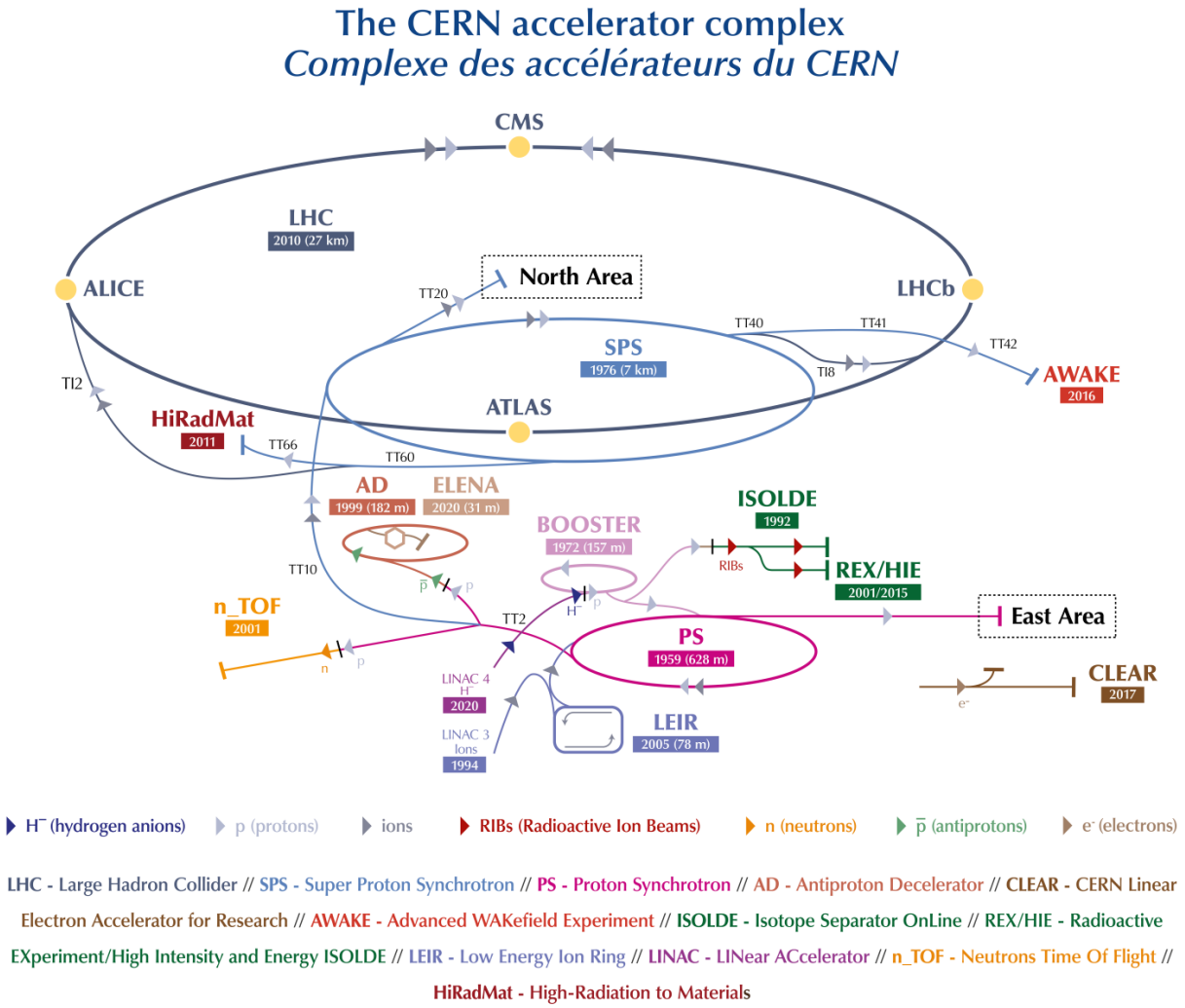

Figure 2.1.: Accelerator chain at CERN [11].

of the most important properties of a particle accelerator is the luminosity. The (instantaneous) luminosity is defined as

$$\mathcal{L} = \frac{fnN_1N_2}{4\pi\sigma_x\sigma_y} \tag{2.1}$$

with the circulating frequency f, the number of particle bunches n within the beam, the spacial dimensions of the beam at the collision point σ_x and σ_y and the number of particles within each bunch in the two beams, N_1 and N_2 [13]. Knowing the luminosity, the rate of events R of a process with the cross section σ can be calculated by $R = \sigma\mathcal{L}$. With a total cross section of $\sigma_{\mathrm{pp}} \approx 0.1\,\mathrm{b}$ at the design center-of-mass energy of 14 TeV and a design luminosity of $\mathcal{L}_{\mathrm{LHC}} \approx 10^{34}\,\mathrm{cm}^{-2}\,\mathrm{s}^{-1}$ in total 10^9 events are expected per second. The integrated luminosity (instantaneous luminosity integrated over time) is the most common variable to quantify the number of collisions collected at a collider experiment. Until the end of Run 2 a maximum collision energy of 13 TeV and a peak luminosity of $2.14 \times 10^{34}\,\mathrm{cm}^{-2}\,\mathrm{s}^{-1}$ have been achieved. The total integrated luminosity since the start of the LHC and until the end of Run 2 is about $193\,\mathrm{fb}^{-1}$. Another important parameter is the pileup, which describes the number of additional inelastic collisions per bunch crossing. The mean number of pileup in the 2018 pp run has been measured to be 32 assuming a minimum bias cross section of 69.2 mb [14]. More information about collision energies, luminosities and pileup and especially the future prospects are presented in Section 3.1.
There are four collision points at the LHC and there is a detector experiment at each of these: ALICE, ATLAS, CMS and LHCb [12]. ALICE (A Large Ion Collider Experiment) is a detector specialized in studying the quark-gluon plasma in Pb-Pb collisions, a state that probably existed shortly after the Big Bang. ATLAS (A Toroidal LHC ApparatuS) is a general purpose detector. As such, it is constructed to perform a wide range of physics studies as for example standard model precision measurements or discovery studies of yet unknown particles. At a size of 46 m length with a cylindrical diameter of 26 m ATLAS is the largest collider detector in volume ever built. LHCb (Large Hadron Collider beauty) is designed to focus on the study of the matter anti-matter asymmetry of particles with a b quark. The last of the four experiments, CMS, and the overall composition of a general purpose detector are discussed in detail in the following section.

2.2. The CMS experiment

The CMS detector is a general purpose detector (like ATLAS) and therefore designed to study a large range of physics subjects. In order to fulfill this objective, the detector is constructed hermetically, which means that it measures particles in all directions around the collision point in order to be able to study all physics processes induced. In this section, the CMS detector and its measurement concept are described in detail.

Concept

CMS is an abbreviation for Compact Muon Solenoid. The detector is **compact** as compared to ATLAS because it is "only" 21 m long with a diameter of 15 m [8, 15]. However, considering

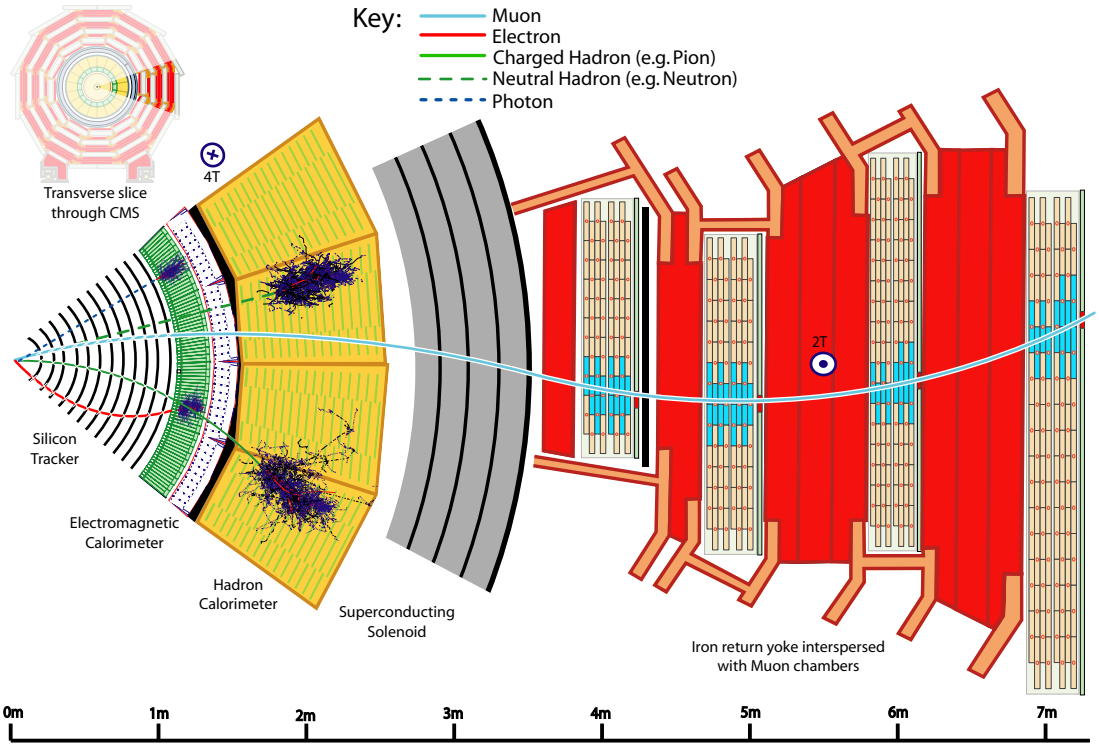

Figure 2.2.: Conceptional sketch of a slice through the CMS detector [16]. The sketch shows the path of different particles produced within the collision at the LHC and their interaction with the CMS detector.

its weight of 14 kt, which is approximately twice the mass of ATLAS, CMS is extremely dense compared to ATLAS and therefore it is called compact. The identification of **muons** is emphasized as CMS is able to measure muons even with high background rates at high precision. High precision momentum and charge measurements are enabled by a strong magnetic field of about 4 T generated by a superconducting **solenoid**.

CMS is constructed in multiple sub-detectors surrounding the collision point. Figure 2.2 shows the sketch of a slice of the detector. Going from the collision point outwards, the first sub-detector is the silicon tracker consisting of the pixel detector and the strip tracker. The path of charged particles through the tracker is measured to determine their momentum and electric charge. Additionally, the primary and secondary vertex are measured as a important analysis parameters to reject pileup and identify particles with b quarks. As the next sub-detector, the electromagnetic calorimeter (ECAL) is used to measure the energy of photons and electrons. Heavier particles (like neutrons or pions) are stopped and their energy is measured in the hadron calorimeter (HCAL). All sub-detectors mentioned before are surrounded by the solenoid and thus positioned within a strong and almost uniform magnetic field. Outside of the magnet, there is the Hadron Outer Calorimeter (HO) to catch the tails of the hadronic showers. The magnetic field flux is returned through an iron return yoke which accommodates the muon detectors. A more detailed description of the different detector components is given in the following.

The acceptance of the different sub-detectors is usually discussed considering the so-called pseudo-rapidity η. It describes the flight direction of the particle from the interaction point. It is calculated by

$$\eta\left(r,z\right) = -\ln\left[\tan\left(\frac{\theta^{*}\left(r,z\right)}{2}\right)\right]\cdot\operatorname{sgn}\left(z\right) \tag{2.2}$$

$$\text{with} \qquad \theta^{*}\left(r,z\right) = \left|\arctan\left(\frac{r}{z}\right)\right| \qquad \text{for } z \neq 0 \tag{2.3}$$

$$\text{and} \qquad \theta^{*}\left(r,z\right) = \frac{\pi}{2} \qquad \text{for } z = 0 \tag{2.4}$$

with the coordinate along the beam z (with $z = 0$ at the interaction point) and the radial distance from the beam r. The thickness of an electromagnetic calorimeter is usually given in so-called radiation lengths, X_0, a material attribute which describes the energy loss of a particle while electromagnetically interacting with the material. The radiation length is defined as the length at which the particle's energy is reduced to e^{-1}. The thickness of a hadronical calorimeter is usually given in units of interaction lengths, λ_{I}. It is defined as the mean free path of a particle between two inelastic interactions.

Magnet

The magnetic field strength of up to 3.8 T is generated by a superconducting solenoid. It consists of four layers of winding made from a NbTi conductor which is reinforced with an aluminum alloy. The almost uniform magnetic field extends to the size of the free bore of 6 m diameter and 12.5 m length [8]. The solenoid stores a maximum energy of 2.6 GJ at a magnetomotive force of 41.7 MA−turn. The ratio of stored energy and the cold mass of 220 t is 11.6 kJ/kg which is large as compared to previously developed detector magnets. The radial thickness of 312 mm cold mass translates to a thickness in electromagnetic radiation lengths of 3.9 X_0. The flux is returned through a yoke of 10 kt of iron. The return yoke houses the muon detectors and filters away remnants of high energetic hadrons so that only muons and neutrinos can pass.

Silicon pixel detector

The silicon pixel detector is the sub-detector component located closest to the beam interaction point. This particular position poses high demands to the pixel detector because of the harsh radiation environment and the high particle density. Therefore, it provides a very high granularity for a precise tracking of charged particles and for vertex reconstruction [8]. In the initial design of the pixel detector, it consisted of three barrel layers at radii of 44, 73 and 102 mm distance from the beam line and two endcap disks on each end at a distance of 345 and 465 mm from the interaction point. As such it covered a pseudorapidity range up to $|\eta| \leq 2.5$, which translates into an angle of approximately 9.4° towards the beam axis. The pixel modules feature a single cell size of 100 µm × 150 µm. As the analogue signal is read out, charge sharing effects can be used to improve the spatial resolution to 15 to 20 µm. The sensor material of choice follows the n-on-n concept that delivers high signals at bias voltages below 600 V after long time irradiation.

In the extended year-end technical stop (EYETS) of 2016/2017, the pixel detector has been replaced to cope with sensitivity losses due to radiation damages [17] and to withstand the challenge of higher pileup that both already had exceeded by a factor of two the design values considered as baseline for the primordial pixel detector. Comparing the former sub-detector with the new, the pixel detector now features a four-hit coverage in the range of $|\eta| \leq 2.5$ that is achieved by positioning the innermost layers of the pixel detector closer to the interaction point and adding an additional layer. The Phase-1 pixel detector has barrel layers at radii of 29, 68, 109 and 160 mm and three disks at both ends at 291, 396 and 516 mm distance from the interaction point. The upgraded pixel modules consist of planar n-in-n sensors with a pixel size of $100\,\mu m^2 \times 150\,\mu m^2$, which are bump bonded onto an array of 2×8 readout chips, each holding 4160 channels. The readout chips are glued and wire bonded to a high-density interconnect flex printed circuit and connected to the token bit manager chip, which controls the readout chips and synchronizes the module data transmission. By digitizing the data output the bandwidth could be increased compared to the initial pixel detector. The total number of channels is increased by a factor of 1.9 while keeping the size of the pixel cells unchanged. In order to be able to reuse parts of the original service structures although the new detector comes with highly increased bandwidth and power consumption, the Phase-1 pixel detector uses DC-DC power converters [18, 19]. These are custom modules designed for the harsh radiation environment of the Phase-1 pixel detector. The cooling of the Phase-1 pixel detector is done by using a system of evaporative CO_2, which comes with the advantage of low viscosity, low density and a high heat transfer coefficient. As a result thin pipes can be used. Additionally, the amount of material budget has been reduced in $|\eta| \leq 1$ for improved performance of tracking and vertex reconstruction. Apart from that region the material budget could be kept almost unchanged.

Silicon strip tracker

The pixel detector is surrounded by the silicon strip tracker occupying CMS at a radius between 20 cm and 116 cm [8]. The strip tracker is divided into four sub-detectors. The innermost part of the strip tracker is formed by the Tracker Inner Barrel (TIB) and the Tracker Inner Disks (TID) extending to a radius of 55 cm. Both rely on 320 µm thick silicon strip sensors which are mounted with the strips being in parallel to the beam (TIB) and pointing radially (TID). With a strip pitch of 80 µm in layer 1 and 2 and 120 µm in layer 3 and 4, the TIB modules achieve a single point hit resolution of 23 µm and 35 µm. The mean pitch of the TID varies between 100 and 141 µm. The Tracker Outer Barrel (TOB) is placed at higher radii up to 116 cm and consists of six layers of 500 µm thick strip sensors with a pitch between 122 and 183 µm with the strips in parallel to the beam. This corresponds to a single point hit resolution of 35 to 53 µm. Both, the TID and the TOB, extend to ±118 cm around the interaction point along the beam axis. At further distances up to 282 cm the tracker endcaps (TEC) are installed. The strip modules are mounted radially on nine disks and up to seven rings on both ends. The inner four rings use sensors with a thickness of 320 µm, the remaining have a thickness of 500 µm. Sensors with higher thickness have the advantage of higher signals, while thinner sensors feature an improved radiation hardness. The strip pitch is between 97 and 184 µm on average. In order to improve the resolution along the strip direction,

additional strip modules are mounted back to back under an angle of 100 mrad to the modules in the innermost two layers of TIB, TID and TOB as well as in ring 1, 2 and 5 of the TEC.

The sensors of the strip tracker are p-on-n type silicon sensors manufactured on 6 inch wafers. In order to meet the requirements within the different sub-detectors of the strip tracker, in total 15 different sensor geometries are used. The TIB and TOB both require two different rectangular sensor types while in sum eleven different wedge shaped sensor types are used in the TEC and TID. The number of strips per sensor is 512 or 768. In total, this sums up to about 9.3 million channels in the strip tracker over an active area of 198 m^2.

The module readout follows a multi staged scheme. At a first stage, the signal is amplified, shaped and stored. For this, a custom front-end ASIC, the APV25, is used. It was designed in an IBM 250 nm bulk CMOS process with a focus on radiation tolerance. Each chip holds 128 channels featuring a trigger latency of up to 4 µs. In case of a positive L1 trigger decision, the pre-processed signal is multiplexed and sent to the so-called front end driver (FED) in the service cavern via an optical transmitter, so that more sophisticated signal processing like pedestal determination can be done outside the detector.

The strip tracker is cooled by a system of mono-phase liquid C_6F_{14} [8]. It can provide up to 77 m^3/h of liquid of down to −35 °C to achieve an operating temperature of slightly below −10 °C. Additionally the entire volume is flushed with pre-cooled dry nitrogen gas up to approximately 25 m^3/h.

Electromagnetic calorimeter

The CMS ECAL is a homogeneous calorimeter made of lead tungstate ($PbWO_4$) crystals that are attached to photo detectors [8, 20]. $PbWO_4$ features a very high density of 8.25 g/cm^3, a short radiation length of only 8.9 mm and a small Molière radius of 2.2 cm. Additionally, it has a short scintillation time (about the bunch crossing time of the LHC) and it is radiation hard. The ECAL consists of two parts: the barrel and the endcaps.

The ECAL barrel consists of 61 200 crystals covering a pseudorapidity range up to $|\eta| < 1.479$. In ϕ the barrel is segmented in 360 crystals, in η the segmentation is 2×85. The crystals have a tapering shape over a length of 230 mm (25.8 X_0) with squared front and rear face with an edge length of approximately 22 mm respectively 26 mm. The front face center of each crystal is at a radius of 1.29 m from the beam axis. Within the barrel, avalanche photo diodes (APDs) are used to detect the scintillation photons. They have an active surface of 5 mm × 5 mm.

The ECAL endcaps cover the rapidity range of $1.479 < |\eta| < 3.0$. The endcap envelope starts at a distance along the beam axis of 315.4 cm from the interaction point. Both endcaps consist of two halves, also called Dees, with 3662 crystals each. The crystals have a length of 220 mm (24.7 X_0) with squared front face of 28.62 mm edge length and a squared rear face of 30 mm edge length. The scintillation photons are measured using vacuum photo triodes (VPTs). Each crystal is attached to a VPT at its rear face. The VPTs have a diameter of 25 mm with an active area of approximately 280 mm^2. VPTs are photo multipliers with only a single gain stage and a fine copper mesh used as the anode.

The preshower detector is located in front of the endcaps in the region of $1.653 < |\eta| < 2.6$ [8]. It is installed to identify neutral pions and to improve the spacial resolution of electron and photon detection. The preshower detector is a sampling calorimeter consisting of lead radiators to initiate electromagnetic showers which are attached to silicon strip sensors for the detection of the shower. The preshower is built up of two pairs of radiator and strip sensor summing up to a total thickness of 20 cm. The first radiator has a radiation length of $2\,X_0$, the second of $1\,X_0$. The strip sensors of the two layers are oriented orthogonally to each other. The silicon sensor dimensions are 63 mm × 63 mm with an active area of 61 mm × 61 mm at a strip pitch of 1.9 mm.
The energy resolution of the ECAL has been studied at a beam test with an electron beam with momenta between 20 and 250 GeV and it was found to be

$$\left(\frac{\sigma}{E}\right)^2 = \left(\frac{2.8\,\%}{\sqrt{E}}\right)^2 + \left(\frac{0.12\,\text{GeV}}{E}\right)^2 + (0.30\,\%)^2\,.$$

Hadronic calorimeter

The HCAL is the next sub-detector going from the inside to the outside. It consist of four sub-detector units: the Hadron Barrel Calorimeter (HB), the Hadron Endcap Calorimeter (HE), the Hadron Forward Calorimeter (HF) and the HO [8, 21]. The HCAL measures hadronical showers originating from hadron jets. The HB is installed between the ECAL and the magnet. Its acceptance ranges up to a pseudorapidity of $|\eta| = 1.3$ at which the HE extends to up to $|\eta| = 3.0$. Outside of the magnet, the HO is used as a tail catcher of high energetic showers. At a pseudorapidity of $3.0 \leq |\eta| \leq 5.2$, the HF is used to measure most forward jets and as a luminosity monitor.
The HB, the HE and the HO are sampling calorimeters using plastic scintillators as the active material. While the HB and the HE are both having brass and steel layers as the absorber material, the HO utilizes the steel return yoke and the magnet material for that purpose. The plastic scintillators use wavelength-shifting fibers to guide the light towards the photo detectors. In the initial design of the detector, hybrid photodiode transducers were used because of their magnetic field tolerance and their high gain. They were operated at −8 kV which creates a strong electric field over 3.3 mm between the cathode and the silicone photodiode each holding 19 pixels. Due to a number of problems related to the high voltage (HV), especially electrical discharges, the hybrid photodiodes have been replaced by silicon photomultipliers (SiPMs) as part of the Phase-1 upgrade of the HCAL. SiPMs are compact devices with a pixel array of in Geiger-mode operated APDs. They usually feature a gain of 10^4 to 10^6 at a bias voltage below 100 V.
In the barrel region the ECAL material accounts for about 1.1 interaction lengths (λ_I). The absorber thickness of the HB is $5.82\,\lambda_\text{I}$ at $\eta = 0$ and increases to about $10.6\,\lambda_\text{I}$ at $|\eta| = 1.3$. Also taking the solenoid coil into account, the absorber material utilized by the HO has a thickness of about $11.8\,\lambda_\text{I}$. In the region of the HE the total absorber thickness (including the ECAL) sums up to about $10\,\lambda_\text{I}$.
The HF is a Cherenkov calorimeter consisting of steel used as the absorber material and quartz fibers that are running parallel to the beam within the absorber to collect the Cherenkov light. The light has been detected by photomultiplier tubes (PMTs). Because of anomalous background signals associated with muons or particle showers passing the PMTs, they had to be replaced by

multi-anode tubes during the Phase-1 upgrade of the HCAL. These enable a significant suppression of the anomalous signals.

Muon detector

The radially most outer sub-detector is the muon detector, which measures the momentum and the charge of the muons [8, 22]. It consists of three detector types considering the initial design of CMS: the drift tubes (DTs), the cathode strip chambers (CSCs) and the resistive plate chambers (RPCs). The DTs are used in the central part of the barrel (up to $|\eta| \approx 1.2$), which has a uniform magnetic field and a low muon and background rate. In DTs, the coordinate of the traversing muon is detected by measuring the drift time towards the anode wire in the center of each drift cell. The spacial resolution per cell is 250 µm or better and approximately 100 µm considering an eight-layer chamber. The endcap regions ($0.9 \leq |\eta| \leq 2.4$) feature a higher muon and background rate as well as a large and non-uniform magnetic field. Therefore, CSCs are used with their strips pointing radially outwards to measure the particle trajectory's bending in the magnetic field. They are operated as multi-wire proportional counters in trapezoidal shaped chambers. The position resolution per chamber varies in dependence on the chamber type between 50 µm and 140 µm. The time resolution per chamber is specified to be 3 ns. The RPCs are used as complementary trigger detectors in the barrel and the endcap regions, up to $|\eta| \approx 1.9$. RPCs are double-gap chambers operated in avalanche mode using electrodes with a high bulk resistivity. With a small response time and good time resolution of 1.5 ns per chamber, they help in the identification of the corresponding bunch crossing. In 2017 the first gas electron multiplier (GEM) chambers (used as demonstrators) have been installed in the forward region. As one of the first steps of the Phase-2 upgrade campaign of CMS, the GE1/1 detector equipped with GEM chambers has been installed in September 2020 [23].

Trigger

The CMS detector is operated at a bunch crossing frequency of 40 MHz. The number of collisions depends on the instantaneous luminosity. At the nominal design luminosity of $1 \times 10^{34}\,\mathrm{cm}^{-2}\,\mathrm{s}^{-1}$ (which by now is at least doubled) the average expected pileup is approximately 20 [8]. Due to the large number of events, the rate of events to be stored is required to be drastically reduced (by a factor of about 10^6). To achieve this, CMS is using a triggering system consisting of two steps.
In the first step, the L1 trigger is applied to reduce the output rate of events to a design value of 100 kHz. It consists of custom made and largely programmable electronics. The L1 trigger uses coarse information of the calorimetry and the muon detector, while the high resolution data are held back in the front-end electronics' memories. The High-Level Trigger (HLT), as the second step, is a CMS reconstruction software system running on commercial processors and can access all read out data and highly sophisticated calculations can be performed. The rate reduction coming from the HLT is required to be at least 100.

3. The CMS Phase-2 upgrade

This chapter describes the course towards Run 4, the launch of HL-LHC operation. Section 3.1 describes the HL-LHC upgrade itself. In Sections 3.2 and 3.3, the Phase-2 upgrade project of CMS is presented.

3.1. HL-LHC

The LHC has started its operation in 2010 at a center-of-mass energy of 7 TeV. The energy has been increased to 8 TeV before the end of Run 1 and was further increased to 13 TeV in Run 2 which ended with the Long Shutdown 2 (LS2) at the end of 2018. In parallel, the instantaneous luminosity has been increased to reach a peak of $2 \times 10^{34}\,\mathrm{cm}^{-2}\,\mathrm{s}^{-1}$, twice the nominal design value, in 2018 [24]. The LHC still is, and is expected to stay for at least the next 20 years, the particle accelerator that reaches the highest energy. To build on the successes of the past and the local competencies, the discovery potential of the LHC will be extended by major technical upgrades. These aim for the extension of operability and an increase of the collision rate, thus increasing the luminosity. Figure 3.1 presents the schedule of the LHC and its upgraded configuration, the HL-LHC. The launch of the HL-LHC (Run 4) is planned for 2029. It will reach an instantaneous luminosity of 5 to $7.5 \times 10^{34}\,\mathrm{cm}^{-2}\,\mathrm{s}^{-1}$ at 14 TeV. The nominal integrated luminosity will be increased by a factor of ten. In absolute terms this means that the HL-LHC will deliver an integrated luminosity of $250\,\mathrm{fb}^{-1}$ per year (300 to $400\,\mathrm{fb}^{-1}$) reaching at least $3000\,\mathrm{fb}^{-1}$ within a twelve years operation[1].
Most of the equipment that will be upgraded is located at the insertion regions of ATLAS and CMS, which have each a length of about 600 m that will almost be completely renewed. Modifications required at other locations sum up to about 2.2 km. The upgrades include the renewal of low-β inner triplet quadrupoles (including the cryogenics, powering and vacuum systems). The insertion regions will be instrumented with a new 1.9 K refrigerator, collimators and crab cavities, amongst others. Additionally, new equipment for beam monitoring will be installed and the civil engineering infrastructure will be improved as underground caverns will be made accessible also during accelerator operation and new buildings will be build on surface.
The instantaneous luminosity in Run 4 will be $4 \times 10^{34}\,\mathrm{cm}^{-2}\,\mathrm{s}^{-1}$, and it will be increased to the nominal value of $5 \times 10^{34}\,\mathrm{cm}^{-2}\,\mathrm{s}^{-1}$ after about two years of operation [24]. The ultimate scenario of increasing the peak luminosity to $7.5 \times 10^{34}\,\mathrm{cm}^{-2}\,\mathrm{s}^{-1}$ within Run 5 will only come into operation if the accelerator performance can be increased and if the detectors can cope with the much more challenging conditions. Therefore, the experiments will receive major upgrades, entitled as 'HL' or Phase-2 upgrade. For pileup handling, ATLAS will replace its tracker and parts of its calorimetry [26]. Additionally, the muon detectors and the TDAQ system will be improved for

[1] The target integrated luminosity from the start of the LHC until the end of Run 3 is $450\,\mathrm{fb}^{-1}$.

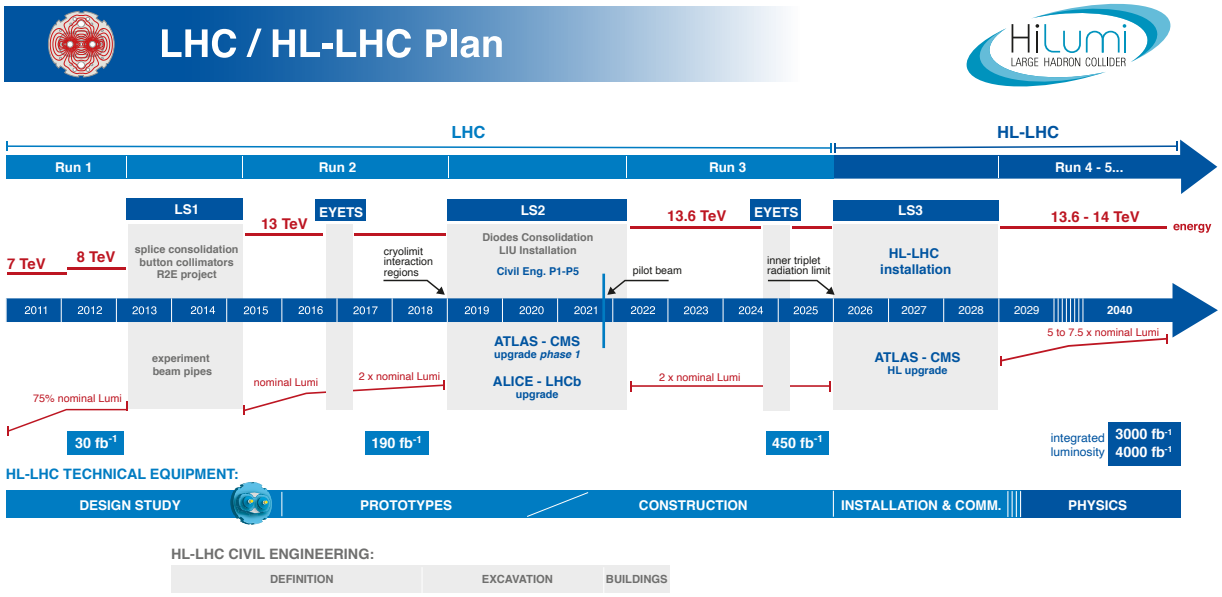

Figure 3.1.: The LHC and HL-LHC schedule [25].

enhanced capabilities concerning the triggering and the readout and a new timing detector will be installed and a high-granularity timing detector will be installed [27]. The Phase-2 upgrade program conducted by CMS is presented in the following.

3.2. Overview of the CMS Phase-2 Upgrades

The highly increased luminosity of the LHC will result in larger pileup, an even more challenging radiation level and higher data rates [28]. In order to maintain the performance of the CMS detector, a dedicated upgrade program has to be conducted. Currently installed detector components that are heavily exposed to radiation, such as the pixel and the strip tracker, will be replaced by sub-detectors with improved radiation hardness. Additionally, to resolve the many particle trajectories, which will occur at a much higher density, the overall spacial granularity needs to be improved. To not waste physics potential, the bandwidth as well as the trigger capabilities have to be enhanced. One important part of the CMS Phase-2 upgrade campaign is the enhancement of the trigger system [29, 30]. The two-stage triggering concept consisting of the L1 trigger and the HLT will be maintained. However, the complete trigger and data acquisition (DAQ) system will be replaced to enable a L1 trigger accept rate of up to 750 kHz and a latency of 12.5 µs as well as a HLT trigger rate of 7.5 kHz. With the upgrade for the first time tracker information and information from the new high granularity calorimeter (HGCAL) will be included in the L1 trigger. By including the tracker information that contain a selection of tracks with a transverse momentum above 2 to 3 GeV, the readout rate of soft interactions is expected to be reduced by a factor of 10. The upgrade of the tracker, of which the design is driven by the new trigger concept, is presented in more detail in Section 3.3.

The muon detector will receive upgraded electronics for the DT and the CSC systems [22]. New back-end electronics of the DTs will improve triggering and reduce constraints. Furthermore, the upgrade will lead to a better accessibility of the electronics. Improved DT on-board electronics will among others reduce the power consumption, so that less cooling capacities are required. In the very forward region (up to $|\eta| = 2.4$) new detectors will be installed. These will be additional GEMs and improved RPCs, so-called iRPCs, which feature an improved spacial resolution. By installing the new detector modules, the overall time and spacial resolution of the muon detector as well as the p_{T} triggering are enhanced. Furthermore, it results in better redundancy.

The Phase-2 upgrades related to calorimetry have to be differentiated between the barrel calorimeter [31] and the endcap calorimeter [32]. The barrel calorimeter detectors will basically be maintained for the HL-LHC operation. However, to meet the trigger requirements the ECAL front-end and off-detector electronics are replaced. The trigger latency will be increased from 4 µs to 12.5 µs. The new front-end electronics will also help to mitigate the APD noise. Furthermore, instead of measuring an array of 5×5 crystals, single crystal measurement data will be transmitted to the L1 calorimeter trigger. This will improve the background rejection. The HCAL barrel back-end electronics will be replaced as well to fulfill the L1 trigger requirements. The back-end electronics technology used for the HCAL barrel is the same as of the boards used for the ECAL barrel. Therefore, spares can be shared and for the operation and maintenance the experience of a larger community can be joined. In the endcap region, the degradation of performance far beyond the design integrated luminosity of 500 fb^{-1} demands a substantial upgrade. Because of this, the ECAL and HCAL endcap will be replaced by the so-called HGCAL. In order to withstand the harsh radiation, the active detector material is chosen to be exclusively silicon in the most challenging part, the electromagnetic compartment. It will consist of 26 sampling layers built up of a 6 mm thick copper cooling plate and two modules of 163 mm wide and hexagonal silicon sensors which are enclosed by a base plate of 1.4 mm thick WCu and the front-end electronics. The absorber material, two 2.1 mm thick lead planes covered by 0.3 mm of stainless steel, will be installed on either side of each of the latter. The silicon sensors have an active thickness of 120, 200 and 300 µm with a cell size of 0.52, 1.18 and 1.18 cm^2, respectively. The overall material of the electromagnetic compartment sums up to a radiation length of 27.7 X_0. The hadronic compartment will be made of in total 21 layers composed of silicon sensors (in the regions of high fluence) or scintillator tiles (in the regions of lower fluence) as the active medium and steel as the aborber material. The structure in the region using silicon sensors is similar to the structure of the electromagnetic compartment but uses only a single sensor per layer. The light from the scintillator is detected by SiPMs. The scintillator tiles will have an active area of about 4 cm^2 at the position closest to the beam and about 32 cm^2 at the position furthest away. The total thickness of the HGCAL in terms of interaction lengths is specified to reach 10.0 λ_{I} including the electromagnetic compartment. The whole HGCAL will be installed in a thermally shielded volume and is operated at $-30\,^{\circ}\mathrm{C}$ achieved by CO_2 cooling.

Another new sub-detector is the MIP timing detector (MTD) featuring a precise time measurement of minimum ionizing particles (MIPs) for enhanced pileup rejection [33, 30]. The fact that, due to the longitudinal extend of the particle beams, the multiple interactions of a single bunch crossing do not occur at the same time is used to reject tracks, which are associated to wrong MTD time measurements and are therefore belonging to a different collision vertex. At the beginning of Run 4

the time resolution will be 30 to 40 ps but will deteriorate to 50 to 60 ps by the end of HL-LHC operation as a result of accumulated dose. The MTD is divided into two sections, the Barrel Timing Layer (BTL) and the Endcap Timing Layer (ETL). The BTL is installed in between the tracker and the ECAL barrel with an acceptance of $|\eta| < 1.5$. It holds one layer of scintillating LYSO crystals [34] each with an area of 3 mm × 3 mm, a length of 5.7 cm and read out by an SiPM. The ETL is installed in front of the HGCAL with an acceptance of $1.6 < |\eta| < 3.0$. Instead of scintillating crystals, two layers of silicon sensors based on the low gain avalanche detector (LGAD) technology are used. The sensors have an active thickness of 50 µm at a size of 1.3 mm × 1.3 mm. The total number of channels of the ETL is about 3.6 millions.

3.3. Tracker Upgrade

3.3.1. Overview

The CMS tracker is performing well at an instantaneous luminosity which already reached more than twice the nominal design value. However, it is expected that the excellent performance cannot be maintained if the current tracker would be operated beyond Run 3 [4]. Therefore, the silicon pixel detector and the strip tracker will entirely be replaced by the so-called Inner Tracker (IT) and the Outer Tracker (OT), respectively. The harsh radiation environment with an expected maximum fluence of $3.5 \times 10^{16}\,\mathrm{n_{eq}cm^{-2}}$ of 1 MeV neutron equivalent at the innermost layer of the IT after $3000\,\mathrm{fb}^{-1}$ poses a challenge to the radiation hardness of the detector. The IT should be kept accessible, so that modules and other damaged components could be replaced during a LS. The OT, however, is not foreseen to receive any maintenance and is required to fulfill the requirements until the end of its expected lifetime.

In order to handle the increased pileup and keep the data taking under control, the tracker needs an improved granularity to reduce the channel occupancy and to have an improved separation of tracks. Nevertheless, the material budget should be minimized to reduce the influence on the performance of the energy measurements by the calorimetry. Additionally, the pattern recognition has to stay robust at the level of the HLT while tracker information is included at the L1 trigger.

The latest version of the Phase-2 IT and OT geometry is presented in Figure 3.2 as a transversal section sketch. Going outwards, the Tracker Barrel Pixel Detector (TBPX) consists of four layers at radii of approximately 30, 62, 105 and 147 mm, spanning up to $|z| \approx 200$ mm. Going further away from the interaction point (250 mm $\leq |z| \leq$ 1400 mm), there is the Tracker Forward Pixel Detector (TFPX) with eight disks per side, each holding four rings of pixel modules. The Tracker Endcap Pixel Detector (TEPX) extends the acceptance in terms of pseudorapidity to $|\eta| \approx 4$ and is installed in the region of 1750 mm $\leq |z| \leq$ 2650 mm. It consists of four disks per side with five rings each. The inner two layers of TBPX and the two innermost rings of TFPX will be equipped with pixel modules holding two readout chips (black and green lines in Figure 3.2) [35]. At the outer layers of TBPX, the outer rings of TFPX and in TEPX the pixel modules hold four readout chips (yellow lines in Figure 3.2).

Going radially further outwards in Figure 3.2 there is the OT between $r \approx 21$ cm and $r \approx 112$ cm. It is subdivided into the TBPS and the TB2S, consisting of in total six barrel layers installed in the

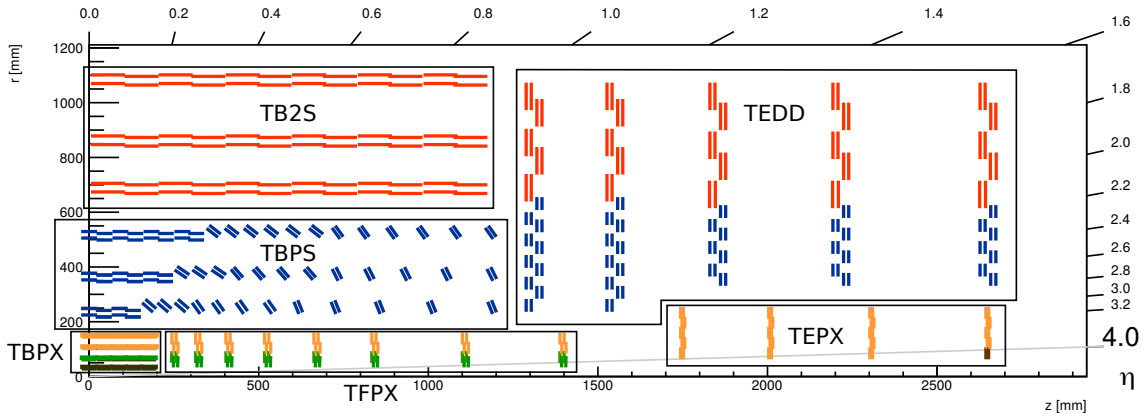

Figure 3.2.: Transversal section of a quarter of the Phase-2 CMS tracker. The figure was created with Version *OT801_IT701* of *tkLayout* [36]. The black, orange and green lines show the mounting positions and orientations of different types of IT pixel modules. The blue and red lines present the OT PS and 2S modules, respectively.

region of $|z| < 1200\,\text{mm}$, and the TEDD with five endcap double-disks on each side in the region of $1200\,\text{mm} < |z| < 2700\,\text{mm}$. The TBPS and the inner rings of the TEDD are equipped with PS modules consisting of a stacked pair of a silicon sensor with macro-pixels and a silicon strip sensor. The TB2S and the outer rings of the TEDD hold 2S modules, which consist of a stacked pair of two silicon strip sensors. More information about the OT modules are presented later in this section.

The TBPS is divided into three parts, each consisting of three concentric layers. In the center region the PS modules are mounted horizontally. The mechanical support is given by flat plank structures consisting of carbon fiber and foam with the cooling pipes embedded. The carbon foam is used as a heat spreader. Small metallic inserts are used to mount the modules. At coordinates of higher $|z|$ the modules are installed tilted with angles between 47° and 74°. In this region the modules are mounted on ring support structures of carbon fiber and foam. The TB2S is composed of ladders made of carbon fiber profiles, which are supported by a wheel structure similar to the current strip tracker support. The 2S modules are mounted onto inserts of aluminum carbon fiber composite material, which are directly connected to the cooling pipe. In the TEDD, the modules are mounted on disks formed by two half-disks with the PS modules located at the inner part and the 2S modules at the outer part. The cooling pipe is embedded in the half-disks. In the PS region carbon foam is used as the thermal contact to the modules, while the 2S modules are thermally coupled to the cooling pipe by aluminum inserts, which are surrounded by a cheaper foam material.

The IT and OT detector volume is expected to dissipate a power of about 50 kW and 100 kW respectively [4]. Additionally, the silicon sensors have to be operated at below −20 °C to avoid thermal runaway. In order to achieve this, a two-phase CO_2 cooling system as already been used for the Phase-1 CMS pixel detector has been chosen [37]. The nominal coolant operating temperature is −35 °C. The resulting temperature at the first module, which is assumed to be the warmest location of the cooling loop, will be −33 °C [4].

3.3.2. The Inner Tracker

The pixel modules of the new IT consist of the so-called High Density Interconnect PCB, the readout chips (called C-ROCs) and the sensor [35, 4]. The sensors have been chosen to be n-in-p planar silicon sensors with a pixel size of 25 µm × 100 µm with an active thickness of 150 µm. In the first layer of TBPX 3D sensors will be used instead of planar sensors because they have the advantage of improved radiation hardness and lower power dissipation. The readout chips will be bump bonded onto the sensors. They have been developed by the RD53 Collaboration for the pixel detectors of ATLAS and CMS but each with their own flavor to meet the individual requirements. A demonstrator chip, the RD53A [38], has been developed to operate at a low power consumption of less than 1 W/cm^2 and effectively avoid single event upsets. It furthermore features serial powering to operate up to twelve pixel modules in a power chain with the chips within a module powered in parallel. The High Density Interconnect PCB is powering the entire module and is used for data distribution and for the communication. It is connected to the readout chips via wire bonds.
The pixel modules are connected to the so-called service cylinder featuring power, cooling and data transmission services. The service cylinder is equipped with so-called portcards, each holding two Low Power Gigabit Transceiver (lpGBT) ASICs [39] for serialization and two Versatile TRansceiver plus (VTRx+) modules [40] for the optical link. The portcards are powered independently by an on-board two-staged DC-DC converter scheme. The lpGBT and the VTRx+ are also used as parts of the OT modules, which will be described in the following in more detail.

3.3.3. The Outer Tracker

The stub mechanism

The improvement of the L1 trigger is an important part of the Phase-2 upgrade project. The overall L1 trigger output rate will be increased from 100 kHz to 750 kHz and the discrimination power will be enhanced, which is a challenging task at higher pileup rates [4]. To mitigate this, the information of the new tracker will be included and the trigger latency will be increased from 3.2 µs to 12.5 µs for processing. This will improve the resolution of transverse momentum measurements at L1 and allows to utilize track isolation. The new tracker has to be able to send out self-selected information to the L1 trigger at the bunch crossing rate of 40 MHz.
The design of the OT and of its detector modules is driven by the concept of providing track information to the L1 trigger. Both types of detector modules, the PS and the 2S modules, consist of two single-sided and planar silicon sensors, which are separated by 1.6 to 4.0 mm. This design allows to take advantage of the strong magnetic field of 3.8 T and reject particles with low transverse momentum, p_{T}. Figure 3.3 presents a sketch of the so-called "stub" mechanism. If a particle hits the first sensor, called seed layer, the bending of the particle's trajectory leads to an offset of the hit position on the second sensor, called correlation layer [41]. Pairs of hits in the seed and the correlation layer are called stubs. By defining a correlation window on the correlation layer and checking whether it is hit, particles that do not exceed a certain value of p_{T} can be rejected. The correlation window size is tuned as a function of the position in the detector and the sensor spacing of the individual module. Stubs within the correlation window are called valid stub and are sent to

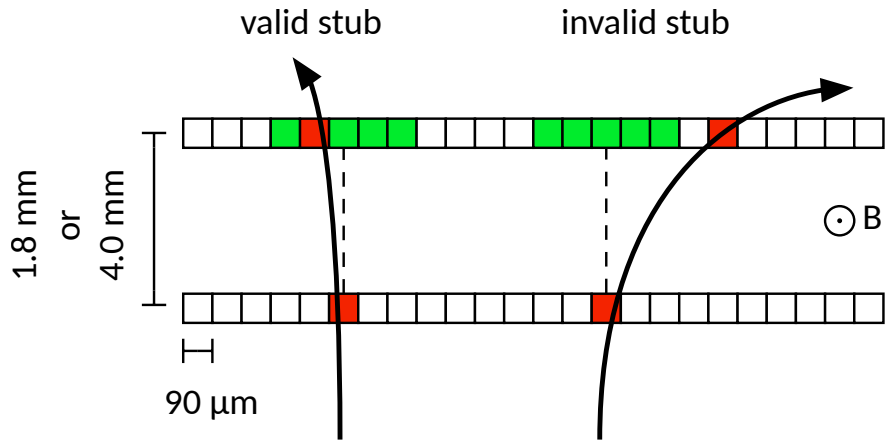

Figure 3.3.: Sketch of the stub mechanism. The sensor spacing and the strip pitch corresponds to the 2S modules. The shown stub mechanism is however also applicable for the PS modules. The particle trajectory is shown as black arrow. The seed layer (correlation layer) is shown on the bottom (top). The red squares symbolize the hit channels of the sensors. The correlation window is represented by the green colored squares.

the off-detector tracking system to reconstruct tracks for the L1 trigger. Otherwise they are called invalid stub. In case the L1 trigger accepts the event and sends out an accept signal, the complete tracker data are read out. By tuning the correlation window corresponding to a p_{T} threshold between 2 and 3 GeV a data rate reduction of a factor of ten is expected.

The 2S modules

The 2S modules consist of **2** silicon **strip** sensors, which are assembled closely separated with the strips oriented in parallel. For the 2S module two different nominal sensor distances will be realized: 1.8 mm and 4.0 mm. The modules with the respective sensor distances are referred to as "1.8 mm module" or "4.0 mm module", respectively, in this thesis. In total 7680 2S modules will be installed into the Phase-2 OT, of which 7256 are 1.8 mm modules. Figure 3.4 presents an exploded sketch of a 2S module. The sensors are segmented in two halves with 1016 strips of approximately 5 cm length each at a strip pitch of 90 µm. The strips are connected to the front-end hybrids (FEHs) to process the signals and form hits and stubs. The service hybrid (SEH) serializes the information, does the communication with the back-end and it supplies the HV to the sensors as well as the low voltage (LV) to the FEHs and its own components.
The sensors have an active thickness of 290 µm and a physical thickness of 320 µm at a size of approximately 9.4 cm × 10.2 cm [42]. The sensors are of n-in-p type with p-stop strip isolation [43]. Figure 3.5 presents the 2S sensor design as a schematic sketch. The negative HV bias voltage is applied at the aluminum backplane to deplete the p-bulk, in which electron-hole pairs are generated on particle passage. Full depletion of the active sensor material is specified to be achieved at a bias voltage below 350 V. The electrons are collected by the n-strip implants, which are guided to the so-called DC-pads on the top side of the sensor. Each of these is connected to the electrical ground with a bias resistor of about 1.5 MΩ. The implants are AC-coupled to the aluminum strips, which are electrically connected to the FEH via wire bonds at the so-called AC-pads.

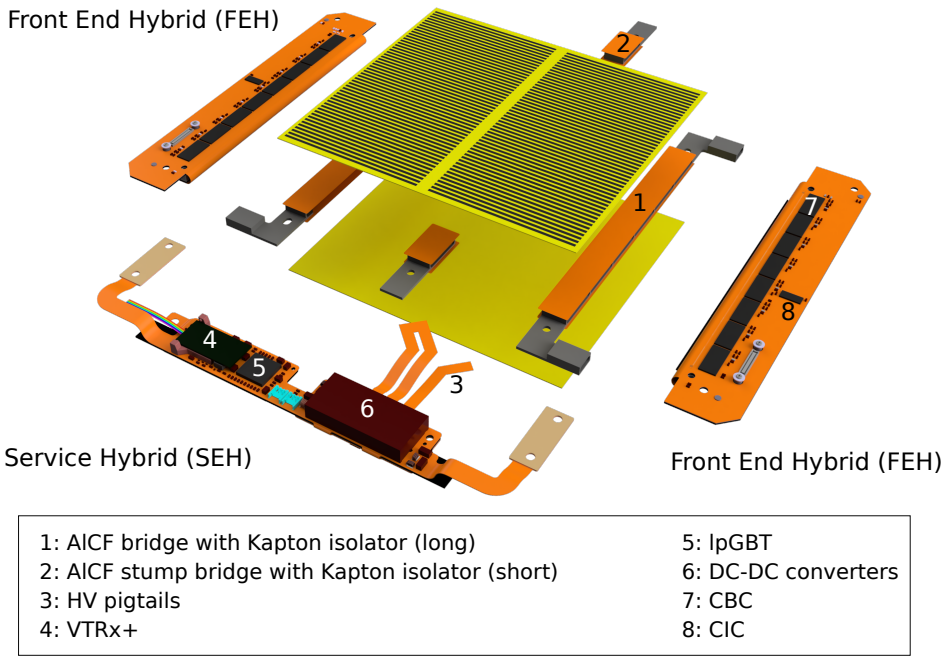

Figure 3.4.: Labeled sketch of the 2S module. The sketch shows the 4.0 mm version with a sixth cooling contact in an exploded view.

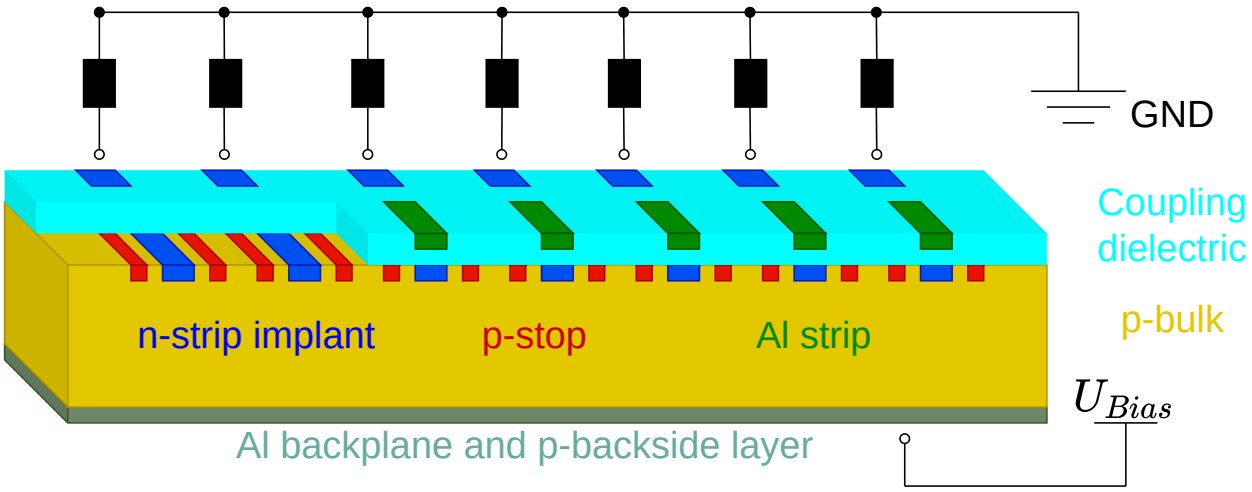

Figure 3.5.: Sketch of the 2S sensor design. The sensor edges with the guard and bias ring are not shown.

The sensors are glued back-to-back with bridges made of aluminum carbon fibre (AlCF) [44] in between, which are the connecting piece to the cooling support on the larger structures of the detector. In order to ensure adequate cooling while minimizing the material budget, the 2S modules will have either five or six cooling contacts depending on their location in the detector. The modules in TB2S layer 1, the first module in each of the layers 2 and 3 and the modules in TEDD will have six cooling contacts and the rest has five cooling contacts. The material of AlCF is used because of its good thermal conductivity and because the coefficient of thermal expansion is extremely similar to silicon. As a result, the cooling of the modules is improved and while cooling (and heating) the mechanical stress on the sensors is minimized. For each type of 2S module, either with 1.8 mm or 4.0 mm sensor distance, there are two long and one (or two) short AlCF bridges. The short AlCF bridge is also called stump bridge. The long bridges are used on the two sides of the FEHs, the stump bridges are assembled at the side of the SEH (and oppositely).

In order to electrically isolate the AlCF bridges from the HV backplane of the sensors, Polyimide films with a thickness of approximately 25 µm are glued between the AlCF bridges and the aluminum backside of the sensors. The material of choice is *Dupont Kapton® MT* [45] featuring a thermal conductivity of 0.45 W/(m K). In the course of this thesis, the Polyimide films are referred to as "Kapton strips".

Each FEH houses eight front-end ASICs, the CMS Binary Chips (CBCs) [46, 47]. The CBC is designed in 130 nm CMOS technology. Its readout architecture is based on the APV25 readout chip of the current strip tracker modules. However, instead of providing analogue hit information, the CBC reads out the signals of 127 channels of each the top and the bottom sensor. The CBC amplifies and shapes the signal. By using a comparator hits are identified. Then it correlates hits on top and bottom sensor and sends out binary stub data at bunch crossing frequency. At a L1 trigger output rate of up to 750 kHz unsparsified binary readout data is provided. For this, the detected hits are stored in a 512 bit deep pipeline resulting in a trigger latency of 12.8 µs. The Concentrator Integrated Circuit (CIC) bundles the data from the CBCs and performs compression and truncation if it is necessary [48].

The SEH is connected to the two FEHs via fine-pitch connectors [49]. It houses the lpGBT, which is a 65 nm CMOS radiation tolerant device for serialization and deserialization [39]. The output of the CIC is transmitted to the lpGBT on the SEH at 320 Mb/s via six differential lines, of which five are dedicated for stub data and one is used for the full readout data. The 320 Mb/s clock is generated for the FEHs by the lpGBT. The lpGBT configures the FEH chips and the VTRx+ via the I^2C protocol. The VTRx+ is a front-end module based on a radiation-hard laser driver used for the communication with the back-end. The lpGBT forwards the data to the VTRx+ at a data rate of 5.12 Gb/s and receives signals from the VTRx+ at 2.56 Gb/s. Furthermore, the lpGBT receives slow control data like voltage measurements and sends trigger and reset signals to the CBCs and CICs. Apart from the communication, the SEH features the module powering. It receives the HV bias voltage, which is filtered and lead through flex cables, which are referred to as "pigtails", to the sensor back planes. The pigtails are plugged into the SEH and glued and wire bonded onto the aluminum surface of the sensor. Additionally, the SEH receives about 11 V as input voltage to a two-stage DC-DC conversion powering. A first stage DC-DC converter, the bPOL12V [50],

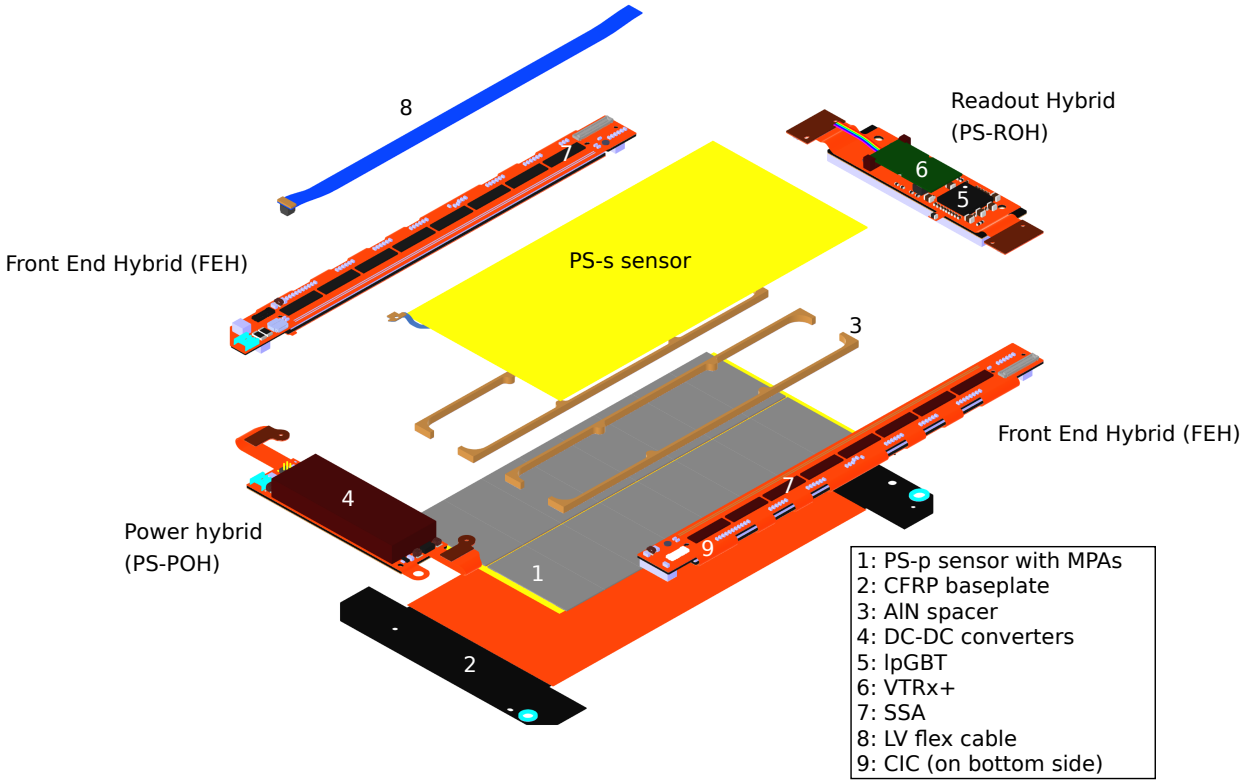

Figure 3.6.: Labeled sketch of the PS module. The sketch shows the PS module version with a sensor distance of 2.6 mm.

converts the input voltage to 2.55 V, which is used by the VTRx+. At a second stage the bPOL2V5 converts the 2.55 V to 1.25 V to power the lpGBT, the VTRx+, the CBCs and the CICs.

The PS modules

The PS module consists of a stacked pair of a macro-**pixel** sensor and a silicon **strip** sensor [4]. There are three different versions of the PS module with distances between the two sensors of 1.6, 2.6 and 4.0 mm. Figure 3.6 presents a sketch of the PS module with 2.6 mm sensor spacing.

The strip sensor, also referred to as PS-s sensor, features 2×960 strips with a pitch of 100 µm and a strip length of about 2.4 cm. The strips are connected to the Short Strip ASICs (SSAs) on the FEHs via wire bonds. The macro-pixel sensor, also referred to as PS-p sensor, has 32×960 pixels of about 1.5 mm $\times$ 100 µm. The pixels are read out by in total 2×8 Macro-Pixel ASICs (MPAs), which are bump bonded directly onto the PS-p sensor forming the Macro-Pixel Sub Assembly (MaPSA). Both front-end ASICs (like the CBCs) have binary readout. The SSAs read out the strip signal to form clusters. The data is forwarded to the MPAs and stored to be provided on request. The MPAs read out the pixel signals and correlate the clusters with those from the SSAs. In case the MPAs find a stub that fulfills the p_{T} criterion, the trigger information is sent through bonded wires to the CICs, which are bump bonded onto the bottom sides of the two FEHs. If an event is requested by the L1 trigger, the L1 data of the SSAs and the MPAs is sent trough the MPAs to the CICs over a single 320 Mb/s or 640 Mb/s differential line.

Instead of having a single SEH used for both the powering and the optical communication with the back-end, the PS module holds two hybrids [51]. The readout hybrid (ROH) houses the lpGBT and the VTRx+. The power hybrid (POH) provides LV for the front-end ASICs (the 16 MPAs, the 16 SSAs and the two CICs) and for the ASICs on the ROH (the lpGBT and the VTRx+). The LV distribution follows a two-stage DC-DC conversion. The input voltage of up to 11 V is converted to 2.55 V using the BPOL12V [50]. This voltage is further converted to 1.05 V and 1.25 V using two BPOL2V5. The FEH ASICs are supplied by two fine-pitch connectors on both sides of the POH. The ROH chips receive the LV through the right-side FEH and an extra flex cable that is directly connecting the POH with the ROH.
To assure proper cooling of the PS-p sensor with the MPAs thermally coupled through bump bonds, the whole module is assembled onto a carbon fibre reinforced polymer (CFRP) baseplate that will be directly coupled to a cooled surface on the large structures. The PS-p sensor is separated from the PS-s sensor by aluminum nitride (AlN) spacers (similarly to the AlCF bridges in the 2S modules). As AlN itself is an isolating material, Kapton strips are not required for HV protection in comparison to the 2S modules. The two FEHs, the POH and the ROH are glued onto the CFRP baseplate at the two ends.

3.3.4. The chronological context

The Physics Institutes IB and IIIB of RWTH Aachen University have committed themselves to contribute as an assembly center of 2S modules for the Phase-2 OT TEDD. Up to 1000 modules will be produced in Aachen, before they are sent to DESY Hamburg, where the so-called burn-in test will be performed and where the modules will be installed onto the larger structures. In the burn-in test, the assembled modules are exposed to a number of temperature cycles and the functionality is evaluated by readout tests. Afterwards, the modules will be sent to CERN for final integration.
The work of this PhD thesis is related to the prototyping phase. Therefore, the discussed 2S modules consist of non-final prototype components. The first modules assembled in Aachen have been built with the 8CBC2 FEHs [52, 46]. Figure 3.7 shows a photograph of a 2S module with 8CBC2 FEHs. This generation of FEHs is not connected to a SEH, instead the chips are powered and read out by a test card, connected on the side via a flex cable. Therefore, a SEH has only been used to connect the HV to the sensors at that time. Compared to the final chip design referred to as CBC3.1, the CBC2 has a lower trigger latency of 6.4 µs, which is half of the nominal value. Additionally, it does not have a stub gathering logic with bend lookup formatting. Starting with the 8CBC3.0 FEH generation [53], CICs were used for the first time with powering and communication through the SEH. The CICs were not yet part of the FEHs but plugged into hybrids as mezzanine cards. As an alternative, the FEH could still be powered and readout with a dedicated interface board. The CBC3.1 is an improved version of the CBC3.0 with bug fixes. Figure 3.8 shows an 8CBC3.1 module with CIC mezzanine cards. The SEH used in the course of this thesis is the SEH3.0 or SEH3.1 [49], which does not yet hold the lpGBT and the VTRx+ that have been in development at that time, but instead the GBTx ASIC with an additional Slow Control ASIC (SCA) used for the slow control and the VTRx with a larger footprint but full functionality. Furthermore, instead of the bPOL12V DC-DC converter the FEAST2.1 [50] and a commercial buck converter are used. During the module

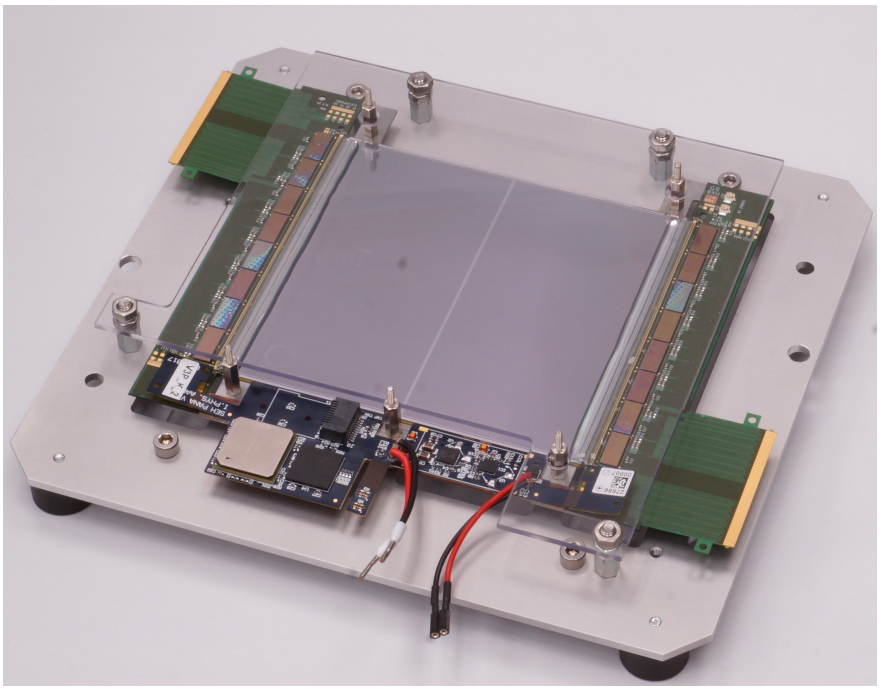

Figure 3.7.: Photograph of a 2S module with 8CBC2 FEHs. The shown module is the first functional 2S module assembled in Aachen (referred to as M1801). The module is mounted into a carrier jig.

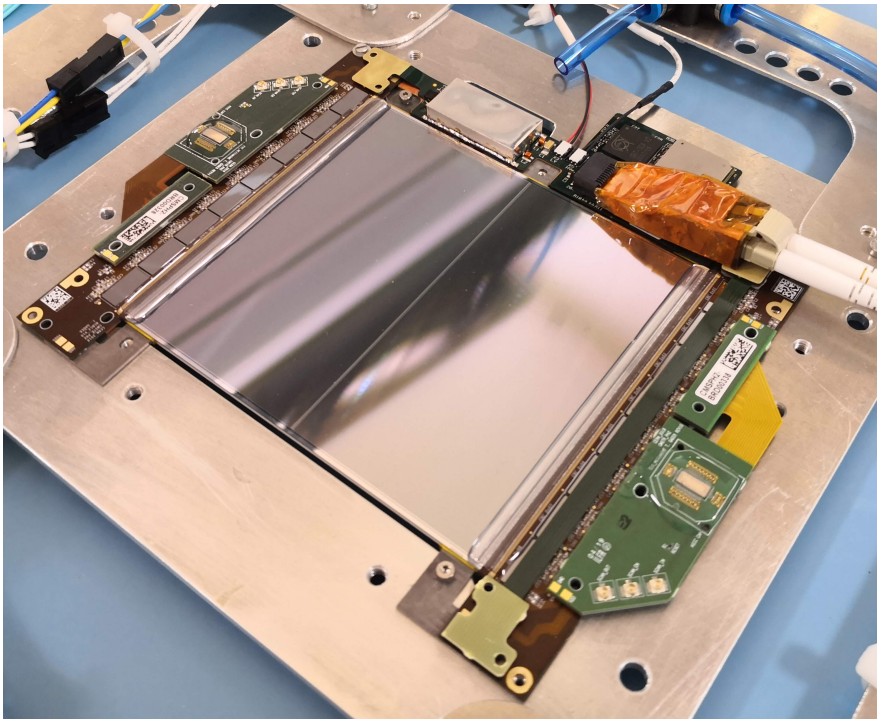

Figure 3.8.: Photograph of an 8CBC3.1 module with CIC mezzanine cards. The module (referred to as M1804) is shown prepared for a beam test.

prototyping phase also different options of the sensor material have been evaluated. Most of the modules assembled in the course of this thesis hold so-called FZ290 sensors with an active thickness of 290 µm. As an alternative, a pair of sensors with an active thickness of 240 µm, called thFZ240, has been tested.
The start of the pre-production is scheduled for June 2023. During the pre-production the module assembly procedure and the quality of the assembled modules are validated. For this, the module's quality assurance (QA) is advanced and the assembly output is reduced as compared to production mode. The production is currently scheduled to start in April 2024 and will be completed until March 2026.

4. Wire bonding

Wire bonding is a standard procedure in electronics industries to establish electrical connections between two components by cold welding. It is used in the production of microelectronic devices like computers or smartphones and nowadays is also applied to manufacture batteries for electrically powered cars. Because of the large scope of application, there are different methods for the wire bonding of different kinds of wires [54].
Particle detectors, especially those used for particle tracking, often rely on semiconductor sensors because of their fast response and a potentially fine resolution at small form factors. The semiconductor sensors usually are connected to readout electronics using wire bonding techniques. The technique chosen for the Phase-2 OT of CMS is the so-called wedge-wedge wire bonding of aluminum wire with a thickness of 25 µm. Figure 4.1 presents the procedure of wedge-wedge wire bonding. The wire is guided through a thin wedge shaped tool (what gives the procedure its name) and held in position by a clamp. The bonding process starts by moving down the wedge onto the "start bond surface" to electrically connect with the "destination bond surface". While moving onto the start bond surface, the bonding machine awaits the touchdown and applies the so-called touchdown force (TDF) to pre-deform the wire. Afterwards, the bonding machine starts to generate the ultra-sonic (US) signal, which is translated to a mechanical movement via the transducer to apply the "US power". The wedge vibrates at about 100 kHz along the bonding direction parallel to the surface with an amplitude of only 1 to 2 µm while additionally applying a bond force (BF) onto the surface [55]. After the welding of the start bond is completed, the clamp is opened and the wedge moves up and to the position of the destination bond. Before reaching the surface, the clamp is closed again and the welding process is repeated. Finally, the wire is torn off by moving up the wedge with closed clamp.
The welding process itself can be divided into three phases: the cleaning phase, the mixing phase and the diffusion phase [55, 57].

1. Cleaning phase: Within the first few milliseconds, the aluminum wire moves synchronously with the wedge and oxide layers as well as contamination of the bond surface are cleaned away. Additionally, atomic lattices of the bond surface and the wire are exposed. The wire deformation and the temperature increase is small in this phase.

2. Mixing phase: The exposed atomic lattices of wire and bonding surface get in contact and the bonding begins to take place. Single spots of metallic interconnection start to grow. The wire becomes more and more immobilized on the side of the contact surface while the top surface still moves. The non-elastically applied deformation and the temperature increase reach their maximum.

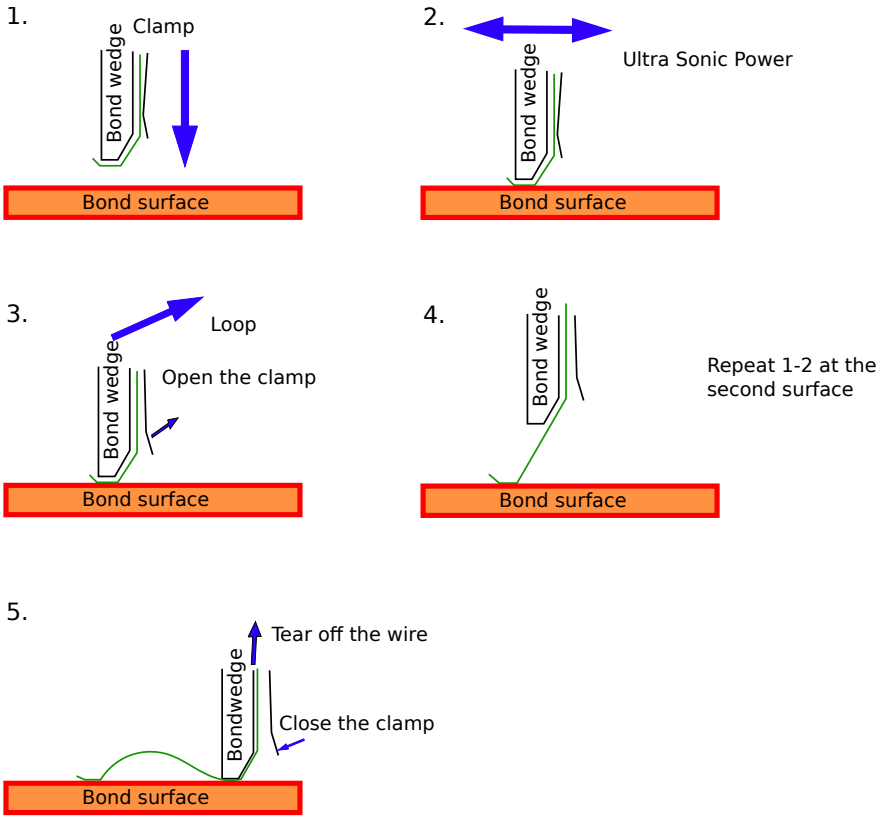

Figure 4.1.: Sketch of the wire bonding process [56].

3. Diffusion phase: The metallic interconnection is grown to the whole bond area. The wire deformation and the temperature increase stagnate. The upper layer of the bond surface now also moves (with highly reduced amplitude) as the metal atomic defects diffuse.

The wire deformation during the three phases is shown in Figure 4.2. Wire deformation is meant as the change of the wire height under the wedge during the bonding process in this thesis.
In order to achieve a strong bonding connection, many bonding parameters have to be carefully tuned. The wire deformation is set up by tuning the US power, the TDF and the BF as well as the bond time. By defining the path of movement between start and destination bond, the wire geometry can be regulated. More information about the optimization of bonding parameters can be found in my master's thesis [56].
The quality of the wire bonds can be tested either non-destructively or destructively using a pull tester machine. The machine features a fine hook of 50 µm (or 75 µm) thickness which is moved underneath the wire to pull it and simultaneously measure the force. In the non-destructive test, the pull tester applies a defined force and checks whether the wire can resist. In the destructive pull test, the pull test machine increases the force until eventually the wire is torn off. The tear force and the breaking mode and position are documented as a result. A "lift-off" (wire completely lifting off from the surface) indicates an unstable bonding process resulting in poor quality of the sample. Breaks at the bond heel ("heel breaks") are preferred because the heel is expected to be the thinnest part of the wire. In case the bond surface breaks, there is a problem with the bonding substrate rather than a problem with the bonding parameters. If the wire breaks at the position

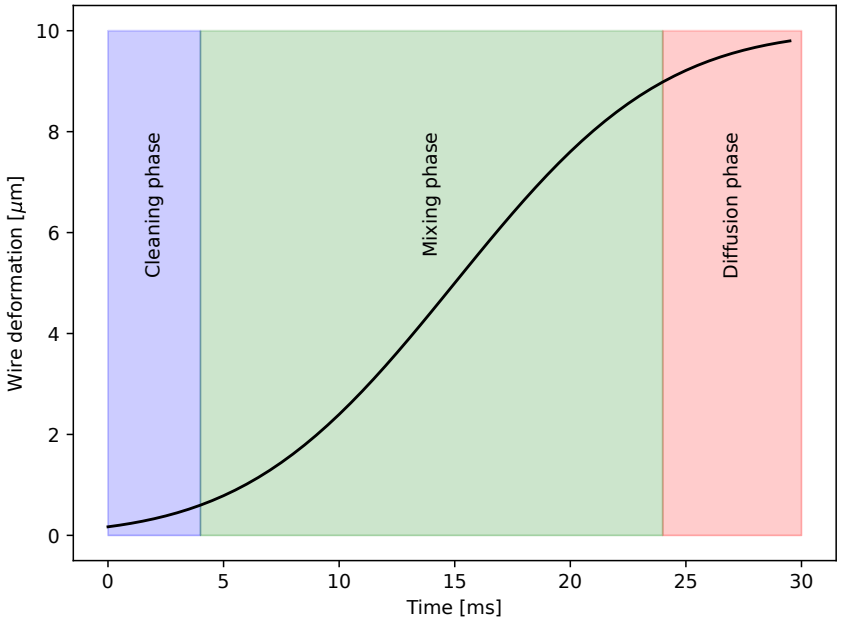

Figure 4.2.: Exemplary deformation curve (artificial). The scale of time and wire deformation are chosen at a realistic order of magnitude.

where the hook is placed, the bonds and even the heels are stronger than the unaffected wire. If in this case the tear force is low, this indicates a problem with the wire material. Because of the geometrical constraints (wire geometry, start and destination bond height) the tear force measured by the pull tester machine needs to be corrected by a correction factor $K_{1/2}$ to determine the force applied to the bond itself which can be calculated by

$$K_1 = \frac{\cos\beta}{\sin(\alpha+\beta)} \qquad \text{and} \tag{4.1}$$

$$K_2 = \frac{\cos\alpha}{\sin(\alpha+\beta)} \tag{4.2}$$

with K_1 (K_2) being the correction factor for the tear force applied on the start bond (destination bond) and α (β) being the angle between the wire and the bond surface at the start bond (at the destination bond).

5. Assembly of 2S modules

Many prototype 2S modules of different generations have been assembled by the working group of Physics Institute 1B and 3B of RWTH Aachen University. Six functional prototypes as well as many nonfunctional dummy modules have been built to evaluate and train the assembly techniques and to study the performance of the current module design. In the course of this PhD thesis, the special focus was set on the wire bonding tasks. Table 5.1 gives an overview of the assembled modules and a short summary of the motivation and studies related to the respective modules.

Table 5.1.: Overview of the assembled modules.

Module name	**Assembly date**	**Motivation / related studies**
M1801	09.2018	First functional 2S prototype module, 8CBC2 FEHs
M4001	02.2019	First functional 4.0 mm prototype 2S module, sensor debugging with IR camera
M1802	07.2019	2S prototype module with thFZ240 sensors, studies for the sensor material decision, stopped assembly after sensor gluing
M1803	07.2019	First prototype 2S module with 8CBC3.0 FEHs, CIC mezzanine and optical readout
M1804	11.2019	First 2S prototype module with 8CBC3.1 FEHs, used for beam test campaign in November 2019
M1805	02.2021	2S prototype module with production sensors, used for X-ray studies in the course of a bachelor's thesis
M4002	06.2021	Close-to-final prototype module with 4 mm sensor spacing used for a beam test, first functional module with new HV pigtail design and sixth cooling contact

The module assembly procedure at RWTH Aachen University as done until mid 2021 is described in Section 5.1 step by step. Afterwards, specific parts of the module assembly and QA are discussed in detail as they were partially or entirely developed within the scope of this PhD (Section 5.2 to 5.3). Section 5.4 presents lab tests performed on prototype modules. In Section 5.5 preparations and planning of module series production in Aachen are presented.

5.1. The assembly procedure at RWTH Aachen University

The assembly of the 2S modules is a multi-stage process which takes several days of time to meet the curing times of the used two-component (2K) glues. Custom jigs are used for the different steps

of module assembly to ensure high precision alignment of the components. The simple design of the assembly jigs enables the affordable multiplication of jigs for parallelization of assembly steps. The module assembly procedure and the design of the jigs will be the same (or at least similar) at the different assembly centers to achieve a module quality that is independent of the assembly center. The assembly procedure and jigs described in this thesis have been used in Aachen during the prototyping phase, before the community has agreed on a common procedure. Therefore, some of the steps have to be considered preliminary.
The assembly centers receive the following components for each module, as produced by different manufacturers:

- two silicon strip sensors,
- a SEH,
- two FEHs, a left side and a right side version,
- two long AlCF bridges and a stump bridge,
- six Kapton strips with four long and two short ones corresponding to the two different types of AlCF bridges,
- two Kapton pigtails for top and bottom sensor to connect the HV.

Each of the listed components is tested after reception in terms of a visual inspection and sensors and hybrids are checked also by conducting electrical tests. Afterwards, the assembly chain as visually summarized in Figure 5.1 starts:

1. The Kapton strips and the HV pigtails are glued onto the sensor back-plane. This step is performed for the top and the bottom sensor. At that point the position (top or bottom) of the sensor in the module is defined by the choice of the respective pigtail as the top sensor type holds a thermistor.
2. The electrical connection of the HV pigtails to the sensor back-plane is made by wire bonding 10 to 15 wires from the pigtail onto the sensor. Afterwards the wires are encapsulated by a silicone 2K glue to protect them from any damage.
3. The top and bottom sensors are combined to a parallel stack. With the AlCF bridges in between the sensors are glued back to back.
4. The two FEHs and the SEH are glued onto the outer ends of the AlCF bridges.
5. The FEHs and the sensors are electrically connected by wire bonding. On each of the four sides (top left, top right, bottom left, bottom right) 1016 channels are wire bonded. Additionally, the FEH ground pads are connected with the bias ring and the antenna pads of the FEH are grounded.
6. The wires connecting the FEH with the sensors are encapsulated with a silicone glue.

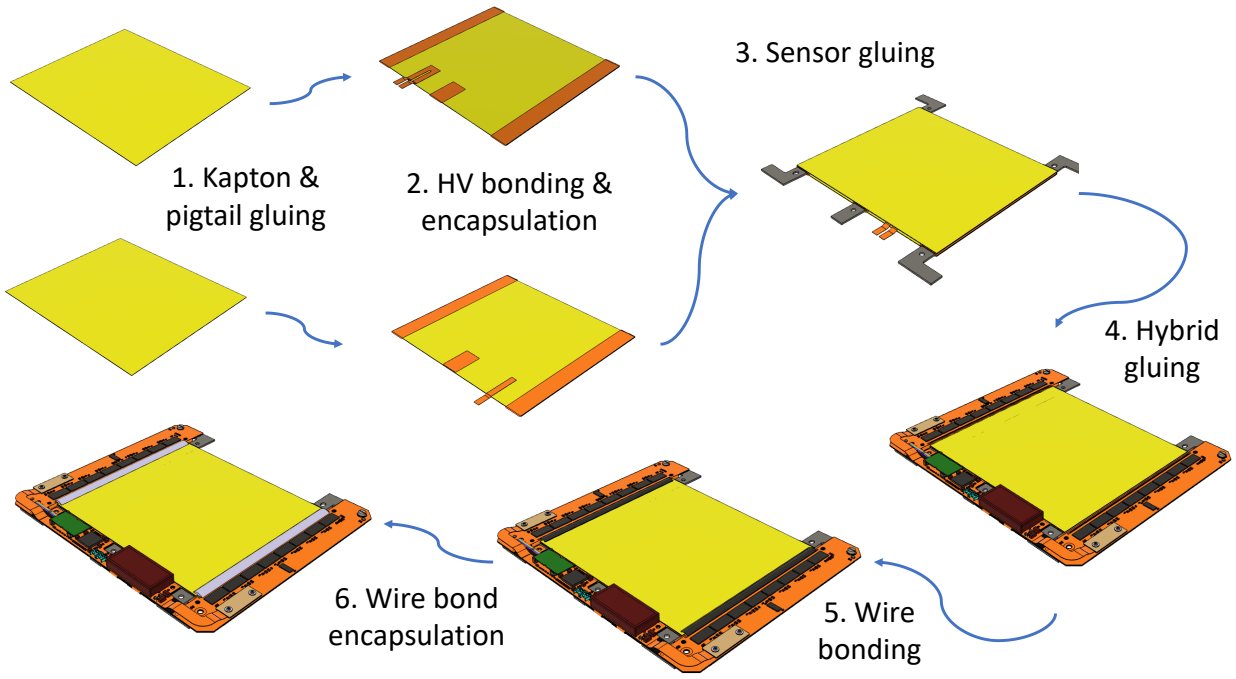

Figure 5.1.: Overview of the 2S module assembly process. The silicon strip sensors are drawn in yellow.

In the following, the different steps and the tools used are described in more detail. The gluing procedures and some of the jigs have been developed by Nicolas Röwert in the course of his master's thesis [58] and his ongoing PhD thesis.

5.1.1. Tools and machines used for module assembly at RWTH Aachen

The 2K glues are mixed using the *Amann Girrbach Smartmix X2* [59] with programmable mixing speed and a vacuum power of −800 mbar to remove bubbles. The glue dispensing is done with the *Nordson EV4* [60] gluing robot with the *Nordson Ultimus IV* as dispensing unit. The *Nordson Ultimus IV* is a volumetric dispenser that uses a bowden cable to press a defined volume out of the syringe. Additionally, a second *Nordson EV4* is available with a *Nordson Ultimus V* [61] which allows parallelization of gluing steps and adds more redundancy. The *Nordson Ultimus V* is an air pressure dispensing unit that can precisely adjust the pressure over time to compensate for viscosity changes of the 2K glue.
The following glues are used for 2S module assembly:

- *Polytec EP 601 LV* [62]: It is a transparent 2K epoxy glue with low viscosity of 240 mPa s in mixed state at 23 °C and it has a pot life of 4 h. The curing time at 23 °C is 16 h but can be decreased by increasing the curing temperature.

- *Polytec TC437* [63]: It is a white colored, thermally conductive and electrically insulating 2K epoxy. It has a viscosity of 5500 mPa s at 23 °C and mixed state. At this temperature the pot life is 2 h. It is filled with boron nitride with a particle size of up to 20 µm. Its thermal

conductivity is specified to (0.6 ± 0.1) W/mK. The curing time at 23 °C is 24 h but can be decreased by increasing the curing temperature.

- *Sylgard 186* [64]: It is a transparent and soft 2K silicone encapsulant with a high viscosity of 66 700 mPa s. It has a pot life of 1.65 h.

Wire bonding is performed using the *F&K Delvotec G5 64000* [65] thin wire wedge-wedge bonding machine. It is equipped with a conveyor system for automated wire bonding of up to four 2S modules without manual interaction of an operator. Additionally, the machine features a system called Bond Process Control (BPC) for optimized bonding quality and advanced monitoring of the bond process. A more detailed description of the BPC and of how it is used for QA of 2S modules in Aachen can be found in Section 5.2. Pull tests for wire bonding quality assurance are performed with the *F&S Bondtec LT-101* [66].
The wire used for the bonding processes is 25 µm thick and made of a composition of 99 % aluminum and 1 % silicon. During the prototyping phase, spools of 100 m and 500 m by *Heraeus* [67] or *Tanaka* [68] have been used. The bonding wedge chosen for the bonding processes of the 2S module assembly is the *4WFV4-1820-W7C-F00* by *Micro Point Pro* [69]. Pull tests are performed with the pull hooks by F&S Bondtec with a hook diameter of 50 µm and a hook length of 135 µm.

5.1.2. Gluing of Kapton strips and HV pigtail

The HV isolating Kapton strips and the HV pigtails are glued onto the sensors with the 2K epoxy *Polytec EP 601 LV*. The design of the gluing jig for this application is based on a version designed by the Fermi National Accelerator Laboratory (FNAL) CMS tracker upgrade group. It consists of two different parts made of aluminum: one part to hold the sensor and the HV pigtail in position (Figure 5.2) and one part to place the Kapton strips (Figure 5.3). In the course of this thesis, both parts have been adapted to make the sensor part compatible with the bonding machine. Further improvements of the FNAL design have been implemented by Nicolas Röwert as part of his PhD.

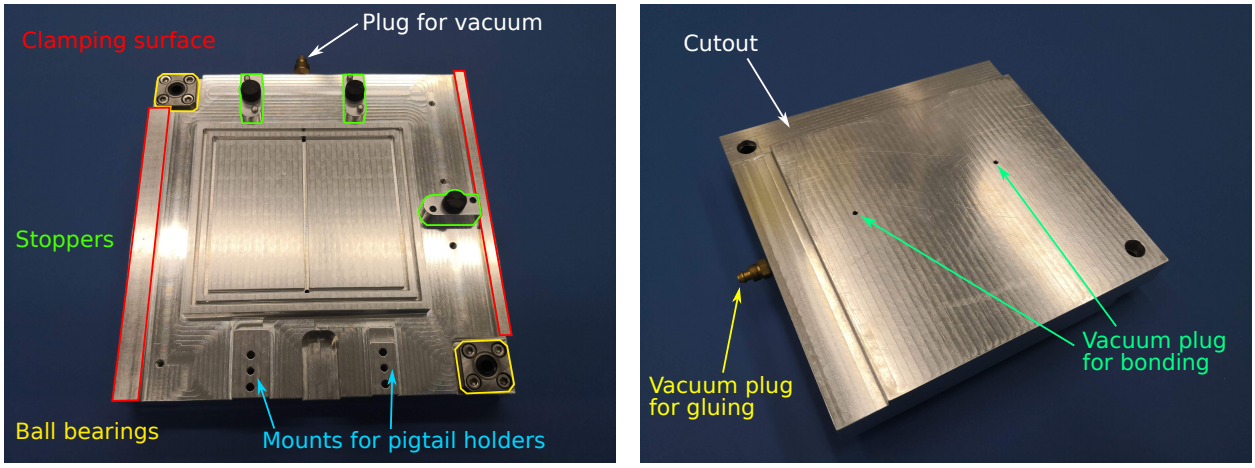

(a) Top side view.

(b) Bottom side view.

Figure 5.2.: The sensor part of the Kapton gluing jig.

By adapting the Kapton gluing jig to the bonding machine the sensor can remain on the sensor part of the Kapton gluing jig to wire bond the HV wires from the pigtails onto the sensor and handling

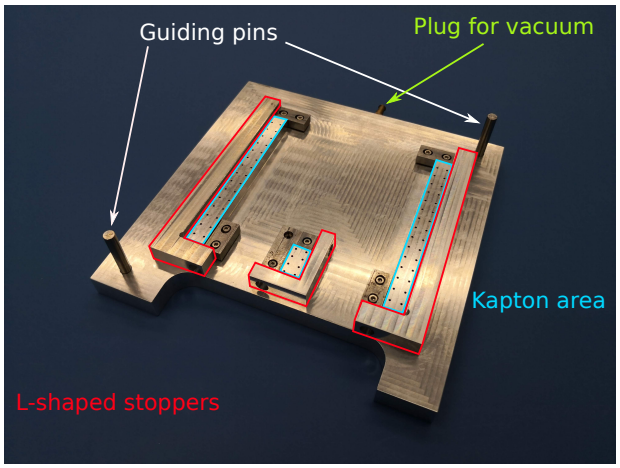

Figure 5.3.: The Kapton part of the Kapton gluing jig.

steps can be reduced to avoid damages during the module assembly. For this, the thickness of the base plate has been increased to 26 mm at the sensor area to reach the working height of the bonding machine. The width and depth have been reduced to exactly the same dimensions as for the wire bonding jig (discussed in Section 5.1.6), i.e. to 156.7 mm by 156.0 mm on top with a cut away of 20 mm on the bottom side to fit the jig to the conveyor system and the fixation within the bonding machine. Additionally, at two sides (left and right side in Figure 5.2 (a)) an even surface has been added at appropriate height for automatic clamp fixation. The vacuum fixation of the sensor during wire bonding is realized by adding an additional inner ring connected to the bonding machine vacuum from the bottom side. It is completely separated from the vacuum ring for the Kapton gluing which surrounds the inner one. The contact area of sensor and jig is covered by a 100 µm thick ESD safe plastic foil to protect the sensor strip side from scratches. In order to enable automated wire bonding of up to four sensors and to avoid a collision of the vacuum connector with the next jig, a recess has been milled on the opposite side of the vacuum connection between the slots that are used to mount the pigtail holders.

The Kapton and pigtail gluing is done in the following way: The sensor is placed carefully onto the Kapton gluing jig sensor part with the strip side pointing down. The strips have to be oriented in a way that they are running parallel to the side of the jig with the pigtail fixation. The three stoppers, of which two are positioned on the side opposite to the pigtail fixation and one being on the orthogonal side, have to be in contact with the two edges of the sensor. This is checked by using a microscope before and after the sensor is fixed by applying vacuum. The Kapton strips are placed onto the Kapton gluing jig Kapton part, which is shown in Figure 5.3. It has three areas dedicated for the Kapton strips. These are provided with vacuum holes to hold them in place during the gluing process. At the edges pointing towards the side at which the SEH will be glued, L-shaped stoppers are clipped and held in position with small permanent magnets. The respective edges of the Kapton strip have to be in contact with these stoppers for precise placement to ensure safe HV protection and to avoid damages from glue that flows around the sensor edge. In this case, the sensor might stick to the jig and break when the sensor is lifted from the jig. Therefore, it is important to check a good contact of the stopper and the Kapton strip at the whole

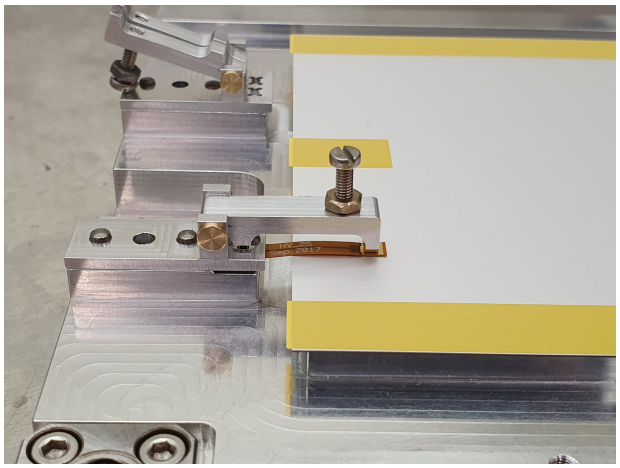

Figure 5.4.: The pigtail holders [70]. In the photograph the pigtail holder for the bottom sensor pigtail is used. The pigtail holder for the top sensor pigtail (shown in the background) works similarly.

edge. Afterwards, the vacuum is applied and the stoppers are removed. A thin pattern of glue is dispensed onto the Kapton strips [58] before the Kapton part is turned upside down and carefully lowered onto the sensor. The Kapton part is guided along guiding pins with ball bearings for a smooth and precise movement. The Kapton gluing jig remains in this position until the glue is cured.

After the glue is cured the Kapton part is lifted and the gluing of the HV pigtails is done. The pigtails for the top and the bottom sensor are different as the top sensor pigtail does also hold a thermistor. The glue is applied as a tiny drop onto the pigtail. It is important not to use too much glue to avoid a large glue spread around the pigtail on the sensor. This might cause severe problems during the wire bonding of the HV connection. After applying the glue, the pigtail is clipped into the pigtail holder and carefully lowered onto the sensor. This is shown in Figure 5.4. The fixation with the holder ensures that the pigtail is glued at a position so that it can be plugged into the SEH at the end of the module assembly avoiding to apply stress to the flex cable or the connector. For glue curing, the holder remains in this position to softly press the pigtail onto the sensor.

During the prototyping phase the Kapton gluing and the gluing of the HV pigtails has been done in two separate steps. However, during series production that would implicate one more day of assembly per module and twice as many Kapton gluing jigs, which require more storage capabilities. Thus, the process will be further developed to combine both steps.

5.1.3. Wire bonding and encapsulation of the HV pigtail

The HV connection of the 2S module is achieved by wire bonding the HV pigtails to the sensor back side. For this procedure, the Kapton gluing jig sensor part is used. The jig is shown in Figure 5.2. The bond pad on the pigtails for both sensors has a size of 3.2 mm by 2.3 mm and is made of gold. As the entire pad can be used to electrically connect the pigtail to the sensor, there is enough space to bond multiple wires for redundancy. In series production at least ten wires have to be bonded. During the prototyping phase, at least twenty to thirty wires were bonded and some of those were

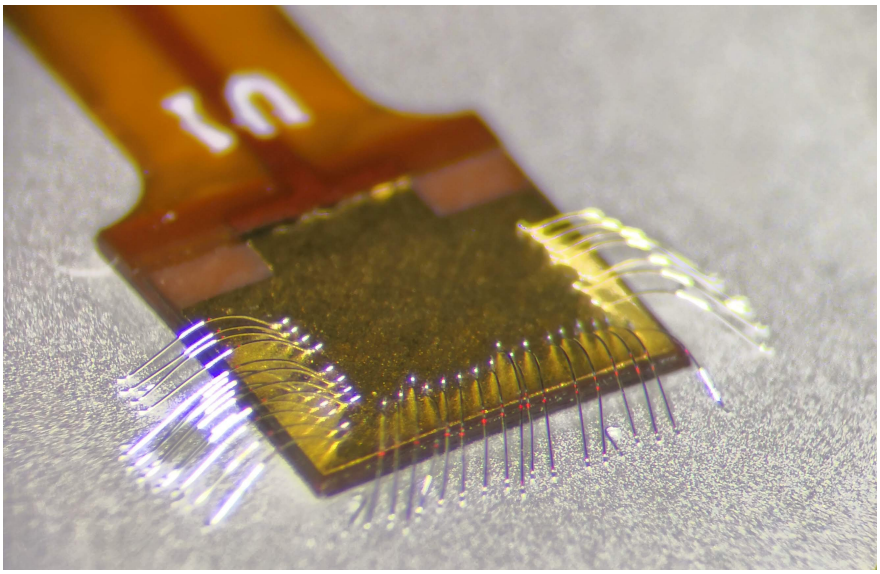

Figure 5.5.: Photograph of the bottom sensor pigtail bonds in the assembly of the *M4002* module.

pull tested for quality control. There is no specific bonding pattern defined by the community. However, a proper clearance between the encapsulated bond wire and the opposite sensor has to be respected to avoid the contact. If the bonding wire height stays below 700 µm above the sensor surface, there is enough clearance with additional margin for variations in the thickness of the encapsulating material. The wires are bonded in the direction from the pigtail onto the sensor to prevent a collision of the bonding wedge with the edge of the pigtail because of the height difference between the pigtail bond pad and the sensor backside. In Figure 5.5 a photograph of the bottom sensor pigtail bonds taken during the assembly of *M4002* is shown as an example.
Subsequently, the HV wires are encapsulated by carefully dispensing Sylgard 186 onto the pigtail. During prototyping this step has been performed either manually or using the dispensing robot. Both methods have worked out well as the encapsulation does not require a sophisticated pattern. However, to reproducibly achieve a defined amount of encapsulant, the usage of programmed dispensing times is recommended.

5.1.4. Sensor gluing and metrology

The sensor gluing process is done using the sensor gluing jig. A photograph of the jig is shown in Figure 5.6 (a). High precision and care is required because a misalignment in the positioning of the two sensors relative to each other, especially a rotational one, would affect the stub mechanism and therefore deteriorate the trigger efficiency of the Phase-2 CMS detector. Therefore, the community has agreed on the following specification for the alignment of the two sensors:

- Maximum displacement of the sensors perpendicular to the strips: 50 µm.
- Maximum displacement of the sensors in strip direction: 100 µm.
- Maximum rotational displacement as angle between top and bottom sensor strips: 400 µrad.

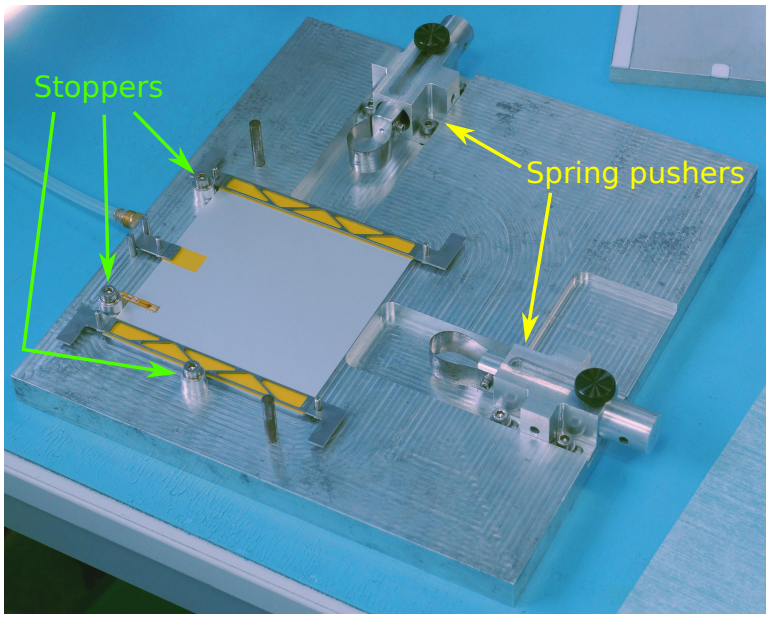

(a) The sensor gluing jig.

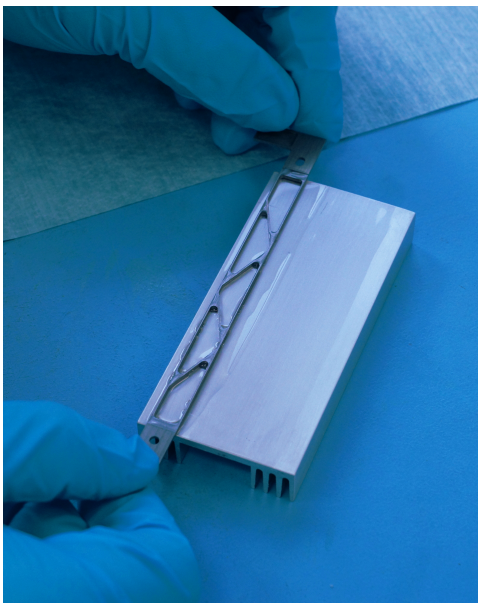

(b) Applying the glue onto the AlCF bridges.

Figure 5.6.: The sensor gluing process. These photographs have been taken during the assembly of the *M1801* module.

For this, the bottom sensor is positioned onto the jig with the sensor's edges being in contact with three stoppers. In order to hold the sensor in position vacuum is applied from the base plate while the contact of the sensor edges and the stoppers is checked by using a microscope. Afterwards, the three AlCF bridges are coated with the *Polytec TC437* by dipping their contacting surfaces into the glue which is uniformly spread on an aluminum plate. This process is shown in Figure 5.6 (b). The bridges are then lowered onto the sensor. The correct positioning onto the Kapton strips is ensured by using guiding pins. The top sensor is placed on top with two edges of the sensor being in contact with the three stoppers. The sensor is kept in position by softly pushing springs from the sides opposite to the stoppers against the sensor edge. Before and after, the contact of stoppers and sensor edges is checked with the microscope. For curing, a weight plate is placed on top. Guiding pins are used for accurate placement and to avoid slipping. The surfaces touching the sensor are covered with Teflon to avoid scratches.

After the glue is cured the sensor to sensor alignment is evaluated using the Double-Sided Metrology (DSM) machine [71]. The DSM is built up of a precise xy-table and two separably movable cameras pointing from the top and bottom side onto the module. By rotating the module and comparing automatically recognized distinct patterns of the sensor, a possible camera axes offset is corrected and afterwards the alignment specifications as described above are checked. Furthermore, a height profile can be measured by scanning the camera's distance to the respective sensor surface by searching its focal point. The sensor distance is determined by comparing the cameras' height coordinates after focusing.

5.1.5. Hybrid gluing

After sensor gluing and checking the sensor alignment precision, the hybrids are glued onto the module. For this, a jig developed by Nicolas Röwert as part of his master's thesis [58] is used. A photograph of the hybrid gluing jig during the assembly of a dummy module is shown in Figure 5.7.

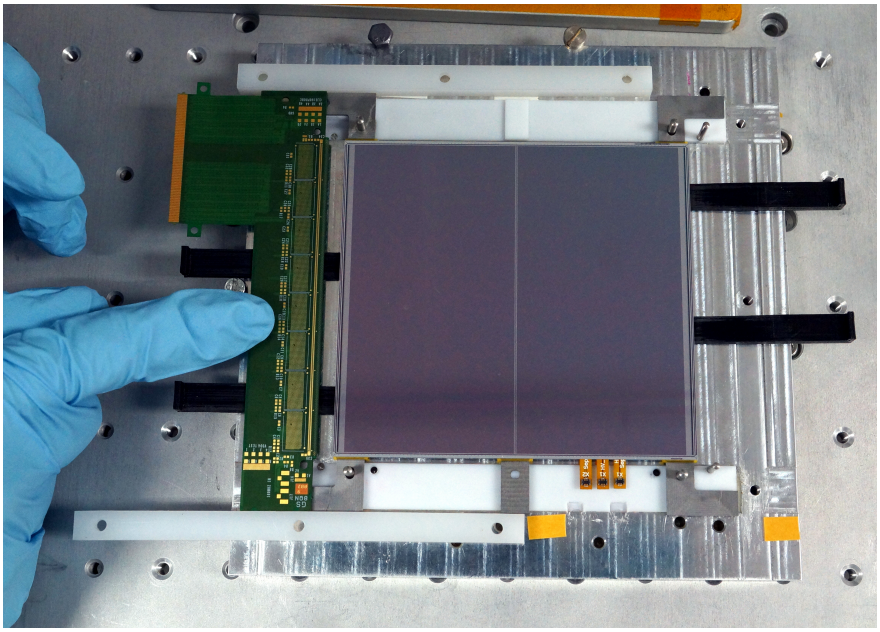

Figure 5.7.: Photograph of the FEH gluing process using the hybrid gluing jig during the assembly of a dummy 2S module [58].

The module is placed onto the jig with only the AlCF touching the jig surface. The contact areas are covered with Teflon to avoid scratches. The module is held in its correct position by guiding pins at the four corners of the module. A drop of *Polytec TC437* is dispensed onto each of the "ears" of the AlCF bridges using the gluing robot. Afterwards, two ramps of plastic are positioned at each side to slowly slide the FEHs onto the ears. The correct positioning of the FEH is ensured by inserting guiding pins at both ends of the hybrid. Finally, a weight is placed onto the gluing points. By checking that a small amount of glue oozes out to the edge it is assured that enough epoxy has been dispensed. A perfect alignment of the bond pads on the FEHs to the strips on the sensor is not required because the bonding positions are automatically aligned by the bonding machine by pattern recognition on both parts. The SEH is attached by plugging the connectors to the FEHs. After that, the *Polytec TC437* is carefully applied onto the AlCF bridges corner. By first plugging the connectors and then gluing the hybrid a safe electrical connection is ensured while a perfect parallelism between SEH and sensor edge is not of relevance. The SEH is lowered onto the bridges. Again, a weight is used to uniformly press the SEH at the gluing points onto the bridges to achieve homogeneous glue layers.

The procedure as described above will not be applied in series production. Instead, the CMS Phase-2 OT community agreed on a common procedure to be conducted at every assembly center. The tooling for this process has been developed at Karlsruhe Institute of Technology (KIT), consisting of a jig to bend the SEH connector tails, a second jig to plug the SEH into the FEHs and a third

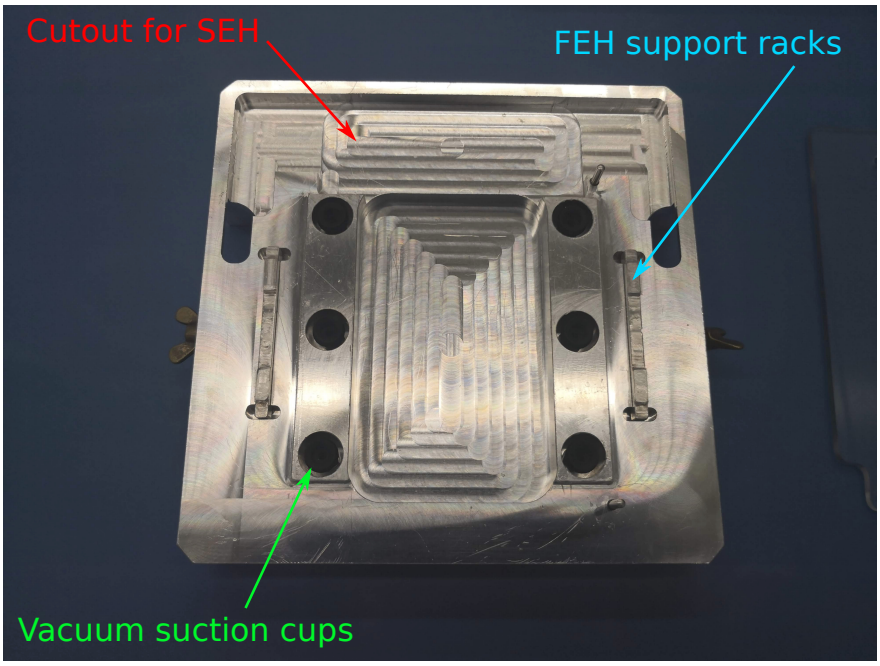

Figure 5.8.: Photograph of the wire bonding jig as used for the 2S module assembly at RWTH Aachen University.

jig for the actual gluing process. The hybrid gluing procedure using these jigs has not been done in the course of this thesis and is therefore not described in more detail.

5.1.6. Wire bonding

After gluing the hybrids, the electrical connection between the sensors and FEHs is established by wire bonding. For this step a jig based on the original design from CERN is used. Figure 5.8 shows the wire bonding jig as used at RWTH Aachen University. It has outer dimensions of 156.7 mm × 156.0 mm at a thickness of 26 mm. The module is aligned at the two mounting holes of the AlCF bridge on one side using two pins of 2.4 mm diameter. While bonding the top sensor, the bottom sensor (or vice versa) lies on two rectangular shaped supports of 16 mm width and 90 mm length. Additionally, the module is held in position by in total six electrostatic discharge (ESD) safe vacuum suction cups. The support surface itself is covered by ESD safe plastic foil of 100 µm thickness. The FEHs are supported by height adjustable racks. The height of the racks has to be set up for each module and each side individually after the module is fixed by vacuum. Contact surfaces to the FEHs are laminated with the same ESD safe foil.
In order to adapt the jig to the locally available bonding machine some minor modifications have been implemented. As the wire bonder is provided by a conveyor system, the outer dimensions have been enlarged to have a free surface to fix the jig within the machine using clamps. Additionally, the vacuum is supplied from the bottom side instead from the side.
After some prototype modules have been wire bonded, the support racks of the FEHs have been identified as a weakness. It is important to have a good support for the FEHs in order to avoid vibrations during the bonding process. However, setting up a proper height of the support rack has turned out to be difficult and very time consuming. On the one hand the gap between the jig

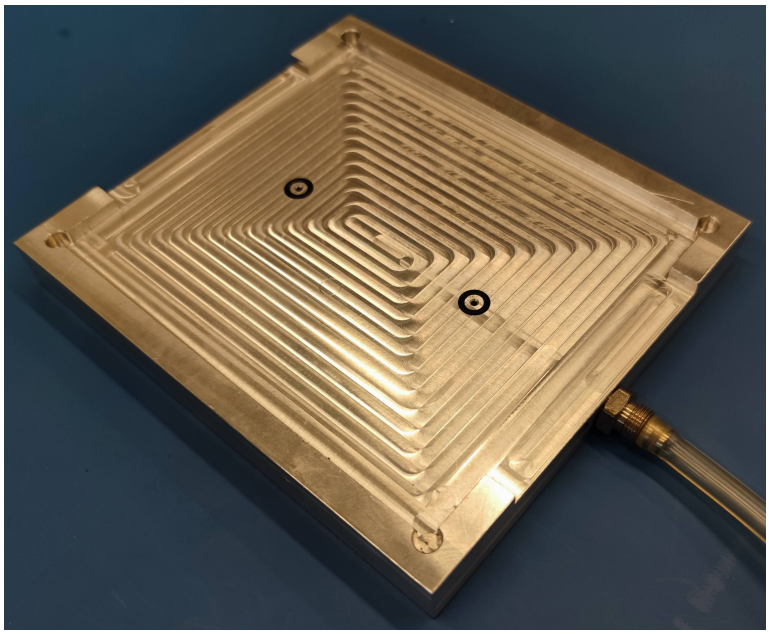

Figure 5.9.: Wire bonding preparation and pull testing jig.

and the module is tight and therefore setting up the rack height while visually checking if the rack is in contact with the FEH is challenging. On the other hand the adjustment has to be done with great care to avoid a bending of the AlCF bridges which could eventually lead to a break. Because of this, the wire bonding jig has been modified to simplify setting up the FEH support.
Instead of using screws to manually adjust the height of the racks, they are lying on tiny springs to softly push the racks against the FEHs. After the module is fixed on the wire bonding jig by activating the vacuum supply, the positions of the two FEH support racks are fastened by screws by pushing from the side. Up to three screws can be used on each side in order to avoid torsion effects. However, a single screw per side proved to be satisfying in tests when wire bonding prototype modules. For the purpose of safely fixing the racks, they have been enlarged in height by 5 mm to increase the surface area used to push against with the fixation screws. The resulting weight of the racks is 4.8 g each. To only softly push against the FEH avoiding any damages, springs with a wire diameter of 0.1 mm, an outer coil diameter of 1.3 mm, a (non-compressed) length of 12.4 mm and a resulting spring constant of 0.032 N/mm (3.2 g/mm) are chosen. Two of these are mounted on each side.
The height position of the FEH support racks is set up before the wire bonding can begin. The height adjustment of the support racks is done as a preparation step to avoid manual steps once filling the wire bonding jigs into the bonding machine during series production. For this, a separate jig has been designed, which can also be used for pull tests. Figure 5.9 presents a photograph of the aluminum jig as manufactured by the workshop of Physics Institute IIIB. The wire bonding jig is placed onto the base plate and it is surrounded by a frame avoiding a misplacement and movement. In this position the wire bonding jig is connected to vacuum to perform pull tests or set up the height of the support racks.
The wire bonding process itself is performed on the top and bottom sensor in an analog way once the wire bonding jig is prepared. It can be divided into two steps:

1. **Bonding of ground bonds:** The ground pads of the FEHs are located at the two ends next to the outermost channel pads on the top and bottom side, summing up to in total four ground pads per hybrid. The ground pads have to be electrically connected with the sensor bias ring to define the electrical potential on the sensor top side and to establish a common ground for the complete 2S module. These wires are bonded with the same wire geometry as the signal wires because the wire length is approximately similar and therefore a uniform wire height is achieved. For redundancy three wires are bonded from the FEH ground pad to the sensor bias ring. Additionally, the ground pads are connected with the two antenna pads which are close by. The antennas are used to perform electrical tests on bare FEHs by inducing a signal, but might induce noise in the detector operation if they are left floating. These wires are bonded with a simple symmetric and low wire geometry as the distance between the start and the destination bond is shorter than 1 mm and the two bonds are on the same height. A well-proven number of wires per antenna pad is three because there is enough space for three bonds on each antenna pad and in doing so there is redundancy in case of failure. In summary each 2S module has 24 bias wires and 48 antenna pad wires connected to the ground pads.

2. **Bonding of signal wires:** After bonding of the ground bonds, the signal wires are bonded. Each FEH holds 1016 channels for the top and the bottom sensor individually. The bond pads on the FEHs are arranged alternating in distance to the fold, so there is a row of short wires and a row of slightly longer wires. In doing so, the distance between the neighboring wires is maximized and the risk of shorting them is minimized. The bond program logic is visualized as a sketch in Figure 5.10. First the row of short wires is bonded, afterwards the row of long wires. Thereby, the risk of touching the already bonded wires with the wedge is reduced as the clearance is significantly larger. The bond position (both, start and destination bond) is programmed to be in the opposite corner of the bond pad with regard to the bond direction to avoid a collision of the bond wedge with remaining bond feet in case a wire requires repair work. In series production the bonding quality is tested on a sample basis by pull tests. Approximately 50 wires are bonded for testing purposes additionally to the regular wires uniformly distributed along the FEHs. The most reasonable way to implement these wires has been found to be by bonding a wire spanning over the regular one so that the test wire is slightly higher and can comfortably be pulled.

5.1.7. Wire bond encapsulation

After wire bonding, the fragile wires are encapsulated with the soft silicone glue *Sylgard 186* to protect them from any mechanical or chemical damage. Before the encapsulation, the noise of the 2S module is measured. Single channels with lower noise indicate that the respective channel could be unconnected and after encapsulation the bonding of the channel cannot be repeated without removing all wires on the respective side. The noise measurement and the encapsulation is performed with the 2S module mounted on the carrier jig, which is shown in Figure 5.11 (a) as a drawing. The module is mounted on the aluminum frame of the carrier jig at the cooling points on the AlCF bridges. The aluminum frame has a cutout to access the bottom sensor from below

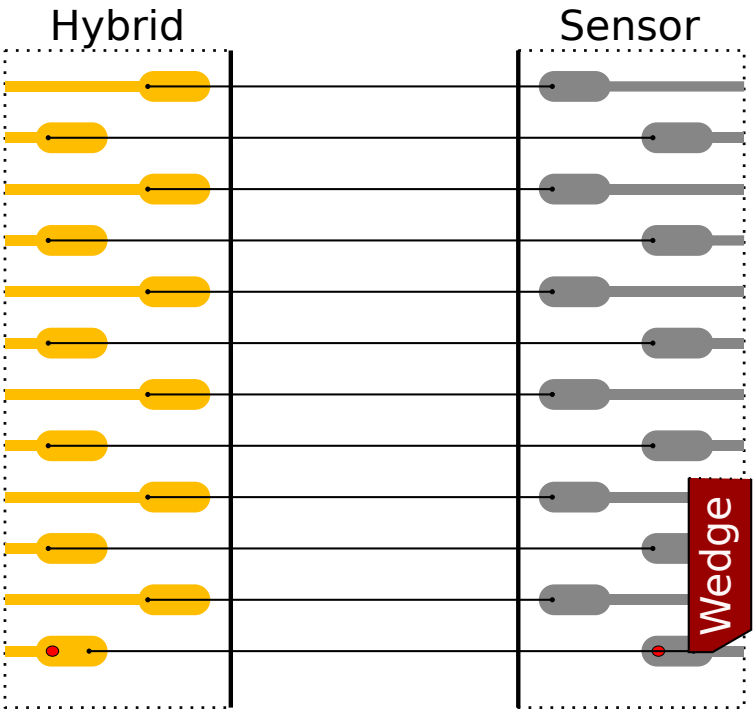

Figure 5.10.: Bonding program sketch. The red ellipses drawn into the last pair of bond pads indicate the position of remaining bond feet after removal of a broken wire.

and to avoid to take the module off from the carrier plate during the encapsulation of the bottom side. To protect the module the cutout is closed by a Plexiglas plate. Another Plexiglas plate can be attached from above. It is cut in a way that the SEH with its components still can easily be accessed.

The encapsulant material is dispensed over the signal wires while moving the glue syringe with the gluing robot with constant velocity in a spiral path. In order to cover the wires completely a spiral of seven parallel lines is set up. The dispensing program is visualized in Figure 5.11 (b). The velocity of the gluing robot can be set up to compensate for viscosity changes of the fluid depending on the time after mixing the Sylgard 186.

5.2. Quality assurance for wire bonding process

The wire bonding is an important step in the assembly of the 2S modules. The persistence of the functionality of each module channel depends on the quality of the bonds. Although it is a standard procedure in the industry of electric devices, the large number of wires and the geometrical constraints pose a challenge. Furthermore, once a 2S module is installed into the CMS tracker a broken wire connection cannot be fixed. Therefore, the QA of the wire bonding process demands special attention.

An effective procedure to set up the correct bonding parameters has been developed as part of my master's thesis [56]. The analysis of machine data to identify weak bonds and to simplify the QA process within the series production of 2S modules is described in Section 5.2.1. Experiences gained during the wire bonding of prototype modules are summarized in Section 5.2.2.

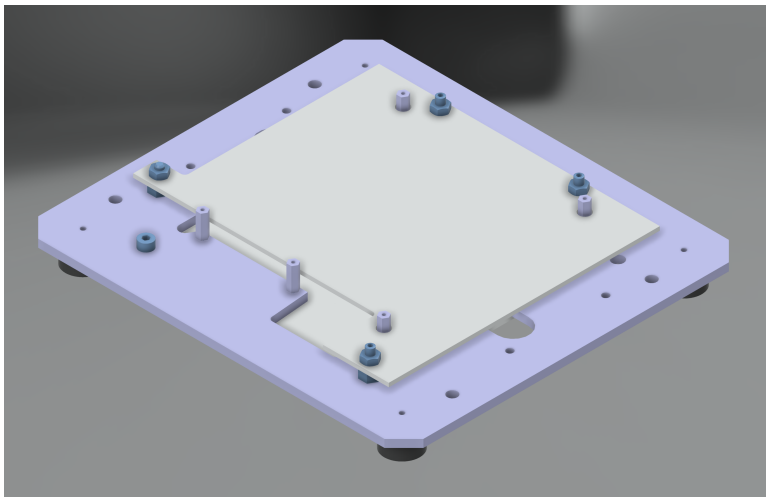

(a) CAD drawing of the carrier jig with Plexiglas plates attached.

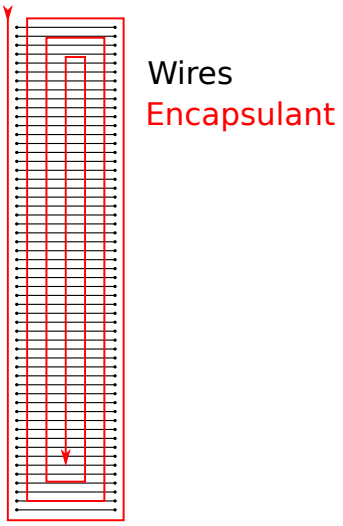

(b) Sketch of the encapsulation dispensing path. A spiral path of seven equidistant lines is dispensed to completely cover all bonded wires.

Figure 5.11.: Sketch of the 2S carrier jig and the dispensing program for wire bond encapsulation.

5.2.1. Analysis of machine data

Machine data

As part of the BPC, the bonding machine holds a database of multiple parameters which can be saved in an SQL formatted file and exported for offline analysis. Besides the settings used during the wire bonding process saved for each bond, also measurements of several quantities are monitored. The most important parameters extracted from BPC for offline analysis are listed in the following:

- Wire deformation: The deformation of the wire is measured every 0.5 ms by a proximity sensor as the vertical movement of the transducer after an adjustable force at touchdown has been exceeded. For this measurement, a proximity sensor is used.
- Bonding time: The time duration from beginning to apply the ultra-sonic power until the adjustable target deformation is reached is measured.
- Quantities related to the ultra-sonic generator (USG):
  - Phase: The electrical phase between the voltage and the current is saved once per bond. The effective ultra-sonic power is maximized at a phase of 0°.
  - Impedance: The electrical impedance is measured by the USG once per bond.
  - Frequency: The effective frequency of the wedge oscillation while applying the US power is measured every 0.5 ms.
  - Current: The electrical current used to generate the US power is measured every 0.5 ms.
- Wire deformation reserve: The wire deformation reserve quantifies the remaining capabilities to deform the wire at the end of the individual bonding process. Low values therefore indicate

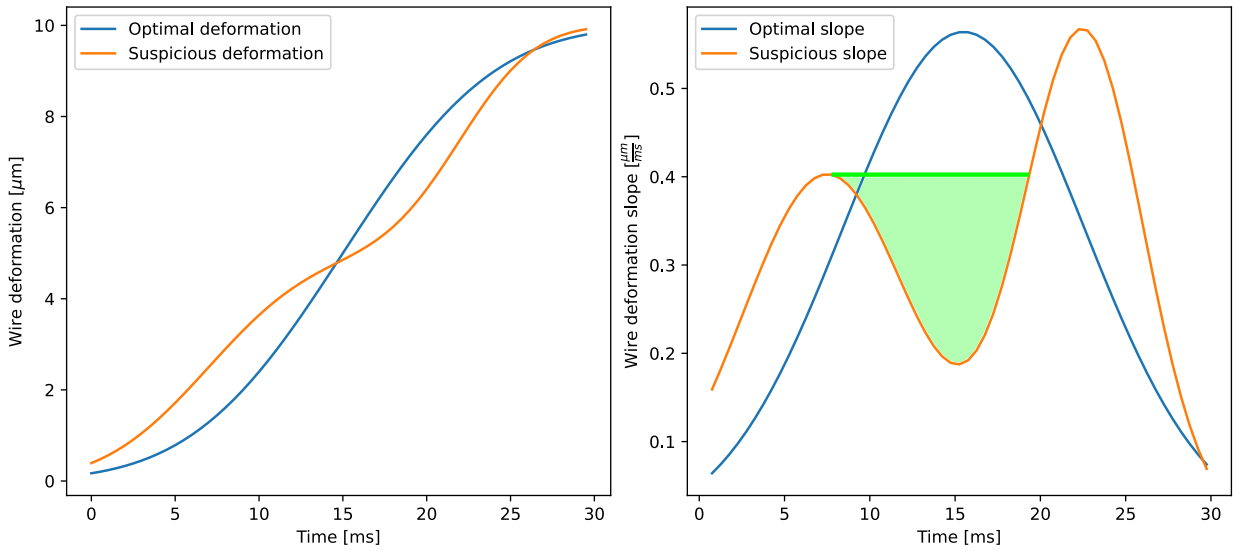

Figure 5.12.: Exemplary wire deformation data. The blue line shows an expected wire deformation time dependence (modeled as an error function) in the case of an optimal bonding process. A non-optimal bonding process (related to for example bad support or contamination) is drawn in orange. The breakdown of the wire deformation slope during the bonding process is quantified as the bond quality index Ψ defined as the integrated area of the slope breakdown colored in green.

a non-optimal setup of the bonding machine. At a value of 0 the machine stops the bonding process even though the target deformation might not be reached.

- Bond position and bond height: The coordinate of the bonds is stored with the height coordinate at touchdown. This information could for example be used to measure a height profile of the bonded material.

A Python module has been developed in order to simplify the access to this data. It contains tools for data handling and plotting, functions to access data from the local pull test database as well as calculation functions of custom observables for more advanced analyses. The Python module is used as a basis for any study related to wire bonding presented in this thesis.
One of the custom observables is the *bond quality index* Ψ which is defined to quantify sudden decreases of the wire deformation slope (called deformation breakdown in the course of this thesis). These could be caused by a problem in the support of the structure or by contaminated bond surfaces. Figure 5.12 presents two sketched wire deformation curves comparing an optimal wire deformation with a "suspicious" process. The left side plot presents the wire deformation curves, the plot on the right side shows the derivative. In the optimal case a slope curve with a single global maximum and no local minima is expected (Section 4). If there is a local minimum in the slope, it is called a slope breakdown in the course of this thesis. The magnitude of breakdowns of the deformation slope is quantified by applying the following procedure: The wire deformation curve (wire deformation in dependence of time) of the respective bond is derived to extract the wire deformation slope by calculating the gradient triangles in between the data points. After finding the global maximum of the slope, the slope curve is scanned for local maxima from the left and the right towards the global maximum. Then, an "optimized slope curve" is calculated by eliminating

the local minima replacing its slope value by the value of the respective local maximum. The integral of the area between the "optimized slope curve" and the original curve is defined as the bond quality index Ψ. The integrated area is highlighted in green in Figure 5.12. In order to avoid unwanted entries from digitization, a Savitzky-Golay filter [72, 73] with a filter window length of 5 and polynomial order of 2 is applied to the deformation curves before calculating their derivatives and determining Ψ. The optimal wire deformation curve would have $\Psi_{\text{opt}} = 0$ while large values of Ψ point to a potential problem.

The frequency is a parameter that reacts sensitively to any change of the bonding material. Therefore its progression during the bonding process should be well monitored. The bonding machine starts at a frequency defined by the operator. During the bonding process the frequency rises or falls until a certain settling frequency is reached. The value of the frequency at the end of the bond process f_{end} can therefore be used to identify irregularities. Additionally, the frequency range during the bond process $\Delta f = f_{\text{max}} - f_{\text{min}}$ is used as an observable.

Error sources

Ideally, the bonding machine is set up once by a bonding parameter optimization (as suggested in Ref. [56]). Afterwards, the parameters should not have to be adjusted anymore to perform the wire bonding process, but this requires that the overall quality and the properties of the bonding material (sensors and FEHs) and the supporting capabilities of the jigs do not change over time or from module to module. However, there are some errors that might occur locally. The most common and known error sources are described in the following.

During the assembly of the module the bond pads could be contaminated. In case of non-optimal clean room conditions or in the cause of transportation in unsealed packaging, dust particles could harm the bonding process. If the bonding wedge pushes onto a dust particle and it is hit away by starting the US power, the bonding machine would measure a movement towards the bonding surface which would falsely be interpreted as wire deformation. The expected wire deformation would feature a steep slope in the beginning before reaching a plateau when the actual bond pad is touched followed by a moderate deformation slope. In case of contamination of bond pads by glue or fingerprints caused by inattentive handling during the module assembly, the wire deformation would significantly be decelerated as compared to optimal conditions. This could lead to higher bonding times.

The bonding surface (for the 2S module either the FEH or the sensor) could be badly supported. This could be caused by inattentive adjustment of the bonding jig or by defective material, e.g. delamination issues of multilayer PCBs. Depending on the force feedback while pushing down the bonding surface the bonding machine falsely measures the wire deformation after reaching a force (which can be tuned by the operator) at touchdown so that effectively the target deformation cannot be reached. Additionally, the US power might result in a vibration of the surface rather than the bond connection.

The BPC to some point compensates these errors by automated readjustment of the US power within a predefined parameter space. However, in case of a false wire deformation measurement also the regulation of US power is affected, which might lead to a degradation of the bonding

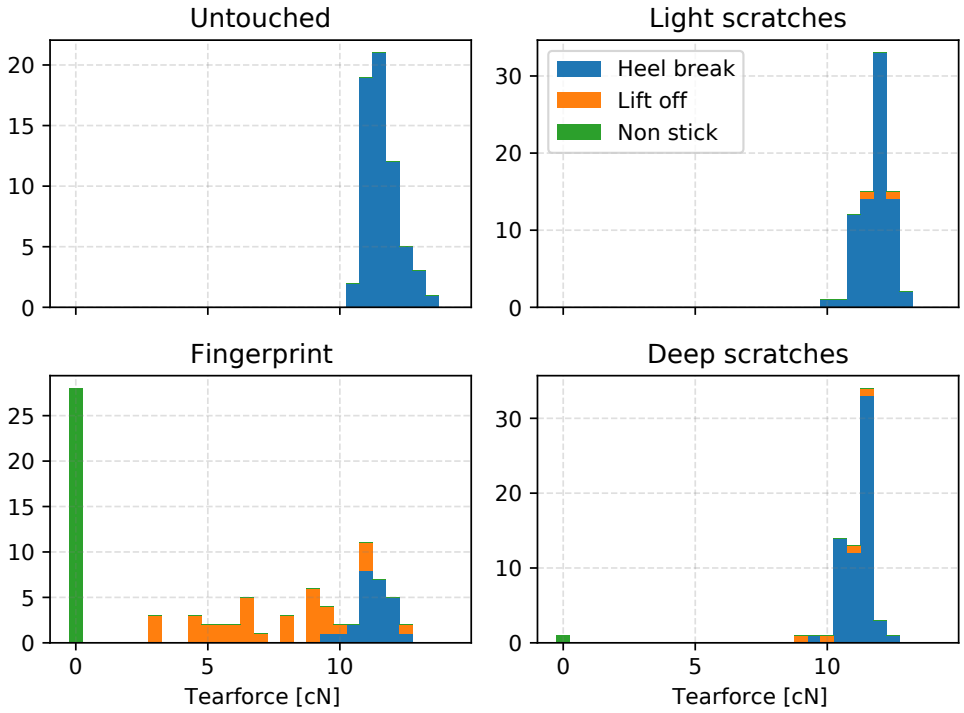

Figure 5.13.: Corrected pull test results in the different areas of the prepared sample. The applied factor is 1.9 for both bonds, the start and the destination bond.

quality. Therefore, pull tests performed on a sample basis and visual inspections supported by software to monitor machine data are of great importance.

The offline analysis of bond machine parameters

The bond machine parameters listed above are analyzed to identify potentially weak bonds. This information can be helpful in the visual inspection of bonded wires, as critical spots can systematically be inspected. For this, a threshold is defined for each parameter to separate the good bonds from the weak.

The offline analysis of the bond machine parameters is tested on a bonding test sample. The sample has large areas of electroless nickel immersion-gold (ENIG) and is fixed within the bonding machine using the 2S module wire bonding jig (Section 5.1.6). The surface has been treated to intentionally achieve a bonding sample of mixed quality. For this, an area has been scratched with the tip of a pair of tweezers, another has been contaminated with fingerprints, an area has been scratched with a screw for a rough surface and a last area has been kept immaculate. In total 300 wires have been bonded across these areas. The bonding has been done in only a few minutes, so the temperature can be assumed to be the same for each bond. All wires that did not stick have been documented and the remaining have been pulled using the pull test machine. The bonding machine data and either the information of non-stick wires or the pull test results are correlated to quantify the effectiveness of the identification of weak bonds.

Figure 5.13 shows the distributions of tear forces and grades measured in the different areas of the prepared sample. Within the untouched and lightly scratched region the corrected tear force is

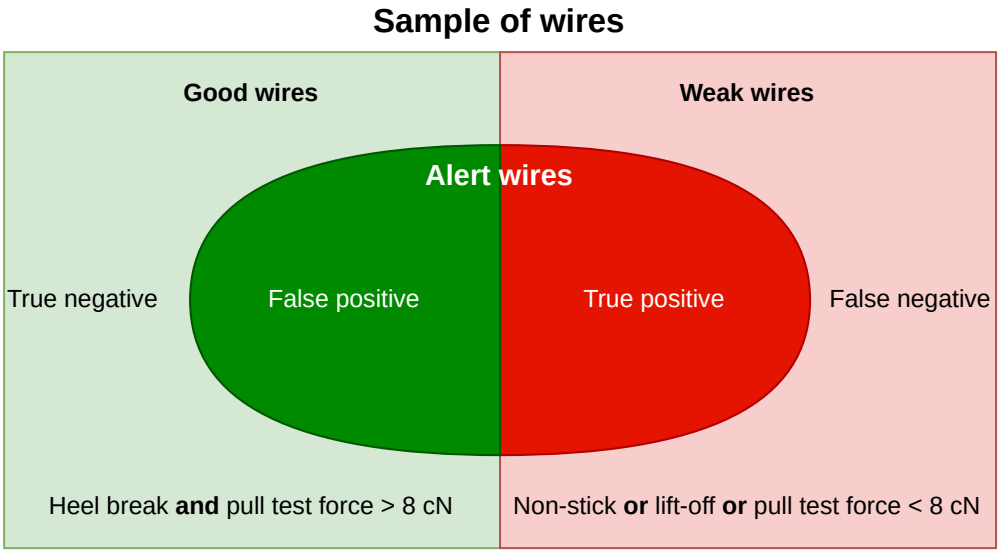

Figure 5.14.: Sketch to define sensitivity, specificity and accuracy.

measured to be 11.6 cN and 11.8 cN, respectively, with a standard deviation of 0.6 cN each. The region of light scratches only has two lift-off wires, while the rest is graded as heel break. The region of deep scratches is only slightly worse, with a mean tear force of 11.0 cN and a standard deviation of 1.4 cN. One wire has not stuck on the surface and four wires are graded as lift-off. By far the worst quality is found in the fingerprint region with a mean tear force of 6.0 cN and a standard deviation of 4.8 cN. A number of 28 of those wires have not stuck, 35 have been pulled as lift-off and only 25 as heel break. From these results, it is clear that working with gloves during module assembly is essential for wire bonding.

Wires are tagged as *weak* if they did either not stick on the surface or if the pull test resulted in a lift-off or the corrected tear force is below 8 cN. The rest of the wires is tagged as *good* wires. Using this definition the sample consists of 230 good and 70 weak wires. The offline analysis of bond machine parameters aims to reconstruct these subsets of the sample. The individual parameters are studied to find a threshold separating the good wires from the weak. If the parameter exceeds the set threshold at either the start or the destination bond, the wire is called an *alert wire* in the following. To evaluate the quality of the threshold, the sensitivity and the specificity are calculated. These are defined as

$$\text{Sensitivity} = \frac{N_{\text{True positive wires}}}{N_{\text{Weak wires}}} \quad \text{and} \tag{5.1}$$

$$\text{Specificity} = \frac{N_{\text{True negative wires}}}{N_{\text{Good wires}}}. \tag{5.2}$$

Figure 5.14 shows a sketch of the different subsets of wires. *True positive wires* are alert wires that are actually weak. The sensitivity therefore quantifies the reliability of finding weak bonds. The *true negative wires* are those whose parameter does not exceed the threshold and is actually a good wire. The specificity therefore quantifies how clean the set of alert wires is or how reliable

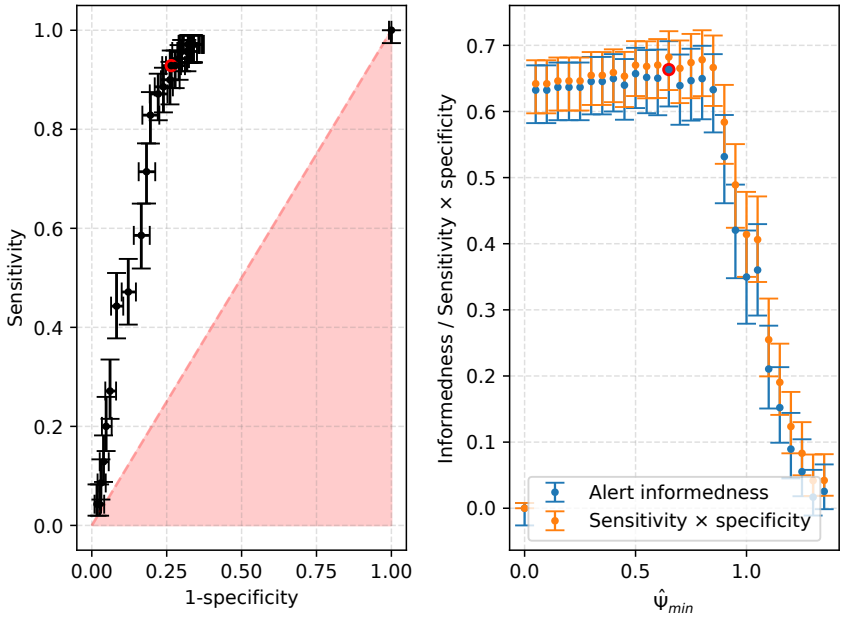

Figure 5.15.: Sensitivity and specificity of the alert wires using $\hat{\Psi}$ with different alert thresholds $\hat{\Psi}_{\text{min}}$ are presented within a ROC curve [75] on the left side. The distribution of J and S is shown on the right side. The red markers in both plots highlight the values at maximum S.

good wires are found. To identify the optimal threshold, the best combination of sensitivity and specificity has to be found. There are two approaches considered:

- Maximization of the Youden's index, also called informedness [74]:

$$J = \text{sensitivity} + \text{specificity} - 1. \tag{5.3}$$

  An informedness of 1 corresponds to a test with 100 % sensitivity and specificity while an informedness of 0 corresponds to a test with random picks. Considering a receiver operating characteristic curve (ROC curve) [75] it is a measure to quantify the distance from the bisecting line at which the test is not better than a random pick and therefore useless.

- Maximization of

$$S = \text{sensitivity} \times \text{specificity}. \tag{5.4}$$

  Mostly, S is maximized when also J is maximized. At some point however, the maximized S is achieved at more equally distributed values of sensitivity and specificity.

As an example, Figure 5.15 shows the calculated sensitivity and specificity of the analysis using the normalized quality index $\hat{\Psi}$ applied with different alert thresholds $\hat{\Psi}_{\text{min}}$ within a ROC curve. Already at small values of $\hat{\Psi}_{\text{min}}$ the specificity rises above 60 % while the sensitivity is still at close to 100 %. This indicates that $\hat{\Psi}$ is well suited to identify weak wire bonds. The best combination of specificity and sensitivity (considering the maximum of S) is achieved at $\hat{\Psi}_{\text{min}} = 0.65$ with a sensitivity of approximately $92.9^{+3.0}_{-4.6}$ % and a specificity of $73.5^{+3.0}_{-3.3}$ %.

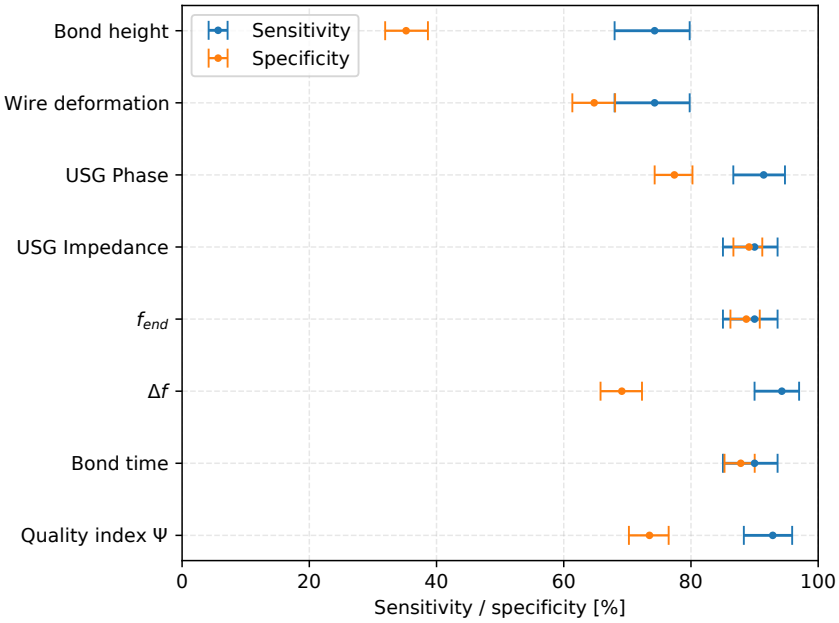

Figure 5.16.: Summary of sensitivity and specificity of the analysis using different bond machine parameters. The combination of sensitivity and specificity achieving the maximized S is shown.

Other parameters are evaluated in the same way. The best achievable combination of sensitivity and specificity for the analysis of each parameter is shown in Figure 5.16. Most of the parameters hold a sensitivity at about 90 % or more and specificity values between 70 and 90 %. Especially the USG impedance, the frequency measured at the end of the bond process and the bond time have been found to reach a sensitivity and specificity both close to 90 %. The bond height and the wire deformation at the end of the bonding process, however, have been found to be not sufficient in the identification of weak bonds for the tested sample.

With the different bond machine parameters performing similar in sensitivity and specificity, the question arises whether the different parameters are correlated and whether there is any added value in considering all of them. Figure 5.17 shows the probability $P(B|A)$ of identifying a wire as alert wire by using parameter B if it is identified as alert wire by using parameter A. By comparing the conditional probabilities of detecting an alert wire in case of a detection by bond time, f_{end} and the USG impedance it becomes clear, that the alert wires detected by using these parameters are congruent. Using the quality index Ψ, Δf and the USG phase for weak bond detection, the detection probability is about 97 % if the latter observables would have a detection, only the specificity is lower. So, there is no additional value in combining parameters.

The listed values of sensitivity and specificity are the best that can be achieved using a constant threshold. However, it is not known that the optimal thresholds found in the analysis of this sample of wires is also sufficient for other bonding scenarios. Bonding on a silicon sensor might for example lead to a shift of the parameter phase space. Additionally, a change of the laboratory temperature might influence the measurements of frequency and the behavior of the BPC. Therefore, instead of using constant threshold values, the threshold is determined for each data sample individually. Assuming that still most of the bonded wires have a good quality, wires are selected as an alert

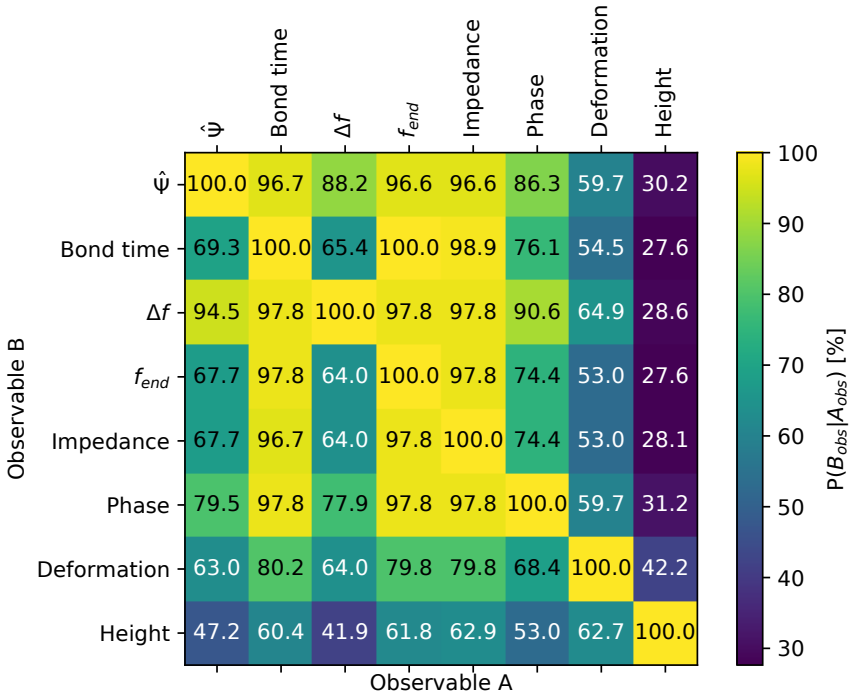

Figure 5.17.: Conditional probabilities of alert wire detection.

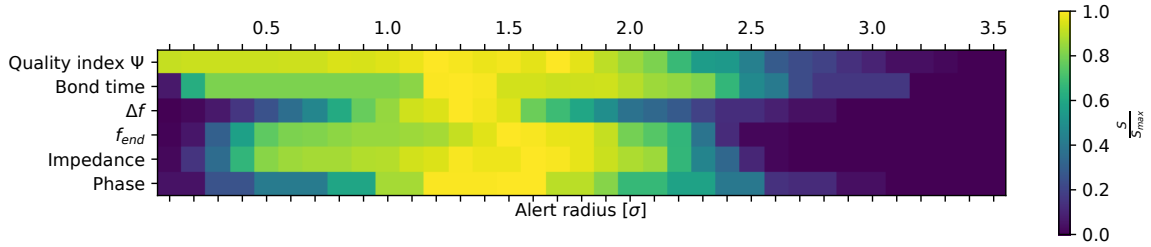

Figure 5.18.: Normalized S for different alert radii and bonding machine parameters.

wire if the considered parameter exceeds a certain radius around the sample's median. The median is considered instead of the mean to reduce the bias due to outliers. To compare sufficient radii independently of the choice of parameter, the radius is set in factors of the sample's standard deviation σ. Analogue to the analysis using individual fixed thresholds, the optimal outlier radius is determined by maximizing S. Figure 5.18 presents the product of sensitivity and specificity S for different radii and the different bond machine parameters. The analysis performs best at radii between 1.2 and 1.6 σ for all bonding parameters. The quality index Ψ stands out with a very broad phase space of good performance. Additionally, it is the only bonding parameter that by construction is expected to behave independently from outer conditions: the larger Ψ is, the more significant are wire deformation breakdowns.

GUI for 2S module wire bonding monitoring

The wire bonding is an important step in the assembly process of the 2S modules. With more than 4000 bonded wires per module, the wire bonding and its QA are time-intensive tasks. Pull

tests will be performed on a sample basis to detect fundamental problems, either related to the preceding assembly process (glue on bond area, non optimal storing conditions, fingerprints, ...), the quality of the bond pads (broken / lifting pads, delamination of multilayered PCBs, ...) or the bonding machine itself (contaminated or damaged wedge / wire, non optimal bonding parameters, ...). Additionally, a visual inspection has to be performed for each module. In doing so, missing or broken wires can be found. Also, irregularities in the wire shape or bond tail length could be detected. However, the large number of wires makes a visual inspection a very tedious task and exceptionally weak bond connections cannot be found.

As a simplification of the visual inspection of the wire bonds, a software interface has been developed (using PyQt [76]) to analyze the bond machine data with the goal to identify potential bonding failures using the techniques that have been described before in Section 5.2.1. The user interface consists of three tabs: a tab for configuration (Figure 5.19 (a)), a tab for the analysis of the bond machine data (Figure 5.19 (b)) and a tab to show the position of wires that triggered an alert on a sketch of the 2S module (Figure 5.19 (c)).

The "Configuration" tab is shown on startup. On the top, the user can select a bond machine data base file via a file browser and by opening it the most important parameters are collected. Below the user can select whether the file contains information of the wire bonding on the 2S module top or bottom side. Instantly after opening, the operator can see an overview of the file with the number of bonded wires, the number of boats, the number of chips and mean values of USG phase and impedance. The number of boats indicates how often the conveyor system has been used to move a jig into the working area of the bonding machine. Therefore, this number will especially be important during series production when automated wire bonding of many modules is activated. Chips are objects related to the wire bond program. They are user defined groups of bonds that can be tuned equally by the bonding machine for example because they are located on the same component part. Below the statistics box, the user can set up the criteria for an alert. For this, two different approaches can be used. If the user chooses the "Simple Thresholds" mode, the software checks whether the USG phase, the impedance or the deformation quality index Ψ is within a definable range. Each of these parameters can be activated or deactivated and its threshold can be adjusted. Choosing the "Outlier Thresholds" mode, the software checks for each selected bonding parameter whether there are bonds with the respective parameter value lying outside an adjustable radius around its median value. Furthermore the user can select how the wires that triggered an alert, should be listed at the "Module Overview" tab, either by its wire number or channel id. The wire number can be used to find the respective wire fast and easily using the bonding machine. The channel id could be used to compare with the results of noise measurements. As the program calculates from the wire number its position / channel ID, it is mandatory that the correct bonding scheme has been used.

The "Analysis" tab is used to monitor the different kinds of bonding parameters. The user can choose from a large list of analysis objects (e.g. distribution of USG phase / current, bonding height, deformation curves) and optionally activate a grid or logarithmic scale for the x and y axis individually. Each plot can be saved for offline usage via a file browser. If a specific wire needs to be monitored, there is an option to highlight it within the plots. Additionally, the user can activate

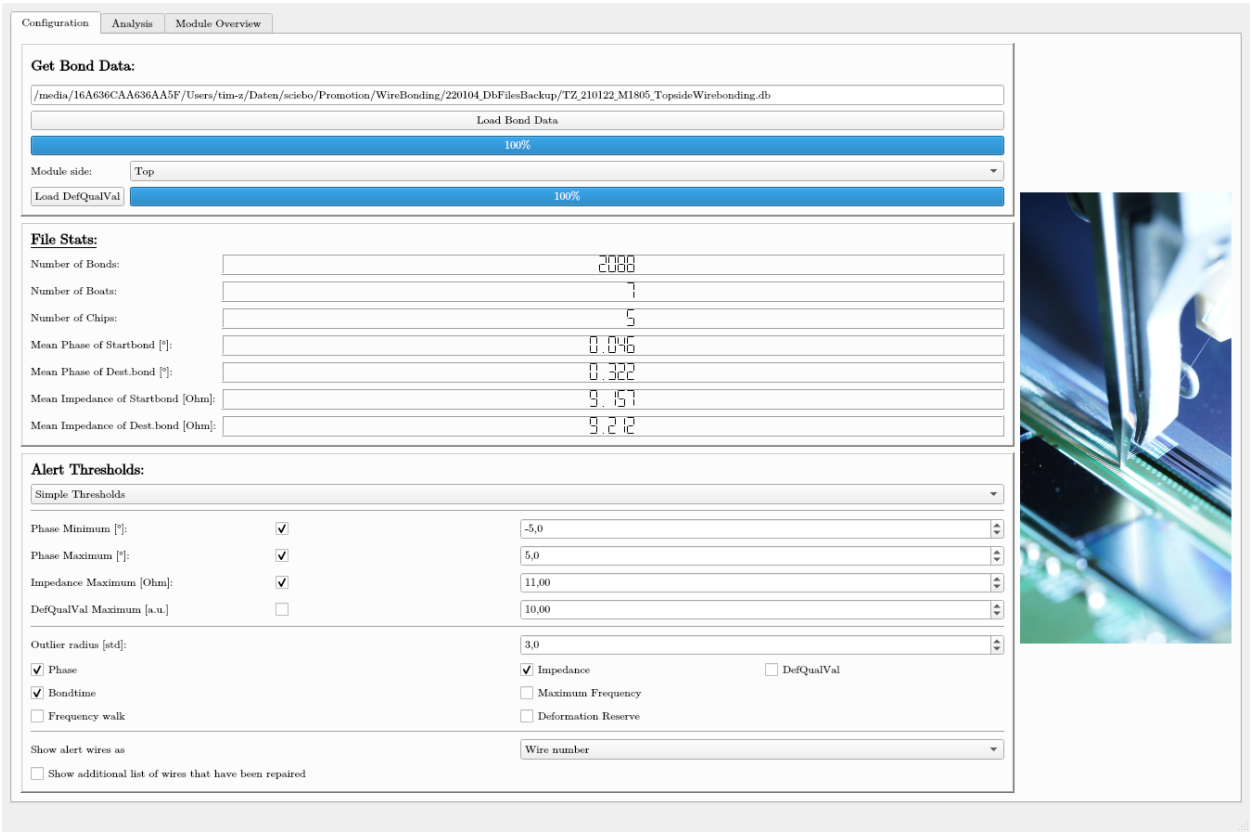

(a) Configuration tab.

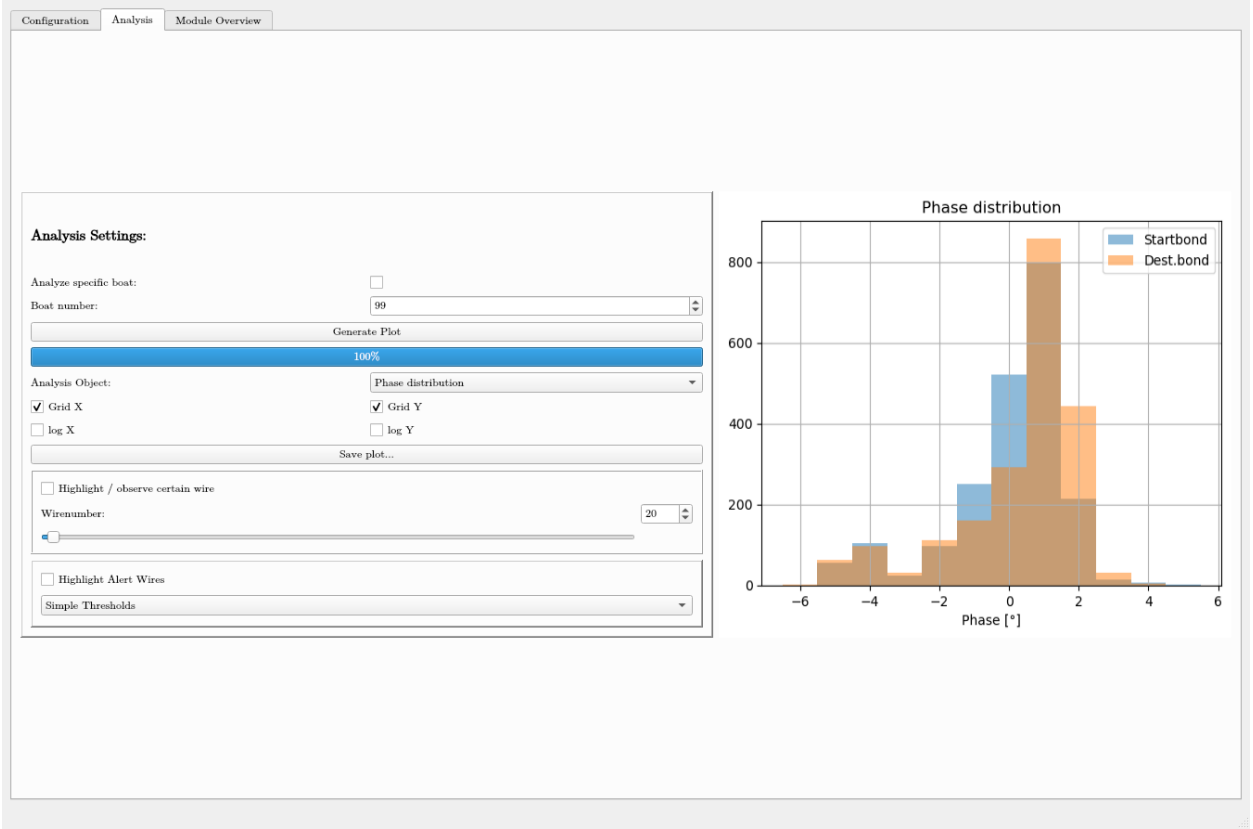

(b) Analysis tab.

Figure 5.19.: GUI for the quick analysis of wire bonding data in the series production of 2S modules.

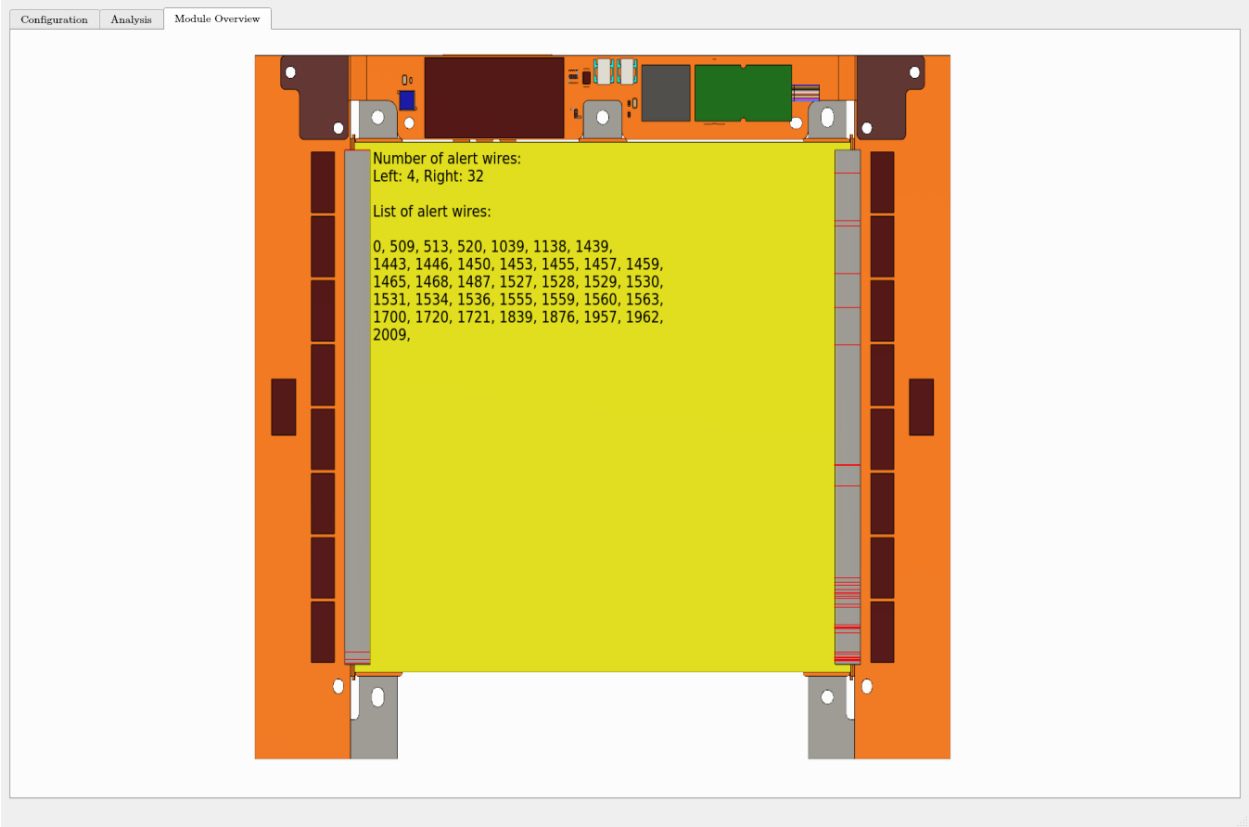

(c) Module overview tab.

Figure 5.19.: GUI for the quick analysis of wire bonding data in the series production of 2S modules.

highlighting of alert wires. In case of automated wire bonding, the user can select individual boats to be analyzed to avoid misidentification of wires on different modules.
The "Module Overview" tab shows the sketch of a 2S module. Depending on the module side chosen on the "Configuration" tab, the respective module side is shown. Each alert wire is highlighted at its position as a red line. This feature can help to find missing or exceptionally weak wires during visual inspection underneath the microscope. Additionally, the wire number or channel id of up to 150 alert wires is listed within the sensor area of the 2S module sketch.

5.2.2. Additional wire bonding studies and prototyping experiences

Evaluation of bonding speed

The wire bonding is assumed to be the assembly step that is most time consuming, considering both the active operator time and the pure machine time. With more than 4000 wires per module, hence 16 000 wires per day at a module assembly rate of four modules per day, it is clear that, depending on the wire bonding speed, the machine time could be a limiting factor in the series production of 2S modules. Extending the wire bonding capabilities by purchasing another machine is not an option. Therefore, the bonding speed has been studied in dependence of different bond machine parameters.
The study has been performed using the bonding test PCB, which has also been used to evaluate the process of the bond machine data analysis discussed in Section 5.2.1. In contrast to the 2S module, at the test PCB the height of the start bond and the height of the destination bond is approximately the same. Additionally, there are no components (like for example the CBCs) near the bonding area that are sticking out in height. The bonding program has been set up similarly to the bonding pattern used for the wire bonding of the 2S module. A set of 508 wires with a length of 4.5 mm and with a distance of 180 µm between each other has been bonded per setting.
The wire bonding speed can be adjusted by tuning different machine parameters. On the one hand, the velocity and the acceleration of the bond wedge can individually and directly be set along the different axes and at different phases of the bonding procedure (like moving between different wires or moving from start to destination bond). High values of velocity and acceleration result in an increased wire throughput, but this comes with the disadvantage that the bonding process could become instable and the risk of failures rises. This is especially the case for large and complex samples, which might be vulnerable to vibrations, like the 2S module. Increasing the velocity or the acceleration of the movement between the start and destination bond would increase the wire throughput of the machine. It would however also strongly affect the wire geometry and as there are tight geometrical constraints on the wire geometry that are related to the module integration on the larger structures and to the HV spark protection. Therefore, it is not considered as a useful option. On the other hand, the traveling distance of the bond wedge can be minimized to save time. This is done by minimizing the height of the wedge above the components while moving from wire to wire. Additionally, the path used to search for the touchdown, along which the wedge is moved with a highly reduced velocity so that the machine can quickly react, stop the movement and start the wire bonding, can be minimized. This path is defined by the so-called touchdown (TD) ramp (the path above the theoretically expected bond height) and the TD overdrive (the path

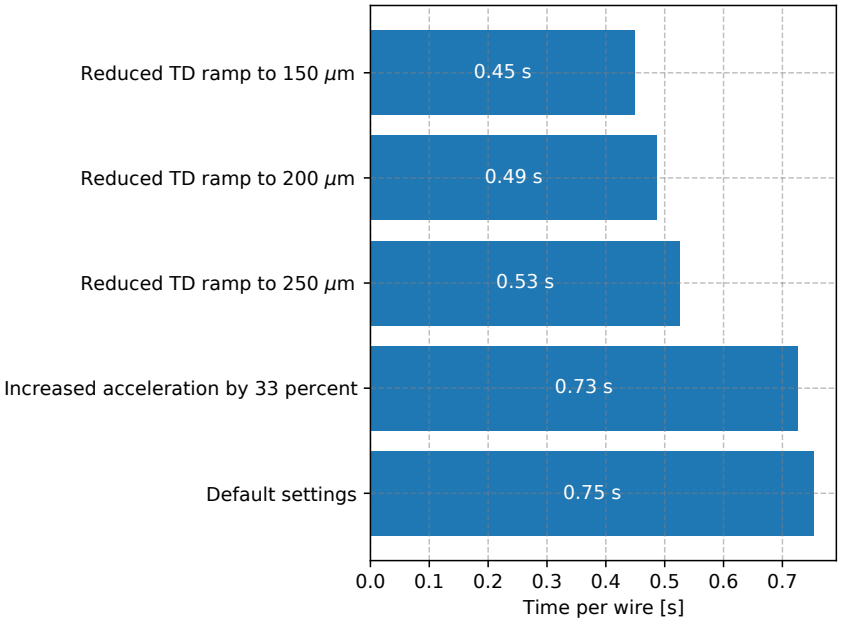

Figure 5.20.: Required time per wire measured for different sets of parameters.

below). The minimization of the movement height leads to a higher risk of crashing the wedge into components, potentially resulting in a damage of both the bonding machine and the 2S module. So, these options have to be handled with great care.

The bonding speed is determined by analyzing the bond machine data. These also contain timestamps for each individual wire. The timestamp is given with a precision of 1 s, so that the bonding speed can only be determined accurately by taking the average time interval between two consecutive wires from a large number of wires. As the starting point, the following parameters have been chosen: The height of the wedge above the test PCB while moving from wire to wire has been set to approximately 2 mm. This value has proven to be safe for the wire bonding of the 2S modules, and has been kept untouched. The maximum velocity and the acceleration along each axis has been set to 1 mm/ms and 7500 mm/s^2, respectively. The starting point of the TD ramp was set to 500 µm, which is the maximum value.

Figure 5.20 presents the measured wire bonding speed for the default setting and after different adjustments of parameters. At the starting point, a time interval of 0.75 s per wire has been measured. By increasing the acceleration from 7500 mm/s^2 to a value of 10 000 mm/s^2 the wire bonding speed was not increased significantly as the time interval has been found to be 0.73 s. Further increasing acceleration or velocity was not considered to avoid a degradation of bonding quality. A systematic quantification of the quality loss induced by increased velocity or acceleration (for example by applying pull tests at different settings) has not been performed. The most significant improvement of bonding time has been achieved by lowering the TD ramp. By lowering the parameter value from 500 µm to 250 µm (while keeping the acceleration increased), the wire bonding time interval could be decreased to 0.53 s, which translates to a wire rate of about 1.89 Hz. By further reducing the TD ramp to 150 µm the time interval is decreased to 0.45 s (2.22 Hz).

The study has shown that a bonding speed of 1.5 Hz can safely be achieved. Whether this value could be increased for wire bonding of 2S modules by tuning the TD ramp depends on the accuracy of the module's bond pad height in the bonding machine, because the current version of the bonding machine firmware only allows to measure the bonding height once before the automated wire bonding of multiple modules starts. The accuracy of the module's bond pad height on the one hand depends on the accuracy of the module support height of the bonding jig. The used bonding jigs are manufactured by the mechanical workshop of the Physics Institute IIIB and an accuracy of $\mathcal{O}(10\,\mu m)$ is expected to be achievable which is negligible. On the other hand the assembly precision plays an important part. The CMS OT Upgrade community has specified that the height of the bond pads of the FEH and the sensors should not be displaced in height by more than 300 µm. Additionally, the absolute distance between the top and the bottom sensor is specified to meet a precision of 100 µm. These specifications would allow that the absolute height of the bond pads on the FEHs of two modules could differ by up to 800 µm. However, it can be assumed that the achieved accuracy of the module assembly is by far better. Therefore, the bond pad height should be checked after some modules of final design have been assembled in the future.

Repair of broken bonds after encapsulation

The M1804 module has been assembled as a 2S module with two right-handed 8CBC3.1 FEHs with left hand side adapter and with plugs to attach a CIC mezzanine card on each side. As one of the first modules of its generation it has been tested as the detector under test (DUT) at the test beam in November 2019 at the DESY-II Test Beam Facility (Chapter 6, page 89). As part of the module QA the noise of the module has been measured before, during and after the beam test to monitor a potential degradation of the module from shipment and handling. In that course, a loss of connectivity of approximately 200 signal wires has been found at the top left side after the beam test. The cause of the connectivity loss could not be identified. Figure 5.21 presents the result of a noise measurement after the beam test. With a conversion factor of 1 Vcth unit $\hat{=}$ 128 electrons [77], a noise level of about 6 Vcth units is well within specifications, while a level of approximately 2 Vcth units is typical for unconnected channels.

Because the M1804 module has been completely encapsulated, the unconnected channels alone could not be removed and repaired. The only way to reconnect the wires after encapsulation is that the encapsulant has to be removed and all wires of the top left side have to be wire bonded again. Before this procedure has been applied to the functional module, wire bonding test structures have been used to test whether *Sylgard 186* harms the quality of the bonding pads in terms of bondability. Therefore, bonding parameters have been optimized on the clean (non encapsulated) test structure and several wires are bonded for pull tests. After pull testing the same structure has been encapsulated. By carefully lifting the encapsulant at the border using tweezers and then pulling it off towards the opposite side, it could be removed easily in one piece and without any residues visible on the surface. Figure 5.22 shows photographs of the test structure and the encapsulant removal process. After removing the encapsulation, again several wires are wire bonded onto the test structure using the same set of bonding parameters as before and pull tested.

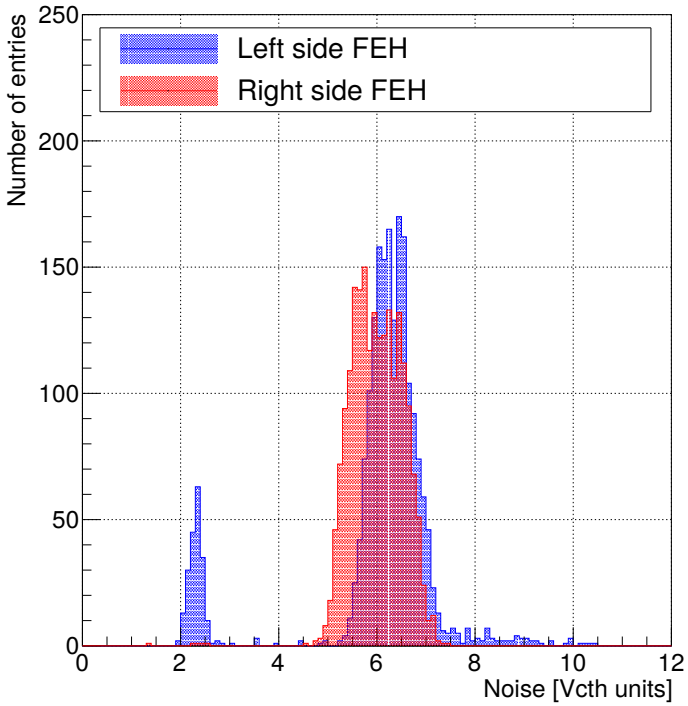

Figure 5.21.: Noise measurement of M1804 after the November 2019 beam test. The typical noise level of unconnected signal wires is approximately 2 Vcth units.

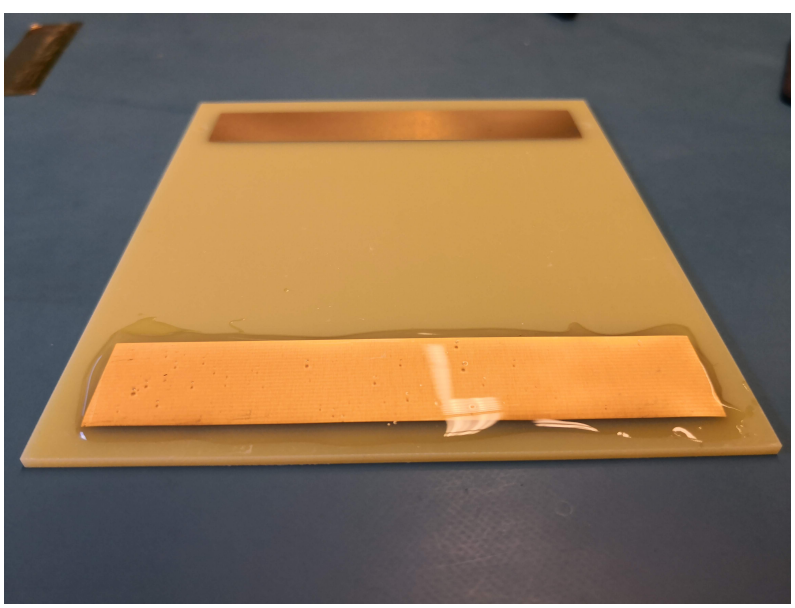

(a) Photograph of the encapsulated wire bonding test structure.

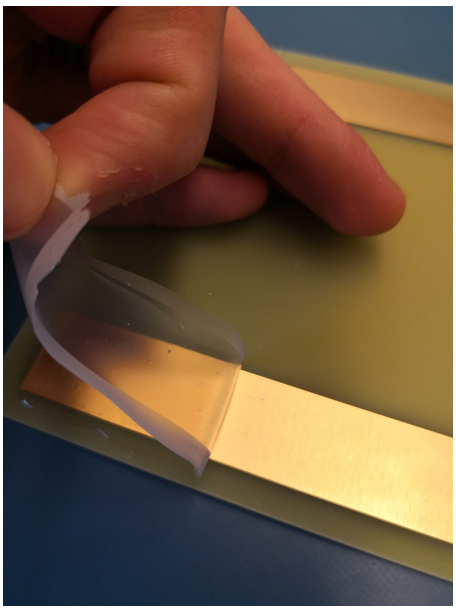

(b) Photograph of the removal of the encapsulant material.

Figure 5.22.: Photographs of the bondability tests on structures that have been potted with encapsulant material which is afterwards removed again.

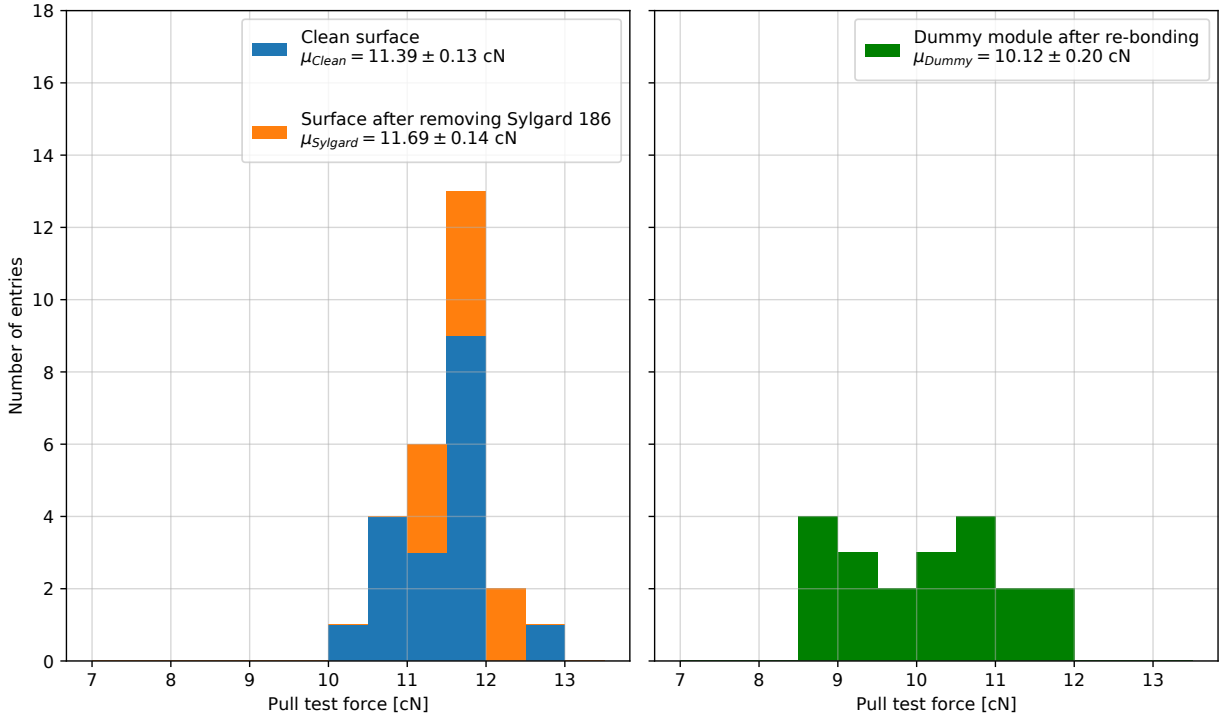

Figure 5.23.: The left plot shows pull test forces of wires that have been wire bonded on a clean surface compared with those of wires bonded after the encapsulant material Sylgard 186 has been applied and afterwards removed. The right plot presents the pull test forces measured after removal of the encapsulant and re-bonding of a dummy module.

The test forces measured while pulling the wires from the clean surface as well as of those pulled from the once encapsulated surface are shown on the left side of Figure 5.23. The pull tests on both surfaces resulted exclusively in heel breaks. On the clean surface, the mean pull test force is (11.39 ± 0.13) cN and on the encapsulant surface the mean value is (11.69 ± 0.14) cN. These results are well compatible and prove that there is no degradation of the material after removing the encapsulant material. In order to check the feasibility of this process on an actual 2S module, an encapsulated row of signal wires of a dummy module has been removed and afterwards bonded again. The removal of the encapsulant from a 2S module has been found to be more difficult because it flows around the sensor edge. Nevertheless, the encapsulant could be removed without leaving residues or damaging the sensor surface. Additionally, repeating the wire bonding is complicated by the circumstance that the bond pads on the FEHs have only limited space, for approximately three bonds, before a surface has to be used twice. The corrected pull test forces of wires re-bonded on the dummy module are shown on the right side of Figure 5.23. Again only heel breaks have been detected and the pull test forces are well above 8 cN.

After proving that repairing signal wires after applied encapsulation is possible, the top left side of the M1804 module could be reconnected except for a single wire. Figure 5.24 shows the noise distribution after repairing the left side. The procedure turned out to be simple but also tedious as the bond position should be corrected to avoid bonding on bond foot remnants. Therefore, it is not recommended on a large scale in series production.

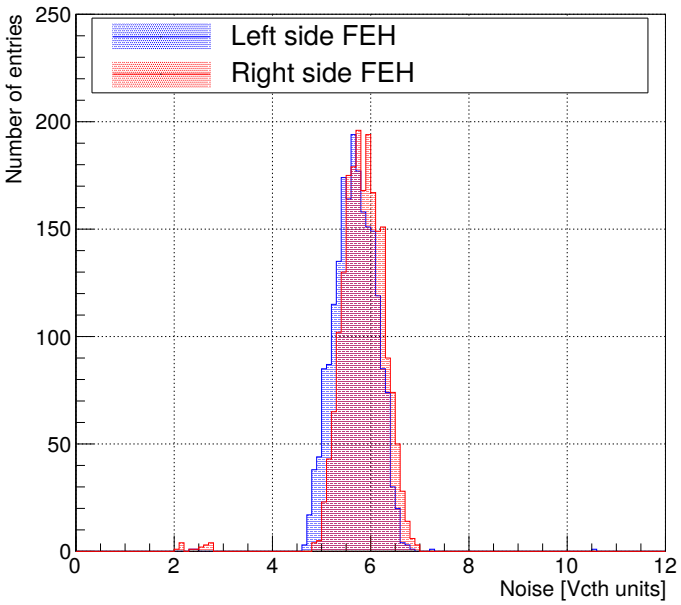

Figure 5.24.: Noise measurement of M1804 after removal of the encapsulant material and re-bonding on the module's left side.

5.3. Reception tests of Kapton strips

The dimensions of the Kapton strips used to electrically isolate the sensor back plane from the AlCF bridges need to be measured to ensure the HV biasing of the module while avoiding sparking. Therefore, a simple and fast procedure has been developed to reproducibly and user indepentently determine the length and width of the Kapton strips. For this, a commercial flat bed scanner is used with a custom picture analysis software for automated Kapton strip recognition and mensuration. The dimensions of multiple Kapton strips can be measured from a single scan image.
Requirements for the flat bad scanner used for this application are summarized in Section 5.3.1. Section 5.3.2 introduces the Kapton strip specifications ensuring a safe operation of the 2S modules with HV biasing. The software for picture analysis and the GUI for simple usage are described in Section 5.3.3. Section 5.3.5 presents measurements of Kapton strip samples as a demonstration of the developed tool.

5.3.1. Choice of the scanner

For the Kapton strip reception any commercial flat bed scanner could be used. So, the setup is cheap and no previous knowledge is required for the measurements. However, there are some aspects which are important to improve the measurement precision and to simplify handling and documentation during the measurements.
There are two different technologies which have to be taken into account [78]:

1. **CCD**: Flat bed scanners with CCD (charge coupled device) technology use a source of white light to illuminate the scan object. The reflection is guided through an optical system of

mirrors and a prism to break red, green and blue light separately. A reduction lens is used to scale down the size of the virtual image to the size of the sensor pixel. This results in a long light path but also in a large depth of field (DOF). Each different color is measured by individual photo sensors and the analogue charge signal is converted into a digital value. The quality of the scan image mostly depends on the quality of the white light source and of the reduction lens.

2. **CIS**: Instead of using a white light source, the CIS (contact image sensors) technology uses three LEDs of red, green and blue light. The reflection at the scan object is guided through lenses to the photo sensors. The DOF usually is much smaller compared to the DOF achieved by CCD scanners. CIS scanners often come with the advantage that they are less expensive, have a lower energy consumption and that they are faster.

The precision of the measurements of length and width of the Kapton strips depends on the resolution of the scanner. The resolution of current generation flat bed scanners is 600 dots per inch (DPI) as default setting for DIN A4 scans, which translates to a pixel size of approximately 42.3 µm. For standard devices the maximum resolution is 4800 DPI (with a pixel size of 5.3 µm). This resolution is usually used for scanning of slide photos. However, high resolution also means higher data size (proportional to the resolution squared) and therefore higher requirements in the RAM of the computer in control of the scanner. The same applies to the time needed to analyze the scan images. So, especially if the setup is used in the series production when thousands of Kapton strips need to be checked and time could be an issue, a trade-off has to be found.
The handling of the strips can be simplified and mistakes in the identification of strips not passing the specifications can be avoided by using a jig with transparent ground plate / foil and with individual cutouts for the Kapton strips. For this, the scanner has to have a large DOF to avoid a degradation of the measurement precision. Thus, a scanner with CCD technology should be preferred as the DOF is typically by many factors larger.
In Aachen the Kapton reception tests have been performed using an *Epson V370* flat bed scanner based on CCD technology. It has an adjustable resolution of up to 4800 DPI and a color depth of 48 bit.

5.3.2. Kapton strip specifications

There are two different types of Kapton strips for HV isolation in the 2S module, the short strips for the stump bridges and the long strips for the long AlCF bridges. Even though the AlCF bridges of the 1.8 mm and the 4 mm modules vary, the same Kapton strips are used. They are designed to have the following nominal dimensions:

- Short strips: 10.1 mm × 17.26 mm and
- Long strips: 9.8 mm × 95.59 mm

with a radius of 0.5 mm in all four corners and a thickness of 25 µm. The tolerances in the positioning of the Kapton strips and the AlCF bridges during the assembly have to be taken into account to achieve safe spark protection and to define proper limits for the Kapton strip measurements,

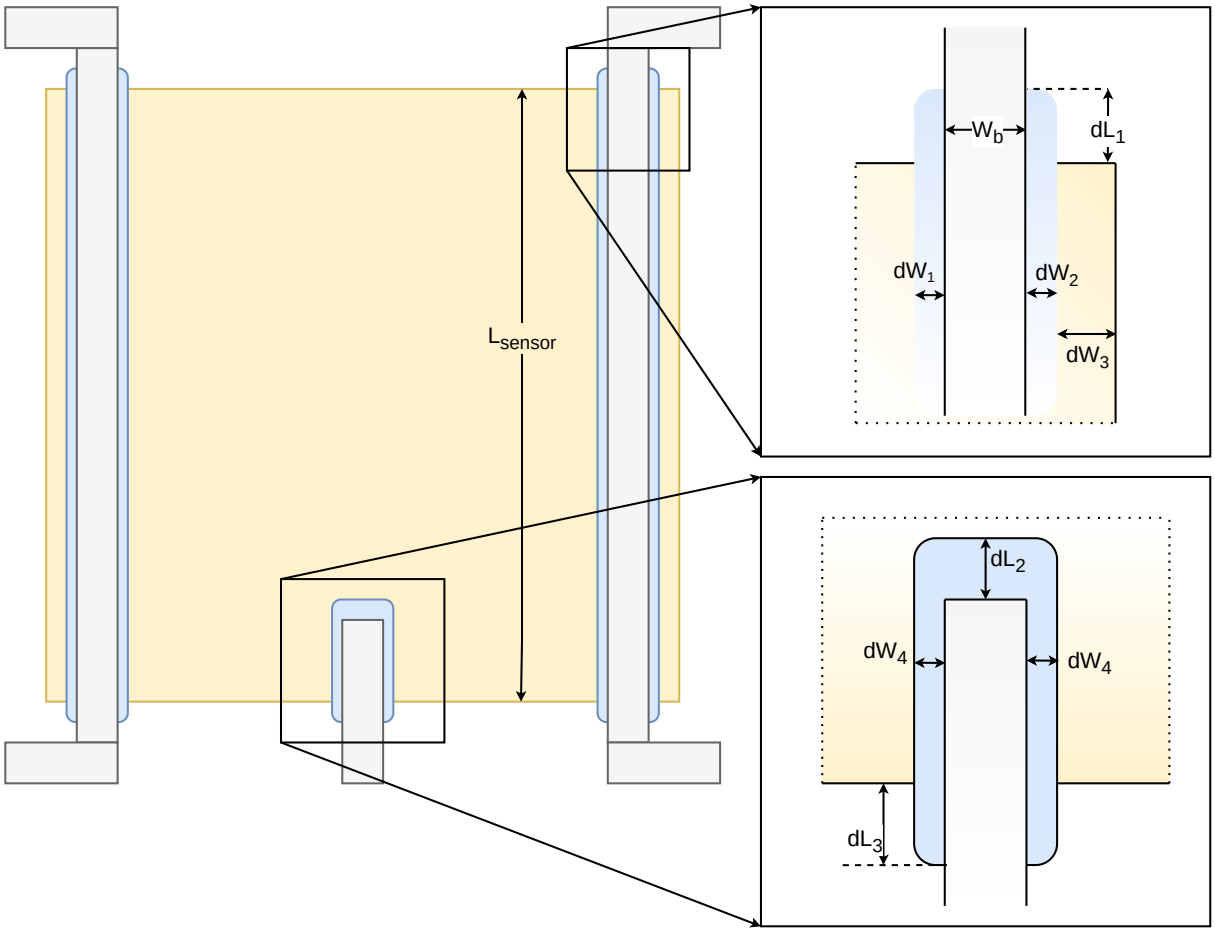

Figure 5.25.: Sketch of the 2S module with its AlCF bridges and Kapton strips. Important distances are defined for further description. The sketch presents the top sensor as well es the bottom sensor as there are only minor differences.

especially as the Kapton strips in the prototyping phase have not been cut with high accuracy and large deviations are expected. Figure 5.25 shows the 2S module with its bridges and isolators and the most important distances are defined. In the sketch and for the evaluation of specifications the 4 mm module is considered because its stump bridge is larger than its counterpart of the 1.8 mm module and because of this the clearances are smaller.

The nominal length of the sensor is $L_{\text{sensor}} = 94.183\,\text{mm}$. During the assembly of prototype modules sensors have not fulfilled this tolerance and in fact a rim of up to 50 µm width has been observed at each of the edges parallel to the strips. This increased the length of the sensor by 100 µm in total narrowing the margin of the size of the Kapton strips. However, final sensors are expected to meet the specifications as described above.

The CMS community agreed on the following specifications for spark protection: The distance between two surfaces with HV potential difference must be at least 500 µm as a path along a surface. The same distance has to be realized if only air is in between. If Kapton or a solid layer of adhesive / encapsulation material separates the two surfaces, the distance must at least be 25 µm or 50 µm, respectively. These specifications are the baseline to formulate specifications for the Kapton strips.

Table 5.2.: Summary of the relevant dimensions to specify dimensions for the reception of the Kapton strips for HV isolation.

Distance label	Nominal value	Tolerance
L_{sensor}	94.183 mm	± 10 µm / ± 100 µm during prototyping
dL_1	0.70 mm	± 200 µm
W_{b}	8.00 mm	not yet specified
dW_1	1.15 mm	± 650 µm
dW_2	0.65 mm	± 150 µm
dW_3	0.20 mm	± 150 µm
dL_2	1.10 mm	± 600 µm
dL_3	0.70 mm	± 200 µm
dW_4	1.05 mm	± 550 µm

The L-shaped stoppers of the Kapton gluing jig are positioned in a way that the long Kapton strips are well aligned at the edges pointing towards the SEH and the near FEHs. This feature of the Kapton gluing jig requires that the edge of the strip is straight so that the position is well defined by the stopper. The following consideration of tolerances assumes straight edges but it is important to note that a curved edge additionally narrows the considered specifications. Because of this, it is important to check the straightness.
Table 5.2 summarizes the nominal dimensions of the relevant variables from Figure 5.25 with their tolerances. Assuming that the Kapton strips are well aligned at the L-stopper the tolerances only have an impact on the opposite sides. Additionally, the dimensions and positioning of the AlCF bridges are assumed to be optimal. The resulting specifications for the Kapton strips during the prototyping phase are:

- Long Kapton strip:
  - length: $95.59^{+1.00}_{-0.10}$ mm,
  - width: $9.80^{+1.00}_{-0.65}$ mm,
- Short Kapton strip:
  - length: $17.26^{+1.00}_{-0.60}$ mm,
  - width: $10.10^{+1.00}_{-0.55}$ mm.

The maximum limit is specified to +1 mm to avoid a clash with screws for the fixation on the larger structures and to sort out strips highly exceeding the nominal dimensions. The dimension with the tightest tolerance is the length of the long Kapton strip.

5.3.3. Software

The software for automated scanner image analysis is based on Python and uses *Numpy* [79] and *Matplotlib* [80] for data handling and the visualization of the results. For image filtering and analysis the *OpenCV* [81] Python library was taken. The GUI was developed using *Qt5* [76].

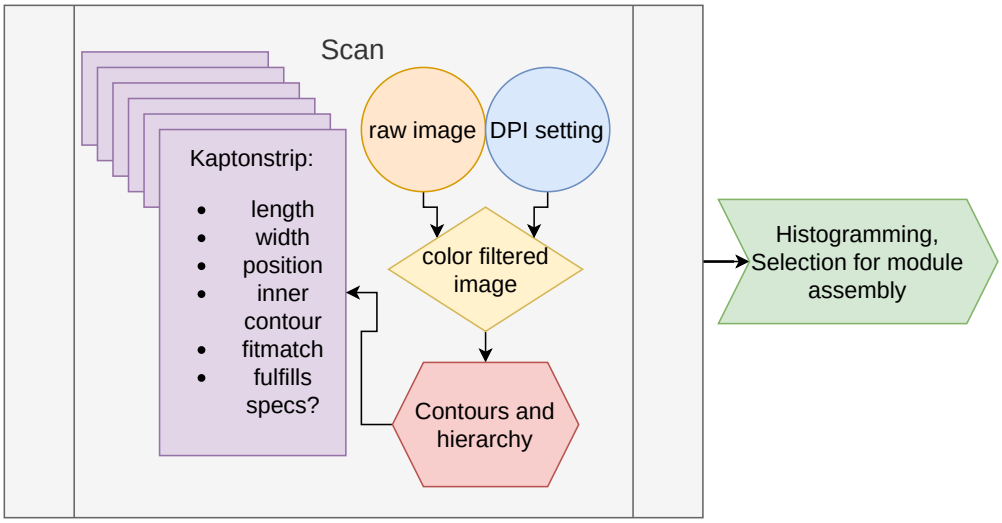

Figure 5.26.: Data flow from the scanner image of the set of Kapton strips to a selection of usable parts for the module assembly.

Picture analysis

The picture analysis software consists of two custom Python classes, the *Scan* object and the *Kaptonstrip* object. The data flow and the most important class members are presented in Figure 5.26. A *Scan* is initialized as received from the flat bed scanner and the DPI setting which was chosen for the process of the respective scan. During the initialization, the *Scan* opens the scan image in JPEG or PNG file format and imports an *OpenCV* image which is readable as a matrix of pixels with each pixel holding information of the color and brightness in the RGB color space (with 8-bit for each color). The DPI setting is interpreted as a scaling factor to transform lengths of unit 'number of pixels' into a metric unit. In the next step, the image is filtered by color so that pixels in the color space corresponding to the typical yellow coloring of Kapton are tagged. The filter color space is chosen by a qualitative evaluation of the color spectrum of the scan image. An exemplary color spectrum is shown in Figure 5.27. It shows the color spectrum of the complete scan image as well as the spectrum of an image generated by cutting into the Kapton strip area. While the background of the scan image is mainly white with RGB color (255, 255, 255) the characteristic yellow of the Kapton strips is approximately (255, 255, 0). So, the background can be distinguished from the Kapton strips mainly by comparing the blue component of the color space. Thus, the phase space from (210, 200, 0) to (255, 255, 60) is filtered for further processing. Each pixel of the color filtered image only holds binary information. This image is used to find contours of the Kapton strips and the contour hierarchy of the entire *Scan* object. By the contour hierarchy the actual Kapton strips are differentiated from contours within the area of a strip that may originate from damages or contamination. Taking this information, an array of *Kaptonstrip* objects is generated with all strips detected from the scan image. The *Kaptonstrip* objects are automatically ordered by their y coordinate of the center of gravity position in the scan image.
A *Kaptonstrip* object holds the information of its mother (the corresponding *Scan* object) and the contour index. By initialization, the *Kaptonstrip* area is determined by counting its pixels and multiplying the metrical size of a pixel determined from the DPI value:

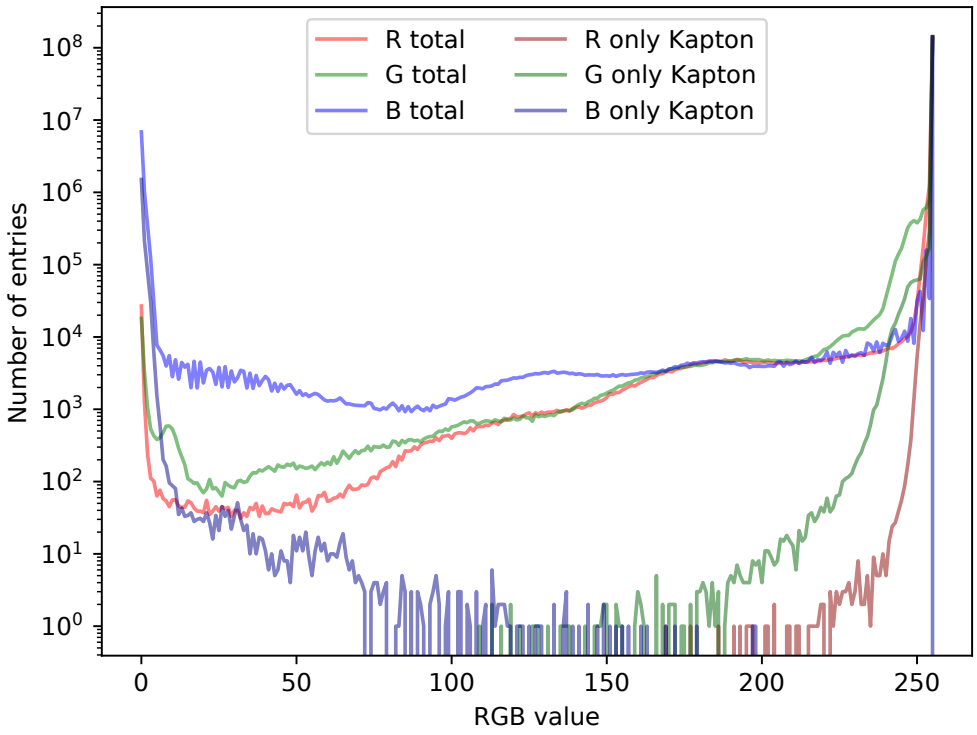

Figure 5.27.: The RGB spectrum of a scan image for the reception of Kapton strips.

$$L_{\text{pixel}} = \frac{25.4\,\text{mm}}{\text{DPI}}, \tag{5.5}$$

$$A_{\text{pixel}} = {L_{\text{pixel}}}^2. \tag{5.6}$$

The length and width of the *Kaptonstrip* is determined by fitting a smallest possible rectangle that contains all parts of the contour. The free parameters of the fit are x and y position, length, width and rotation of the rectangle. The uncertainty of the width and length determined in this procedure is assumed to be $\sigma_{\text{width/length}} = \frac{2}{\sqrt{12}} \times L_{\text{pixel}}$. In case of a scan image taken at 600 DPI, which is a standard resolution for many flat bed scanner devices, the size of a pixel is $L_{\text{pixel,600}} \approx 42\,\mu\text{m}$ and therefore the resulting uncertainty for width and length measurements is $\sigma_{\text{width/length,600}} \approx 24\,\mu\text{m}$.

The quality of the rectangle fit is quantified by the ratio of the *Kaptonstrip* area as determined by counting pixels and the area calculated by multiplying the fitted width and length:

$$\epsilon_{\text{fitmatch}} = \frac{A^{\text{meas}}_{\text{Kapton}}}{A^{\text{fit}}_{\text{Kapton}}}. \tag{5.7}$$

In case of a perfect representation of the Kapton strip by the fitted rectangle, $\epsilon_{\text{fitmatch}}$ is 1. The parameter $\epsilon_{\text{fitmatch}}$ could either be reduced because of a fitting problem or because of a non-rectangular shape of the Kapton strip. Deviations from the rounded corners of the Kapton strips

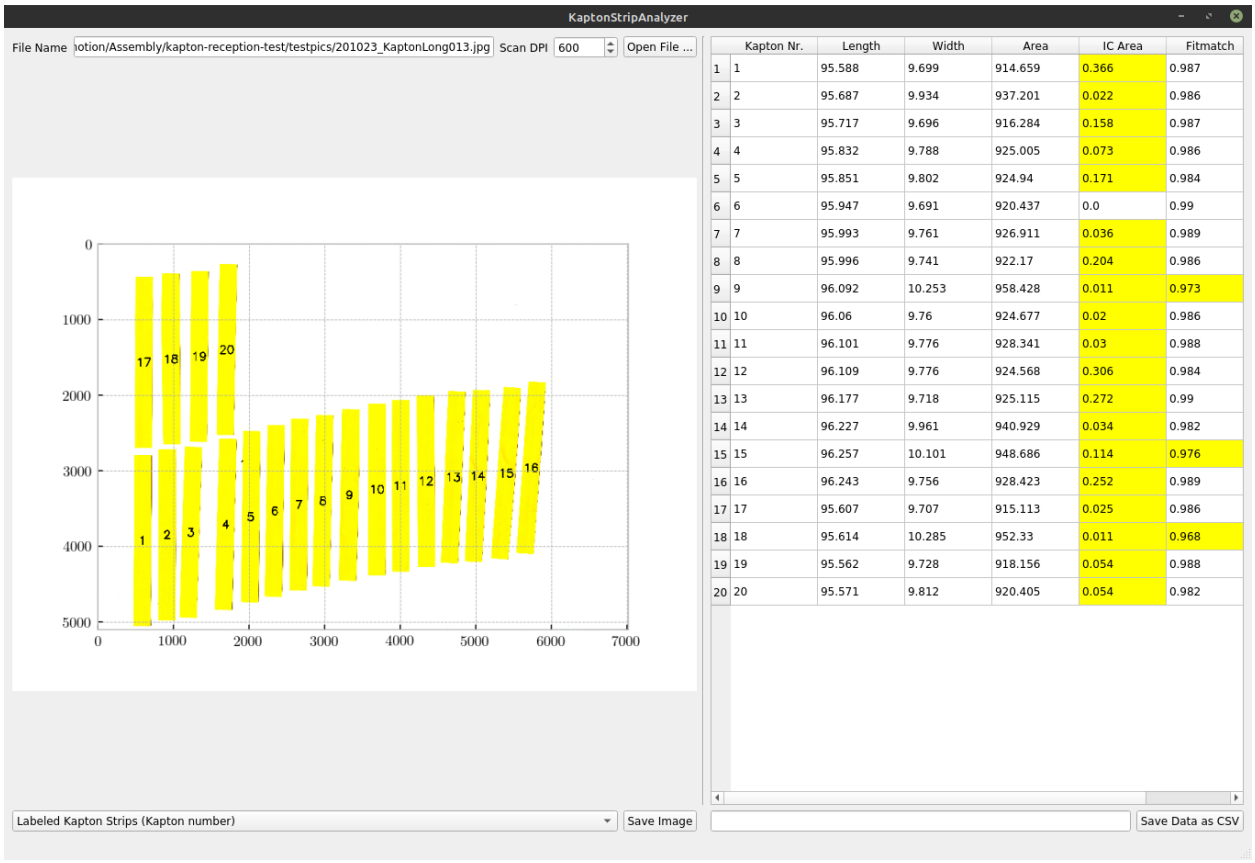

Figure 5.28.: Exemplary view of the GUI for the automated Kapton strip reception testing.

are negligible. For the long Kapton strips the expected deviation is 2.3×10^{-4} and for the short strips it is 1.2×10^{-3}. If the strip is cut with a significant bow which is visible with the resolution of the scanner, a larger deviation of $\epsilon_{\text{fitmatch}}$ from 1 could be an indicator for this. It is important to note that bows, $\Delta w = w_{\text{max}} - w_{\text{min}}$ with w being the width of the Kapton strip, smaller than L_{pixel} cannot be measured reliably. Using Kapton strips with a significant bow in the assembly should be avoided, because the bow could result in a rotational misplacement of the strip during the Kapton strip gluing as the contact at the L-shaped stopper is not well defined.

Contours inside the Kapton strip contour are detected as well. This is included in the hierarchy information of the Scan object. Any contour (featuring a resolvable color gradient) inside the Kapton strip area is found and its inner area is determined as number of pixels. The number of pixels are again transformed into a metrical inner contour (IC) area by multiplying with the size of a pixel A_{pixel}. The IC area of the individual Kapton strips is measured as an indicator for holes or contamination of the surface.

GUI

In order to enable a simple and fast access to the software for the operator, a GUI was developed. The user can use any flat bed scanner to scan the Kapton strips with a user-defined DPI setup. Figure 5.28 presents an exemplary view of the GUI. The produced scan image is selected in the top corner with the respective DPI setup. Afterwards, the image is analyzed to detect and measure the

Kapton strips using the software described above. The table on the right side gives an overview of the detected Kapton strips and their dimensions. It lists the length, the width, the overall area, the IC area and the *fitmatch* factor $\epsilon_{\text{fitmatch}}$ (Equation 5.7) of the individual Kapton strips. If one of the dimensions (length or width) exceeds the specifications as listed in Section 5.3.2 the respective cell of the table is colored red. In this case the Kapton strip should not be used for module assembly. If an IC area is measured for a strip (IC area larger than 0) the cell is colored yellow. The same applies if $\epsilon_{\text{fitmatch}}$ is smaller than 98 %. In these cases the user should check for contamination that could be cleaned away. If $\epsilon_{\text{fitmatch}}$ heavily falls below 98 %, the straightness of the edges should be checked manually or the strip should be discarded for module assembly.
For simplification of the Kapton strip identification, the scan image is shown on the left side of the GUI with the Kapton strip indices. As an alternative, histograms with the different measured variables from the table can be displayed by selecting in a drop-down menu on the bottom side of the GUI. The image which is currently displayed and the data from the table can both be saved for offline usage. Exemplary histograms are presented in Section 5.3.5.

5.3.4. First tests with a Kapton reception jig

In series production a large number of Kapton strips will have to be visually inspected. As a simplification of handling and to avoid mistakes in the transfer (permutation and false assignment of strips) from the scanner setup to the module assembly a carrier jig could be used. A first version of the carrier jig has been designed, manufactured and tested.
The carrier jig has to fit into the flat bed scanner setup. Because of this, a plastic sheet of 2.5 mm thickness in DIN A4 format (210 mm × 297 mm) has been used. Cutouts of 1.5 cm × 10 cm are designed to hold either type of Kapton strip. The cutouts are positioned in groups of four (the number of long strips needed per module) and placed with an offset to ensure intuitive numbering within the software and also to have a rotational asymmetrical pattern for distinct identification. The material color is chosen to be grey to clearly differentiate it from the Kapton strip color. Figure 5.29 shows a photograph of the first version of the carrier jig sheet. An overhead transparency is glued onto the bottom side to safely carry the strips.
Analyzing a scanner image of the Kapton strips within the jig cannot be done with the same RGB filter parameters. Therefore, the evaluation of the scan image RGB spectrum has been repeated. Figure 5.30 shows the RGB spectrum of the scan image of a Kapton strip within the Kapton reception jig. If the color spectrum of the scan image without using the reception jig is compared to the one with, not only the background shifts towards darker colors because of the dark plastic sheet but also the blue and green component of the Kapton strip spectrum change. Shadows originating from the depth of the jig and scanner image processing could cause these differences. However, the scan image is still properly analyzed and Kapton strips are detected by setting up the color filter for Kapton strips to the range from (220, 200, 60) to (255, 255, 100).

5.3.5. Results

As an example, the Kapton strip reception measurements in the preparation of the M1805 module assembly are presented. In total 20 long strips have been analyzed to find a selection of four

Figure 5.29.: Photograph of a first version of the Kapton strip reception test jig.

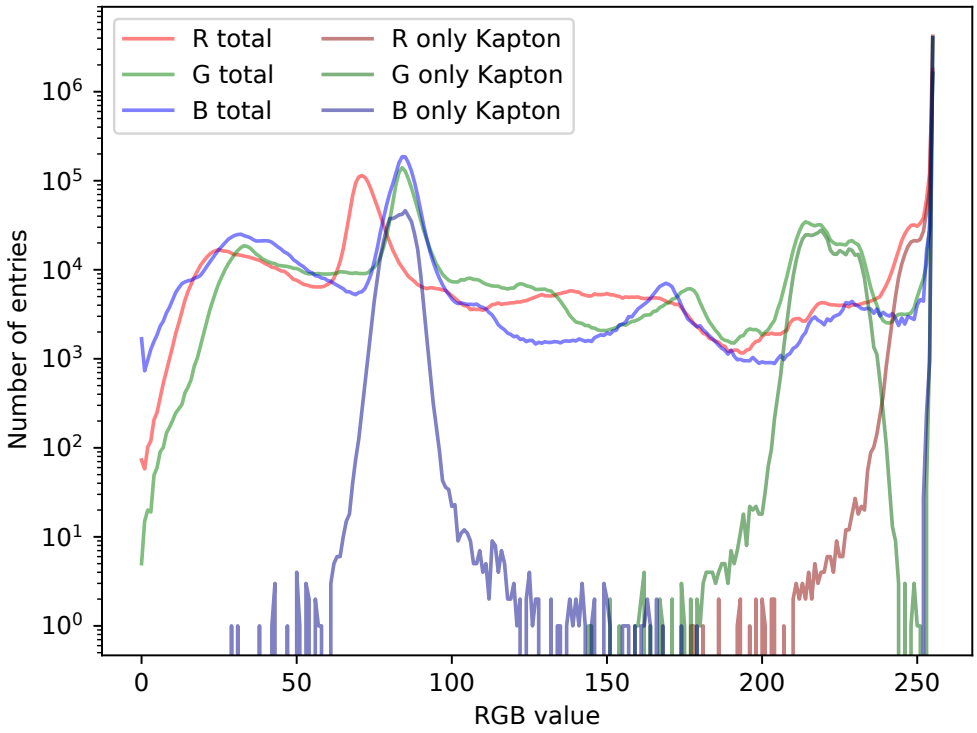

Figure 5.30.: Color spectrum of the scan image using a first version of a Kapton strip carrier jig.

strips to be used for assembly. Figure 5.31 presents the distribution of the widths and lengths of the sample. The red colored areas indicate the exclusion limits. The mean width of the sample of Kapton strips has been measured to be (9.75 ± 0.04) mm, which is slightly smaller than the nominal width. Nevertheless, all strips comply with the specifications for the width. However, the mean length of the Kapton strips has been measured to be (95.81 ± 0.05) mm, which is well above the nominal length. Three strips do not satisfy the specifications as they are too short. These strips are excluded from the module assembly.

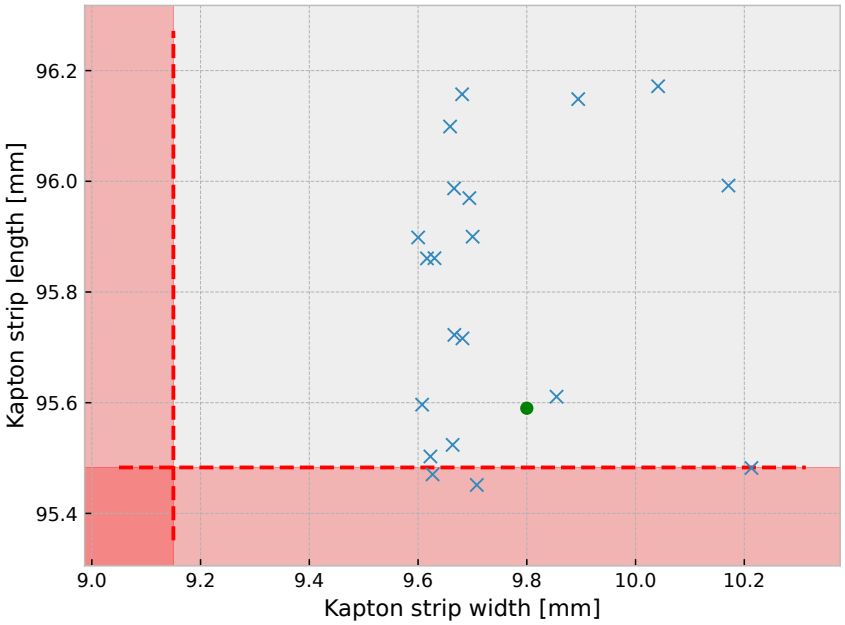

Figure 5.31.: Widths and lengths of the analyzed Kapton strips in the preparation of the M1805 module assembly. The red colored area visualizes the dimensions of strips to be excluded from assembly. The green circle presents the nominal dimensions.

Besides measuring the width and length of the Kapton strips, also the straightness is checked. For this, the fitmatch parameter $\epsilon_{\text{fitmatch}}$ is calculated. The distribution of the Kapton stips' fitmatch parameter is presented in Figure 5.32. Most of the Kapton strips have been measured with $\epsilon_{\text{fitmatch}} > 0.98$. The four remaining strips have been excluded for the module assembly of the M1805 module.
After excluding some strips , the remaining are visually checked to avoid strips with damages (holes and kinks). The inner contour measurement of the scanner software can be used as an indication. After cleaning, the remaining set of Kapton strips can then be safely used for modules assembly.

5.4. Module and sensor lab tests

5.4.1. Evaluation of thin sensors for 2S modules

During the prototyping phase of the 2S modules different sensor materials have been evaluated before the final decision on a specific material was made [42]. As an assembly center, RWTH Aachen received different types of sensors for module assembly: FZ290 sensors and thFZ240 sensors.

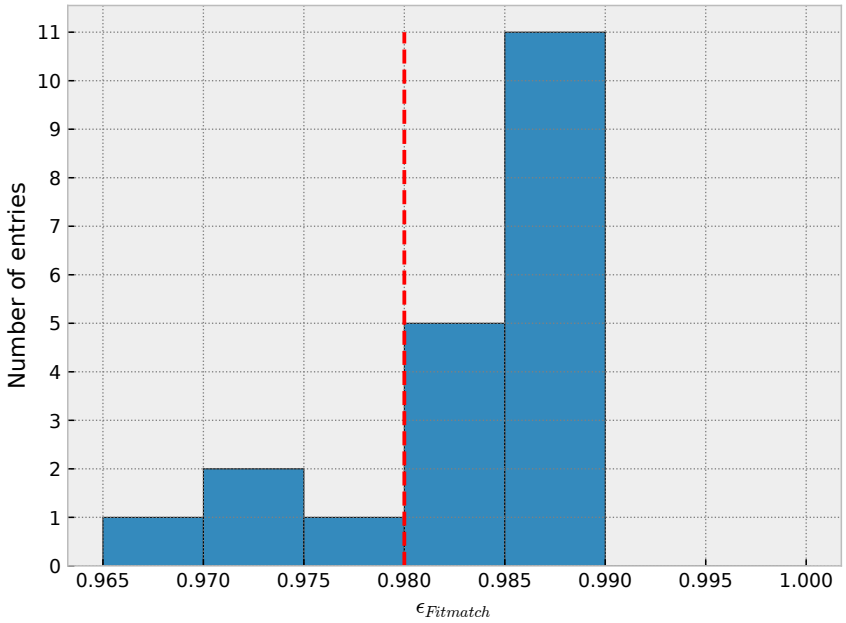

Figure 5.32.: Fitmatch values of the analyzed Kapton strips in the preparation of the M1805 module assembly. The red dotted line shows the suggested threshold of 98 %.

Both sensor types are produced on p-type 6 inch wafers of float zone (FZ) technology. The FZ290 sensors are from standard wafers with an active thickness of 290 µm and a total physical thickness of 320 µm. The thFZ240 sensors are made of thinned silicon material with a physical thickness of 240 µm and a similar active thickness. This section describes tests to evaluate a pair of thFZ240 sensors.

As a first step of the sensor evaluation after reception, the two thinned sensors have been visually inspected in detail. On the strip side only few small scratches and a very light grade of dust contamination have been found. However, on the bottom side both sensors show long scratches mostly populated at the corners. Figure 5.33 shows a photograph of a bottom sensor corner with scratches. The rectangle pattern leads to the assumption of a systematical damage caused at the manufacturer side. The origin could certainly not be identified, though.

As a second step, IV measurements have been performed. For these studies, the *Form Factor PA200* [83] probe station with a light tight shield, dry air supply and temperature controllable chuck is used. A *Keithley 2410* [84] is used as source measure unit. All measurements presented have been performed inside the dry air flooded cabinet (with a relative humidity below 5 %) and at lab temperature (approximately 20 °C) if nothing else is specified.

A first reception test with measurements of the electrical functionality of the two thinned sensors has been performed at the Institute of High Energy Physics (HEPHY) Vienna. Both sensors have not shown distinctive features at this instance. At Aachen, IV measurements have been performed to evaluate the electrical functionality. These are done by contacting the sensor at the back plane and the bias ring and measuring the current while slowly increasing the biasing voltage. The sensor back plane is contacted through the probe station chuck while the sensor is fixed with vacuum and a probe needle is placed to contact the bias ring. The voltage is increased in steps of 10 V and

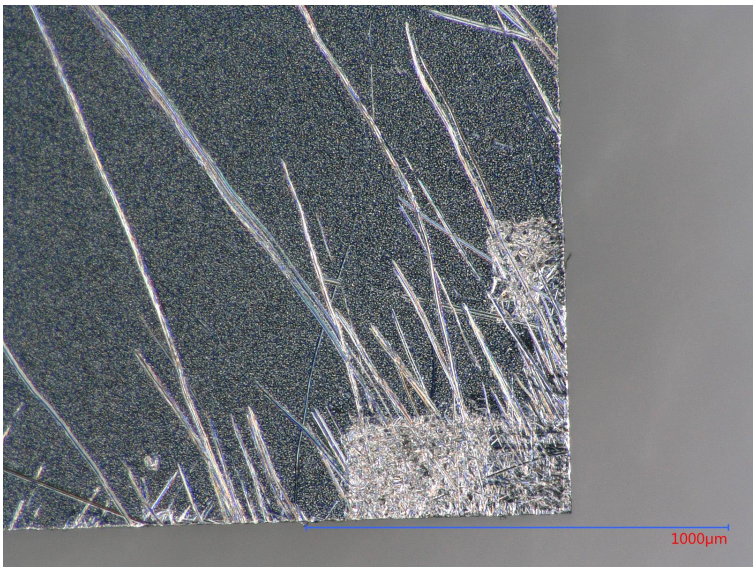

Figure 5.33.: Photograph of a thFZ240 sensor backside. The picture has been captured with a *Keyence VHX-900F* digital microscope [82].

after each increment there is a pause of five seconds before a set of five measurements is taken with a time lag of 1 s in between. The current measured in Aachen is not in agreement with the measurements taken at HEPHY, as shown in Figure 5.34. The presented measurements are not normalized to a constant temperature. HEPHY measured a current below 1 µA at 1000 V bias voltage while in Aachen the set up compliance current of 5 µA has been exceeded below 500 V. The current breakdown of sensor 43 is at about 200 V with a linear increasing current, the breakdown of sensor 11 is at approximately 240 V with exponentially rising current.

A possible reason for the early rise of the leakage current could be that the sensors collected humidity from the atmosphere, although the sensors are stored in dry cabinets and measurements are performed in dry atmosphere. To test this hypothesis, the IV measurement is repeated at a chuck temperature of 50 °C and after reaching the compliance of 7 µA the voltage is held to measure the current again every minute for about two hours. Figure 5.35 presents the leakage current in dependence of the bias voltage and the measurement number. The compliance current is reached at 620 V. Afterwards, the current drops exponentially below 5 µA. So, the sensor shows a significant healing effect over time. However, it is assumed that humidity is not the only cause for the high leakage current.

As another study, the reproducibility of the IV measurements is tested. For this, the IV measurement is automatically repeated multiple times without changing any other measurement condition. The humidity and the temperature inside the probe station are assumed to stay constant over the time of the test as the lab is temperature controlled and the cabin is flooded with dry air. Figure 5.36 (a) presents the IV measurements of sensor 11 repeated multiple times with vacuum fixation applied. The measured current is perfectly reproducible up to a bias voltage of 200 V, at which the current breakdown begins. At higher bias voltages, the currents measured vary only slightly, with the current being lower from measurement to measurement. The compliance current of 7 µA is reached between 330 V and 340 V. If however the test is repeated without vacuum fix-

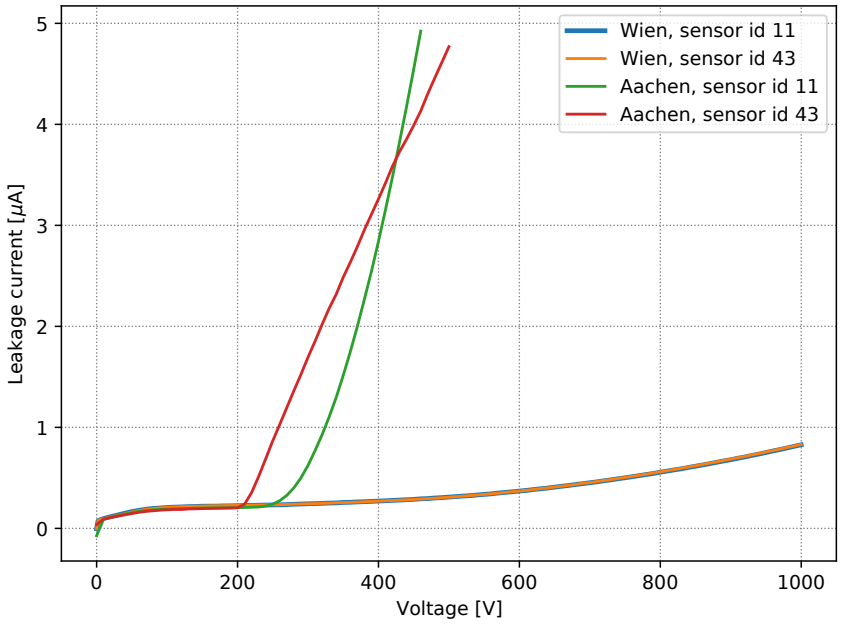

Figure 5.34.: IV measurements of the thinned sensors performed at HEPHY and in Aachen. The measurements are not normalized to a constant temperature.

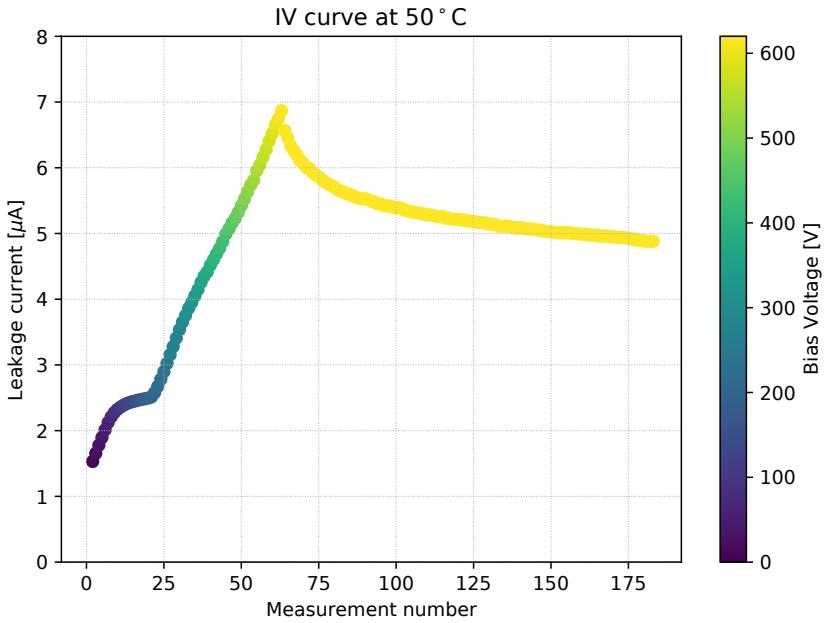

Figure 5.35.: IV measurement of sensor 11 with the chuck at 50 °C. After reaching the set up compliance current of 7 µA the bias voltage is held at this level and a measurement is taken after each minute for approximately two hours.

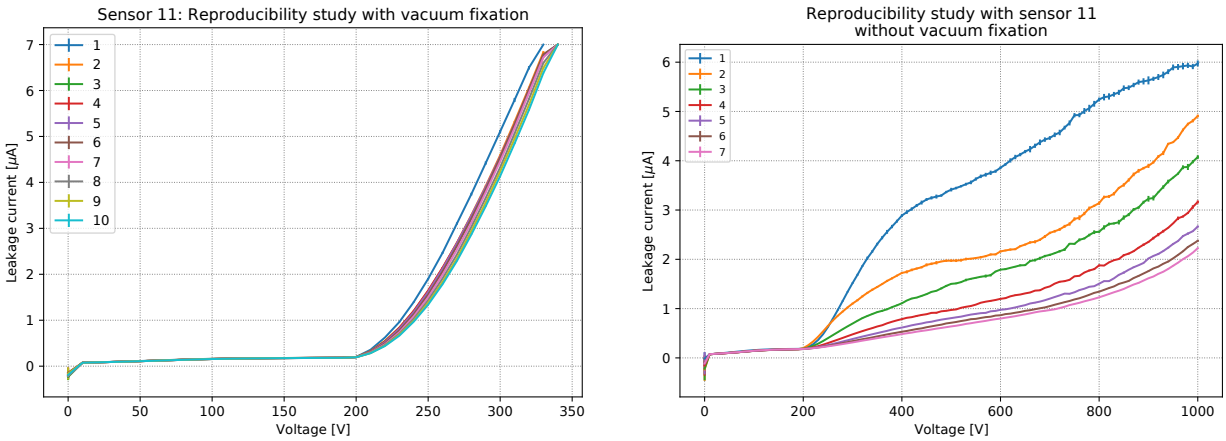

(a) Multiple IV measurements with vacuum fixation.

(b) Multiple IV measurements without applying vacuum.

Figure 5.36.: Reproducibility study with sensor 11. IV curves are repeated several times without changing any measurement condition. Sensor 43 has shown a similar behavior.

ation, the improvement becomes much larger, as shown in Figure 5.36 (b). The last measurement of the series is a leakage current of 2.2 µA at 1000 V bias voltage. This result arouses the suspicion that the increased leakage current may be caused from mechanical stress applied on the sensor. The same study has been performed with sensor 43 that showed a similar behavior.
In order to quantify the mechanical stress applied to the sensors, when the vacuum fixation is used and the sensor is forced to planarity, the intrinsic sensor bow is measured using the DSM. Instead of using the standard mount, which requires the sensors being assembled to the AlCF bridges, the sensor is placed onto a glass plate with the strips pointing up in between the two cameras of the DSM. To measure the sensor bow the camera is manually moved to in total 25 approximately equally spaced positions of the sensor while having the focal point on the sensor surface. Figure 5.37 shows the height profile of the strip surface after applying a correction to compensate for the glass plate being non-perpendicular to the camera axis. The sensors are measured to have a concave bow at the sensor center of about 260 µm for sensor 11 and 280 µm for sensor 43.
These measurements lead to the hypothesis that the FZ240 sensors are vulnerable to mechanical stress leading to early breakdowns. If this is a common issue of the thinned sensors, it could cause critical problems during the series production of modules and the operation of the detector. The experience of module assembly with FZ290 in Aachen on the other side has proven more robustness. In order to come to a decision regarding the sensor design, the CMS tracker upgrade community has performed extensive studies on a larger set of sensors and collected the measurements from all involved institutions including the one presented above. Eventually, the decision has been made to use the FZ290 sensors [42].

5.4.2. Sensor debugging with IR camera / Facing sensor issues

The module assembly during the prototyping phase is done with checks after each assembly step to identify mistakes and weaknesses of the assembly procedure. Besides visual inspections, IV curves are measured. In doing so, scratches on the sensor surface and severe contamination are traced back

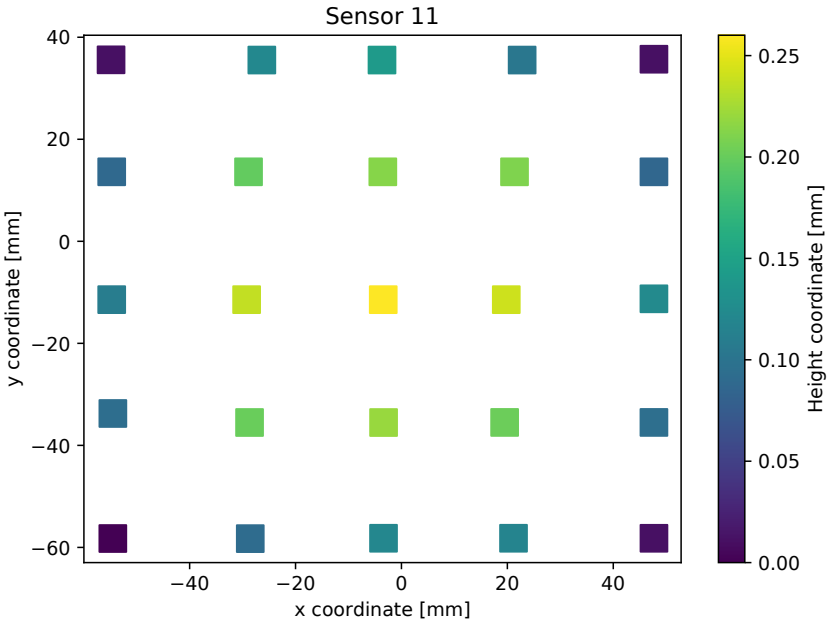

Figure 5.37.: Bow of thin sensor with id 11 measured using the DSM.

to particular handling steps and actions can be taken to avoid these in the future. Additionally, the identification of a particular problem at an early state might enable a repair of the module.

During the assembly of the first functional 4 mm 2S module, M4001, a breakdown of the leakage current of the top sensor has been observed after the wire bonding of the signal wires. Figure 5.38 presents the development of the top sensor IV measurements in the course of the module assembly. The presented uncertainties are the calculated standard deviations of five subsequently taken measurements at the same bias voltage with a delay of 1 s. All IV measurements taken during the assembly process, before wire bonding of the signal wires, do not exceed the compliance current of 7 µA up to a bias voltage of 800 V. The leakage current seems to improve after hybrid gluing. That effect could be caused by exposure to humidity, as the glue curing processes take place under lab conditions to avoid any movements after applying the glue. After wire bonding, a breakdown of the leakage current has been observed immediately when the sensor is biased so that the compliance current is reached at 50 V already. Drying the module inside a dry air flooded cabinet for many days has not changed the IV performance. Furthermore, a rigorous visual inspection could not reveal a definite reason for the breakdown as no significant scratch or contamination has been found in comparison to the visual inspections related to the assembly steps before.

In order to further investigate the cause of the IV breakdown of M4001, an infrared (IR) camera setup has been developed. For this, a light tight box made up with aluminum bars as frame and plastic surrounding is used. The inner walls are covered with black textile to reduce reflections inside the volume. The 2S module is placed onto the bottom of the box. The *FLIR Systems Thermovision A40* [85] IR camera is mounted above at an adjustable aluminum bar slightly inclined in order to avoid capturing the camera emission at the sensor surface. Camera cabling and power cables for the 2S module are guided through a drill hole at the top of the box. The drill hole is sealed light tight

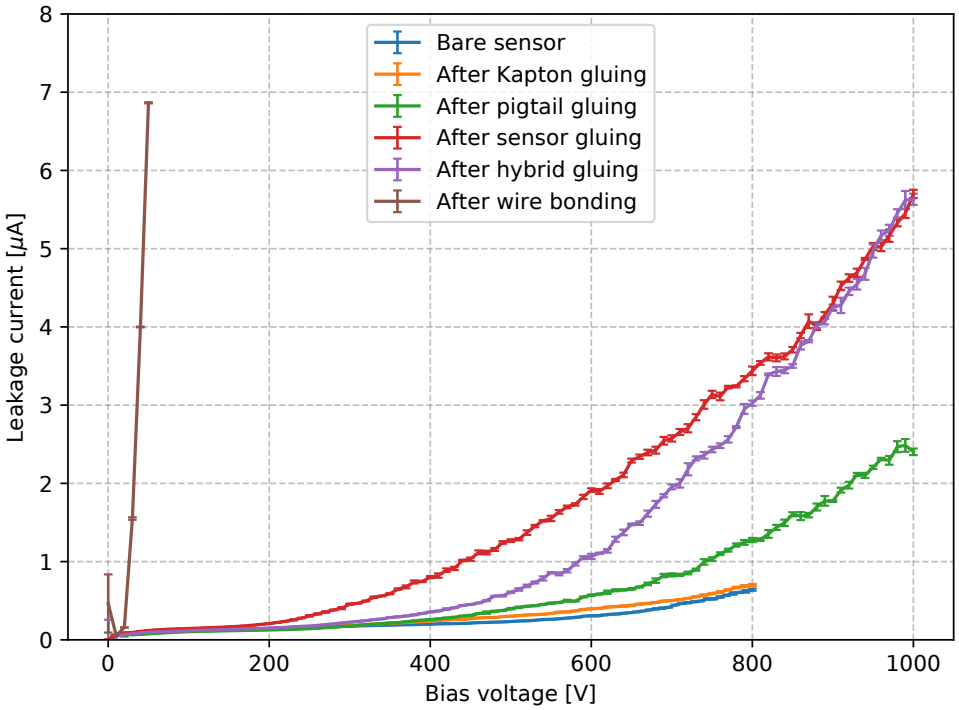

Figure 5.38.: M4001 top sensor IV measurements in the course of the module assembly.

with aluminum foil and tape. The module surroundings, especially the aluminum carrier plate, are covered with clean room tissue to avoid reflections.

To find the cause of the high leakage current, the 2S module is biased at 400 V with deactivated compliance current. At this bias voltage the leakage current has increased to approximately 2.5 mA so that a powering of 1 W is achieved and a measurable emission of infrared radiation is expected. Figure 5.39 (a) shows the IR camera photo of the unbiased 2S module. If this photo is compared to the photo of the biased module shown in Figure 5.39 (b), a bright spot is clearly visible close to the module center at the side opposite to the SEH. By inspecting the center of the particular region under the microscope a tiny but deep scratch visually only affecting a single strip has been found which is shown in Figure 5.39 (c).

In order to further study the damage at the respective strip (sensor strip id 1183), the module has been biased at 60 V within the probe station and the voltage between the AC pad and the bias ring has been measured. This measurement has been performed at the respective strip and is compared to the measurements at the surrounding 20 strips. As a result the voltage measured at the scratched strip has been found to be about 30 times higher than that of the neighboring strips (Figure 5.40). If the same voltage measurement is applied between the DC pad and the bias ring, no difference has been found between the scratched strip and its neighbors.

These measurements indicate that the damage on the strip is deep enough to generate a high current from the HV back plane and through the bulk to the AC pad. By wire bonding the signal wires, the AC pad is connected to the CBC on the FEH which is connected to the HV ground. This leads to a high current. As the wires have not been encapsulated yet, the wire connected to the damaged strip could easily be removed using the pull tester. Figure 5.41 presents the IV

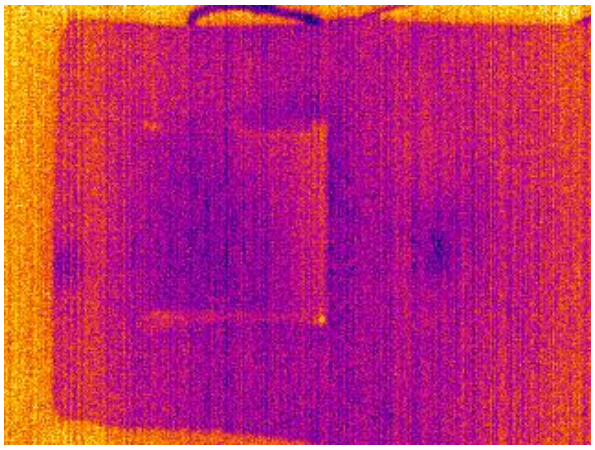

(a) IR camera photo of the unbiased M4001 module.

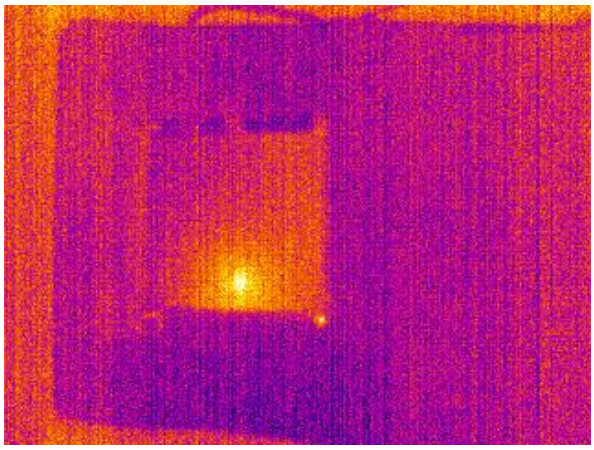

(b) IR camera photo of the M4001 module at 400 V bias voltage and 2.5 mA leakage current.

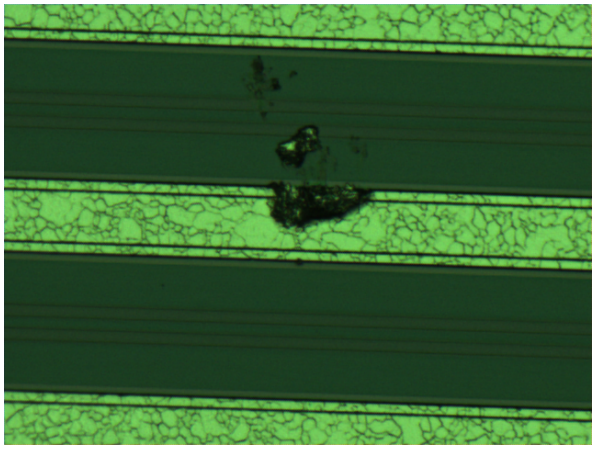

(c) Microscope photo of a damage found at the position of the IR photo hot spot.

Figure 5.39.: Photos of the M4001 2S module taken with the IR camera and the microscope.

measurements taken before and after pulling the respective wire. The measurement after removing the wire features a significant improvement compared to the IV performance before the removal as the compliance current of 7 µA is not reached until a bias voltage of 730 V, which is well above the sensor depletion voltage. As a result the prototype module could be used for readout tests.

5.5. Series production

The two institutes, Physics Institute I B and Physics Institute III B, of RWTH Aachen University have accepted to assemble and test approximately one-thousand 2S modules for the Phase-2 CMS OT. The series production of such detector modules requires elaborate preparations and detailed planning. Reaching the goal of one-thousand modules within one year, with another year to compensate for delays and hardware defects, would require the completion of at least four modules per day on average, assuming that a year has 250 working days. This will only be possible by a parallelization of the steps as the assembly of a single module requires up to seven days due to glue curing. Additionally, large effort has to be made in the QA ensuring that the good quality of the assembled prototype modules can be preserved in the series production. For this, environmental

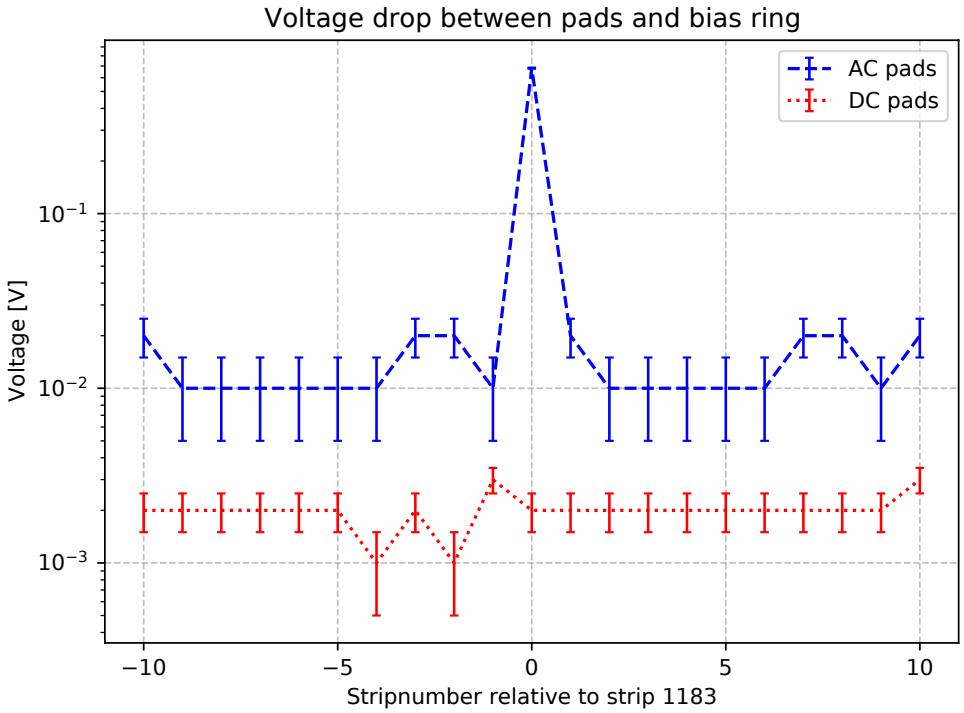

Figure 5.40.: Measurement of the voltage drop between pads and bias ring.

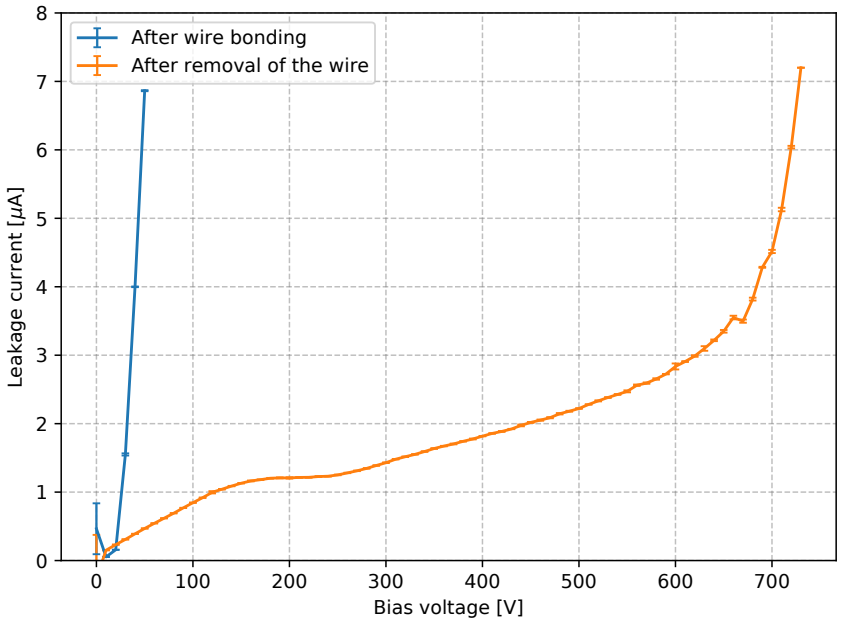

Figure 5.41.: IV measurements taken at the M4001 top sensor before and after pulling the wire connected to the damaged strip.

parameters of the clean room that is used for the assembly are monitored and capabilities for clean and safe storage are prepared.
Section 5.5.1 describes the workflow of the series production taking into account the experiences gained in the assembly of prototype detector modules. Section 5.5.2 presents working and machine time estimations to extrapolate the manpower needs and to identify potential bottle necks. The clean room for the series production is described in Section 5.5.3.

5.5.1. Workflow overview

Parallelization of assembly steps during the series production of 2S modules is mandatory to achieve a completion of four modules per day on average. Otherwise, the jig and machine availability would have to be increased by a factor of up to seven in order to maintain the same assembly completion rate. In this case, for example the wire bonding machine time would be heavily exceeded as 28 modules (4 modules per day times 7 avoiding parallelization) would have to be bonded on a single day. Instead, the 28 modules are uniformly distributed over all assembly steps in parallel series production. Details of machine time estimations during the series production are described in Section 5.5.2.
Figure 5.42 shows the module assembly workflow parallelization of assembly steps. The reception test of components can be done batch wise and independently of the actual module assembly as long as there are always enough tested components for the assembly process. Every day, the assembly of at least four modules (as described in Chapter 5) starts. Each row represents a batch of at least four modules and each column shows a day. After seven days of module assembly all steps are done in parallel and four modules are completed each day. The color of the frames indicate whether a special machine is used. Each day, the wire bonding machine is used to wire bond the HV wires and to electrically connect the FEHs to the sensors. Gluing robots will be used daily for the gluing of Kapton strips and HV pigtails, for the hybrid gluing and for the encapsulation of signal wires (and optionally for the encapsulation of HV wires). Red arrows indicate the propagation of assembly jigs from one module batch to the next. All jigs can directly be used for the next batch except of the Kapton gluing jig sensor part. This part is also used for the wire bonding of HV wires and their encapsulation and therefore twice as many jigs have to be prepared. Furthermore, it is important to note that the Kapton gluing jig is occupied once per sensor (and not once per module). Consequentially, if a production rate of four modules per day is targeted, at least eight Kapton gluing Kapton parts and 16 Kapton gluing sensor parts are required.
Table 5.3 summarizes the numbers of required jigs in the production workflow assuming a daily output of four modules. The table also contains information about the footprint of the particular jigs for detailed estimations of storage capacities at different stages of the assembly process. Jigs which are used for a gluing step also need to be safely stored for curing of the glue. The jig has to remain in a horizontal position in order to avoid unwanted glue spread from flowing by gravity. Additionally, the storage place needs to be ESD safe, dry and closed to protect the sensor material and the electronics from damages or contamination induced by the environment. Optionally, the curing of the glues can be sped up by increasing the atmospheric temperature. In order to meet these requirements, different storage cabinets have been acquired:

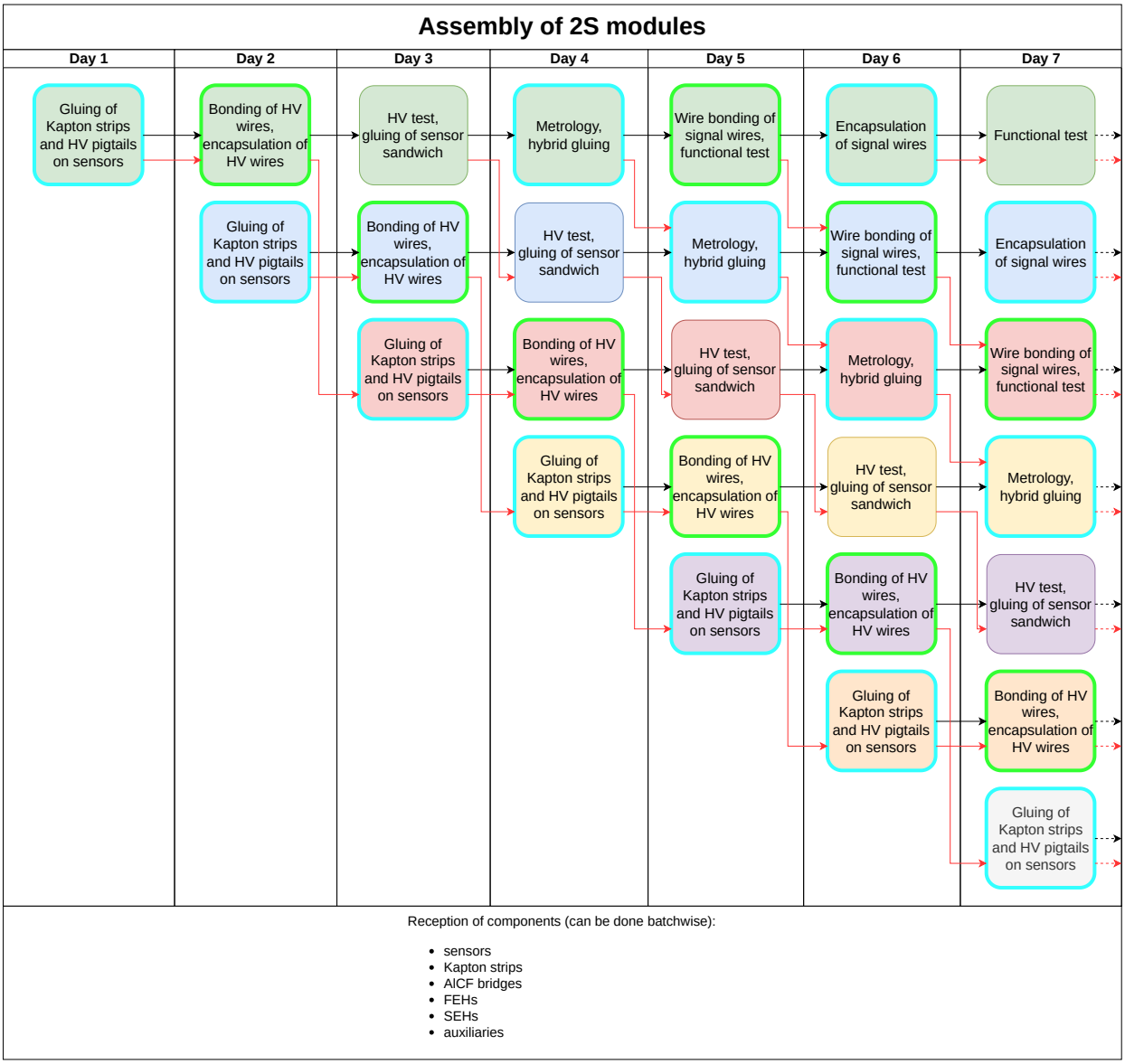

Figure 5.42.: Parallelization of steps during series production. Each column shows the workload of a day in series production. The red arrows indicate the propagation of assembly jigs. The bright blue and green highlighting of process frames indicates that either a gluing robot (blue) or the bonding machine (green) is occupied for this process.

- Superdry Totech SD+ 1106-22 [86]: The cabinet provides a large volume of 1139 l on six planes of approximately 119 cm × 63 cm. The available space is therefore large enough to store the expected number of jigs while curing the glues. The interior surfaces are ESD safe. The cabinet is equipped with an active air drying unit capable for 24 hours operation reaching a relative humidity of down to 2 %. Additionally, a heater is installed to achieve temperatures of up to 40 °C to accelerate the glue curing processes.

- Sicco Maxi 1 Exsiccator [87]: The cabinet provides a usable volume of 311 l with four shelves of 495 mm × 540 mm. The air humidity is measured by a hygrometer and drying is done using desiccant.

Table 5.3.: Overview of jigs with minimum of required numbers and the footprint. For the minimum number of jigs required a daily completion of four modules is assumed. If a higher output shall be considered, the number scales linearly.

Jig type	**Min. number**	**Footprint per jig [mm^2]**	**Storage Conditions**
Kapton gluing: Kapton part	8	156.7 × 156.0	Curing of *Polytec EP601LV* with sensor part
Kapton gluing: Sensor part	16	156.7 × 156.0	Curing of *Polytec EP601LV* and curing of *Sylgard 186*
Sensor gluing	4	250.0 × 250.0	Curing of *Polytec TC437*
Hybrid gluing	4	160.0 × 160.0	Curing of *Polytec TC437*
Wire bonding	4	156.7 × 156.0	
Carrier (encapsulation)	4 / 8	176.6 × 197.5	Curing of *Sylgard 186*

In Aachen the reception tests, the module assembly and module tests cannot be done in a single room during the series production because there is no room available which fulfills the spacial requirements and can be used as a clean room. Instead it is planned to have a clean room which is dedicated for the whole assembly (gluing, wire bonding, glue curing) and additional labs for functional tests (module readout test, skeleton test, cold test) and module QA (metrology, HV isolation test, IV measurements). The lab used for functional tests is nearby to the module assembly room as only its locker room lies in between. The second testing lab for assembly QA is in another floor. Figure 5.43 shows the path a module travels between the different rooms. The reception test can be carried out batch wise and does not need to occur shortly before the respective components are used for assembly. After the reception test is passed the components are collected at the assembly room. There, the module assembly is carried out until the HV connection is established and the wires are encapsulated. Then, the HV isolation test is done in the second testing lab before sensor gluing in the assembly clean room is resumed. Afterwards, the sensor alignment is checked using the DSM which occurs in the second testing lab again. For hybrid gluing and wire bonding the module is brought back to the assembly clean room. After the channels are successfully connected to the sensor the first functional test is performed in the first testing lab. If the test is passed, the wires are encapsulated in the assembly clean room as the last assembly step. Finally,

the module runs through another functional test in the first testing lab. Here, the module is also prepared for shipping to DESY where the burn in test takes place and the modules are mounted onto the larger structures. Following this plan, each module travels seven times between rooms before it is finalized.

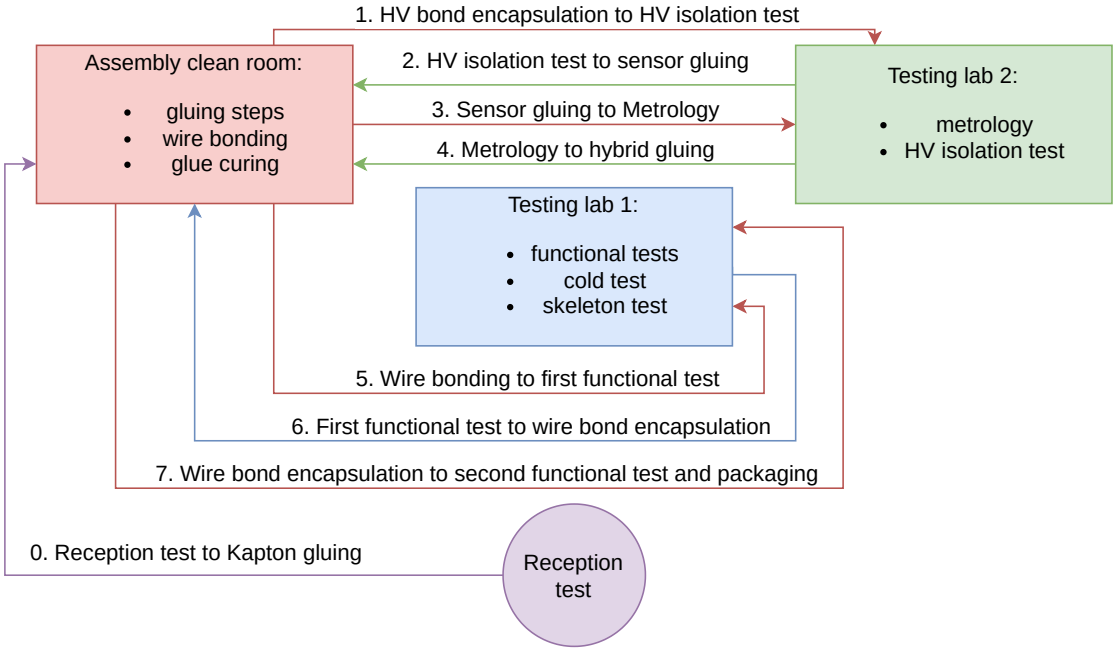

Figure 5.43.: Diagram of the traveling of a 2S module between different rooms during the series production.

5.5.2. Time estimations

Based on the experiences gained assembling prototype modules, the assembly time is estimated in detail. Assembly times have been measured and projected on the series production scenario to the best of knowledge. The study aims for the most realistic estimation of assembly time possible. It is used to evaluate the manpower required and to check whether the machine capabilities are adequate. However, the assembly during the prototyping phase has partially been found to be much more time-intensive than realistically estimated for series production. On the one hand this is because some assembly techniques are not yet final and still tuned while assembling. On the other hand during prototyping some components have been found to be of non-optimal quality, so that workaround has been required. It is assumed, that routine and components, that are well known and of good quality, will accelerate the process significantly. As some of the assembly and QA tasks are not yet defined for series production there are some uncertainties.
For the estimations a daily output of four modules is assumed. If another assembly rate should be considered the times have to be scaled. However, it is important to emphasize that there are some handling steps which do not become faster by reducing the number of modules, e.g. mixing the glue, which would be done once for many modules. Additionally, a daily output of multiples of four modules could be advantageous as the working area of the gluing robot as well as the length of the conveyor system attached to the bonding machine fits four times the footprint of most of

the respective assembly jigs. An output of eight modules per day, however, is expected to be not realistically achievable.

Figure 5.44 shows the overview of the times estimated for the different steps of module assembly and QA. The steps are roughly ordered on the y axis according to their order in module assembly. Because of the parallelization of module assembly, each step is however done each day and the steps must not necessarily be completed in a fixed order. The estimated times are listed in detail in Tables A.1 to A.9 which can be found in the Appendix A. Each step listed is considering two minutes of documentation per module and five minutes per step and per day for transport between work spaces or labs. For all of the gluing steps, a time of 20 minutes is estimated for mixing the respective glue, preparing the syringe and cleaning the tools.

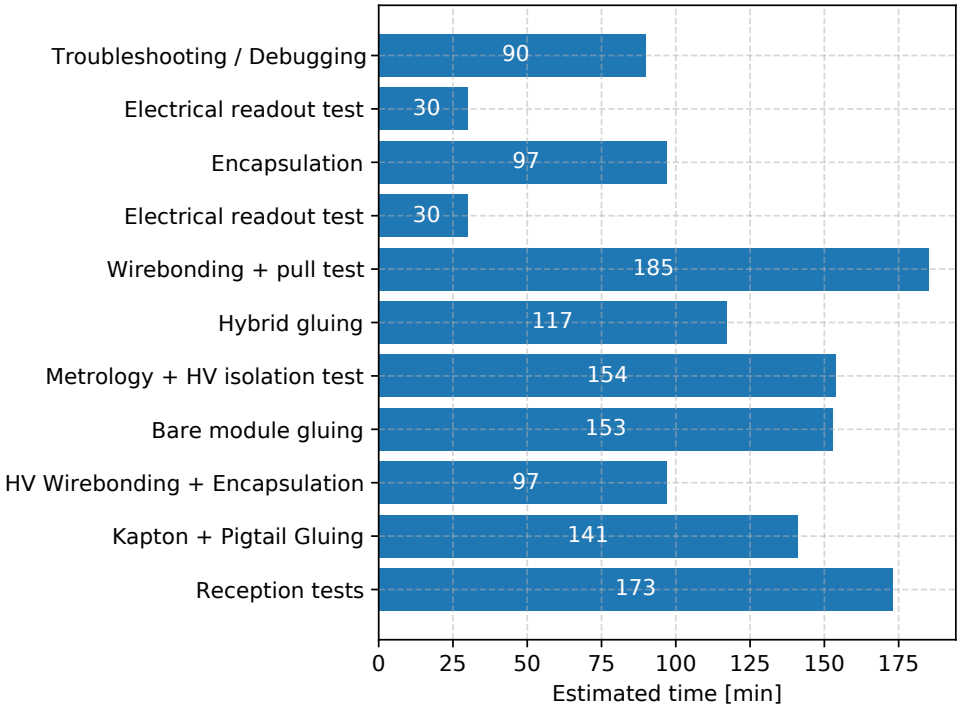

Figure 5.44.: Bar chart of the expected assembly time per step for four modules.

The reception test is estimated to take in total 173 minutes. This includes the electrical test of the hybrids and the sensor reception (optical inspection and IV curves). After pre-production the sensor reception however might be dropped at that point and not be done until the HV test before the sensor gluing. That would save an estimated time of 20 minutes per module. Reception tests of other components are expected to consist of only a visual inspection. The estimated times for these are included as part of the step, when the respective component is used for module assembly. The Kapton and pigtail gluing step sums up to 141 minutes including visual checks of the Kapton strips and the pigtails as well as checks of the sensor before and after the gluing. The HV wire bonding and encapsulation is estimated to in total 97 minutes. For this, a fully automated bonding with conveyor system is assumed. This has not been tested yet on modules because of the low number of components available for the entire community. However, automated wire bonding has successfully been done using test structures. The sensor gluing step has been evaluated to take 153 minutes

every day. This includes a visual check and cleaning of the AlCF bridges with eight minutes per module. The step of the DSM and HV isolation test also includes a sensor inspection procedure and is estimated to take 154 minutes per day. Following the hybrid gluing procedure developed by the CMS group from KIT, this step takes about 117 minutes for four modules. The step of wire bonding and pull testing the signal wires is estimated to take 185 minutes. For this the machine time is not considered, but the time to fill and start the bonding machine and to perform visual and pull tests. Most of those can be carried out while the machine is running. In case of an unstable bonding process, which requires many interventions by the operator, this step would take much longer. The pure machining time can be calculated with a bonding speed of 1.5 wires/s summing up to approximately 45 minutes per module and three hours per day (Section 5.2.2). The work of replacing empty spools or any other service work related to wire bonding is not included. Assuming that spools of 500 m wire are used, an exchange has to be done once every six days with a wire consumption of about 75 m per day. The electrical readout test is estimated to take 26 minutes of work. This includes connecting the modules, starting the test program, disconnecting the modules and documentation work. The pure machine time is not included and as the extend of these tests is not yet defined the machine time cannot yet be estimated. The time for the encapsulation of the signal wires has been rated to 97 minutes each day for both sides of four modules. This includes also minor manual corrections after completion of the dispensing program. For any unforeseen problems that necessitate troubleshooting of assembly setups or modules, debugging of analysis code or additional IV curves a daily time of 90 minutes is included. Of course these tasks can temporarily demand much more work, but in times of regular production also much less.

Based on the estimated assembly times, an exemplary day in the 2S module series production is outlined. Figure 5.45 presents a possible scenario of a day in series production as a sketch for only three persons involved. The assembly steps are assigned to the three persons ordered by professions and machines used. These persons could for example be a physicist (person 1), a technician from the mechanical workshops (person 2) and a technician from the electrical workshops (person 3). The times listed in the sketch are rough estimates as compared to the numbers described above. Red dashed arrows indicate dependencies between different steps. If those cannot be fulfilled, the storage capabilities and number of required jigs have to be increased. Additionally, each person can only effort at maximum eight hours per day and has to take a break. Person 1 would be responsible for reception and module tests. Person 2 would do any gluing step. At last, person 3 would be the expert for wire bonding. Summing up the work loads of each, person 2 would probably exceed the limit of eight hours. In that case, either a fourth person needs to be involved or person 1 or 3 would have to help out.

5.5.3. Clean room planning

To ensure the high quality of the modules, certain requirements for the laboratory environment must be met. The CMS OT upgrade community therefore agreed on the following environmental specifications:

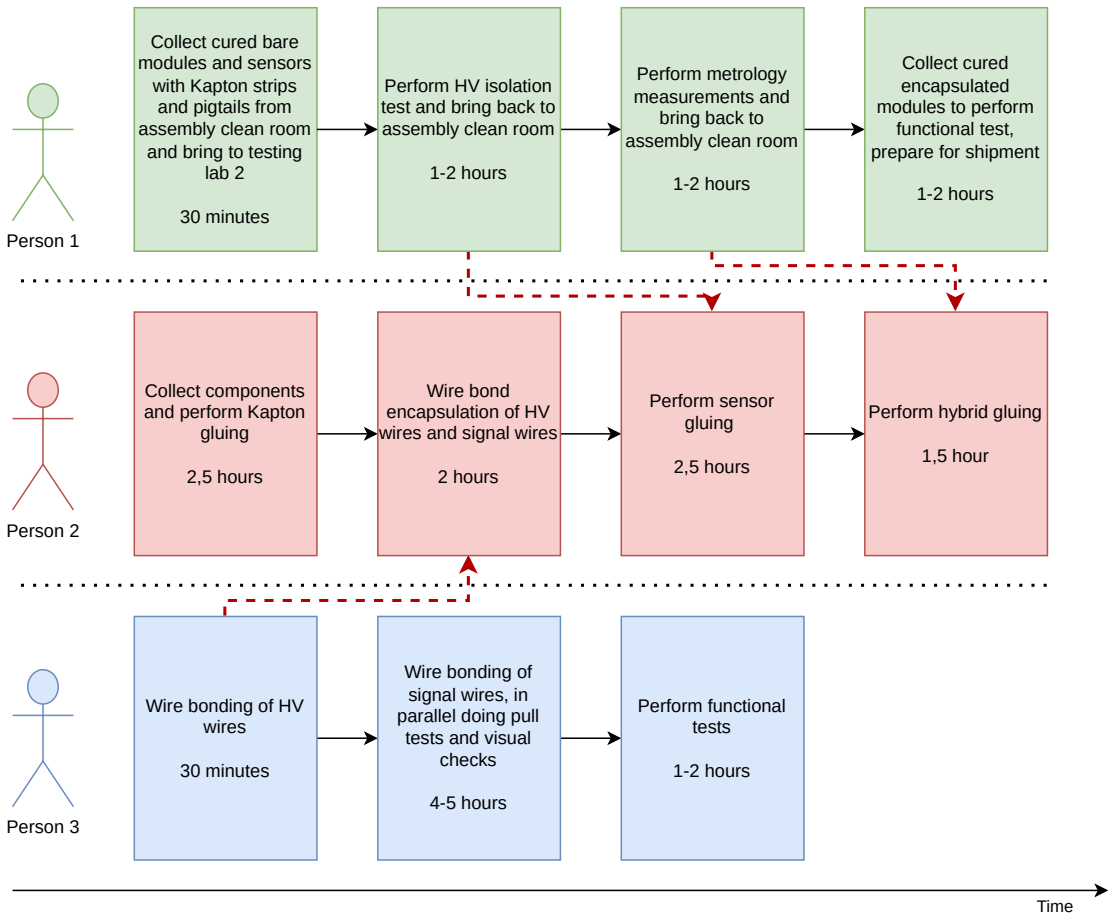

Figure 5.45.: Sketch of a day in the 2S module series production.

- The clean room has to achieve an atmospheric particle concentration equivalent to class 7 according to ISO 14644-1 (or class 10000 according to US-FED-STD 209 E) or better. Dust particles could harm the bonding quality and lead to bad wetting quality of glue layers.
- The temperature has to be between 17 °C and 28 °C with a daily deviation below 3 °C. A larger deviation could harm the calibration of temperature sensitive devices. Additionally, the viscosity of 2K glues varies with temperature, so dispensing programs might have to be adjusted.
- The relative humidity has to be in the range between 35 % and 65 %. The dew point has to be at least 5 °C below ambient temperature. A relative humidity below or above could lead to sparking or surface leakage currents that could damage electrical devices. Furthermore, the sensors could absorb humidity leading to higher currents.
- The quantities listed above have to be continuously monitored and measured at least once per day per lab used for module assembly.
- Surfaces and tools have to be cleaned on a daily bases. The floor and walls have to be cleaned at least weekly with a mop and a vacuum cleaner with HEPA filtration.

In order to fulfill the specifications listed above, a monitoring system of the atmospheric conditions of the clean room has been developed in the course of a bachelor's thesis by Max Beckers [88]. It is based on a network of Raspberry Pi devices distributed across the labs and each of those can modularly be equipped with sensors. Temperature, relative humidity and air pressure are measured using *BME280* sensors [89] which have been cross calibrated for improved comparability. The atmospheric particle concentration is measured using *Piera IPS-7100* sensors [90]. Additionally, infrared sensors (*Omron D6T* [91]) and reed switches at the doors have been installed to track presence inside the lab. As the clean atmosphere is achieved by flow boxes that filter the air, current probes (*Shelly EM 50A*) are used to monitor the power consumption as a measure for the correct operation. The sensor data are visualized via a locally hosted *Grafana* interface [92]. The measurements are saved into a time-series database using *InfluxDB* [93].
The clean room for module assembly is shown as a sketch in Figure 5.46. The lab space is divided into two task oriented areas, the wire bonding and the gluing area. The wire bonding area is equipped with the bonding machine and the pull tester which is positioned on a table providing some work space for jig preparation. Additional work space is provided within the flow box. The gluing area is equipped with the two dispensing setups, two glue mixing robots and two tables as well as two flow boxes that are used as work space. Near the clean room entrance there are two microscopes that can be used for visual inspections and the *SuperDry Totech* storage cabinet mainly used to safely store modules during assembly and accelerate glue curing at temperatures up to 40 °C.
The clean room is accessed through the changing room where each operator can put on his / her clean room clothes. A set of clean room clothes consists of an overall, clean room shoes, a hair net and optionally a face mask. Besides the clean room entrance the operator can use the ESD personnel test station *222564* by *Desco Europe* [95], whether the clothing fulfills proper ESD safety

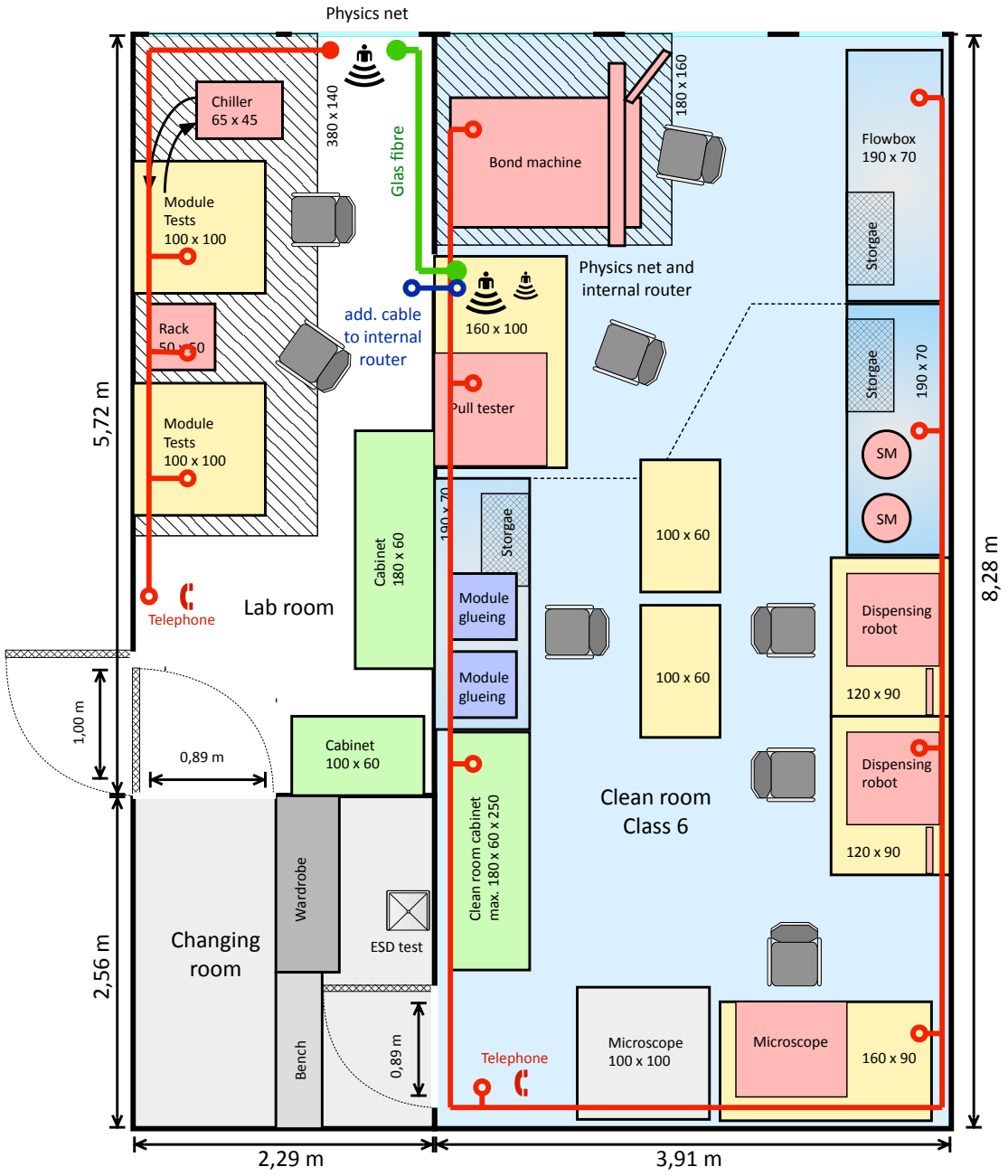

Figure 5.46.: Sketch of the clean room for module assembly and lab for module tests [94]. The red lines present the network infrastructure with the circles indicating the coarse position of the network socket.

criteria. Additionally, there is an RFID scanner used to check in when entering the clean room and out on leaving. For this, every operator has its RFID chip. Should it be desired, this procedure can be anonymized.
The lab besides the clean room will be used for functional tests. After the module is wire bonded and after the wire bond encapsulation the modules are brought through the changing room to perform readout tests. For this purpose, a multi module test station has been developed by Christian Dziwok [96] which is capable of testing up to four modules at temperatures down to $-35\,^{\circ}\mathrm{C}$. Additionally, there are two test stations for module tests at room temperature developed and distributed by the KIT CMS group. Those setups also feature a readout test with signal induction by a pulsed infrared array [97].
Another clean room is located in the Physics Institute I B (earlier referred to as "testing lab 2"). It is used for the module metrology and IV and isolation tests in the probe station.

6. Beam test

In November and December of 2019, the generation of 2S prototype modules with 8CBC3.0 and 8CBC3.1 FEHs with CIC mezzanine cards and SEHs 3.1 (with GBTx and VTRx) used for powering and communication has been tested in a test beam for the first time. By testing the prototype modules in a beam test with a dedicated beam telescope, the performance could be evaluated with precise track information, which enables position dependent measurements of efficiency, cluster size and detector resolution. Furthermore, the performance of the stub mechanism has been tested and for the first time multiple modules have been read out synchronously in a beam test setup.
Additional beam tests, probing the same generation of modules, have been performed in 2020. Because of the Covid-19 pandemic and tight contact and travel regulations, a physical participation was not possible but support in the analysis of data taken has been given. In August 2020 beam test studies have been performed with a 2S module with irradiated sensors and in November 2020 scans which could not be done in 2019 for lack of time have been done.
Table 6.1 lists the modules and the measurement goals of the beam test mentioned above. This thesis presents analyses that have been performed on the AC-M1804 module during the beam test campaign of 2019. Additionally, the performance of the KIT-3 module has been analyzed at different bias voltages. Tests of synchronous readout of multiple modules have been performed in 2019, however only preparation work, the alignment of modules at the downstream end of the telescope (Section 6.4) and track resolution analysis at these positions (Section 6.6), is done as part of this thesis.

Table 6.1.: Overview of the three beam test campaigns to test the performance of 8CBC3 2S module prototypes.

Beam test campaign	**DUT modules**	**Measurement goal**
November 2019	AC-M1803, AC-M1804, KIT-1, Brown-SF1902	First efficiency studies with CIC and optical readout, synchronous readout of multiple modules
August 2020	KIT-3	Full size 2S module with irradiated sensors to compare with campaigns with un-irradiated modules
November 2020	KIT-5, DESY-1	Add missing beam test measurements

The analysis framework, *FABEL*, used for the presented analyses has been developed in cooperation together with Christian Dziwok [96]. It provides a common base in the processing of beam test data to link clusters to telescope tracks after tracking and track alignment performed with the EUTelescope framework [98]. The linking mechanism and the data management has been implemented by Christian Dziwok. FABEL furthermore features tools for the alignment process of the

DUT in the interaction with EUTelescope as well as a number of predefined tags for the implementation of analysis selection criteria. The development of the latter features and the presented higher level analyses have been performed in the course of this thesis. The framework is described in Section 6.3.2. Details on the DUT alignment are presented in Section 6.4, which is followed by the high level analysis.
Parts of the results presented in this chapter will be published as a CMS tracker paper. The measurements leading to these results have been performed at the Test Beam Facility at DESY Hamburg (Germany), a member of the Helmholtz Association (HGF) [5, 99].

6.1. DESY II Test Beam Facility

The DESY II Test Beam Facility provides an electron or alternatively positron beam with a selectable momentum in the range of 1 to 6 GeV [5] at three beam lines. The test beam does not consist of primary particles from DESY II. Instead, the test beam is generated by creating bremsstrahlung photons in the interaction of DESY II electrons or positrons with a fiber target in their orbit. The photons produce electron-positron pairs in a secondary target. Using a dipole magnet, the polarity and momentum of the beam particles is selected. Figure 6.1 shows the test beam particle generation for beam line 21 as a schematic.

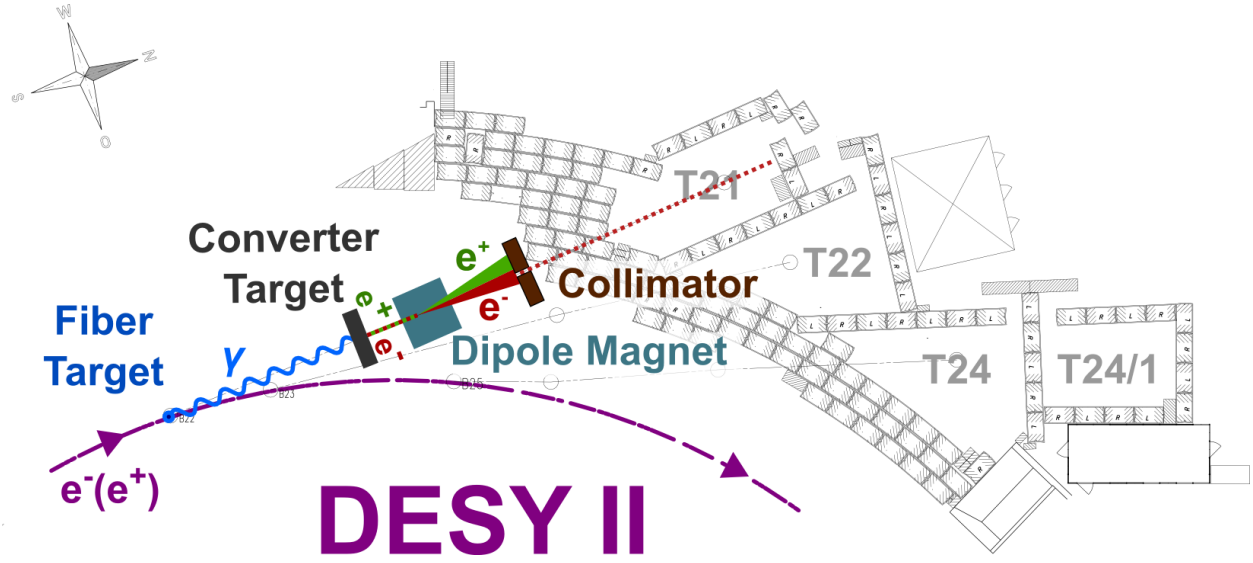

Figure 6.1.: Schematic of the particle beam generation at the DESY II Test Beam Facility [5]. The beam particle generation is shown for beam line 21.

The DESY II Test Beam Facility additionally provides slow control units, bore magnets for magnetic field tests and EUDET type pixel beam telescopes for precise spatial resolution. The EUDAQ framework [100] is used as the DAQ interface to offer a simple integration of the DUT into the beam telescope DAQ and its trigger system, the Trigger Logic Unit (TLU). Details of the beam telescope and the DAQ are discussed in Section 6.2.
The test beam particle rate in the individual test beam areas depends on the DESY II beam intensity as it affects the amount of bremsstrahlung photons [5]. Furthermore, the settings of the beam lines like selected particle momentum, primary target position or the opening of the primary

collimator strongly impact the effective rate. The particle rate measured during the beam test campaign of November 2019 has been approximately 2 kHz at 4 GeV.

The particle momentum is set up by the operator by adjusting the current of the test beam magnet. The momentum spread has been studied by calibration measurements and simulations and found to depend strongly on the particle momentum [5]. The relative spread ranges from 1.5 % at 6 GeV to 12.7 % at 0.9 GeV. At the default beam energy of 4 GeV used during the beam test campaign of 2019 the relative momentum spread is specified to be approximately 3.2 %.

6.2. Description of the beam test setup

All beam test campaigns considered in this thesis have made use of the DATURA telescope in beam line 21 of the DESY Test Beam Facility. Section 6.2.1 introduces the DATURA telescope in detail. The description of the integration of the DUT is following up in Section 6.2.3.

6.2.1. The DATURA telescope

DATURA is an EUDET-type telescope [101] which is permanently available at beam line 21 of the DESY Test Beam Facility. It consists of six Mimosa26 pixel modules [102] with an active area of approximately 224 mm^2 and a squared pixel pitch of 18.4 µm. The pixel matrix is composed of 576 rows and 1152 columns. Each of the latter is connected to an offset-compensated analog-to-digital-converter (ADC). Taking charge sharing into account, the single point resolution is improved from simple binary resolution of 5.3 µm to a resolution below 4 µm. The Mimosa26 module has an integration time of 115.2 µs, as a rolling-shutter with 16 cycles of 80 MHz readout per row is applied.

Figure 6.2 (a) presents the described DATURA telescope setup as used in the beam test campaign of November 2019 as a sketch, Figure 6.2 (b) shows a photograph of the beam telescope. In the telescope center the DUT can be mounted on a remotely movable stage, allowing translation in x and y and additionally a rotation around the y axis. The xy plane is defined as perpendicular to the beam axis z with x being horizontal and y being vertical. During the beam test campaign of 2019 the power supplies of the stages needed to be disabled because they induced noise to the DUT. Therefore, the stages have only been moved in between the beam test runs and the y axis has been fixed mechanically to prevent falling of the stage. At the downstream end there is enough space for another DUT. Section 6.2.3 describes the boxes housing the 2S modules in detail.

At the upstream end of the telescope a crossed pair of scintillators attached to PMTs is mounted for trigger purposes. The DAQ chain including the triggering is described in Section 6.2.2.

A time reference detector is needed to select tracks matching the 25 ns readout cycle of the DUT. For this, an ATLAS FE-I4 pixel detector [103] was used during the beam test campaign of November 2019 and the CMS FPIX module [17] was used during the 2020 beam test campaigns. The FE-I4 holds a pixel matrix of 80 by 336 pixels with a pixel size of $50 \times 250\,\mu\mathrm{m}^2$. The CMS FPIX module has an active area of $16.2 \times 64.8\,\mathrm{mm}^2$ with a pixel size of $100 \times 150\,\mu\mathrm{m}^2$.

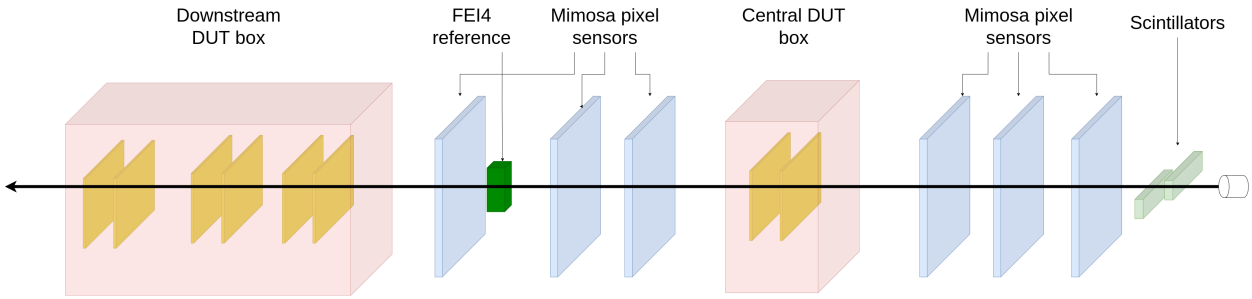

(a) Sketch of the DATURA telescope setup as used in the November 2019 beam test campaign. The Mimosa26 pixel planes are shown in blue, the FEI4 time reference plane is colored dark green and the 2S module sensors are sketched in yellow. The telescope is shown with the beam going from the right (upstream) to the left (downstream). The telescope sketch is not to scale.

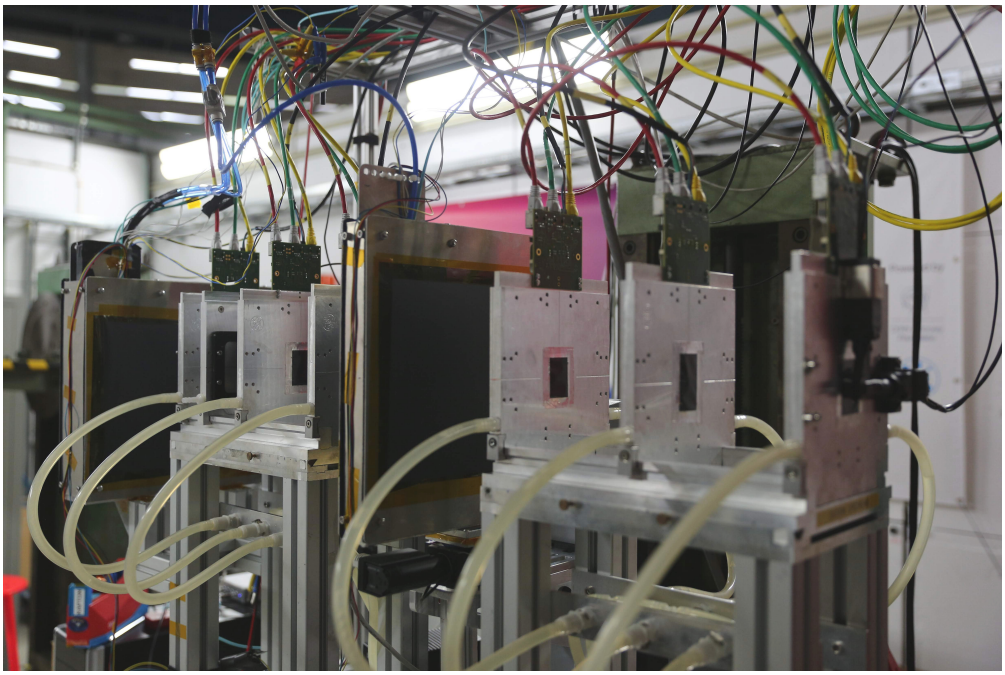

(b) Photograph of the DATURA telescope during the beam test campaign of November 2019.

Figure 6.2.: The DATURA telescope.

6.2.2. DAQ

Dataflow

The data flow from detector level to the high level analysis is shown in Figure 6.3. The different detectors used in the DATURA telescope are shown as rectangles. Each of the detectors is connected to its back-end board. The 2S modules are plugged via an optical fiber to an FMC connector on the FC7 [104]. The time reference detector in use, either FEI-4 or CMS FPIX, uses its own detector specific readout. The Mimosa26 detector planes are processed by a National Instruments FlexRIO board [105].
Each of the readout devices is connected to the TLU [106] which receives the signals from the two PMTs mounted onto the scintillator plates at the upstream end of the telescope and triggers at coincidence. The TLU distributes the trigger signal back to the back-end boards to launch the readout and reads back whether the detector is busy.
The data are processed in software in the next step. Each device (DUT, time reference detector, Mimosa26) has a dedicated *producer*. A producer is a standardized interface for communication and data handling. The 2S module producer *Ph2Producer* is based on *Ph2ACF* [107] which is the acquisition and control framework for the Phase-2 CMS tracker. The different producers are controlled by the *RunControl*, the top level interface used by the beam test user.
The *RunControl* collects the data and stores them in a *rawFile* which only holds the bare readout information. The *EUTelescope* framework [98] is used to clean data from noisy pixels and to form clusters before the telescope planes are aligned and tracks are fitted. More details about the *EUTelescope* framework are presented in Section 6.3.1. The DUT and time reference detector data for high level analysis are written by *EUTelescope* into a *ROOT* file with tree structure [108]. A custom analysis framework, Framework for Aachen's Beam test studies with Extended Linking (FABEL), has been developed for the high level analysis, which is introduced in Section 6.3.2.

Hit / stub detect logic

The 2S modules can be configured with different hit and stub detect logics [41]. The detect logic defines the way, how the comparator is evaluated to form the analog to digital conversion output. During the beam test campaigns of 2019 two different detect modes have been tested, sampled and latched mode. The comparison of these two is done in the beam test analysis performed by Christian Dziwok as part of his PhD. Most of the runs analyzed within this thesis use the sampled detect mode. If another detect mode is used, it is mentioned within the analysis. In the following, the different detect modes are described.
Figure 6.4 shows a sketch to illustrate the two different detect modes used for the beam test measurements. In the upper part of the sketch two analogue signal amplitudes are drawn in dependence of time as an example. A dashed line indicates the set up threshold value. The threshold is set in digital-to-analog-converter (DAC) units called *Vcth unit*. A high threshold given in Vcth units corresponds to a low analogue signal threshold, a low threshold corresponds to a high analogue signal threshold. For the analyzed generation of 2S modules the conversion factor is approximately 1 Vcth unit $\hat{=}$ 128 electrons [77]. The red rectangles highlight the time over

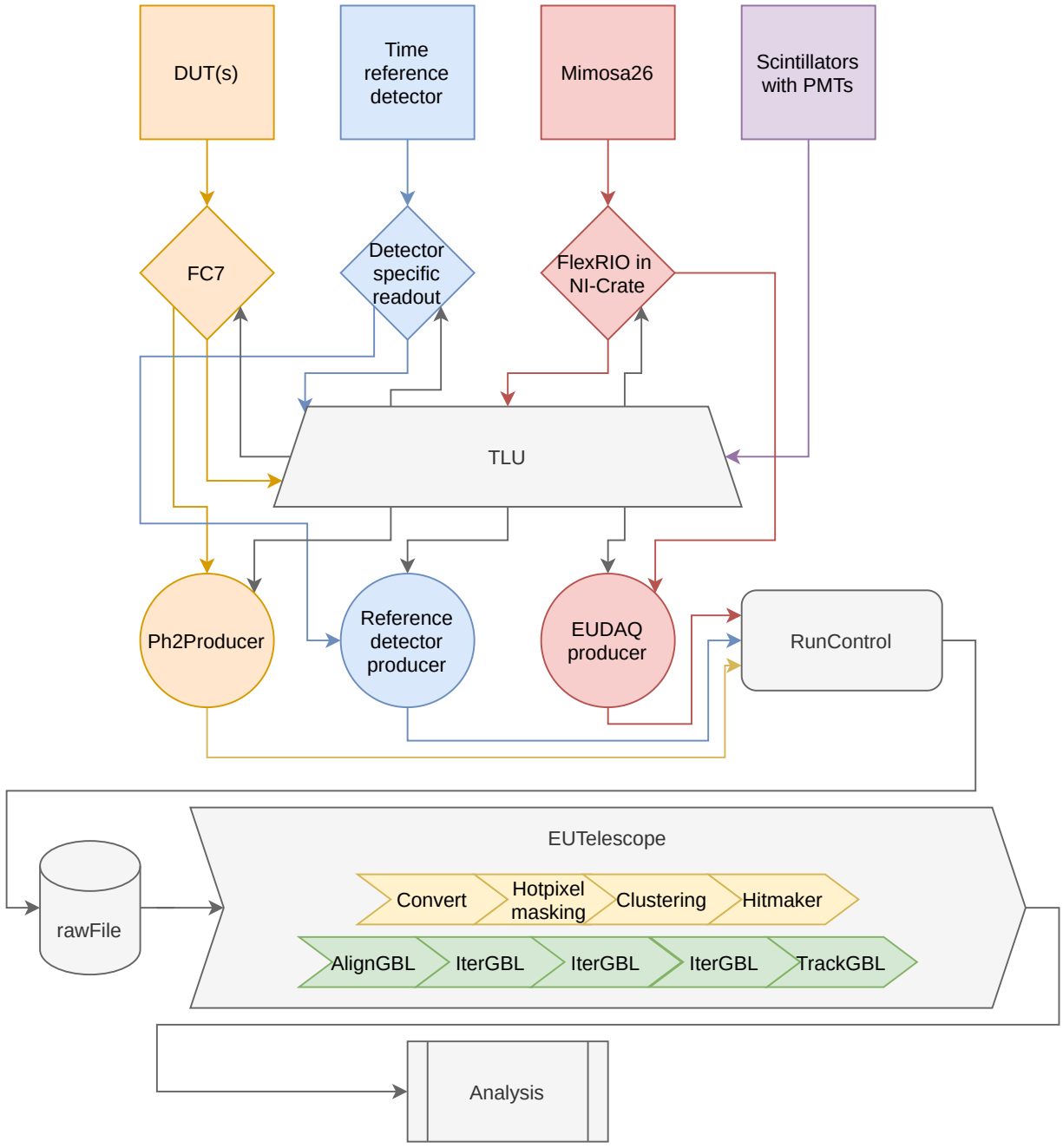

Figure 6.3.: Sketch of the data flow in the full DAQ chain.

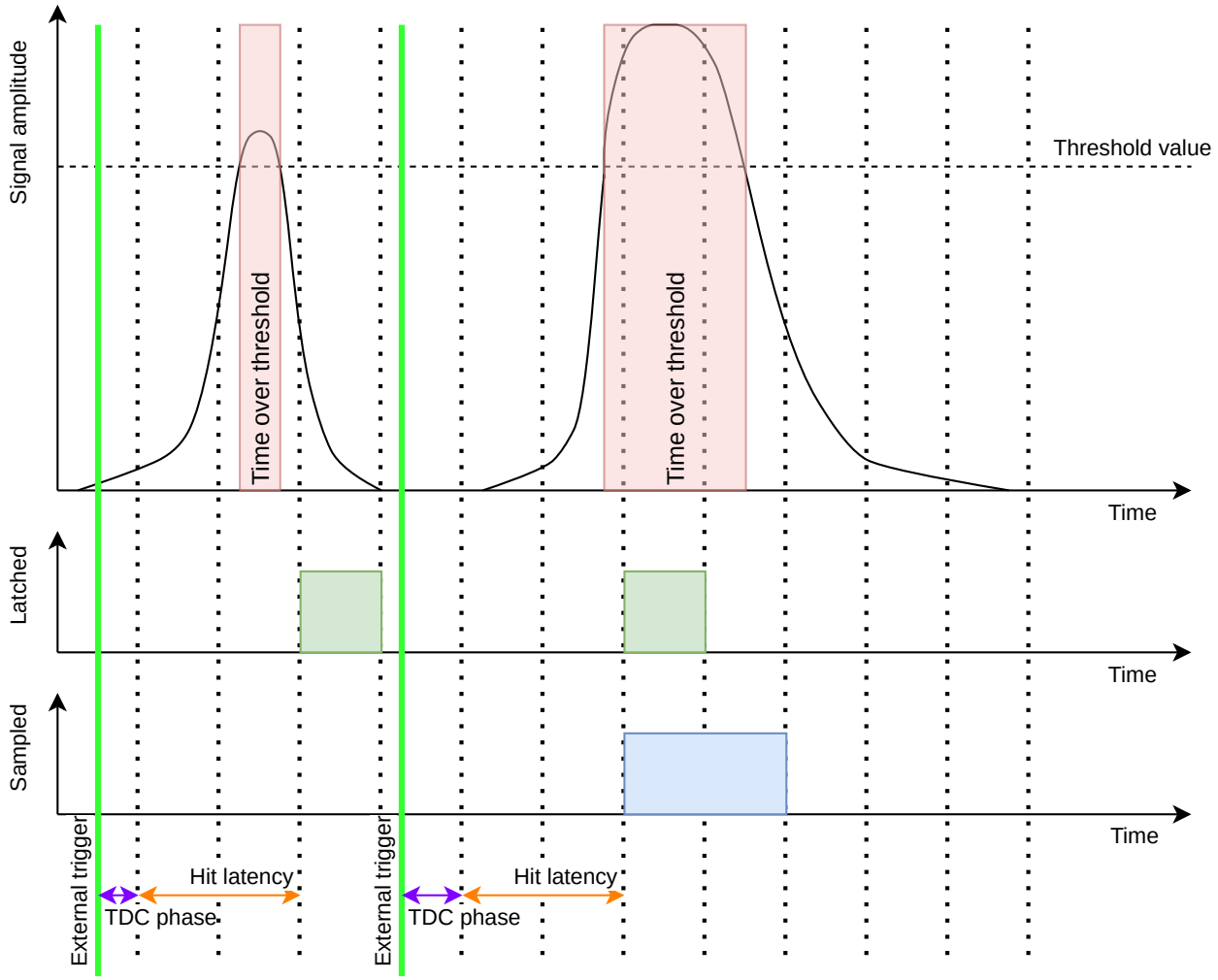

Figure 6.4.: Sketch to illustrate the hit / stub detect logic and the TDC phase. In the upper part two examples for analogue signals are shown as amplitude over time. The set up threshold is drawn as dashed horizontal line. The BX times are highlighted as dotted vertical lines. The time over threshold is shown as red rectangle. Below, the hit signal is shown for the different detect logics. The green vertical line marks the time of the external trigger.

threshold. The dotted lines divide the time into periods of 25 ns corresponding to the 40 MHz clock of BXs at the LHC.

Using the latched mode, a hit is detected if a rising edge above the threshold is measured within the prior BX period. The duration of the time over threshold does not change the duration of the output hit signal. However, if the comparator receives multiple shortly timed pulses with non overlapping time over threshold, multiple hits are detected.

In case of the sampled mode, a hit is detected if at BX time the threshold is exceeded. If the time over threshold covers more than one BX the output signal is longer accordingly. If the threshold is exceeded for a short time and between two BXs no hit is detected correspondingly.

The same mechanism applies for the stub detect mechanism. It could be set independently from the hit detect logic, but in the case of the presented beam test campaign runs it has been kept

the same. The stub correlation window has been set up to be ± 5 channels for all runs presented within this thesis and used for a stub related analysis.

TDC phase

The time relation between the external trigger signal and the detected hit is measured as the TDC phase. For illustration, Figure 6.4 is used. The green vertical line highlights the arrival of the external trigger signal.

A latency scan is performed to compensate for delays between the trigger and the DUT for hits and stubs. The number of collected hits is measured while the latency is scanned. The latency is set up in units of BX to the value maximizing the number of hits.

The TDC phase is measured as the temporal distance between the hit and the acceptance of the external trigger after applying the latency setup. The TDC phase is measured as the phase within the BX cycle with eight bins in total which translates to a time period of $\frac{25\,\text{ns}}{8} = 3.125\,\text{ns}$.

6.2.3. DUT mount

The boxes used for the beam test campaign in November 2019 have been designed and manufactured by the DESY CMS group. Two boxes were provided with different dimensions to house either a single module or three modules in parallel in a row. Both boxes consist of aluminum plates which are light proof sealed by foam rubber and aluminum bars used as spacers and for fixation. The single module box and the multi module box (MMB) are shown as CAD drawings as provided by the DESY CMS group in Figure 6.5 (a) and Figure 6.5 (b), respectively. Each of the carrier plates of the 2S modules is fixed on a 2 mm thick aluminum sheet which is provided with holes for guidance of the HV and LV cabling as well as for the optical fiber and a dry air tube. The contact points of the carrier and the aluminum plate are electrically isolated by Kapton tape. The dry air is used to ensure a dry atmosphere and additionally to cool down the DC-DC converter on the SEH. Aluminum profiles are used as spacers between the aluminum sheets holding the carrier plate and the front and backside plates. Those have a thickness of 2 mm with an opening window for the transition of the electron beam which is sealed by light tight Kapton foil of 80 µm thickness. Both boxes have drill holes on the bottom side for mounting sockets used for the integration into the telescope. The contact points of the sockets and the aluminum plates have been electrically isolated by Kapton tape and nylon screws were used. *BME680* sensors [109] for monitoring of temperature, humidity and air pressure are attached to the front side plates of both boxes and read out with a micro controller continuously.

During the beam test campaign of August 2020, a 2S module with irradiated sensors has been tested and active cooling had to be applied to avoid annealing effects. Therefore, the DUT modules have been mounted on a cooling jig attached to a chiller instead of the 2S module carrier plate. However, the same boxes could be used.

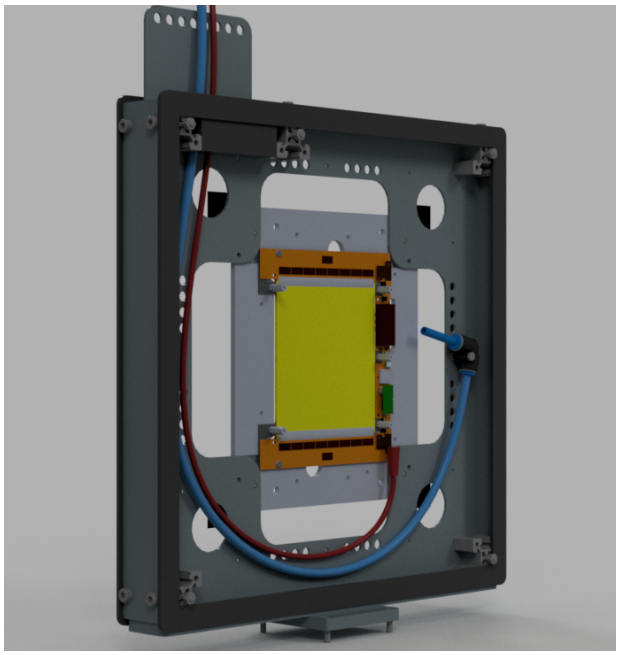

(a) The single module box.

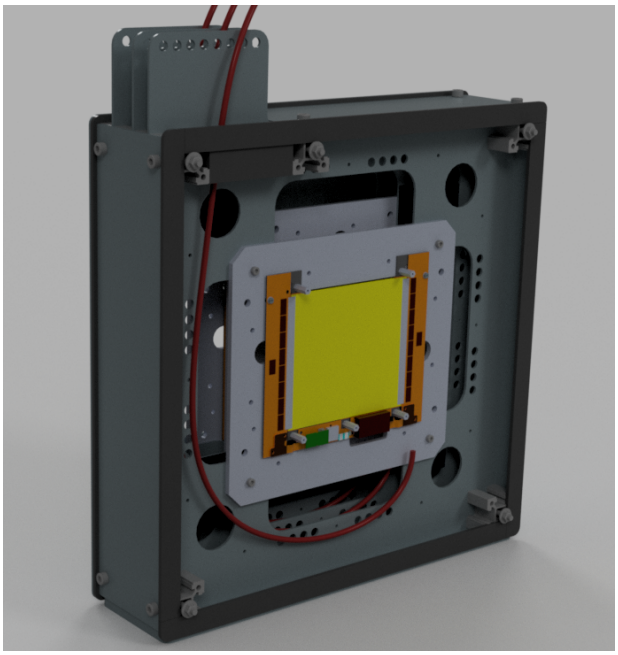

(b) The MMB.

Figure 6.5.: CAD drawings of the DUT boxes used for the beam test campaigns of 2019 and 2020 at DESY. Both boxes are shown without the front and back plate for better illustration. The drawings were provided by the DESY CMS group who also took the responsibility to design and manufacture the boxes.

6.3. The analysis frameworks

6.3.1. EUTelescope

EUTelescope [98] is a modular software framework developed to reconstruct and to analyze beam test data. It can be used for data synchronization, conversion of the data format and positional alignment of sensor planes combined in a single framework. The modular design of EUTelescope allows for an analysis of data taken at different beam telescopes and from any DUT designed for positional measurements of particle passage. It is developed within the EUDET framework.
EUTelescope makes use of MARLIN [110] processors (C++) which are running independently. The format used in the handling of detector data is LCIO [111, 112]. Information is ordered by events which hold the data of an entire particle passage through the beam telescope. The geometrical setup of the telescope is handled with GEAR [113] files (in the XML data format) holding the coordinates of all sensor planes within the telescope. For track fitting and sensor alignment EUTelescope uses the linear algebra software package Eigen3 [114], Millepede-II [115] and General Broken Lines (GBL) [116]. ROOT [108] is included for additional features like for example process monitoring.
The event reconstruction is a multi-stage process consisting of many different MARLIN processes. The processes itself can be configured by the user. The different stages of the event reconstruction are listed in the following:

1. **Convert**: The raw file format from the beam telescope DAQ system is converted into the LCIO format.

2. **Hot pixel masking**: By producing occupancy maps of each sensor, noisy pixels are identified and masked. The occupancy threshold used for the identification of a noisy pixel can be configured by the user.

3. **Clustering**: Neighboring pixels of LCIO event collections are grouped as clusters. If single pixels within the found clusters have been tagged as noisy before, the found cluster is tagged as a noisy cluster. The user can define whether a common edge or a common corner is required to form a cluster.

4. **Hitmaker**: The position of the cluster is calculated as the charge weighted center of gravity in a local coordinate system. The calculated hit coordinate is once again written into the LCIO file.

5. **Alignment**: Two dimensional correlation plots of the hits within the telescope are generated and the GEAR file is generated in order to initially correct for x- and y-shifts (perpendicular to the beam axis z). Afterwards, preliminary tracks are formed within a global coordinate system and the track prediction is compared to the measurement to further align the position of the telescope sensor planes. This procedure can be repeated multiple times to improve the precision.

6. **Track fitting**: A final track fit is done after applying all corrections held by the GEAR file.

The multi-stage reconstruction process is visualized in Figure 6.3 (on page 94). The output of the EUTelescope event reconstruction is a ROOT file with different data trees. It is used as the input for the high level analysis performed using a custom framework, which is discussed in the following Section.

6.3.2. FABEL

The *FABEL* is mainly used to link clusters to tracks which are validated by hit information from the time reference detector and to sort data in preparation of high level analyses. It is based on the data analysis framework ROOT [108] developed at CERN using especially its tree structure and file classes as well as the data analysis and plotting capabilities. The linking mechanism has been developed aiming for the best possible track-to-cluster matching. FABEL furthermore avoids double counting and takes detector resolution and uncertainties of the telescope prediction into account.

Track cluster linking

The DUT sensor hit information in the EUTelescope output is given as the center of the cluster in both directions in the local coordinate system. The y axis is defined along the strip direction. The x axis is perpendicular to the y axis within the sensor plane and therefore is directly related to the module channel number. As the coordinate system origin is defined in the center of the sensor in both directions, a positive y coordinate corresponds to the right side FEH and a negative y coordinate to the left side FEH consequently. Charge sharing along the strip direction (y axis)

is only measured in the center region of the sensor ($y \approx 0\,\text{mm}$) where the 5 cm long strips of the 2S module are facing each other. Therefore, events with charge sharing along y are very rare. Considering a beam test run with a 4 GeV electron beam at perpendicular incidence angle, the rate of hits with charge sharing along y and a reconstructed track within $\pm 50\,\mu\text{m}$ from the center of the module is only 1.8 %. Those clusters hold the y coordinate $y = 0\,\text{mm}$[1] while all other clusters are assigned $y = \pm 25\,\text{mm}$ depending on which side of the module the hit has been measured.
The EUTelescope output holds the information of all available track reconstructions. As the time resolution of the Mimosa26 planes largely exceeds the DUT readout time, only tracks with a link to a cluster on the time reference detector are considered as candidates.
The mechanism in order to make best use of the hit information in y for the linking of tracks and clusters is described in the following. There are two cases, which are handled in different ways:

1. A tolerance zone is defined in the center of the module, $|y_{\text{track}}| < 300\,\mu\text{m}$. It is introduced to cope with uncertainties with respect to the track alignment in y. The distance of tracks within this zone to any cluster is determined only in the direction perpendicular to the strips (x axis).

2. Tracks outside the tolerance zone are moved temporarily to $y = \pm 25\,\text{mm}$ depending on the sign of the original track y position to make the DUT's limited resolution in y compatible with the tracks. Based on the shifted value, the distance of the tracks to any cluster is determined as Euclidean distance [117].

Tracks are linked to the clusters of closest distance. If two clusters would have the same track as a match, the pair with lower distance is chosen. If there are more tracks than clusters in an event, all tracks without a match are tagged. Thus, they are still available for the analysis. If there are more clusters than tracks, tracks can be used more than once and the linking is performed in a way that the sum of all distances is minimized. This case is rare at a rate of approximately 0.3 %.
Figure 6.6 shows the distribution of the number of clusters (Figure 6.6 (a)) and tracks (Figure 6.6 (b)) recorded per event with at least one reconstructed telescope track and before any quality selections are applied. The beam test run has been performed with the beam spot at the center of the module, at perpendicular incidence and at nominal threshold. The most probable number of clusters per event for both sensor planes is one (58 %). The probability of measuring higher numbers falls approximately exponentially. The probability of measuring two clusters is approximately 10 %. The most probable number of tracks per event is measured to be six and reaches values of up to 27.
The procedure is shown in Figure 6.7. In this example, there is a single cluster (shown as red star) and three tracks (shown as crosses with different colors). The cluster is measured on the left side of the sensor. The track symbolized by the blue cross is on the same sensor side but it has the highest distance to the cluster in x. The track symbolized by the green cross would have the closest distance in x but is on the other side of the sensor. Therefore, in this case the blue track would be preferred. However, the red track is positioned in the tolerance zone and the distance in x to

[1] It is assumed that the cluster size in x on both sides is the same, otherwise the hit y position is in the respective barycenter.

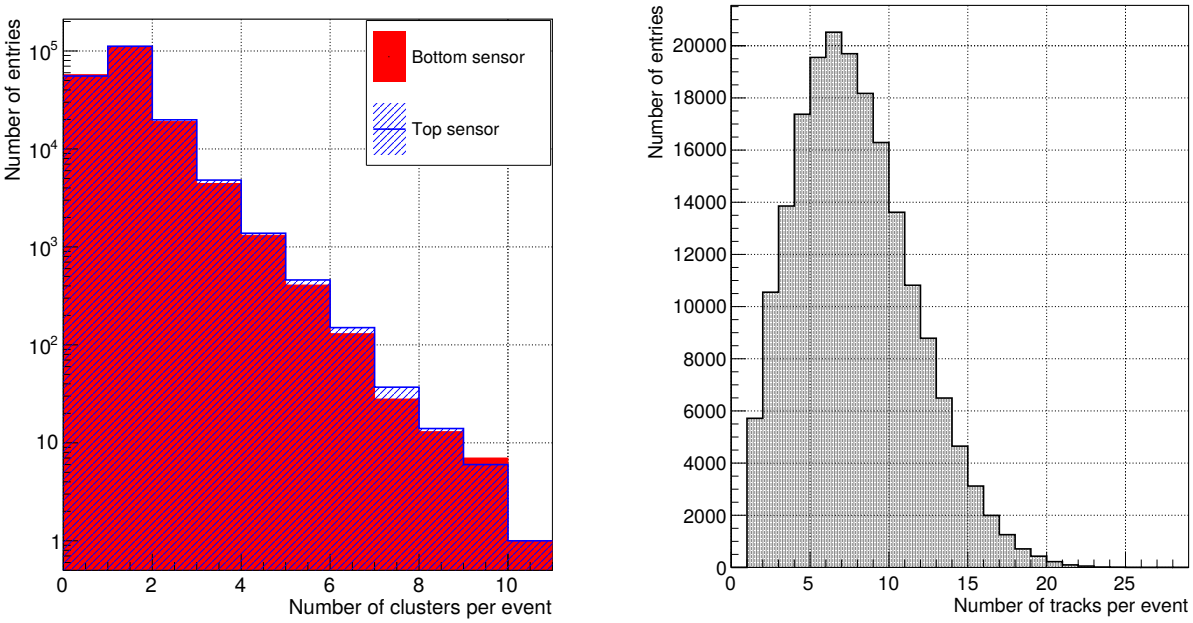

(a) Number of clusters per event as measured by the two sensor planes of the 2S module at center position of the beam telescope.

(b) Total number of tracks per event. No selections are applied.

Figure 6.6.: Number of clusters and tracks.

the cluster is smaller. So the red track is linked to the cluster in this example. Both of the other tracks are tagged as unmatched tracks and would therefore contribute to inefficiency.
The same procedure is also applied in order to link stubs to tracks. The linking procedure in this case compares the stub position with the track information on the seed layer. Track information of the correlation layer is included in the higher level analysis.

Data processing

The data processing of FABEL is shown as a sketch in Figure 6.8. The EUTelescope output is structured into the following data containers (focusing only on the information used by FABEL):

- The **hit data** hold the hit information of the time reference detector and all available DUTs. The cluster positions are stored as coordinates in the local coordinate system of the sensor. Additionally, the hit data contain cluster sizes in x and y.
- The **track data** contain the telescope prediction in the same coordinate system and χ^2 values from the corresponding track fits.
- The **stub data** hold the information of the channel number, CBC number and FEH number corresponding to a measured stub. Additionally, the bend code of the stub is given, which is the relative difference of the x coordinates of the top and bottom sensor in units of strips.
- The **raw data** contain information on detector level. The hit information is provided as channel and FEH id. Furthermore, the TDC phase is stored for each event.

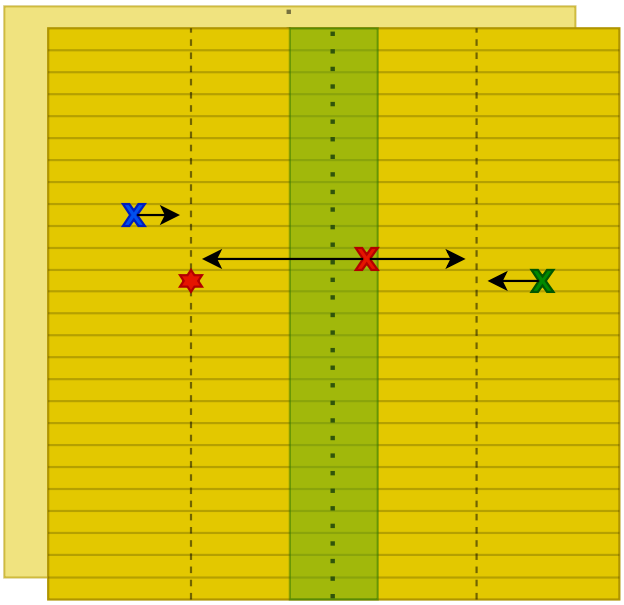

Figure 6.7.: Sketch of the cluster to track linking technique. The yellow box represents the strip sensor. The dashed lines highlight the $y = \pm 25\,\text{mm}$ lines. The dotted line indicates the center of the module ($y = 0\,\text{mm}$). The star symbolizes the position of a hypothetical hit as measured with a 2S module. The crosses indicate different track projections which are candidates to be linked to the cluster. The green colored area indicates the tolerance zone of $\pm 300\,\mu\text{m}$ around $y = 0\,\text{mm}$.

- The **status data** hold information about CBC error codes.

As the first step, the data are sorted into the different detector layers. Information of the time reference detector and each sensor layer of all available DUTs is split from the EUTelescope data structure and merged into *PlaneObjects* holding all information of a single sensor layer. As part of the initialization of these objects, the tracks are linked to the clusters as described above to form *HitTrackObjects*. The seed layer *PlaneObjects* also hold the information of stubs. Stubs which are generated online by the CBCs are named *hardware stubs*. Stubs which are reconstructed from clusters measured on the seed and correlation layer are named *emulated stubs*. The *PlaneObjects* corresponding to a single detector module (e.g. the DUT module at center position in the telescope) are collected and combined to *MultiModuleObjects*. As *MultiModuleObjects* are initialized, all *HitTrackObjects* are sorted by the track id, which is the primary key in the further analysis, so clusters on different sensor planes produced by the same beam electron are logically connected. In a next step, the processed data is prepared for the output. All *MultiModuleObjects* are merged into the *ObjectStreamer* which prepares a tree structure. The structure enables simple and fast access to the data for highly sophisticated analyses which are performed independently after the pre-processing step has been done once. For this, predefined selection criteria are prepared to analyze specific sets of tracks by using a simple tag. For each type of analysis like for example scans over different incidence angles or thresholds a dedicated analysis is prepared. As the alignment of the DUT planes is not performed by EUTelescope, FABEL also provides routines to automatize the alignment and to forward the updated plane coordinates to EUTelescope to repeat the tracking process. A detailed description of the DUT plane alignment procedure is presented in Section 6.4.

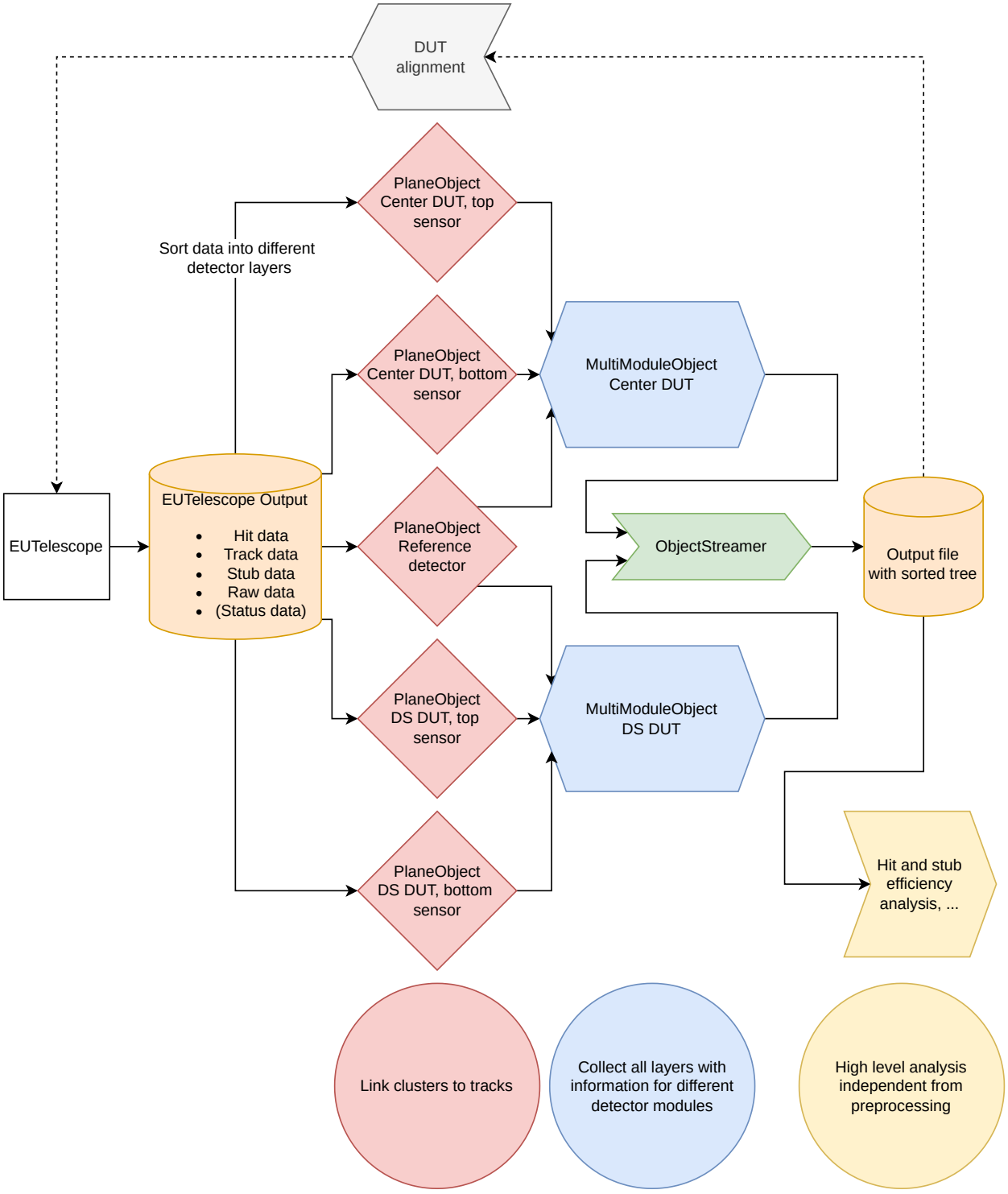

Figure 6.8.: Data flow of FABEL from EUTelescope output data to the output file for physics analysis.

Definitions and selections

Measurements at a beam test with a beam telescope enable efficiency measurements with a precise track prediction which is compared to hit information. However, constraints have to be defined to only select valid tracks which are distinguishable from other tracks and are measured within the correct time frame. In the following, the hit and stub efficiency is defined.
The hit efficiency is defined as

$$\epsilon_{\text{hit}} = \frac{N_{\text{tracks}}\left(\text{Link on DUT} \wedge \text{Track isolation} \wedge \text{Link on reference plane}\right)}{N_{\text{tracks}}\left(\text{Track isolation} \wedge \text{Link on reference plane}\right)} \tag{6.1}$$

with

- **Link on DUT**: The distance in x direction of the respective track to the linked cluster on the particular DUT plane is smaller than 200 µm.
- **Track isolation**: All tracks of the respective event have a radial distance of at least 600 µm to the next track on the time reference plane.
- **Link on reference plane**: The distance of the respective track to the linked cluster on the time reference plane is smaller than
  - 200 µm in x and 80 µm in y in case of the FE-I4 and
  - 150 µm in x and 100 µm in y in case of the CMS FPIX.

The *link on the reference plane* selection is applied to only consider tracks which fit the synchronized time frame of the DUT. If this criterion is not fulfilled, the respective test beam projectile could not be measured by the DUT and therefore is not of relevance for any analysis discussed in this thesis. The *track isolation* selection ensures that all tracks considered in the analyses are clearly distinguishable.
The stub efficiency is defined as

$$\epsilon_{\text{stub}} = \frac{N_{\text{tracks}}\left(\text{Stub from CBC} \wedge \text{Hit efficient cluster pair} \wedge \text{Valid cluster size}\right)}{N_{\text{tracks}}\left(\text{Hit efficient cluster pair} \wedge \text{Valid cluster size}\right)} \tag{6.2}$$

with

- **Stub from CBC**: The track is linked to a stub which is formed by the CBC.
- **Hit efficient cluster pair**: The track is linked to a pair of clusters fulfilling the hit efficiency criteria as described above in both sensors so that a stub can be reconstructed offline which can be compared with stub information from the CBC.
- **Valid cluster size**: The CBC only accepts clusters with up to four strips for the stub generation. Therefore, offline reconstructed stubs containing clusters with more than four strips are not accepted.

Some analyses require additional selection criteria which are described in the respective section. The stub efficiency as defined in Equation 6.2 describes the pure chip stub generation performance,

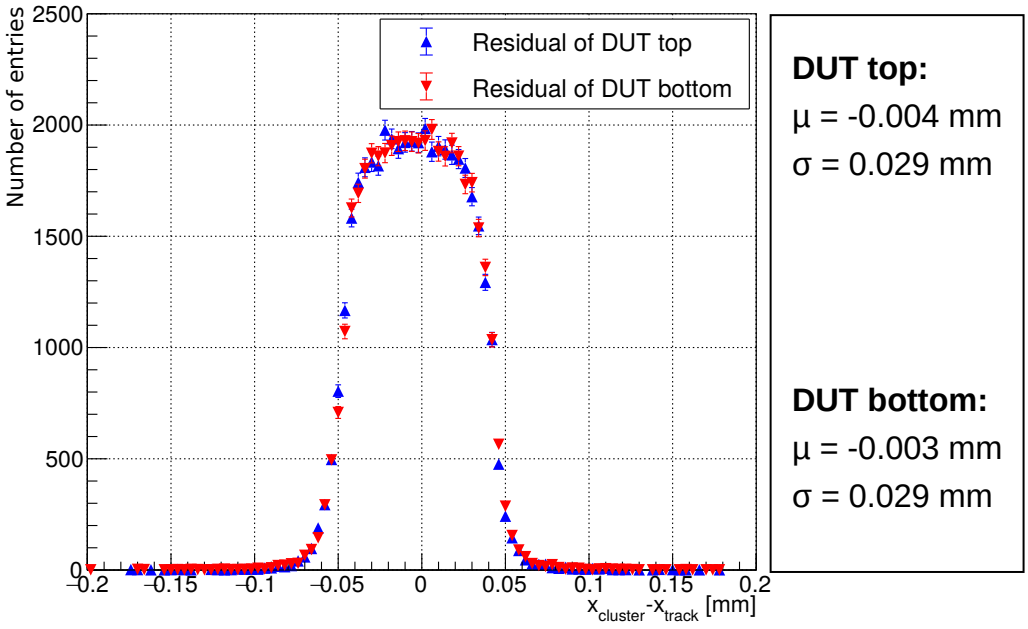

Figure 6.9.: Exemplary residual distribution for x coordinate alignment.

but allows for inefficiencies originating from a cluster pair measured by different FEHs. This effect is studied in detail in Section 6.10.2.
All analyses described in this thesis including the alignment have been performed with a requirement on the TDC phase selecting the two most efficient ones.

6.4. Alignment of runs

The track alignment is differentiated between the alignment of the active Mimosa26 layers of the DATURA telescope and the passive DUT sensors. The alignment of the Mimosa26 layers is done as part of the multi-stage reconstruction process by EUTelescope (Section 6.3.1). With a comparably low resolution in the direction along the strips, the DUT sensors need to be aligned manually by analyzing the data and applying corrections to the sensor plane positions. For this, the hit positions are compared to the preliminary fitted track positions and corrected in an iterative process until residual deviations become sufficiently small and remain static. Only tracks, which fulfill the *track isolation* and *link on reference plane* selection criteria, are used for the alignment procedure. In the following the control plots used for DUT alignment are introduced.
The alignment along the x axis (perpendicular to the strips) is checked by analyzing the residual $\Delta x = x_{\text{cluster}} - x_{\text{track}}$. Figure 6.9 shows an exemplary residual distribution used for x coordinate alignment. The sensor position used for the track fitting by EUTelescope is corrected by the mean residual value of the distribution for the top and the bottom sensor separately.
The y coordinate cannot be aligned in the same way because of the poor DUT resolution along the strip direction. Instead the alignment is performed via the following procedure: For each sensor plane the distribution of y coordinates of tracks linked to a cluster with $y_{\text{cluster}} > 0$ are compared

to the distribution of y coordinates of tracks linked to a cluster with $y_{\text{cluster}} < 0$. At the true coordinate of the sensor half ($y = 0$) the two distributions merge. This procedure can only be applied for runs with the beam spot covering the sensor half. Other runs need to be aligned by comparing the coordinates of the mounting stage with the ones of properly aligned runs with the beam spot in the sensor center. As an example the distributions for the y alignment are shown in Figure 6.10 for the top sensor of the M1804 module. As the two distributions in the example merge at approximately $y_{\text{track}} = 0$ the sample is already well aligned.

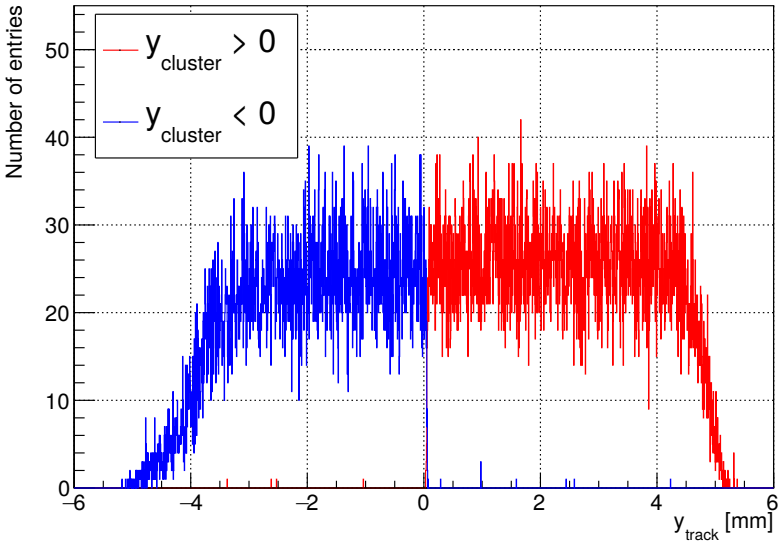

Figure 6.10.: Example for the y coordinate alignment. The red distribution holds track y coordinates linked to clusters with $y_{\text{cluster}} > 0$, the blue distribution the ones linked to clusters with $y_{\text{cluster}} < 0$.

The rotation of the sensor plane around the z axis is checked by analyzing the dependence of the x axis residual on the position in y. A misalignment in the rotational orientation ϕ_z would result in a residual of

$$\Delta x\left(y_{\text{track}}\right) = y_{\text{track}} \cdot \tan\left(\phi_z\right) \tag{6.3}$$

on average. The mathematical relation can easily be understood by Figure 6.11 (a) which shows a rotational misalignment as a sketch. An example for the residual dependence of the track y coordinate is shown in Figure 6.11 (b). Uncertainties are calculated as the standard mean uncertainty. A rotational misalignment around the y axis is checked by analyzing the residual in dependence of the x coordinate. Figure 6.12 (a) shows a sketch to illustrate the mathematical relation of the residual and the x coordinate which results in

$$\cos\phi_y = \frac{x_{\text{cluster}}}{x_{\text{track}}} \tag{6.4}$$

$$\Rightarrow x_{\text{cluster}} - x_{\text{track}} = x_{\text{track}} \cdot \left(\cos\phi_y - 1\right) \tag{6.5}$$

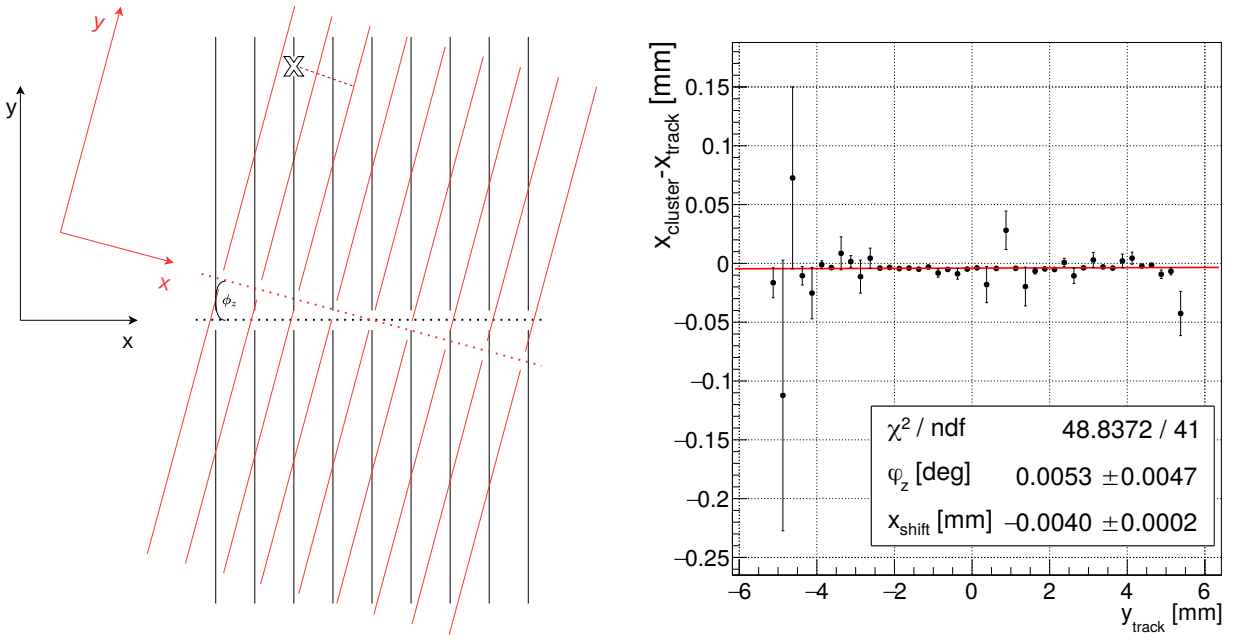

(a) Sketch of the rotation around the z axis. The black lines represent the real sensor strip orientation, the red lines represent strips in a tilted coordinate system. The cross indicates the position of particle passage. The dashed line is the x coordinate of the track in the unaligned system.

(b) Example for the alignment of the rotation around the z axis.

Figure 6.11.: Alignment of rotation around the z axis.

with ϕ_y being the rotational misalignment around the y axis. The mathematical model assumes the rotation axis to be at the center of the DUT coordinate system ($x = 0$) and approximately perpendicular incidence. If the rotation axis is misplaced in either x or z, an angular dependent constant offset adds to the residual. If the incidence angle is not perpendicular to the sensor plane but set up to ϕ_0, an additional term adds to Equation 6.5 resulting in

$$x_{\text{cluster}} - x_{\text{track}} = \text{Offset} + x_{\text{track}} \cdot (\cos\phi_y + \sin\phi_y \tan\phi_0 - 1)\,. \tag{6.6}$$

Figure 6.12 (b) presents an example for the alignment of the rotation around the y axis. The parameter ϕ_0 has been kept fixed for the fit.

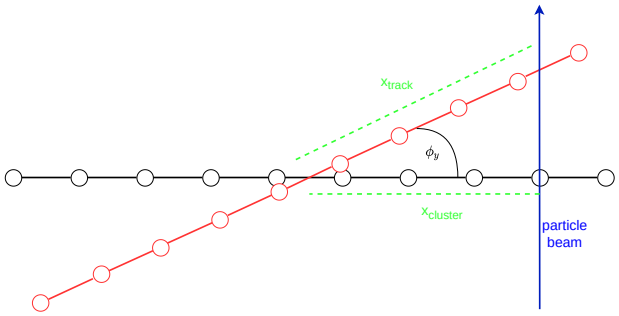

(a) Sketch of a rotational misalignment around the y axis. The black line represents a perfectly aligned sensor with the strips drawn as circles. The red copy represents a misaligned sensor with its strips. The particle beam is drawn in blue.

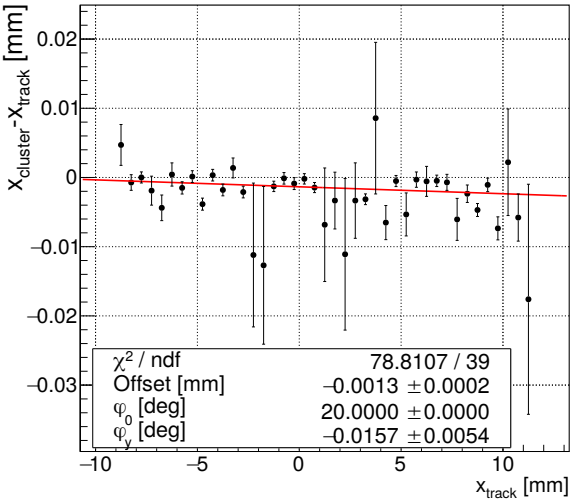

(b) Example for the alignment of the rotation around the y axis for a beam incidence angle ϕ_0 of 20°.

Figure 6.12.: Alignment of rotation around the y axis.

The z coordinates (along the beam axis) of the DUT planes have been aligned once at the center position of the telescope and at the first and second position of the multi module box. As a starting point the coordinates as measured with a measuring tape were used and the other coordinates were aligned as described above. Then, the z coordinate is varied for the EUTelescope track fitting and the standard deviation of the x coordinate residual distribution at the bottom sensor of the respective module is minimized. Figure 6.13 presents the standard deviation of the residuals at the three positions in dependence of the aligned z coordinate.

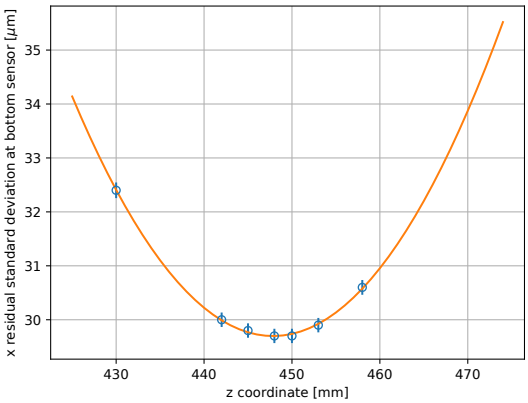

(a) Center position of the beam telescope.

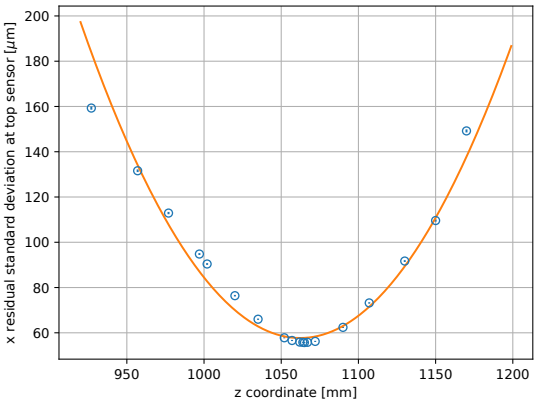

(b) First position within the multi module box.

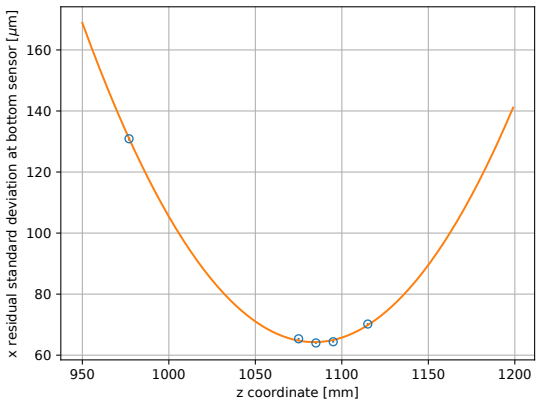

(c) Second position within the multi module box.

Figure 6.13.: Alignment of the DUT z coordinates. The blue markers show the measured x coordinate residual at the differently aligned z coordinates. The orange line shows a polynomial fit of second order for the determination of the residual minimum z coordinate.

6.5. Uncertainties

6.5.1. Statistical uncertainties

Cluster (and stub) efficiency tests are binomial experiments. A detector channel has the state of *hit* or *not hit* in an event of a particle traversing the sensor. Thus, uncertainties of efficiencies are calculated by ROOT [108] as a Clopper-Pearson interval [118] with the confidence level $1 - \alpha = 68.3\,\%$.

The Clopper-Pearson interval gives the upper and lower limit in an efficiency experiment with a total of N events, k hit entries and the real efficiency ϵ. The interval is calculated to be $S_{\leq} \cap S_{\geq}$ with

$$S_{\leq} = \left\{ \epsilon \mid P\left[\mathrm{Bin}\left(N;\epsilon\right) \leq k\right] > \frac{\alpha}{2} \right\} \qquad \text{and}$$
$$S_{\geq} = \left\{ \epsilon \mid P\left[\mathrm{Bin}\left(N;\epsilon\right) \geq k\right] > \frac{\alpha}{2} \right\}.$$

Mean values of variables like cluster size are given with the conventional uncertainty on mean values. Fit parameters are given with the resulting fit uncertainty.

6.5.2. Systematic uncertainties

The precision of the telescope track position at the DUT sensor planes is limited by the resolution of the beam telescope sensors and the precision of the z coordinate measurement respectively its alignment (Section 6.4). The evaluation of the systematic uncertainty on the telescope track position is described in detail in Section 6.6 and it is found to be $(10.0 \pm 0.9)\,\mu\mathrm{m}$ for the center DUT top sensor and $(9.7 \pm 0.8)\,\mu\mathrm{m}$ for the center DUT bottom sensor. This uncertainty has been determined for the track x coordinate but due to the quadratic shape of the Mimosa26 pixels the same uncertainty is taken into account for the track y coordinate.

Systematic uncertainties on hit and stub efficiency arise from the choice of the values in the event selection criteria. Table 6.2 summarizes the different systematic uncertainties. The estimation of systematic uncertainties is done using a beam test run at nominal CBC threshold, at 300 V bias voltage, at 0° incidence angle and with the beam spot set up approximately at the center of the module. The listed values are absolute efficiency uncertainties determined by varying the respective selection criteria by conservatively chosen numbers. The statistical uncertainty is 0.03 % for the mean of $\epsilon_{\mathrm{cluster}}$ and 0.02 % for the mean of ϵ_{stub}. Therefore, the systematical uncertainties are small but nevertheless significant.

Table 6.2.: Overview of the systematic uncertainties of the hit and stub efficiency for the nominal scenario. The uncertainty is given as the largest deviation from the nominal value. The uncertainty on the cluster efficiency is given as the largest deviation found for either the top or the bottom sensor.

Source of systematic uncertainty	**Estimation procedure**	**Uncertainty**	
		$\epsilon_{\mathrm{cluster}}$	ϵ_{stub}
TDC phase selection	Variation of included TDC phases (1 more / less)	$\pm\,0.06\,\%$	$\pm\,0.02\,\%$
Link on DUT, hit track distance	Variation by $\pm\,10\,\%$	$\pm\,0.03\,\%$	$< \pm\,0.01\,\%$
Track isolation requirement	Variation by $\pm\,25\,\%$	$\pm\,0.02\,\%$	$\pm\,0.01\,\%$
Link on reference plane	Variation by $\pm\,10\,\%$ in x and y simultaneously	$\pm\,0.01\,\%$	$< \pm\,0.01\,\%$
Tolerance zone for hit track linking	Variation by $\pm\,33\,\%$	$\pm < 0.01\,\%$	$\pm\,0.01\,\%$

Systematic uncertainties on the efficiency measurements at another incidence angle are summarized in Table 6.5 (page 130) and discussed in Section 6.10.1, which presents the respective analysis. Systematic uncertainties from the application of the listed requirements on the cluster size are assumed to be negligible as compared to the statistical uncertainties.

6.6. Resolution of the DUT and track uncertainties

The CBCs convert the measured charge into a digital signal. Therefore, if only clusters with a single strip hit are considered and charge sharing effects are neglected, the distribution of the residual ($\Delta x = x_{\text{track}} - x_{\text{hit}}$) is expected to be uniform over the width of a single strip. This distribution is smeared out by the telescope track uncertainty. Mathematically the expectation of the residual distribution can be described by a rectangle function in convolution with a Gaussian distribution:

$$P_{res}(\Delta x) = \int_{-\infty}^{\infty} \left[\Theta\left(t + \frac{w}{2}\right) - \Theta\left(t - \frac{w}{2}\right)\right] \cdot \frac{1}{\sqrt{2\pi\sigma^2}} \exp\left(-\frac{(t-\Delta x)^2}{2\sigma^2}\right) dt \tag{6.7}$$

$$= \frac{1}{2}\left[\text{erf}\left(\frac{\Delta x + \frac{w}{2}}{\sqrt{2\sigma^2}}\right) - \text{erf}\left(\frac{\Delta x - \frac{w}{2}}{\sqrt{2\sigma^2}}\right)\right] \tag{6.8}$$

with the Heaviside step function Θ [119], the strip pitch w and the telescope track uncertainty σ. Solving the integral results in two error-functions (erf) [119] which are subtracted from each other. Figure 6.14 shows the residual distribution of the M1804 module in the center position of the beam telescope. The distribution is filled with residuals $x_{\text{track}} - x_{\text{cluster}}$ for clusters of cluster size 1 to match the mathematical model as described above. However, the distribution has to be normalized as the model also implies that the strip of the module is hit by test beam particles uniformly. However, by applying a requirement on the cluster size, hits in the transition region between two strips are suppressed because the probability for charge sharing and thus larger clusters rises. This effect is shown in Figure 6.15. It presents the distribution of x coordinates of tracks passing the hit efficiency criteria and linked to single strip clusters folded into the coordinates of a single strip, the intra-strip position, with 0 mm being the center of the strip. The hit detection probability of single strip clusters is reduced by approximately 10 % at the borders of the strip compared to its center. The distribution is fitted by a Gaussian distribution. The resulting fit function is used for the normalization of the residual distribution depending on their intra-strip position. The model of Equation 6.8 is used as a fit function for the normalized residual distribution. In order to correct for a slight shift of the residual caused by non-perfect alignment, another free parameter has been added to the model. As the normalization is only valid for the region between −45 µm and 45 µm the fit is constraint to this respective range.

The resulting fit parameters are summarized in Table 6.3. The rectangle width is in good agreement with the expectation of $w = 90\,\mu\text{m}$ for both of the two sensors. The telescope track uncertainty σ is fitted to be $(10.0 \pm 0.9)\,\mu\text{m}$ for the top sensor and $(9.7 \pm 0.8)\,\mu\text{m}$ for the bottom sensor.

These values for the track resolution are rather large compared to the nominal precision of the DATURA telescope (Section 6.2.1). The reason for the low resolution is a non optimal spacing

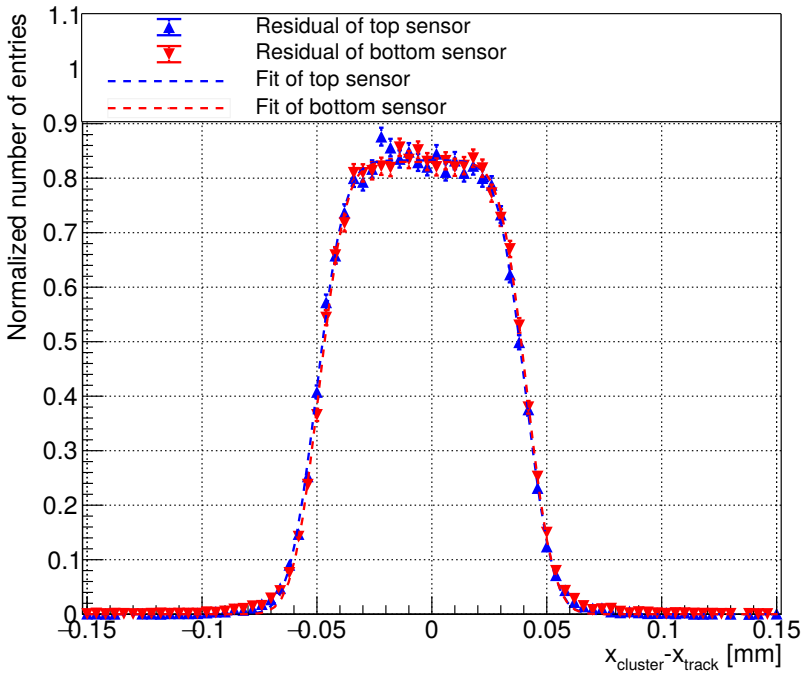

Figure 6.14.: Residual distribution along the x coordinate of the M1804 module at the center position of the telescope. The blue markers represent the top sensor residual distribution, the red ones correspond to the bottom sensor. The distributions are normalized by the single strip hit probability of the intra-strip coordinate of the respective track. The dashed lines show the the fitted model function. The fit has been constrained to the region between −45 µm and 45 µm.

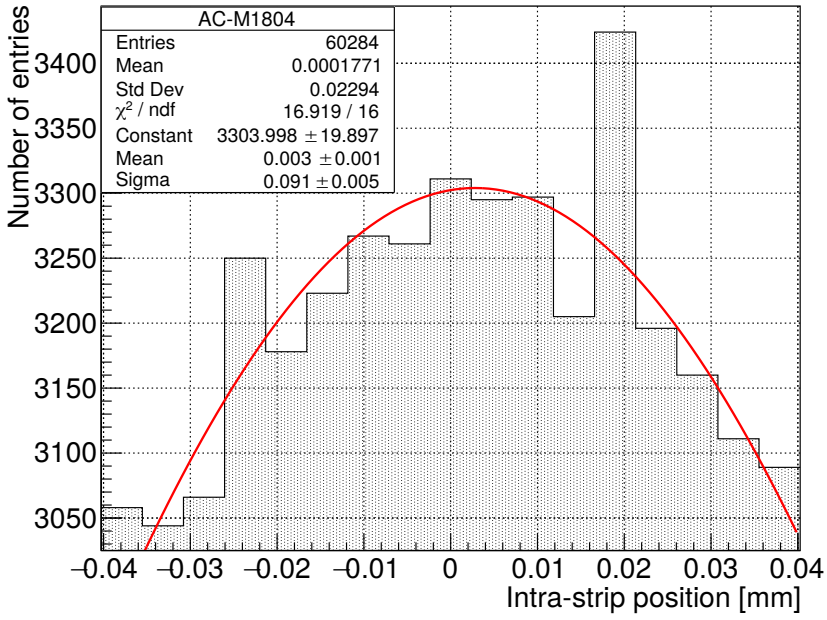

Figure 6.15.: Distribution of track x coordinates of tracks passing the hit efficiency criteria and linked to a cluster with only a single strip hit, exemplarily shown for the M1804 bottom sensor. The track x coordinate is folded into a single strip with 0 mm being the center of the strip. The distribution is fitted with a Gaussian distribution, which is shown as red line.

Table 6.3.: Summary of parameters from convolution fit of the residual of the ACM1804 prototype 2S module.

Parameter	Top sensor	Bottom sensor	Expectation value
χ^2/ndf	13.72 / 18	10.86 / 18	
Shift [µm]	-4.9 ± 0.3	-4.1 ± 0.3	0
Width [µm]	91.3 ± 1.1	91.1 ± 1.1	90
σ [µm]	10.0 ± 0.9	9.7 ± 0.8	$9.4^{+0.3}_{-0.4}$

of the Mimosa26 planes in terms of the precision of the center DUT. These were placed with approximately 15 cm distance to each other to achieve a proper track resolution not only for the center DUT but also for the modules mounted at the downstream (DS) end of the telescope in the multi module box. Additionally, as the center DUT is rotated for certain studies and an adequate spacing is required, the distance of the DUT sensor planes to the next Mimosa26 sensors has been set up to 12.5 cm on the upstream side and 15 cm on the DS side. However, the track resolution as expected from the spacing of the DATURA planes is simulated using the *GBL Track Resolution Calculator* [120] and found to be $\sigma_{\text{track,sim}} = 9.4^{+0.3}_{-0.4}\,\mu\text{m}$ for both sensor planes at 4 GeV. The uncertainties are systematic errors as derived from a variation of the beam energy by 5 % [101, 5]. The energy dependence of the telescope resolution as determined by the simulation is shown in Figure 6.16. The resolution as determined by the fit (Table 6.3) is in good agreement to the simulation results.

The standard deviation of the residual distribution without applying any requirements on the cluster size is 28.7 µm for the top sensor and 28.8 µm for the bottom sensor. The pure DUT resolution σ_{DUT} can be calculated by quadratically subtracting the telescope track uncertainty from these values. The resolution is calculated to be $\sigma_{\text{DUT,top}} = (26.9 \pm 0.3)\,\mu\text{m}$ for the top sensor and $\sigma_{\text{DUT,bottom}} = (27.1 \pm 0.3)\,\mu\text{m}$ for the bottom sensor. This result is in acceptable agreement with $\frac{90\,\mu\text{m}}{\sqrt{12}} = 26.0\,\mu\text{m}$, which is the expected resolution of a single strip with binary readout.

The same analysis was done for the modules at the DS end of the telescope, mounted in the MMB. In this case, the standard deviation of the residual distribution applying the same selection criteria as described above was measured to be approximately 64 µm for the first position in the multi module box and 69 µm for the second position. Because of the telescope resolution being much worse at the DS end of the telescope and therefore the Gaussian function in Equation 6.7 dominates and the fit cannot be applied. Assuming the 2S module resolution is the same as for the module in the center position of the telescope and the telescope track uncertainty σ and the DUT resolution are uncorrelated the telescope track uncertainty can be calculated by $\sigma_{\text{track}}^{\text{MMB,first}} = \sqrt{(64\,\mu\text{m})^2 - (27\,\mu\text{m})^2} \approx 58\,\mu\text{m}$ and $\sigma_{\text{track}}^{\text{MMB,second}} = \sqrt{(69\,\mu\text{m})^2 - (27\,\mu\text{m})^2} \approx 63\,\mu\text{m}$. Due to the severe degradation of the tracking precision at the DS position of the telescope, selection criteria values for efficiency definitions are relaxed for those modules compared to the DUT in the center position.

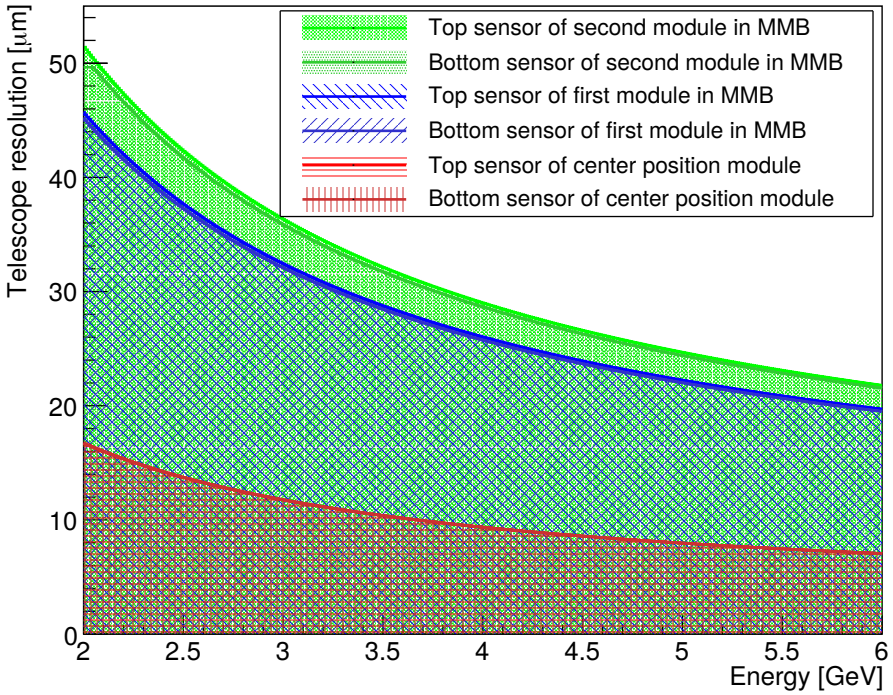

Figure 6.16.: Simulation of the energy dependence of the telescope track resolution at center position and DS position of the DATURA telescope. The simulation has been performed using the *GBL Track Resolution Calculator* [120] framework. The simulated resolution values of the top and the bottom sensor of the modules at the different positions are almost identical.

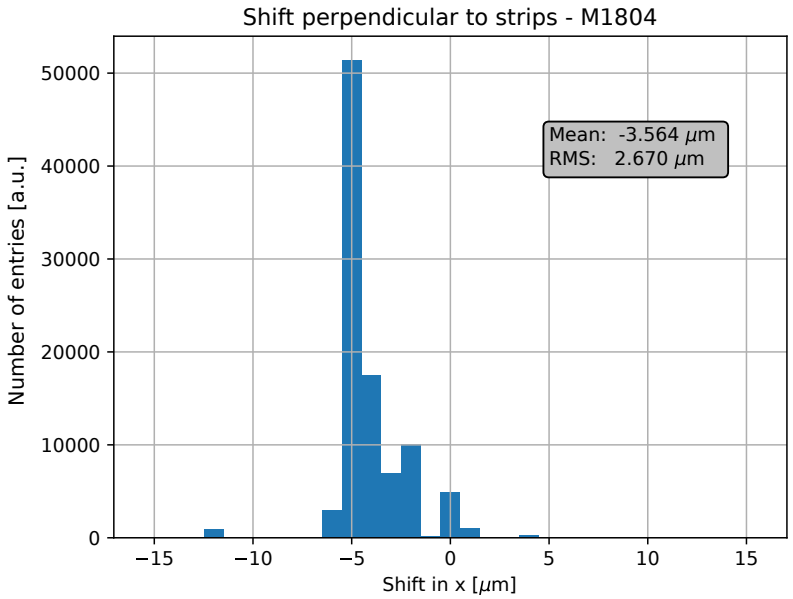

Figure 6.17.: Distribution of displacement values in x of individually aligned runs for the AC-M1804 module.

6.7. Evaluation of module assembly precision

The beam test data can also be used to evaluate the assembly precision. As part of the quality control during the module assembly, the alignment of the two stacked sensors has been measured with the metrology setup. The misalignment of the top and bottom sensor of the M1804 module has been measured to be −5 µm perpendicular to the strips, −10 µm along the strips and 13 µrad rotational misalignment. With these results, the sensor alignment is well within the specifications (summarized in Section 5.1.4, page 37). In order to crosscheck these results multiple runs at nominal threshold and with perpendicular incidence angle have been aligned separately.

The EUTelescope alignment positions (in the global coordinate system) of the top and bottom sensor in x are compared to calculate a mean displacement perpendicular to the strip direction. As the alignment might not be perfect and sensor displacements of the order of magnitude of few micro meters should be detectable the alignment positions are corrected by the residual mean values of the respective runs. The distribution of top to bottom sensor displacements extracted from the individual runs and weighted by the inverse mean uncertainties is presented in Figure 6.17. The resulting mean is −3.6 µm with an RMS of 2.7 µm. This result is in good agreement with the metrology measurement.

The alignment of the top and the bottom sensor along the strip direction is checked in an analogue way. However, because of the bad resolution along this direction the EUTelescope coordinates cannot be corrected by residual means. Instead, the mean of the position of the falling edge of y coordinates of tracks linked to clusters detected on the negative y axis and the position of the rising edge of y coordinates of tracks linked to clusters detected on the positive y axis is used to correct the EUTelescope alignment coordinates. Figure 6.10 on page 105 shows an example of the two described distributions. The resulting distribution of top to bottom displacements along strip

direction is presented in Figure 6.18 weighted by their uncertainties. The mean displacement is measured to be −1.1 µm with an RMS of 4.5 µm. The result fits the metrology measurement within two standard deviations.

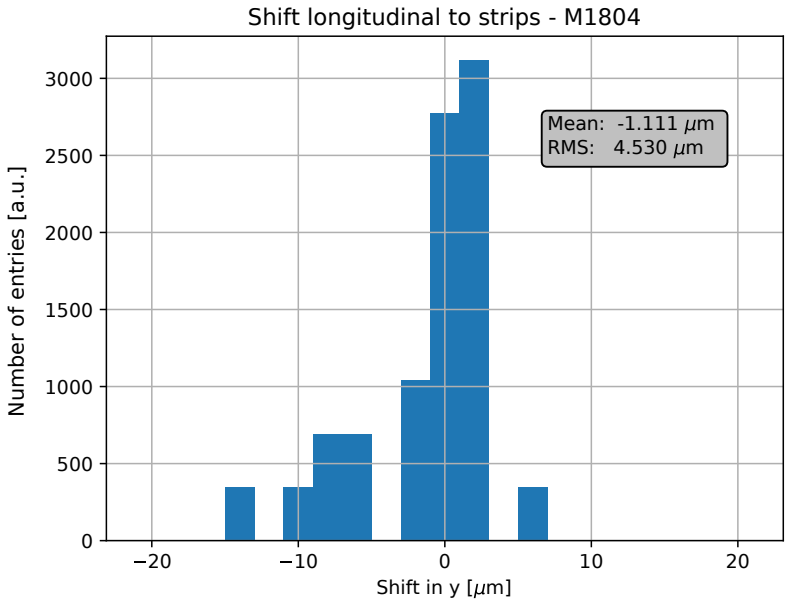

Figure 6.18.: Distribution of displacement values in y of individually aligned runs for the AC-M1804 module.

The rotational misalignment between the top and the bottom sensor is analyzed by comparing the EUTelescope alignment coordinates corrected by the residual means of two beam test runs with the beam spot close to the FEHs maximizing the average distance along the strips. The mean y coordinate of tracks linked to a hit of the two runs is measured to be (39.37 ± 0.02) mm and (-40.61 ± 0.02) mm, respectively. This results in a mean distance of $L = (79.98 \pm 0.03)$ mm. The difference of the displacement in x at the two different positions of the beam spot and for top and bottom sensor has been measured to be $\Delta X = (1.27 \pm 0.29)$ µm. Based on these measurements the rotational sensor displacement is calculated to be $\Delta\phi = \arctan\left(\frac{\Delta X}{L}\right) = (15.94 \pm 23.83)$ µrad. This result is in good agreement with the metrology measurement and well within the specifications for module assembly.

6.8. Uniformity of efficiencies

The hit efficiency of the AC-M1804 module has been measured as a function of the respective hit position. As the effectively illuminated area has a size of approximately 16 mm (horizontally) by 11 mm (vertically), multiple runs with the beam spot at different module coordinates have to be combined. The efficiency measurements along the x axis are performed at the module center ($y = 0$ mm), so that both sensor halves are illuminated. For the y axis scan, the module has been turned by 90° and moved with the stepping motor horizontally. As the powering of the motors induced noise to the modules, their power supplies have been shut down during the data taking

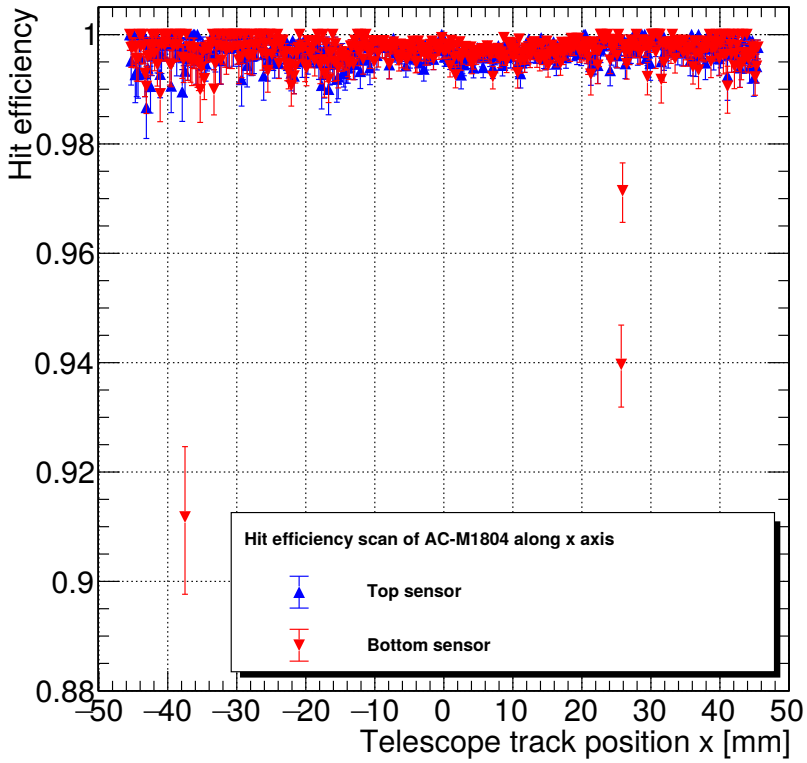

Figure 6.19.: Hit efficiency of the M1804 module along the x axis (perpendicular to the strip direction). The top sensor is shown in blue, the bottom sensor is shown in red. The plotted error bars are pure statistical errors derived as Clopper-Pearson interval.

and the module was fixed in the vertical position to prevent it from falling. Moving the module horizontally therefore has simplified the positioning of the module box between the runs.

The hit efficiency as defined in Equation 6.1 as a function of the track x coordinate is shown in Figure 6.19 with a binning of 200 µm. The hit efficiency is above 99 % over the whole sensor region within the uncertainties except for the two regions of $x_{\text{track}} \approx -38\,\text{mm}$ and $x_{\text{track}} \approx 26\,\text{mm}$ on the bottom sensor. The corresponding strips seem to be disconnected from the FEHs. However, the efficiency in these regions is still above 90 %. The first reason for this effect is that in Figure 6.19 there is no differentiation between the two half sensors and the respective channel on the opposite side is connected to the FEH. The second reason is that the distance between cluster and track for an efficient hit is defined to be up to 200 µm while the unconnected silicon strips have a width of 90 µm so that charge sharing to the neighboring connected channels would increase the efficiency. And as a third reason the binning in the plot of Figure 6.19 is chosen to be 200 µm so that the connected neighboring channel is also represented in this data point.

The hit efficiency in dependence of the y coordinate is shown in Figure 6.20. The efficiency is well compatible with 99 % or higher, except for the region at $y_{\text{track}} \approx 0\,\text{mm}$ where the strips of the two half sensors are facing each other. With the chosen binning in the track y position of 200 µm the hit efficiency is found to be reduced by about 2 %. A loss of only 2 % in hit efficiency in the region

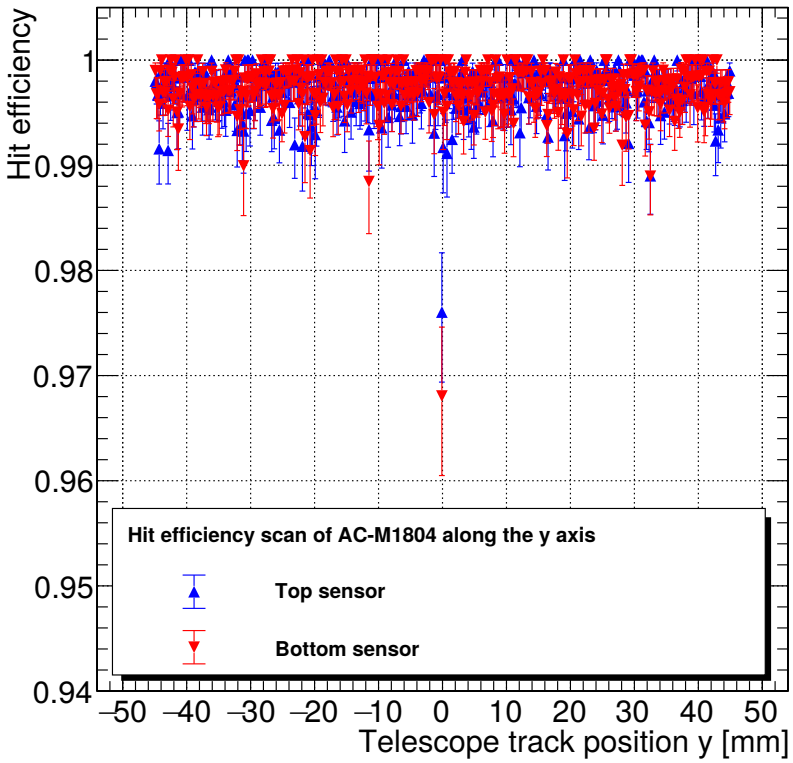

Figure 6.20.: Hit efficiency of the M1804 module along the y axis (along the strip direction). The top sensor is shown in blue, the bottom sensor is shown in red. The plotted error bars are pure statistical errors derived as Clopper-Pearson interval.

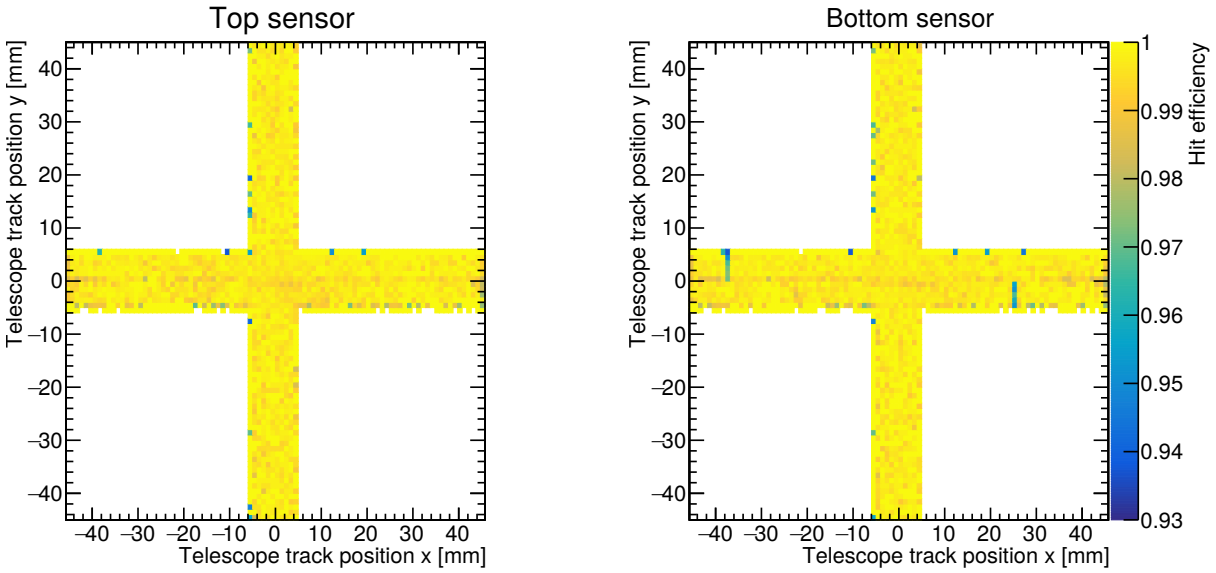

Figure 6.21.: Hit efficiency of the M1804 module along the x and y axes. The left (right) plot shows the hit efficiency at different positions of the top (bottom) sensor. The same color scale is applied both plots.

of 200 µm at the center of the 2S module sensors is an insignificant effect for the operation in the Phase-2 CMS detector.

Figure 6.21 shows both the x and y axis scan combined as an efficiency map for the top (left) and the bottom sensor (right). White areas in the plot have not been covered by the beam spot. Efficiency outliers appear at the border of the illuminated area. These bins do not hold significant statistics and the efficiency is still compatible with 99 % within their uncertainties. With the binning of 1 mm by 1 mm the efficiency loss in the sensor center is only faintly visible. As the efficiency drop of the bottom sensor at $x_{\text{track}} \approx -38\,\text{mm}$ and $x_{\text{track}} \approx 26\,\text{mm}$ seems to be constant in y on a half sensor the hypothesis of two unconnected channels is fortified.

During the scan along the module y axis, also stubs have been measured. Figure 6.22 shows the stub efficiency as a function of the track y coordinate. The stub efficiency is well above 99 % over the whole scanned y range. However, there is a loss of efficiency in the center region of the sensor at $y_{\text{track}} = 0$ of approximately 0.3 %. In this region the stub efficiency is decreased because the beam particle produces a cluster on different half sensor sides on the two different sensors. As the stub is formed within the CBCs which only handle signals either the right or the left side half sensors the respective events account for inefficiencies. This is proven by comparing with the stub efficiency calculated only considering events with the clusters linked to the respective track on the two sensors being on the same side, also shown in Figure 6.22.

6.9. Bias voltage scan

During the November 2020 beam test campaign, a bias scan within the test beam telescope with beam has been performed. For this test, the KIT-5 module has been used in the center position.

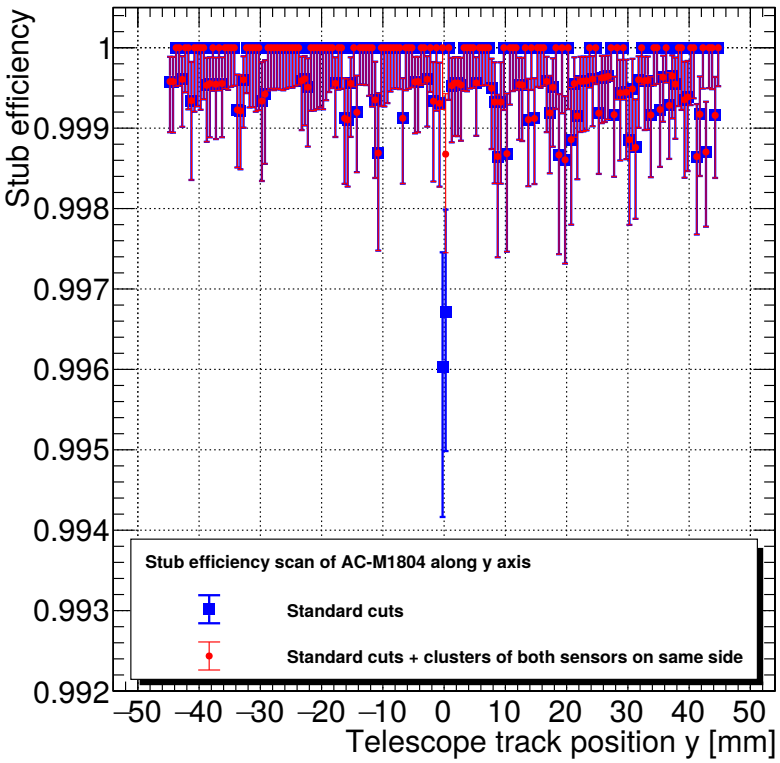

Figure 6.22.: Stub efficiency as a function of the track y coordinate. The blue graph shows the stub efficiency as defined in Equation 6.2. The red graph shows the stub efficiency with an additional selection requiring the hits on the different sensors to be on the same sensor half.

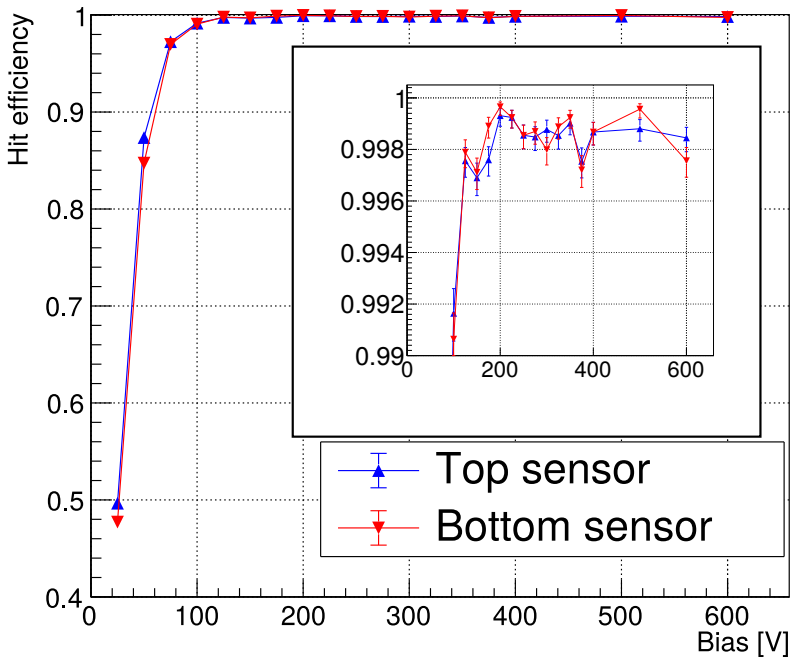

Figure 6.23.: Hit efficiency in dependence of the bias voltage for the KIT5 module. The top sensor hit efficiency is plotted in blue, the bottom sensor efficiency in red. The inserted top right side box shows a zoom into the high efficiency plateau. All shown uncertainties are pure statistical uncertainties.

Figure 6.23 presents the hit efficiency of the top and the bottom sensor in dependence of the bias voltage. At low bias voltage the hit efficiency is low. A voltage of 25 V leads to a hit efficiency of 50 %. By increasing the bias voltage also the hit efficiency increases rapidly. At a bias voltage of 100 V the hit efficiency was about 99 % and from approximately 150 V the hit efficiency stayed constant at about 99.8 %.

Figure 6.24 presents the mean cluster size in dependence of the applied bias voltage. The cluster size is at about 1.02 strips at a bias voltage of 25 V and it increases almost linearly up to 1.11 strips at approximately 275 V at which the cluster size reaches a plateau. Differences between the top and the bottom sensor (especially above 400 V) cannot be explained without further investigation. One reason could be statistical fluctuation. The plateau in the cluster size indicates that the depletion voltage has been reached. Figure 6.24 also shows the squared inverse capacitance, which has been measured in the lab in Karlsruhe as part of the module assembly quality control. The kink at 275 V bias voltage for the squared inverse capacitance confirms that the plateau of the cluster sizes originates from the sensor depletion.

Comparing Figure 6.23 and Figure 6.24 shows that the hit detection efficiency is already at a very high level before the full depletion voltage is reached.

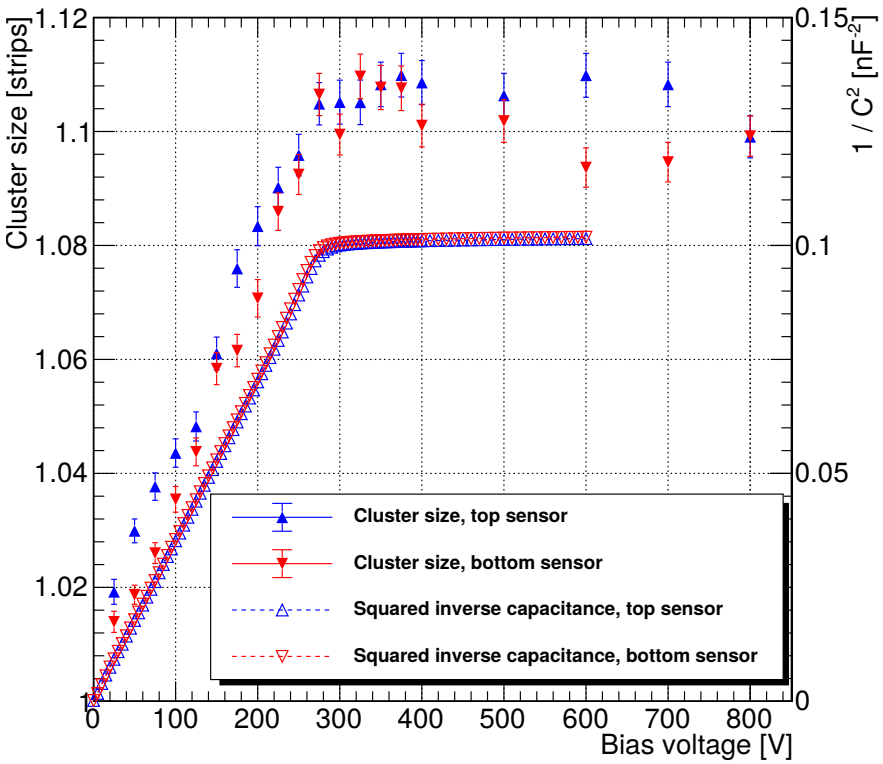

Figure 6.24.: Cluster size in dependence of the bias voltage for the KIT5 module measured during the beam test in November 2020. The cluster size is compared to the squared inverse capacitance which has been measured as part of the sensor QA in Karlsruhe.

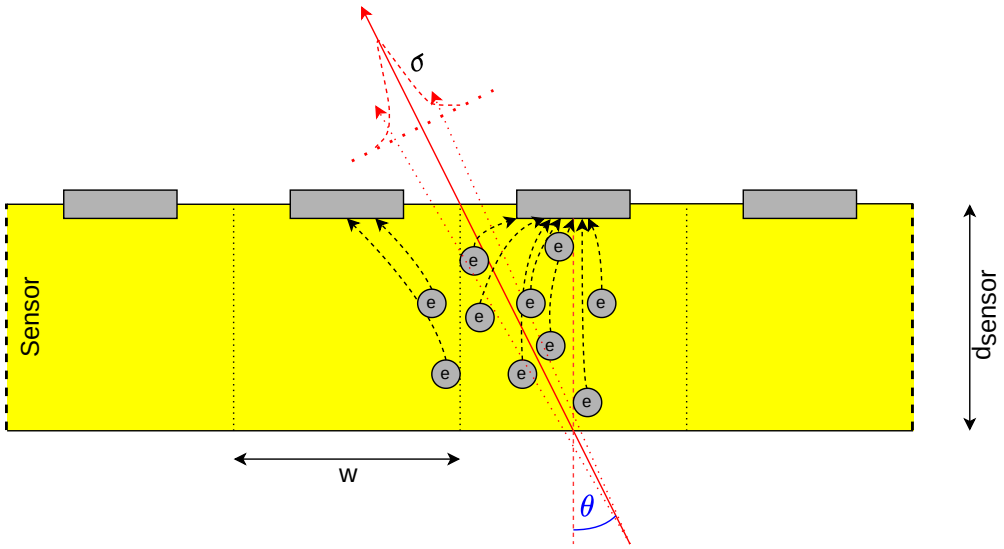

Figure 6.25.: Sketch showing the charge sharing between different strips.

6.10. Angle scan measurements

During the beam test campaigns, the 2S module performance has been evaluated under different incidence angles. With precise telescope track information, this analysis allows the testing of the stub trigger efficiency. The incidence angle can be translated into an emulated transverse momentum p_{T} at a specific position within the OT. Therefore, the stub trigger efficiency can be measured as a function of the p_{T}. The analysis of the stub trigger performance is described in Section 6.10.1. The incidence angle along the strip direction will vary in the OT in dependence of the pseudorapidity η of the mounting position. The influence of this angle on the uniformity of the stub efficiency is analyzed in Section 6.10.2.

6.10.1. Particles with different emulated p_{T}

Cluster size at different incidence angles

The DUT box is mounted on a precise rotation stage which is controlled remotely. Even though the stage itself is set up precisely, the DUT might be mounted with a rotational offset. A potential offset is checked by analyzing the mean cluster size in dependence of the set up angle. The expected cluster size derived in a purely geometric consideration [107] is described by

$$s\left(\theta\right) = s_0 + \frac{d_{\mathrm{sensor}}}{w} \cdot \left|\tan\left(\theta - \theta_0\right)\right| \tag{6.9}$$

with s_0 being the cluster size at perpendicular incidence and d_{sensor} being the active sensor thickness. The variable w represents the strip pitch and θ_0 is the rotational offset. Figure 6.25 shows a sketch of the charge collection at non perpendicular incidence angle of the test beam particle at the sensor.

The non-uniform electric field present in the sensor however affects the charge collection. Additionally, the hit detection threshold of the CBC plays a role. As an approximation $\frac{d_{\mathrm{sensor}}}{w}$ (visualized

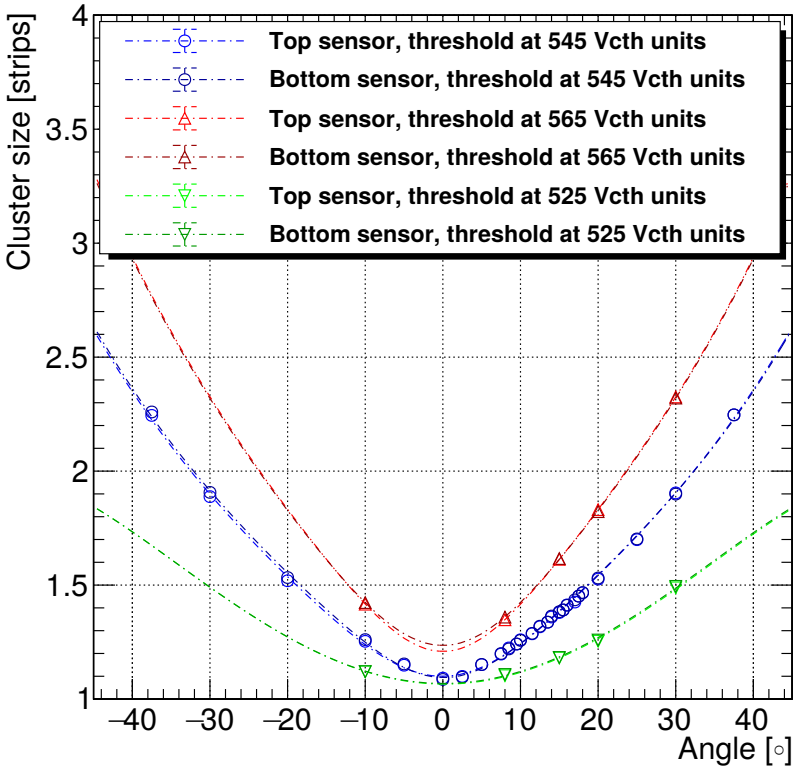

Figure 6.26.: Cluster size dependence on the incidence angle for different hit detection thresholds. The cluster size is shown at different hit detection thresholds: 525 Vcth units (green, triangles pointing down), 545 Vcth units (blue, circles) and 565 Vcth units (red, triangles pointing up). The individually applied fits are shown as dashed lines. The fit parameters are summarized in Table 6.4.

in Figure 6.25) is replaced by the parameter α to summarize all of these effects. It represents the cluster enlargement compared to perpendicular physical particle incidence at 45° (or $\frac{\alpha}{2}$ at about 26.6°). Additionally, the geometric model (Equation 6.9) is convoluted with a Gaussian distribution to cover charge diffusion, resulting in

$$s(\theta) = \frac{1}{\sqrt{2\pi\sigma^2}} \int_{-\infty}^{\infty} [s_0 + \alpha \cdot |\tan(t - \theta_0)|] \cdot \exp\left(\frac{(t-\theta)^2}{2\sigma^2}\right) \mathrm{d}t, \tag{6.10}$$

which is used as fit function for the beam test measurements.

Figure 6.26 shows the cluster size dependence on the incidence angle with different settings of hit detection thresholds. The plot contains cluster size information of hits fulfilling the hit efficiency criteria (Equation 6.1). The mean cluster size is plotted against the rotation angle set up at the rotation stage. The plotted uncertainty is the standard error of the mean. The cluster size is fitted by the model as described above (Equation 6.10). The fit parameters are summarized in Table 6.4. It is important to note that the angle scan at nominal threshold of 545 Vcth units holds much more data points and covers a larger angular range.

Table 6.4.: Overview of the parameters obtained in the fit of the cluster size dependence on the incidence angle.

Threshold [Vcth units]	Sensor	s_0 [strips]	α [strips]	θ_0 [°]	σ [°]
525	Top	0.804 ± 0.024	1.069 ± 0.033	0.210 ± 0.104	16.537 ± 0.955
	Bottom	0.806 ± 0.023	1.070 ± 0.031	0.082 ± 0.099	16.557 ± 0.877
545	Top	0.926 ± 0.002	1.651 ± 0.004	-0.078 ± 0.023	7.472 ± 0.095
	Bottom	0.940 ± 0.002	1.648 ± 0.004	0.128 ± 0.022	6.647 ± 0.089
565	Top	0.996 ± 0.004	2.261 ± 0.008	0.015 ± 0.043	6.696 ± 0.260
	Bottom	0.995 ± 0.005	2.238 ± 0.008	-0.002 ± 0.046	7.602 ± 0.256

The angular offset θ_0 as fitted for both sensors at different threshold values is in the range between -0.08 ° and 0.13 °. The weighted mean of θ_0 is $0.03^\circ \pm 0.01^\circ$. As the deviation from zero is negligible, the angle is not corrected for the stub efficiency analysis and for the calculation of an emulated transverse momentum. However, the minimum and maximum of the range of θ_0 are used to calculate systematic uncertainties on results of this analysis. The fitted values for s_0 are below 1 strip, which (at first glance) is not consistent with the expectation from the applied selections and the plot in Figure 6.26. The cluster size at 0° seems to be heavily affected by the Gaussian distribution convolution with the width σ. Evaluating Equation 6.9 with the variables as determined by the fit and $\frac{d_{\text{sensor}}}{w} = \alpha_{\text{fit}}$ at $\theta = \sigma_{\text{fit}}$, the calculated cluster size is in perfect agreement with the measurement value at 0° for each configuration of the signal threshold. The influence of different signal thresholds is clearly visible. The variable α increases linearly with decreasing physical threshold. While the Gaussian distribution width σ is similarly fitted for signal thresholds of 525 Vcth units and 565 Vcth units, it is more than twice as large at 525 Vcth units, the largest tested physical threshold. An interpretation of this effect could be, that hits with high charge deposition are more affected by diffusion and that it does not scale linearly.

Stub efficiency of particles with different emulated p_{T}

The stub efficiency at different incidence angles in the rotation around the strip axis is shown in Figure 6.27. It presents the stub efficiency as defined in Equation 6.2 as well as the stub efficiency using a requirement on the bend code as additional selection criterion, which is called **bend cut** in the following. The bend cut requires the CBC bend code to be consistent with a displacement of the track positions of the top and the bottom sensor of less than 270 µm, which corresponds to three sensor channels. Independently of the stub efficiency definition applied, the stub efficiency drops at approximately 16°. With the stub correlation window set to ± 5 strips, which corresponds to an allowed maximum bending of 450 µm, the turn-on angle expected for a 2S module with 1.8 mm sensor distance[2] is $\arctan\left(\frac{5 \times 90\,\mu\text{m}}{1.8\,\text{mm}}\right) \approx 14^\circ$. However, the physical sensor distance of the DUT has been measured to be approximately 1.6 mm, center-to-center. The deviation from the nominal originates from an old but still used design of the AlCF bridges. Taking the measured sensor distance into account the turn-on angle is in good agreement with the expectation of about

[2]Ideally, this distance is achieved between the centers of active material of the top and the bottom sensor.

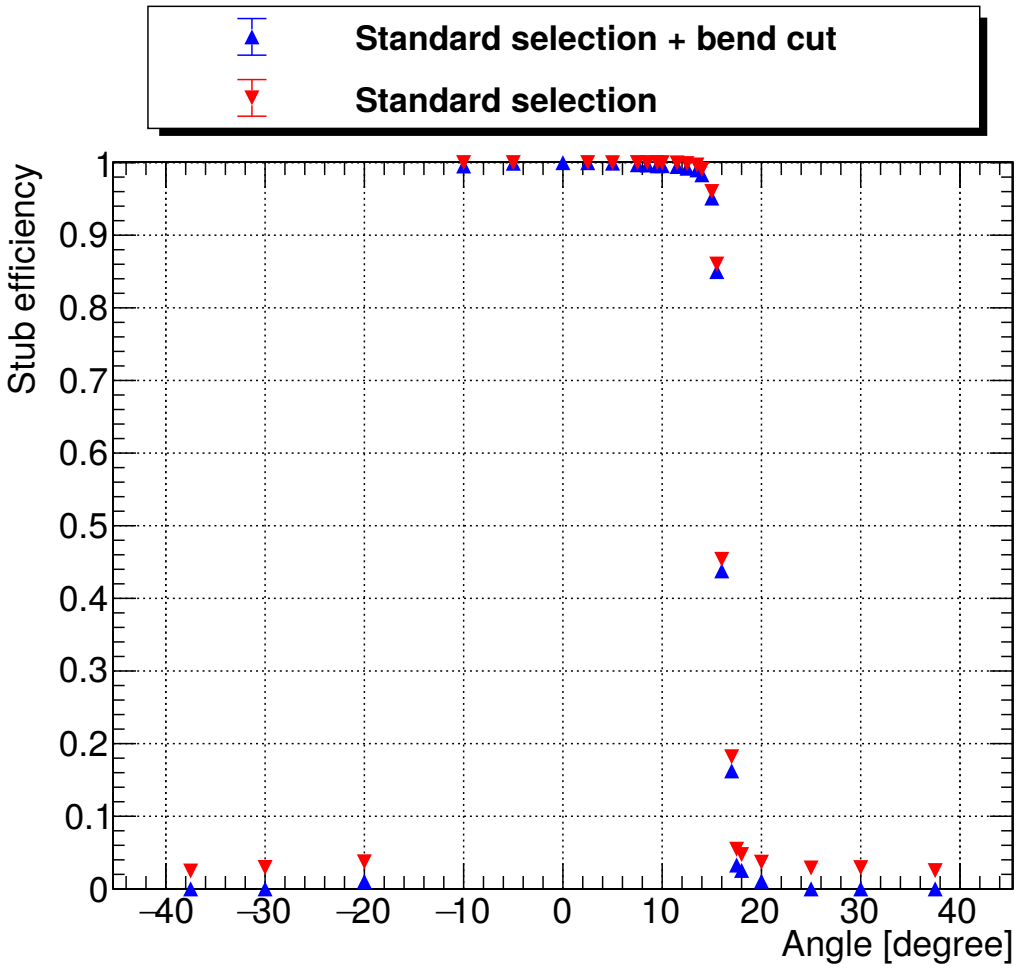

Figure 6.27.: Stub efficiency in dependence on the test beam particle incidence angle. Two different stub efficiency definitions are compared: the standard definition as defined in Equation 6.2 and the standard definition with the bend cut.

16°. The average cluster efficiency has been measured to be in the range of 99.6 % to 99.8 % over the different incidence angles. So the cluster efficiency is not of significant relevance in the discrimination of different p_{T} particles.
The stub efficiency without bend cut is almost 100 % up to approximately 15° (within the correlation window) but does not drop to 0 % at higher incidence angles. Instead the stub efficiency remains at approximately 2.5 %. Stubs contributing to this "stub noise" have a uniformly distributed bend code and only appear if there is more than one cluster measured by either the top or the bottom sensor. Thus, secondary particles might cause this effect. By applying the bend cut, the stub noise at high incidence angles disappears. The stub efficiency at small incidence angles decreases towards the turn-on angle to about 99 %. An explanation for this could be the following: If there is more than one pair of clusters on the seed and the correlation layer to form a stub, the CBC always decides for the stub candidate with lower bending. The average bend code of the stub noise hit pairs is 0 as it is uniformly distributed. With increasing incidence angle, the true bend code rises and therefore the probability of having stub noise with smaller bend code increases. So, the probability of not passing the bend cut rises and the stub efficiency decreases with increasing incidence angle.
The incidence angle can be transformed into a transverse momentum p_{T} which would correspond to a particle inside the magnetic field of the CMS detector. The transformation is done by

$$p_{\mathrm{T}}\left(\theta\right)\left[\mathrm{GeV}\right] = 0.3 \cdot B\left[\mathrm{T}\right] \cdot D\left(\theta\right)\left[\mathrm{m}\right], \tag{6.11}$$

$$D\left(\theta\right)\left[\mathrm{m}\right] = \frac{R\left[\mathrm{m}\right]}{2 \cdot \sin\theta} \qquad \text{and} \tag{6.12}$$

$$\Rightarrow p_{\mathrm{T}}\left(\theta\right)\left[\mathrm{GeV}\right] = 0.15 \cdot B\left[\mathrm{T}\right] \cdot \frac{R\left[\mathrm{m}\right]}{\sin\theta} \tag{6.13}$$

with D being the curvature radius of the particle path while traversing the detector and B being the magnetic field strength. The variable R is the distance of the detector module to the interaction point and θ represents the incidence angle. The following analysis assumes the magnetic field within CMS to be $B = 3.8\,\mathrm{T}$ and a 2S module at the center position of the first layer of TB2S is considered, which has a distance from the interaction point of $R = 0.715\,\mathrm{m}$. The emulated transverse momentum scales linearly with the distance to the considered position in the detector.
Figure 6.28 shows the stub efficiency dependence on the emulated transverse momentum. The presented stub efficiency is measured with bend cut. The stub efficiency dependence of the emulated transverse momentum can be described by

$$\epsilon_{\mathrm{stub}}\left(p_{\mathrm{T}}\right) = \frac{1}{2}\left[\mathrm{Offset} + \mathrm{Scale} \cdot \mathrm{erf}\left(\frac{p_{\mathrm{T}} - p_{\mathrm{T},\mu}}{\sigma_{p_{\mathrm{T}}}}\right)\right] \tag{6.14}$$

with $p_{\mathrm{T},\mu}$ being the transverse momentum at 50 % efficiency and $\sigma_{p_{\mathrm{T}}}$ being the width of the turn-on. The fit is restricted to the range around the turn on (approximately ± 25 % of the approximate expected turn-on p_{T} of 1.5 GeV) to achieve the best possible representation of the respective region. The turn-on transverse momentum $p_{\mathrm{T},\mu}$ has been measured to be $p_{\mathrm{T},\mu} = (1.467 \pm 0.004)\,\mathrm{GeV}$. With

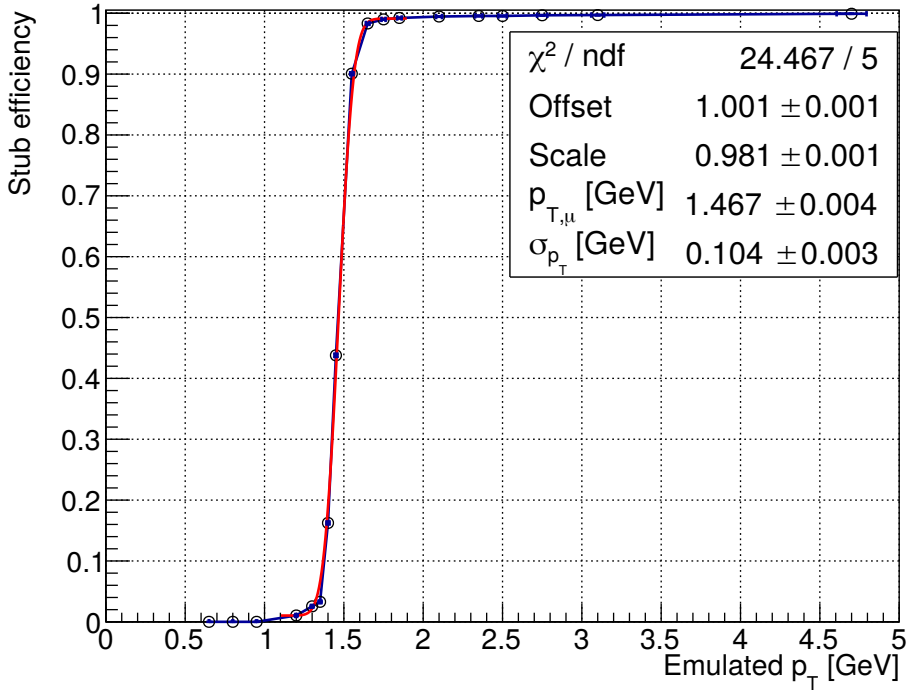

Figure 6.28.: Stub efficiency in dependence of the emulated transverse momentum. The emulated p_{T} has been calculated from the incidence angle using the geometric relation of Equation 6.13.

the width of the turn on $\sigma_{p_{\mathrm{T}}}$ measured to be $\sigma_{p_{\mathrm{T}}} = (0.104 \pm 0.003)\,\mathrm{GeV}$ the p_{T} resolution

$$\Delta p_{\mathrm{T}} = \frac{\sigma_{p_{\mathrm{T}}}}{p_{\mathrm{T},\mu}} \tag{6.15}$$

is calculated to be $(7.1 \pm 0.2)\,\%$. The uncertainties of the stub efficiency are calculated as the Clopper-Pearson interval (Section 6.5.1) and the uncertainties of the emulated p_{T} are calculated by error propagation from the maximum range of the angle deviation as described earlier in the section. Earlier beam test studies with mini 2S prototype modules[3] of past generations have found a p_{T} resolution of 5 %, which is slightly better than measured within this analysis [121]. However, the DUT had different sensors, a sensor spacing of 2.75 mm and it held CBC2 chips. Therefore, the results are not easily comparable.

Simulation of p_{T} resolution

In order to better understand the measured value of the p_{T} resolution, a toy simulation has been conducted. The hit position at the first sensor, x_1, is randomly set within -45 and 45 µm and meant to be the coordinate within a strip with the strip center at 0. The hit position at the second sensor, x_2, is calculated by $x_2 = x_1 + d_{\mathrm{sensor}} \cdot \tan\theta$ for incidence angles θ randomly generated from a Gaussian distribution with a mean between 2° and 25° and a standard deviation of 0.5° to include scattering effects. The incidence angle is scanned in steps of 0.01° and 250 hit pairs are generated

[3] Mini modules house only two instead of eight CBCs. The number of strips of each sensor is only 254 accordingly.

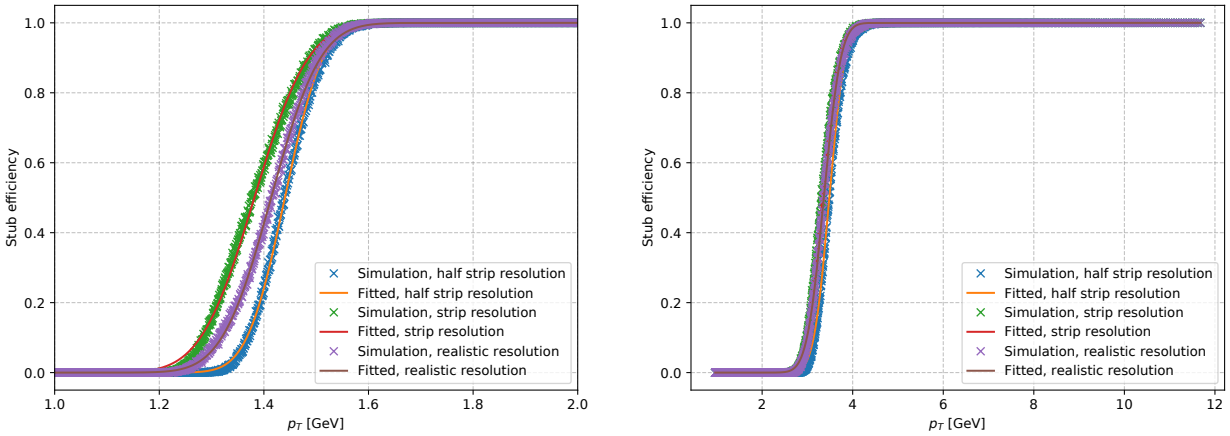

(a) Sensor spacing of 1.6 mm.

(b) Sensor spacing of 4.0 mm.

Figure 6.29.: Simulated stub efficiency as a function of the emulated p_{T}. The simulation has been conducted with half strip resolution, strip resolution and with a more realistic resolution model. The stub window is set to ± 5 strips.

per angle. Both coordinates x_1 and x_2 are transformed into the measured hit coordinates, $\hat{x}_1$ and $\hat{x}_2$, according to a specific resolution: either strip resolution (in case of only 1-strip hits) or half strip resolution (which would be achieved if hits closer to the strip border than to its center would always have a cluster size of 2 strips). The true hit resolution at different incidence angles is much more complex and depends on parameters like the hit detection threshold, the bias voltage or the accumulated dose, which influence the cluster formation. As a simple approach to test a more realistic model, the probability of measuring a 2-strip cluster as a function of the incidence angle $p_{\mathrm{cs2}}(\theta) = \alpha \cdot \tan\theta$ with $\alpha \approx 1.65$ from Equation 6.10 and Table 6.4 is used to either apply strip or half strip resolution. This means that, if by random choice the cluster size is 1, the strip resolution is applied for the respective hit. Otherwise the half strip resolution is used. The toy model stub efficiency is determined for each incidence angle by checking whether the bending $\hat{x}_2 - \hat{x}_1$ is compatible with the considered stub window and calculating the average of the 2500 hit pairs. The emulated p_{T} is calculated using Equation 6.13. The distance of the 2S module from the interaction point is again set to $R = 0.715\,\mathrm{m}$. The p_{T} resolution is calculated as described in Equation 6.15 after fitting the model of Equation 6.14. In the following, the results of the toy simulation are used and the presented uncertainties are determined as deviation from the full and half strip resolution model.

The simulated stub efficiency as a function of the emulated p_{T} is presented in Figure 6.29 with a stub window of ± 5 strips. In Figure 6.29 (a) it is shown for a 2S module with a sensor spacing of 1.6 mm, which should be comparable with the beam test DUT. The toy simulation samples are well represented by the fit model, especially for the realistic resolution. The largest deviations are found at the start and end of the turn-on. The transverse momentum of the turn-on is $p_{\mathrm{T},\mu}^{\mathrm{sim}} = 1.414^{+0.026}_{-0.032}\,\mathrm{GeV}$. Comparing the simulated stub efficiency turn-on with the measurement of the beam test (Figure 6.28 and Figure 6.29 (a)), this value is slightly smaller than the measurement of the beam test with $p_{\mathrm{T},\mu}^{\mathrm{TB}} = (1.467 \pm 0.004)\,\mathrm{GeV}$. The turn-on width is found to be $\sigma_{p_{\mathrm{T}}}^{\mathrm{sim}} = 0.104^{+0.010}_{-0.024}\,\mathrm{GeV}$, which is in perfect agreement with the beam test measurement of $\sigma_{p_{\mathrm{T}}}^{\mathrm{TB}} = (0.104 \pm 0.003)\,\mathrm{GeV}$. Fig-

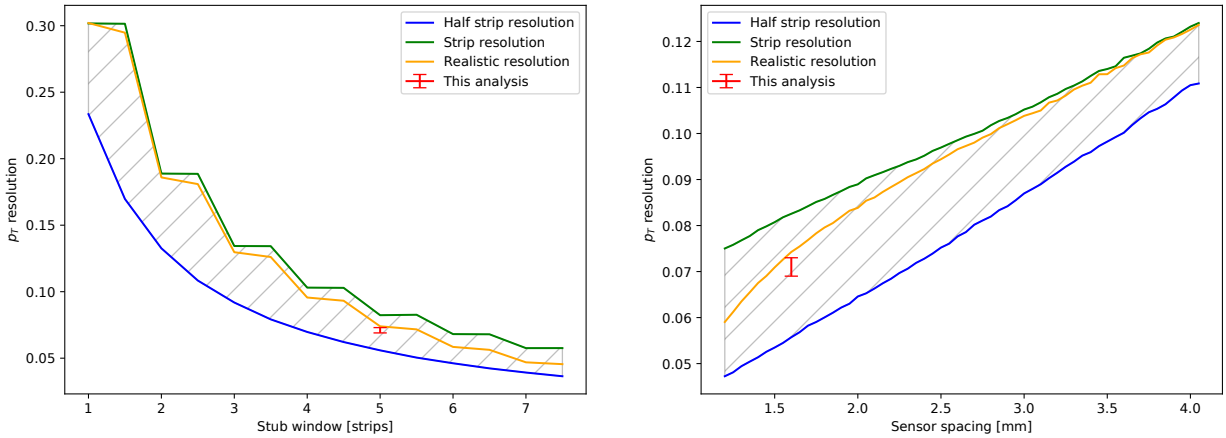

(a) The p_T resolution as a function of the stub window. The sensor spacing is kept constant at 1.6 mm.

(b) The p_T resolution as a function of the sensor spacing. The stub window is kept constant at ± 5 strips.

Figure 6.30.: Results of a toy model simulation. The blue line shows the p_T resolution with the assumption of a half strip hit resolution, the green line represents the p_T resolution assuming strip hit resolution and the realistic resolution model is shown by the orange line. The red marker shows the p_T resolution measured at the beam test.

ure 6.29 (b) presents the simulated stub efficiency as a function of the emulated p_T for a sensor spacing of 4.0 mm. As the stub window has been kept at ± 5 strips the transverse momentum of the turn-on increases to $3.362^{+0.122}_{-0.031}$ GeV with a width of $0.414^{+0.000}_{-0.028}$ GeV.
Figure 6.30 presents the p_T resolution as a function of the stub window and the sensor spacing. The p_T resolution measured at the beam test (presented as a red marker) is in perfect agreement with the simulation. In Figure 6.30 (a) the sensor spacing has been kept constant at 1.6 mm, while the stub window has been varied over a range between 1 and 7 strips. A stub window of 7 strips is the maximum value that can be set [41]. At small stub windows the p_T resolution is at a maximum value of $30.2^{+0.0}_{-7.0}$ %. By increasing the stub window, the p_T resolution falls and reaches its global minimum of $4.7^{+1.1}_{-0.8}$ % at a stub window of 7 strips. The steps in the p_T resolution are caused by the fact that the stub window is set in half strip resolution, while the hit resolution is worse for the strip and realistic resolution scenarios. In Figure 6.30 (b) the stub window has been kept constant at 5 strips, while the sensor spacing has been varied over a range between 1.2 and 4.0 mm. The transverse momentum is resolved best at small sensor spacing, so that at a sensor spacing of 1.2 mm the p_T resolution is found to be $5.9^{+1.6}_{-1.2}$ %. By increasing the sensor distance, the p_T resolution rises approximately linearly and at a sensor spacing of 4.0 mm a value of $12.2^{+0.1}_{-1.2}$ % is found.

Systematic uncertainties

The systematic uncertainties listed in Section 6.5.2 have been evaluated at perpendicular beam incidence. As the uncertainty is expected to be larger at stub efficiency turn-on (with a stub efficiency at 50 %), the same evaluation of systematic uncertainties has been repeated at 16.2°. The resulting numbers for the absolute systematic uncertainties of cluster and stub efficiency are summarized in Table 6.5. The bend cut is considered as an additional source of systematic uncertainty. The largest uncertainty values are measured for the TDC phase selection with 0.12 % for $\epsilon_{\text{cluster}}$

and 0.90 % for ϵ_{stub}. With the statistical uncertainty of the mean value of $\epsilon_{\text{cluster}}$ at 0.03 % and the statistical uncertainty of the mean of ϵ_{stub} at 0.3 %, the systematic uncertainty now clearly dominates. The effect of having an offset in the incidence angle $\theta_0^{\text{max}} = 0.21^\circ$ (Table 6.4) would result in an uncertainty of approximately 0.02 GeV at turn-on.

Table 6.5.: Overview of the systematic uncertainties of the hit and stub efficiency for an incidence angle of 16.2° which approximately corresponds to the average turn on angle at the used stub window setting. The uncertainty is given as the largest deviation from the nominal value. The uncertainty on the cluster efficiency is given as the largest deviation found for either the top or the bottom sensor.

Source of systematic uncertainty	**Estimation procedure**	**Uncertainty**	
		$\epsilon_{\text{cluster}}$	ϵ_{stub}
TDC phase selection	Variation of included TDC phases (1 more / less)	± 0.12 %	± 0.90 %
Link on DUT, hit track distance	Variation by ± 10 %	± 0.06 %	± 0.01 %
Track isolation requirement	Variation by ± 25 %	± 0.01 %	± 0.04 %
Link on reference plane	Variation by ± 10 % in x and y simultaneously	± 0.01 %	± 0.01 %
Tolerance zone for hit track linking	Variation by ± 33 %	± 0.01 %	± 0.01 %
Bend cut radius	Variation by ± 1 strip		± 0.37 %

6.10.2. Investigation of the stub-insensitive area

Stubs are formed by the CBC chips on the FEHs. The CBCs process the signals of the top and the bottom sensor to correlate the hits. However, they only process signals from either the left or the right side of the sensors and there is no interconnection between the two sides. Because of this, particles hitting the top and bottom sensor on different sides of the sensors do not form stubs. Therefore, the 2S module is expected to have a stub-insensitive area at the center of the module. This effect is visualized in a sketch in Figure 6.31. The width of this area W depends on the incidence angle and the distance between the sensors d_{dist} and can be calculated based on a simple geometric approach by

$$W(\theta) = d_{\text{dist}} \cdot |\tan\theta| \,. \tag{6.16}$$

The 2S modules will be mounted into the outer barrel section (TB2S) consisting of three layers and into the outer rings of the TEDD disks. The modules inside TB2S will be positioned with the strips orientated along the beam axis and within the TEDD the modules mounted radially. This geometry and module orientation is chosen to optimize the stub mechanism as the particle path curvature can be measured by comparing the hit information of the two sensors. The incidence angle along the 2S module strips will vary depending on the mounting position inside the detector. The stub efficiency in dependence of this particular incidence angle is analyzed in this section.

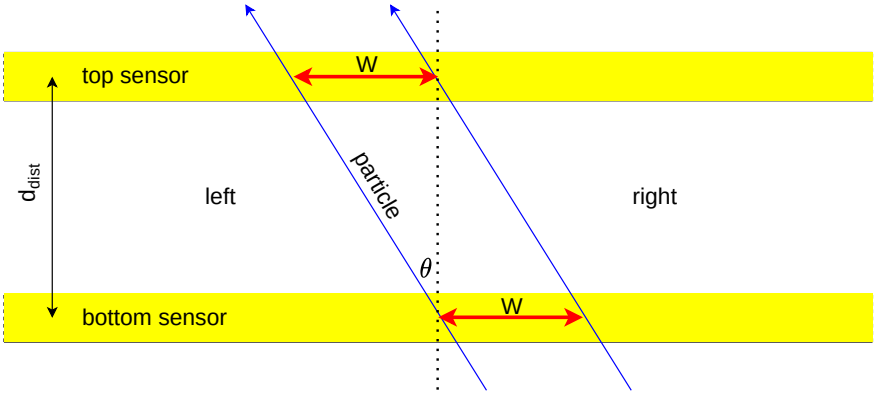

Figure 6.31.: Sketch visualizing the origin of the stub insensitive area at the center of the 2S module.

For this, the center DUT box has been turned by 90° around the beam axis. Thus, the rotation stage of the beam test telescope could be used to precisely set the incidence angle. Analogue to the analysis of the rotation around the strip axis, a potential rotational offset is measured by analyzing the cluster size dependence on the rotation angle. In this case, however, the cluster size along y is considered instead of x. So, the cluster size can be understood as a measure for the rate of hits corresponding to a single event but measured on both the left and right side of the sensor, in the following called hit duplication rate. The model to fit the cluster size in dependence on the incidence angle is the same as for the rotation around the strip axis (Equation 6.10). The analysis only considers clusters fulfilling the cluster efficiency criteria and linked to a telescope track with the y coordinate from -1 to 1 mm. Figure 6.32 shows the cluster size in y in dependence of the incidence angle for the top and the bottom sensor. The rotational offset θ_0 is compatible with 0° within its uncertainty for both sensors. Therefore, the incidence angle is not corrected for the stub analysis. The cluster size is approximately 1.006 strips at 0° and increases to about 1.037 strips at ±30°. This means that at perpendicular incidence and in the center area of the sensor the hit duplication rate is 6 ‰ and 3.1 % higher at an incidence of 30°. It is important to note that the fit parameters determined in this fit cannot be compared trivially with the fitting parameters obtained in the fit of the cluster size in x in the rotation around the strip axis.

The stub efficiency with bend cut is shown in Figure 6.33 (a) in dependence on the incidence angle and the y coordinate of the track linked to a pair of clusters on the top and the bottom sensor. The stub efficiency is close to 100 % everywhere except for the center region, where the stub efficiency drops significantly (to approximately 10 %). The center border of the stub insensitive area is relatively sharp at $y_{\text{track}} = 0$ mm which proves a good alignment of the y axis. The width of this area becomes larger for higher incidence angles. The width has been measured by calculating the distance of the coordinates at which the stub efficiency falls below 75 %. This threshold is chosen conservatively. The width is shown as a function of the incidence angle in Figure 6.33 (b). The model of Equation 6.16 is fitted to determine a cross check value for the distance between the two sensors. The fitted value is perfectly compatible with the distance measured with a microscope.

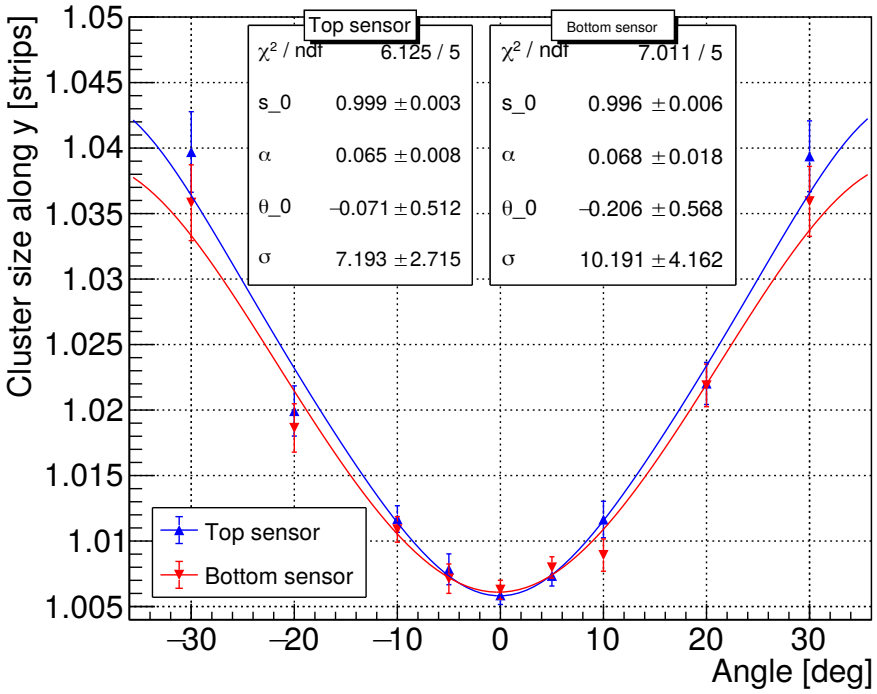

Figure 6.32.: Cluster size in y in dependence of the incidence angle along the strip axis. Only clusters fulfilling the cluster efficiency criteria and linked to a track with y coordinate from -1 to 1 mm are considered. The top sensor cluster size is shown in blue, the bottom sensor cluster size in red.

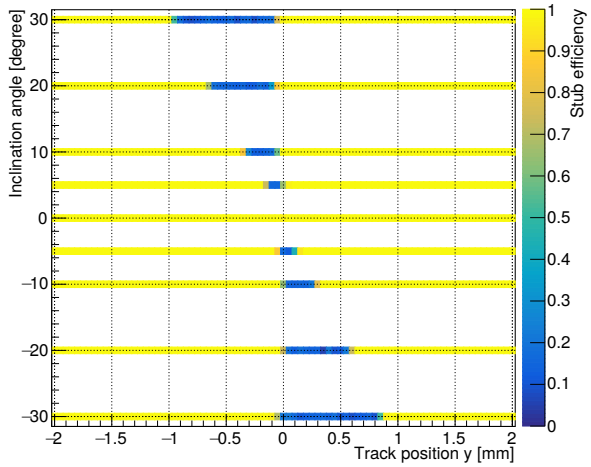

(a) Stub efficiency of the AC-M1804 module in dependence on the position along the strip direction and the incidence angle. White areas are not filled with data.

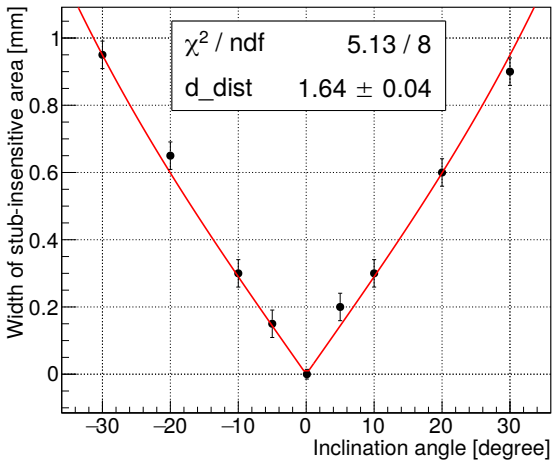

(b) Width of the stub-insensitive area in dependence on the set up incidence angle. The insensitive area has been measured as the distance in y for which the stub efficiency is below 75 %.

Figure 6.33.: Effect of stub insensitivity in the center of the 2S modules for increased inclination angles.

6.11. Conclusions for the operation in the Phase-2 CMS OT

The beam test analysis provides information of the expected performance of stub efficiency under different scenarios. These results can be used to draw conclusions of the performance of 2S modules in the Phase-2 CMS detector. In the following, the stub sensitivity as referring to the geometrical constraints in the stub measurement presented in Section 6.10.2 is projected to the tracker geometry in Phase-2 (Section 6.11.1). Additionally, the found stub noise is set in relation to the expected spectrum of transverse momentum (Section 6.11.2).

6.11.1. Stub sensitivity at different positions of the Phase-2 OT

The effect of losing stub sensitivity in the central region of the OT modules (described in Section 6.10.2) is analyzed in the context of the Phase-2 tracker geometry. The locations of the modules are analyzed considering the latest *tkLayout* design *OT801-IT701* [36].
The PS and 2S modules will be mounted in the barrel section, ranging up to almost $|z| \approx 1200\,\text{mm}$ along the beam axis with radial coordinates of $r \approx 220\,\text{mm}$ - $1100\,\text{mm}$. Additionally, modules are mounted in the TEDD region at higher absolute z coordinates, up to $|z| \approx 2600\,\text{mm}$. Figure 6.34 (a) shows a map of the mounting positions as a quarter of the Phase-2 OT. The modules in the TEDD are mounted with the strips pointing radially away from the beam axis. Within the barrel region all 2S modules have the strips orientated parallel to the beam axis. The PS modules in the innermost part are mounted in the same way. In order to compensate the effect of losing stub sensitivity at increased incidence angles, PS modules at higher z coordinates are mounted tilted with regard to the beam axis. Modules are mounted with tilt angles of 0°, 47°, 60°, 72° and 90°. The positions of different mounting tilt angle are shown in Figure 6.34 (b). In order to realize a coherent p_T filtering in the stub mechanism, the OT modules are assembled with different sensor spacing depending on the mounting position [122]. Figure 6.34 (c) shows the mounting position of the OT modules with different sensor spacing. PS modules will exist with 1.6 mm, 2.6 mm and 4 mm spacing. 2S modules come in 1.8 mm and 4 mm flavor.
The information summarized above can be used to calculate the incidence angle along the sensor strip axis per module for each individual position inside the Phase-2 tracker. For this, a straight particle path is assumed with the center of the CMS detector coordinate system as the origin. The distribution of incidence angles for the different parts of the detector is shown in Figure 6.35 (a). The highest incidence angles of up to 59° are reached in TB2S layer 1 in the region close to the TEDDs. The maximum incidence angle for PS modules is only 33° because of the tilted region in the barrel and as the modules in the TEDD are closer to the beam line. The effective area sensitive for stubs is evaluated based on the results of the beam test analysis (Section 6.10.2). The distribution of the stub sensitive areas (shown as the relative proportion of the total sensor area) is presented in Figure 6.35 (b) for the different parts of the OT. Although the incidence angles of PS modules are significantly lower than for the 2S modules the relative reduction of stub sensitivity is higher. In TEDD1 the PS modules at maximum radial distance from the beam line lose more than 4 % of stub sensitivity. The maximum loss for 2S modules is 3 % in TB2S layer 1 where the highest incidence angles are reached. The reason for losing more sensitivity at lower incidence angles for PS modules is that the sensor spacing in the respective regions is 4 mm. Furthermore, the length

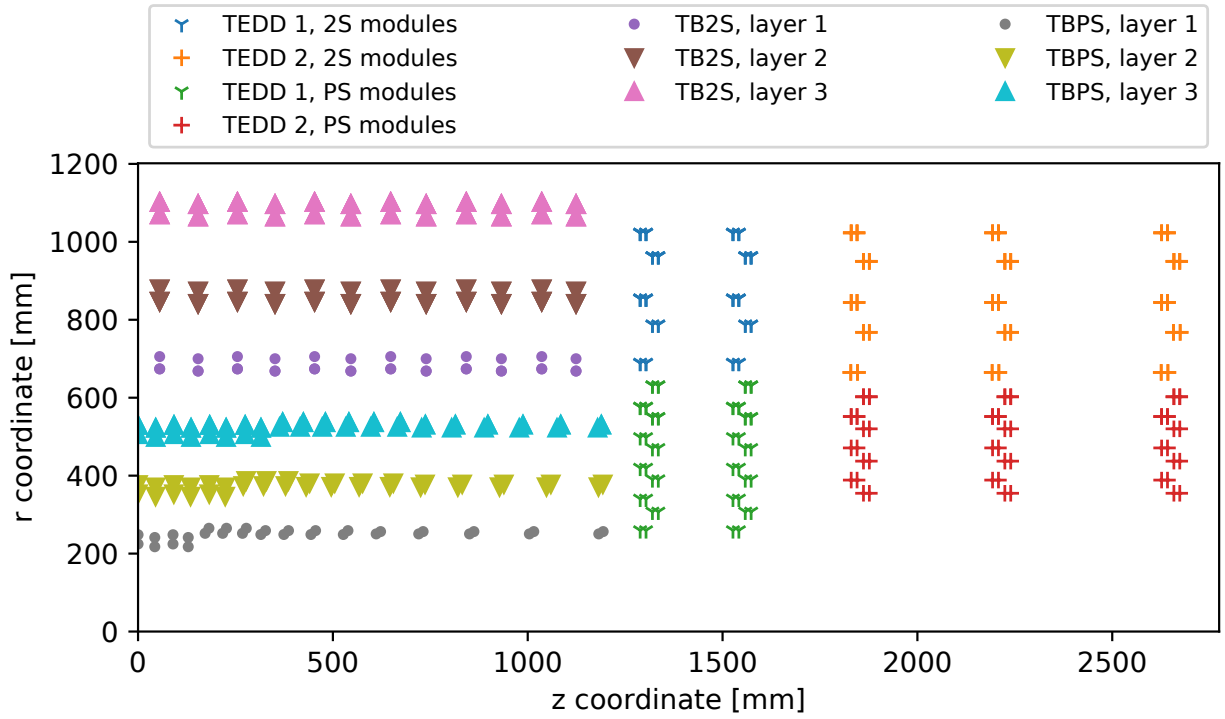

(a) Quarter map of the mounting positions of 2S and PS modules within the Phase-2 OT. The geometry has been extracted from the tkLayout design *OT801-IT701* [36].

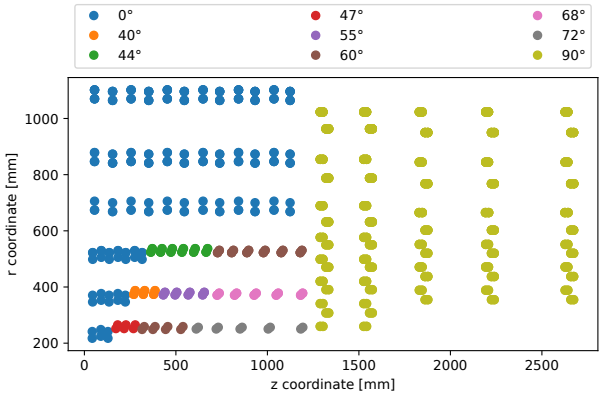

(b) Position map of the OT modules presenting the tilting angle of the strip axis relative to the beam axis.

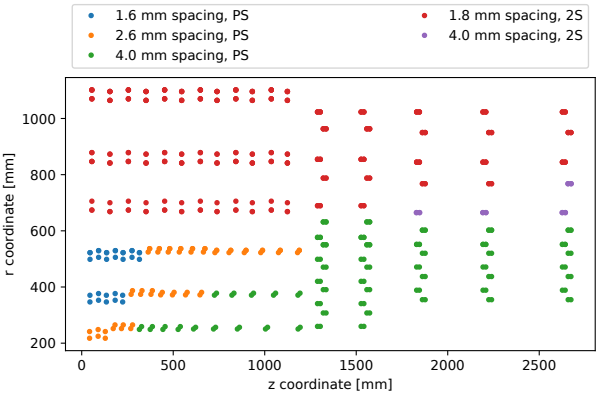

(c) Position map of the OT modules presenting the spacing between the top and the bottom sensor.

Figure 6.34.: Position maps of the OT modules.

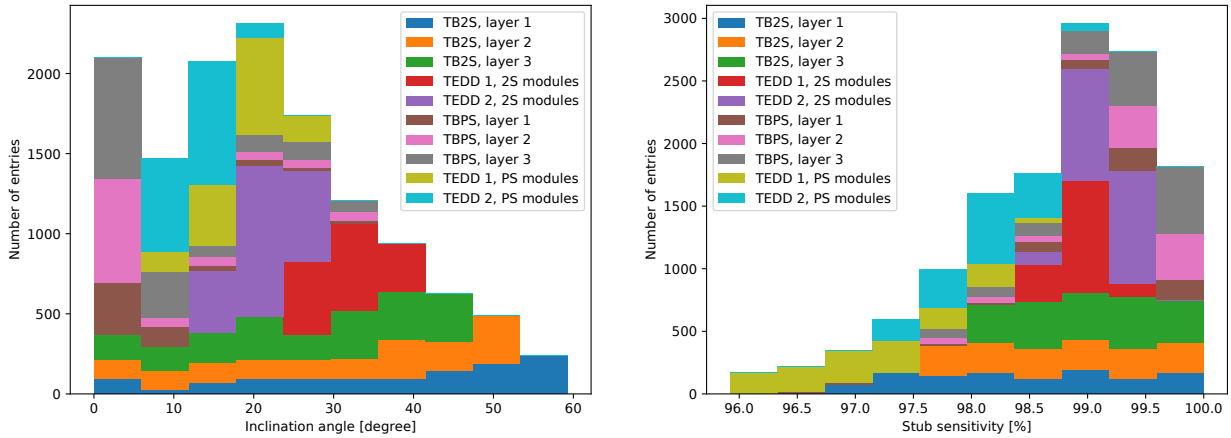

(a) Stacked distributions of incidence angles for the different parts of the Phase-2 OT.

(b) Stacked distributions of calculated stub efficiency for the different parts of the Phase-2 OT.

Figure 6.35.: Distributions of incidence angles and resulting stub sensitivities.

of the strips of the PS modules is approximately half of the 2S module strip length, so that the impact on the relative stub sensitive area is larger.

Using the geometry information described above, the number of modules hit by a particle with flight direction η is calculated. For this, the pseudorapidity range from -3 to 3 is scanned with a bin size of 0.01. Figure 6.36 presents the mean number of modules in the particle path as a function of η. The mean numbers are calculated from a sample of thousand randomly picked coordinates of ϕ and η each and per bin to avoid systematic effects. On average more than seven modules are hit in the pseudorapidity range from -2.4 to 2.4 and the number of hits in the insensitive region of the modules is well below 1. At $|\eta| \approx 1.7$ the average number of hit modules reaches its maximum of about 10.

6.11.2. The stub mechanism applied on the LHC p_T spectrum

The measured module performance at the beam test is evaluated in consideration of the Phase-2 scenario at the LHC. A special focus is put on the effect of "stub noise" (described in Section 6.10.1) assuming that it is not only a beam test feature but also present at LHC conditions. For this a CMS Monte Carlo simulation is analyzed using the CMS event data model and data processing framework CMSSW [123]. The simulation sample has been generated with Pythia 8 [124] with the CP5 tune [125]. It contains 3000 top quark pair production ($t\bar{t}$) events at a center-of-mass energy of 14 TeV. Additionally, an average pileup of 200 minimum bias events per bunch crossing is included. The sample has been generated with the Phase-2 detector geometry *2026D76*, which includes the tacker layout *OT800_IT615* [126]. The interaction with the detector is simulated using Geant4 [127]. The Monte Carlo sample is analyzed only considering particle track information for simplification.

Figure 6.37 shows the distribution of the pseudorapidity η of the tracks of charged particles. The charged particles account for approximately 79 % of the sample. About 48 % of these hit more than four tracker layers considering both the IT and the OT. The red lines present the η acceptance

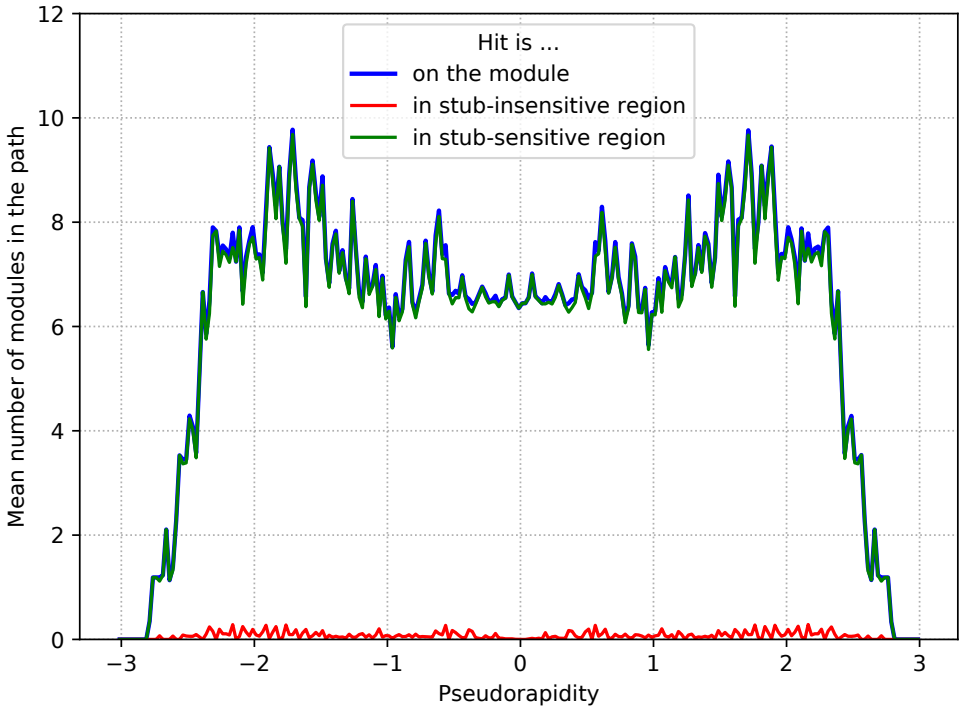

Figure 6.36.: Number of modules in the path of particles traversing the Phase-2 CMS OT at different pseudorapitities η. The number of modules displayed is the average value of a sample of thousand randomly picked values of ϕ and η each. By selecting both coordinates randomly, systematic effects emerging from periodically mounted modules are avoided.

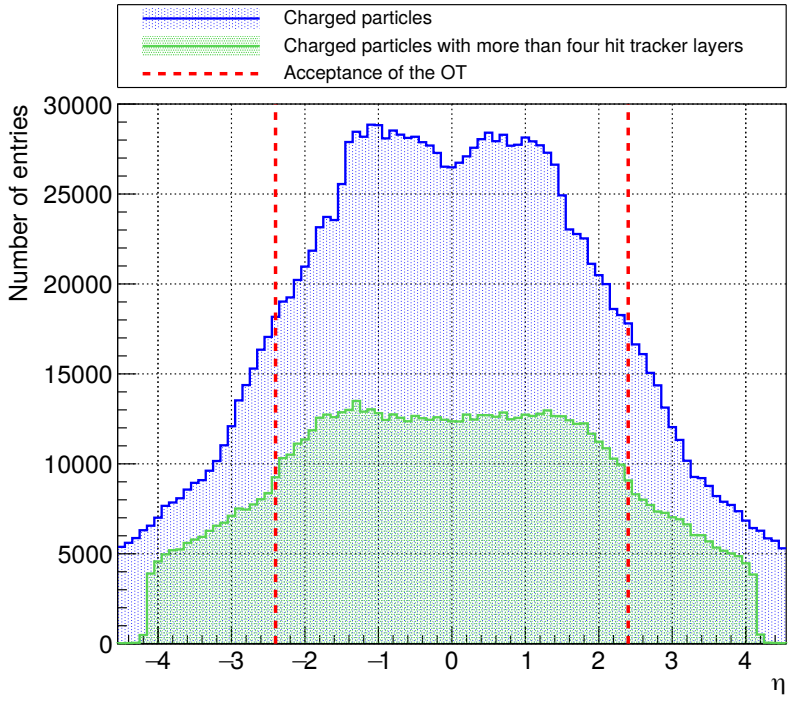

Figure 6.37.: Distribution of the pseudorapidity of the tracks of charged particles. The η distribution of all charged particles is presented in blue. The particles hitting more than four tracker layers (both IT and OT) is shown in green. The vertical red dashed lines indicate the OT acceptance ($|\eta| \leq 2.4$). The distribution is accumulated over 3000 events.

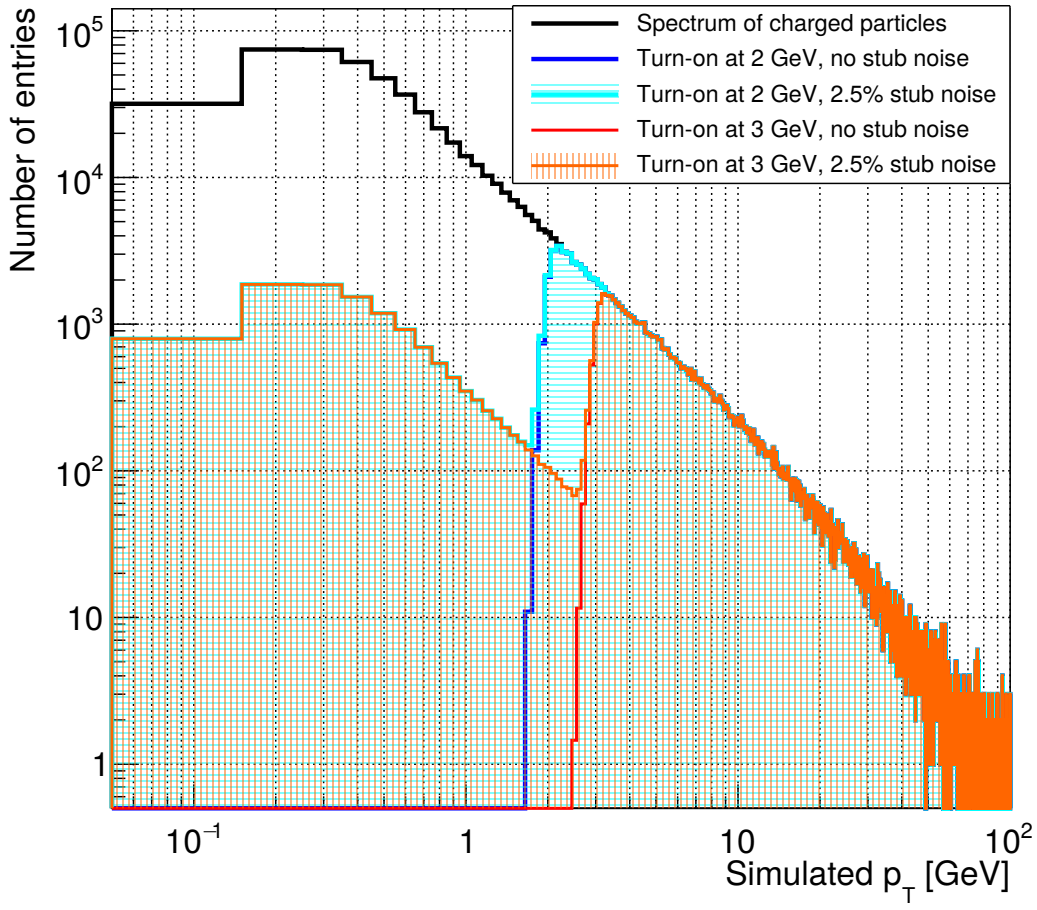

Figure 6.38.: Spectrum of transverse momentum p_{T}. The distribution includes particles with $|\eta| \leq 2.3$ and with more than four hit tracker layers (IT and OT). The p_{T} spectrum of all charged particles is presented by a black solid line. To study the stub turn-on effects, this spectrum is weighted by the stub efficiency with a turn-on at 2 GeV (3 GeV), simulated with stub noise effects ($\epsilon_{\text{stub noise}} = 2.5\,\%$) shown in turquoise (orange) and without shown in blue (red). Each of these distributions features a p_{T} resolution of 7.1 % (as measured at the beam test). The presented numbers are absolute numbers of entries accumulated over 3000 simulated events. A binning of 100 MeV is applied.

of the OT of approximately $-2.4 \leq \eta \leq 2.4$. The most probable value of pseudorapidity is about ± 1.0. For larger absolute values of η, the number of particle tracks decreases. The relative number of charged particle tracks, which fit the OT acceptance is approximately 73 %.

The spectrum of the transverse momentum is shown in Figure 6.38 for tracks within $|\eta| \leq 2.3$ and with more than four tracker layers hit. The most probable value of p_{T}, both for the total spectrum and the spectrum of charged particles, is about 0.2 GeV. The number of particle tracks decreases exponentially for higher transverse momenta. In order to study the stub turn-on and especially the significance of the stub noise in the context of the p_{T} spectrum at the LHC, the p_{T} spectrum of charged particles is weighted by the stub efficiency as a function of p_{T} (Equation 6.14). Different functions of stub efficiency have been considered. For each of these, the p_{T} resolution has been

Table 6.6.: Overview of the properties of the stub efficiency weighted p_{T} spectra. Only the region of $|\eta| \leq 2.3$ and tracks with more than four hit tracker layers are considered.

Stub noise level	**0 %**		**1 %**		**2.5 %**	
Turn-on at	**2 GeV**	**3 GeV**	**2 GeV**	**3 GeV**	**2 GeV**	**3 GeV**
Fraction of the weighted spectrum compared to the spectrum of charged particles	16.0 %	10.9 %	16.8 %	11.8 %	18.1 %	13.2 %
Fraction of the weighted spectrum up to turn-on compared to the total weighted spectrum	3.3 %	2.9 %	8.1 %	10.2 %	14.5 %	19.3 %
Mean p_{T} of the weighted spectrum	7.25 GeV	9.46 GeV	6.91 GeV	8.80 GeV	6.47 GeV	7.97 GeV

kept at the value measured at the beam test, $\Delta p_{\mathrm{T}} = 7.1\,\%$. The stub turn-on has been studied at 2 GeV and 3 GeV. The turn-on width has been scaled accordingly to 142 MeV and 213 MeV. The level of stub noise at low p_{T}, $\epsilon_{\text{stub noise}}$, was simulated at 0.0 %, 1.0 % and 2.5 %. This was realized by tuning the functional parameters

$$\begin{aligned} \text{Offset} &= 1 + \epsilon_{\text{stub noise}} && \text{and} \\ \text{Scale} &= 1 - \epsilon_{\text{stub noise}} && \text{from} \\ \epsilon_{\text{stub}}\left(p_{\mathrm{T}}\right) &= \frac{1}{2}\left[\text{Offset} + \text{Scale} \cdot \text{erf}\left(\frac{p_{\mathrm{T}} - p_{\mathrm{T},\mu}}{\sigma_{p_{\mathrm{T}}}}\right)\right]. \end{aligned}$$

A loss of stub efficiency at high p_{T} is not included.

Table 6.6 lists the characteristics of the weighted spectra. Comparing the p_{T} spectrum of charged particles with the stub efficiency weighted spectrum without stub noise ($\epsilon_{\text{stub noise}} = 0\,\%$), the number of entries is reduced to 16.0 % in the case of a turn-on at 2 GeV and further reduced to 10.9 % with the turn-on at 3 GeV. Only 3.3 % respectively 2.9 % of the entries of the weighted spectrum have a transverse momentum lower than the turn-on. This is purely related to the turn-on width. At a stub noise level of $\epsilon_{\text{stub noise}} = 2.5\,\%$, the fraction of the weighted spectrum as compared to the spectrum of charged particles is 18.1 % with the turn-on at 2 GeV and 13.2 % with the turn-on at 3 GeV. In this case, the relative number of entries with transverse momentum below the turn-on is increased to 14.5 % or 19.3 %, respectively. As a consequence, the mean transverse momentum of the weighted spectrum decreases with rising stub noise. Without stub noise the mean p_{T} is 7.25 GeV with a turn-on at 2 GeV (or 9.46 GeV with a turn-on at 3 GeV) and decreases to 6.47 GeV (7.97 GeV) considering a stub noise of 2.5 %.

So, the stub noise is expected to have a significant effect on the number of stubs if it is present under LHC conditions. If however only coincidences of multiple modules result in a trigger decision, the stub noise effect is assumed to be highly suppressed. The increased number of stubs would nevertheless require a higher bandwidth. In order to understand the origin of the stub noise to

estimate whether it for sure is present under LHC conditions, further investigations need to be done. Furthermore, a much more realistic simulation should be conducted to study the effect on the L1 trigger in more detail.

7. Summary and outlook

The LHC will experience an extensive upgrade for highly increased luminosities. To maintain the excellent performance, which has been proven over the last decade, and to be able to profit from the increased particle collision rate, also the CMS detector requires a dedicated upgrade campaign. As part of the Phase-2 upgrade, the CMS tracker will entirely be replaced. The new CMS OT will consist of detector modules, the 2S and the PS modules, each consisting of two stacked sensors to feature on-module measurements of transverse momenta. The work of this PhD thesis is related to the prototyping phase of the 2S modules with the main topics in the broad field of module assembly and beam test studies.

Several modules have been assembled by the working group, starting with the first functional full-size module (referred to as M1801) and eventually building a close-to-final module (the M4002). The focus of module assembly in the framework of this thesis has been placed on the wire bonding step. As a result, the jig for the bonding of the signal wires as well as the Kapton and HV pigtail gluing jig, which is now also used to bond the HV connection, have been improved. A spring based solution is used to simplify the preparation of the bonding of signal wires. Additionally, the bond process parameters have been analyzed and a software tool has been developed to simplify the QA of the wire bonding. On a test sample, the analysis of process parameters has been found to have a sensitivity of more than 90 % at a specificity of up to 90 %. The usefulness of this software tool will be tested on a larger scale during the series production of 2S modules in Aachen. As a preparation study for the series production, the wire bonding speed has been evaluated and it was found that unconnected channels can be repaired even after encapsulation. In order to simplify the selection of Kapton strips usable for module assembly, a software tool has been developed to analyze scan images from a commercial flat bed scanner. This rather simple and low cost approach features a fast way to reliably and reproducibly measure the size of multiple strips at once. As part of the QA during the module assembly, the IV characteristics of the sensors is tested. In the course of these measurements, a set of thinned sensors (thFZ240) has been characterized and the measurements have contributed to the selection of the sensor thickness for the Phase-2 upgrade of the OT [42]. One of the assembled modules (the M4001) developed a high leakage current after wire bonding. To eventually find the cause of that, an IR camera has been used and the module could successfully be repaired. In addition to that, the experiences gained during the module assembly were used to perform a detailed evaluation of series production workflow. The required number of jigs and the corresponding storage capabilities were estimated as well as working and machine times to scale these to a series production scenario. At latest during the pre-production, which currently is scheduled to start early 2023, the assembly conditions and the module output will approach the series production situation and the estimations of time and storage capabilities will be examined.

During a beam test campaign, which has been conducted in late 2019, the performance of 2S module prototypes was evaluated. For this, a dedicated analysis framework, FABEL, has been developed in cooperation with Christian Dziwok [96]. It is used to link the telescope tracks to hits on the detector module avoiding double counting and makes data easily accessible for high level analysis. Furthermore, it provides tools to simplify the DUT alignment as well as a set of predefined selection criteria for the analysis.

Besides doing the alignment of the beam test samples, an analysis of the track uncertainty has been conducted. The hit and stub efficiency have been analyzed in detail as a function of the hit position and were found to be well above 99 %, except for the center region of the module ($y = 0\,\text{mm}$). There, the hit efficiency on both sensors is decreased by approximately 2 % in a region of 200 µm width and depending on the incidence angle there is a region that is insensitive to stubs. Considering the Phase-2 OT geometry, this effect was proven to be not a significant problem. Additionally, the stub mechanism was tested by measuring the stub efficiency under different incidence angles of the beam to mimic particles of varying transverse momentum. The stub mechanism was found to perform well with a p_T resolution of $(7.1 \pm 0.2)\,\%$, which is in perfect agreement with a toy simulation, that was performed to study the p_T resolution as a function of the sensor distance and the applied stub window. However, also at high incidence angles (low values of p_T) valid stubs were measured, which is referred to as stub noise. The significance of the stub noise has been studied by projecting this effect into the HL-LHC p_T spectrum of a $\text{t}\bar{\text{t}}$ Monte Carlo sample. It was found that at a stub noise level of 2.5 % and with a p_T turn-on at 3 GeV with a p_T resolution of 7.1 %, almost 20 % of all valid stubs, that a 2S module would measure, would originate from a particle with a transverse momentum below the turn-on value. As the origin of the stub noise measured at the beam test has not yet definitely been found and the simple Monte Carlo study indicates that it indeed has a significant effect, a more detailed study should be conducted to study whether the L1 trigger could be affected. The effect of stub noise could be studied in future beam tests in more detail (possibly with a proton beam at CERN or FNAL). The effects on the L1 trigger could be analyzed by a more sophisticated analysis with hit information that intrinsically include stub noise.

In summary, the work performed in the framework of this thesis contributed significantly to the evaluation of prototype 2S modules, and to the preparation of the RWTH Aachen module assembly center in view of the module series production.

Bibliography

[1] CERN. *The Large Hadron Collider*. 2021. URL: https://home.cern/science/accelerators/large-hadron-collider (visited on May 9, 2022).

[2] NobelPrize.org. *The Nobel Prize in Physics 2013*. 2021. URL: https://www.nobelprize.org/prizes/physics/2013/summary/.

[3] G. Apollinari et al. "Chapter 1: High Luminosity Large Hadron Collider HL-LHC. High Luminosity Large Hadron Collider HL-LHC". In: *CERN Yellow Report* arXiv:1705.08830. 5 (May 2017). 21 pages, chapter in High-Luminosity Large Hadron Collider (HL-LHC) : Preliminary Design Report, 1–19. 21 p. DOI: 10.5170/CERN-2015-005.1. URL: https://cds.cern.ch/record/2120673.

[4] The CMS Collaboration. "The Phase-2 Upgrade of the CMS Tracker". In: *CERN CDS* (June 2017). URL: https://cds.cern.ch/record/2272264.

[5] R. Diener et al. "The DESY II test beam facility". In: *Nuclear Instruments and Methods in Physics Research Section A: Accelerators, Spectrometers, Detectors and Associated Equipment* 922 (Apr. 2019), pp. 265–286. ISSN: 0168-9002. DOI: 10.1016/j.nima.2018.11.133. URL: http://dx.doi.org/10.1016/j.nima.2018.11.133.

[6] K. Aamodt et al. "The ALICE experiment at the CERN LHC". In: *JINST* 3 (2008), S08002. DOI: 10.1088/1748-0221/3/08/S08002.

[7] G. Aad et al. "The ATLAS Experiment at the CERN Large Hadron Collider". In: *JINST* 3 (2008), S08003. DOI: 10.1088/1748-0221/3/08/S08003.

[8] The CMS Collaboration. "The CMS experiment at the CERN LHC". In: *Journal of Instrumentation* 3.08 (Aug. 2008), S08004–S08004. DOI: 10.1088/1748-0221/3/08/s08004. URL: https://doi.org/10.1088/1748-0221/3/08/s08004.

[9] A. Augusto Alves Jr. et al. "The LHCb Detector at the LHC". In: *JINST* 3 (2008), S08005. DOI: 10.1088/1748-0221/3/08/S08005.

[10] CERN. *CERN's accelerator complex*. 2022. URL: https://home.cern/science/accelerators/accelerator-complex (visited on Nov. 16, 2021).

[11] Esma Mobs. "The CERN accelerator complex - 2019. Complexe des accélérateurs du CERN - 2019". In: *CERN CDS* (July 2019). General Photo. URL: https://cds.cern.ch/record/2684277.

[12] CERN Education, Communications and Outreach Group. *LHC faq. the guide*. 2017. URL: https://home.cern/sites/home.web.cern.ch/files/2018-07/CERN-Brochure-2017-002-Eng_0.pdf (visited on Nov. 17, 2021).

[13] Claude Amsler. *Kern- und Teilchenphysik*. Stuttgart: UTB, 2007. URL: https://cds.cern.ch/record/1138739.

[14] The CMS Community. *Public CMS Luminosity Information*. 2022. URL: https://twiki.cern.ch/twiki/bin/view/CMSPublic/LumiPublicResults (visited on Apr. 8, 2022).

[15] The CMS Experiment at CERN. *The detector*. 2021. URL: https://home.cern/science/accelerators/large-hadron-collider (visited on Nov. 30, 2021).

[16] David Barney and Sergio Cittolin. "CMS Detector Drawings". In: *CERN CDS* (Jan. 2000). URL: https://cds.cern.ch/record/2629816.

[17] The CMS Tracker collaboration. "The CMS Phase-1 pixel detector upgrade". In: *Journal of Instrumentation* 16.02 (Feb. 2021), P02027–P02027. DOI: 10.1088/1748-0221/16/02/p02027. URL: https://doi.org/10.1088/1748-0221/16/02/p02027.

[18] Martin Lipinski. "System Tests and Qualification of Pixel Modules and DC-DC Converters for the Phase-1 Upgrade of the CMS Pixel Detector". PhD thesis. 2019. URL: https://cds.cern.ch/record/2666514.

[19] Lutz Werner Feld et al. "A DC-DC Conversion Powering Scheme for the CMS Phase-1 Pixel Upgrade". In: *Proceedings, Topical Workshop on Electronics for Particle Physics (TWEPP 2012)* (Dec. 2012). URL: https://cds.cern.ch/record/1498686.

[20] The CMS Collaboration. *The CMS electromagnetic calorimeter project: Technical Design Report*. Technical design report. CMS. Geneva: CERN, 1997. URL: https://cds.cern.ch/record/349375.

[21] J Mans et al. "CMS Technical Design Report for the Phase 1 Upgrade of the Hadron Calorimeter". In: *CERN CDS* (Sept. 2012). URL: https://cds.cern.ch/record/1481837.

[22] The CMS Collaboration. "The Phase-2 Upgrade of the CMS Muon Detectors". In: *CERN CDS* (Sept. 2017). This is the final version, approved by the LHCC. URL: https://cds.cern.ch/record/2283189.

[23] Giovanni Mocellin. "Performance of the GE1/1 detectors for the upgrade of the CMS muon forward system". Dissertation. Aachen: RWTH Aachen University, 2021. DOI: 10.18154/RWTH-2021-07066. URL: https://publications.rwth-aachen.de/record/822893.

[24] I. Béjar Alonso et al. (Eds.) "High-Luminosity Large Hadron Collider (HL-LHC): Technical design report". In: *CERN Yellow Reports: Monographs* CERN-2020-010 (2020). ISSN: 2519-8076. DOI: https://doi.org/10.23731/CYRM-2020-0010.

[25] CERN. *The HL-LHC project*. 2022. URL: https://hilumilhc.web.cern.ch/content/hl-lhc-project (visited on Apr. 26, 2022).

[26] Vincenzo Izzo. "ATLAS Upgrades". In: *Proceedings, 8th Conference of Large Hadron Collider Physics (LHCP), Online* (Sept. 2020). DOI: 10.22323/1.382.0094. URL: https://cds.cern.ch/record/2732959.

[27] M.P. Casado. "A High-Granularity Timing Detector for the ATLAS Phase-II upgrade". In: *Nuclear Instruments and Methods in Physics Research Section A: Accelerators, Spectrometers, Detectors and Associated Equipment* 1032 (2022), p. 166628. ISSN: 0168-9002. DOI: https://doi.org/10.1016/j.nima.2022.166628. URL: https://www.sciencedirect.com/science/article/pii/S0168900222002005.

[28] D Contardo et al. "Technical Proposal for the Phase-II Upgrade of the CMS Detector". In: *CERN CDS* CERN-LHCC-2015-010, LHCC-P-008, CMS-TDR-15-02 (June 2015). Ed. by D. Contardo et al. DOI: 10.17181/CERN.VU8I.D59J. URL: https://cds.cern.ch/record/2020886.

[29] The CMS collaboration. "The Phase-2 Upgrade of the CMS L1 Trigger Interim Technical Design Report". In: *CERN CDS* (Sept. 2017). This is the CMS Interim TDR devoted to the upgrade of the CMS L1 trigger in view of the HL-LHC running, as approved by the LHCC. DOI: 10.17181/CERN.UUWZ.FMIS. URL: http://cds.cern.ch/record/2283192.

[30] Oliver Brüning et al. "The scientific potential and technological challenges of the High-Luminosity Large Hadron Collider program". In: *Reports on Progress in Physics* 85.4 (Mar. 2022), p. 046201. DOI: 10.1088/1361-6633/ac5106. URL: https://doi.org/10.1088/1361-6633/ac5106.

[31] The CMS Collaboration. "The Phase-2 Upgrade of the CMS Barrel Calorimeters". In: *CERN CDS* (Sept. 2017). URL: https://cds.cern.ch/record/2283187.

[32] The CMS Collaboration. "The Phase-2 Upgrade of the CMS Endcap Calorimeter". In: *CERN CDS* (Nov. 2017). URL: https://cds.cern.ch/record/2293646.

[33] The CMS Collaboration. "A MIP Timing Detector for the CMS Phase-2 Upgrade". In: *CERN CDS* (Mar. 2019). URL: http://cds.cern.ch/record/2667167 (visited on May 9, 2022).

[34] A. Benaglia et al. "Detection of high energy muons with sub-20ps timing resolution using L(Y)SO crystals and SiPM readout". In: *Nuclear Instruments and Methods in Physics Research Section A: Accelerators, Spectrometers, Detectors and Associated Equipment* 830 (2016), pp. 30–35. ISSN: 0168-9002. DOI: https://doi.org/10.1016/j.nima.2016.05.030. URL: https://www.sciencedirect.com/science/article/pii/S016890021630393X.

[35] S. Orfanelli. "The Phase 2 Upgrade of the CMS Inner Tracker". In: *Nucl. Instrum. Meth. A* 980 (2020), p. 164396. DOI: 10.1016/j.nima.2020.164396.

[36] The CMS Tracker Layout Modelling Group. *CMS tkLayout: OT801-IT701*. CMS. 2021. URL: https://cms-tklayout.web.cern.ch/cms-tklayout/layouts/recent-layouts/OT801_IT701/index.html (visited on July 19, 2021).

[37] Max Philip Rauch. "Thermal Measurements and Characterizations for the CMS Phase-1 Barrel Pixel Detector and the CMS Phase-2 Upgrade Tracker 2S Module with Evaporative CO_2 Cooling Systems". PhD thesis. 2020. URL: http://cds.cern.ch/record/2740861.

[38] Maurice Garcia-Sciveres. "The RD53A Integrated Circuit". In: *CERN CDS* (Oct. 2017). URL: http://cds.cern.ch/record/2287593.

[39] The lpGBT group. *LpGBT-FPGA Documentation*. 2022. URL: http://lpgbt-fpga.web.cern.ch/doc/html/ (visited on Apr. 12, 2022).

[40] Jan Troska et al. "The VTRx+, an optical link module for data transmission at HL-LHC". In: *Proceedings, Topical Workshop on Electronics for Particle Physics (TWEPP 2017)* TWEPP-17 (2017), 048. 5 p. DOI: 10.22323/1.313.0048. URL: https://cds.cern.ch/record/2312396.

[41] Mark Prydderch. *CBC3.1 User Manual*. ASIC Design Group. Science and Technology Facilities Council, 2018. URL: http://www.hep.ph.ic.ac.uk/ASIC/cbc3.1/CBC3p1_User_Manual_V1p3.pdf (visited on June 28, 2021).

[42] The CMS Tracker Community. "Selection of the silicon sensor thickness for the Phase-2 upgrade of the CMS Outer Tracker". In: *Journal of Instrumentation* 16.11 (Nov. 2021), P11028. DOI: 10.1088/1748-0221/16/11/p11028. URL: https://doi.org/10.1088/1748-0221/16/11/p11028.

[43] W. Adam et al. "P-Type Silicon Strip Sensors for the new CMS Tracker at HL-LHC". In: *JINST* 12.06 (2017), P06018. DOI: 10.1088/1748-0221/12/06/P06018.

[44] H. Kurita et al. "Simple Fabrication and Characterization of Discontinuous Carbon Fiber Reinforced Aluminum Matrix Composite for Lightweight Heat Sink Applications". In: *Acta Metallurgica Sinica (English Letters)* 27 (2014). DOI: 10.1007/s40195-014-0106-7. URL: https://doi.org/10.1007/s40195-014-0106-7.

[45] Dupont. *Polyimide Films*. 2022. URL: https://www.dupont.com/electronic-materials/polyimide-films.html (visited on Apr. 16, 2022).

[46] G. Hall et al. "CBC2: A CMS microstrip readout ASIC with logic for track-trigger modules at HL-LHC". In: *Nuclear Instruments and Methods in Physics Research Section A: Accelerators, Spectrometers, Detectors and Associated Equipment* 765 (2014). HSTD-9 2013 - Proceedings of the 9th International "Hiroshima" Symposium on Development and Application of Semiconductor Tracking Detectors, pp. 214–218. ISSN: 0168-9002. DOI: https://doi.org/10.1016/j.nima.2014.04.056. URL: https://www.sciencedirect.com/science/article/pii/S0168900214004690.

[47] Mark Prydderch et al. "CBC3: a CMS microstrip readout ASIC with logic for track-trigger modules at HL-LHC". In: *Proceedings, Topical Workshop on Electronics for Particle Physics (TWEPP-17)* (2018). DOI: 10.22323/1.313.0001.

[48] Sebastien Viret. "CIC2 a radiation tolerant 65nm data aggregation ASIC for the future CMS tracking detector at LHC". In: *Proceedings, Topical Workshop on Electronics for Particle Physics (TWEPP 2021), Online* (Oct. 2021). URL: http://cds.cern.ch/record/2797676.

[49] Katja Klein et al. "Service hybrids for the silicon strip modules of the CMS Phase-2 Outer Tracker upgrade". In: *Proceedings, Topical Workshop on Electronics for Particle Physics (TWEPP2018)* (2019), p. 127. DOI: 10.22323/1.343.0127.

[50] The CERN DCDC project. *DCDC CONVERTER PROJECT WEBSITE*. 2022. URL: https://project-dcdc.web.cern.ch/project-dcdc/ (visited on Apr. 25, 2022).

[51] Angelos Zografos et al. “Power, Readout and Service Hybrids for the CMS Phase-2 Upgrade”. In: *Proceedings, Topical Workshop on Electronics for Particle Physics (TWEPP 2021), Online* (Oct. 2021). URL: http://cds.cern.ch/record/2797682.

[52] M. Kovacs et al. “Flexible front-end hybrids for the CMS outer tracker upgrade”. In: *JINST* 10.01 (2015), p. C01046. DOI: 10.1088/1748-0221/10/01/C01046.

[53] Tomasz Gadek et al. “Front-end hybrids for the strip-strip modules of the CMS Outer Tracker Upgrade”. In: *Proceedings, Topical Workshop on Electronics for Particle Physics (TWEPP 2018)* (2019), p. 019. DOI: 10.22323/1.343.0019.

[54] Heraeus Deutschland GmbH & Co. KG. *Bonding Wires for Semiconductor Technology*. 2017. URL: https://www.heraeus.com/media/media/het/doc_het/products_and_solutions_het_documents/bonding_wires_documents/Brochure_Bonding_Wire.pdf (visited on Feb. 14, 2022).

[55] Dr Josef Sedlmair, Dr Franz Schlicht, Dr Farhad Farassat for F&K Delvotec Bondtechnik GmbH. *Which Frequency is Best for Wirebonding?* 2015. URL: https://www.fkdelvotec.com/fileadmin/media_fuk/dokumente/160809E_TN_15_01_Frequency.pdf (visited on Feb. 14, 2022).

[56] Tim Ziemons. “Wire Bonding on 2S Modules of the Phase-2 CMS Detector”. MA thesis. RWTH Aachen University, Sept. 2017. URL: http://cds.cern.ch/record/2292301.

[57] Dr.-Ing. Farhad Farassat. *Bondprozesskontrolle*. 2017. URL: https://www.fkdelvotec.com/fileadmin/media_fuk/dokumente/Bondprozesskontrolle.pdf (visited on Feb. 14, 2022).

[58] Nicolas Maximilian Röwert. “Assembly and Characterization of a First Functional 2S Module for the CMS Phase-2 Upgrade at LHC”. MA thesis. RWTH Aachen University, Nov. 2018. URL: http://cds.cern.ch/record/2671895.

[59] Amann Girrbach AG. *smartmix X2*. 2021. URL: https://www.amanngirrbach.com/en/products/model-fabrication/smartmix-x2/ (visited on June 9, 2021).

[60] Nordson Corporation. *3-Axis EV Series Automated Fluid Dispensing Robot*. 2021. URL: https://www.nordson.com/en/divisions/efd/products/automated-dispense-systems/ev-series-automated-dispensing-system (visited on June 9, 2021).

[61] Nordson Corporation. *EFD Precision Fluid Dispensers*. 2021. URL: https://www.nordson.com/en/divisions/efd/products/fluid-dispensing-systems (visited on June 9, 2021).

[62] Polytec PT GmbH. *Polytec EP 601-LV: Unfilled Epoxy Adhesive, Technical Data*. 2017. URL: https://www.polytecstore.fr/polytec_images/documents/FT_PT/ep/polytec-ep-601-lv_en.pdf (visited on Mar. 11, 2022).

[63] Polytec PT GmbH. *Polytec TC 437*. 2017. URL: https://www.polytecstore.fr/polytec_images/documents/FT_PT/tc/polytec-tc-437_engl.pdf (visited on Mar. 11, 2022).

[64] The Dow Chemical Company. *SYLGARD^{TM} 186 Silicone Elastomer: Technical Data Sheet*. 2017. URL: https://www.dow.com/documents/en-us/productdatasheet/11/11-12/11-1253-sylgard-186-silicone-elastomer.pdf (visited on May 9, 2022).

[65] FK Delvotec Bondtechnik GmbH. *WIRE BONDER G5 SINGLE: Produktdatenblatt*. 2021. URL: https://www.fkdelvotec.com/fileadmin/media_fuk/dokumente/Produktblatt_Drahtbonder_G5_Single.pdf (visited on June 9, 2021).

[66] FS Bondtec Semiconductor GmbH. *Bond Pull Tester LAB-Tester*. 2021. URL: https://www.fsbondtec.at/portfolio/lab-tester/ (visited on June 9, 2021).

[67] Heraeus Deutschland GmbH & Co. KG. *Technical Data Sheet*. 2022. URL: https://www.heraeus.com/media/media/het/doc_het/brochures_en_1/TDS_ALW-29S_ALW-29S_CR_Wire.pdf (visited on Mar. 14, 2022).

[68] TopLine, Tanaka. *Bonding Wire*. 2018. URL: factronix.com/_downloads/Bonding-Wire-Catalog-2018.pdf (visited on Mar. 14, 2022).

[69] Micro Point Pro. *Bonding Wedge Catalog*. 2020. URL: https://mpptools.com/wp-content/uploads/2020/08/wedge_catalog.pdf (visited on Mar. 14, 2022).

[70] Nicolas Röwert. *Photograph of the pigtail holders for the Kapton gluing jig*. 2020.

[71] Christian Käseberg. "Doppelseitige Vermessung von 2S-Modulen für das Upgrade des CMS-Spurdetektors". Bachelorarbeit. 1. Physikalisches Institut B, RWTH Aachen University, 2017. URL: https://web.physik.rwth-aachen.de/service/wiki/pub/Feld/CMSxBachelorarbeiten/Bachelorarbeit_online.pdf (visited on Mar. 15, 2022).

[72] Abraham Savitzky and M. J. E. Golay. "Smoothing and Differentiation of Data by Simplified Least Squares Procedures." In: *Analytical Chemistry* 36.8 (1964), pp. 1627–1639. DOI: 10.1021/ac60214a047. eprint: https://doi.org/10.1021/ac60214a047. URL: https://doi.org/10.1021/ac60214a047.

[73] The SciPy community. *scipy.signal.savgol_filter*. 2021. URL: https://docs.scipy.org/doc/scipy/reference/generated/scipy.signal.savgol_filter.html (visited on Jan. 7, 2022).

[74] W. J. Youden. "Index for rating diagnostic tests". In: *Cancer* 3.1 (1950), pp. 32–35. DOI: https://doi.org/10.1002/1097-0142(1950)3:1<32::AID-CNCR2820030106>3.0.CO;2-3. eprint: https://acsjournals.onlinelibrary.wiley.com/doi/pdf/10.1002/1097-0142%281950%293%3A1%3C32%3A%3AAID-CNCR2820030106%3E3.0.CO%3B2-3. URL: https://acsjournals.onlinelibrary.wiley.com/doi/abs/10.1002/1097-0142%281950%293%3A1%3C32%3A%3AAID-CNCR2820030106%3E3.0.CO%3B2-3.

[75] Tom Fawcett. "An introduction to ROC analysis". In: *Pattern Recognition Letters* 27.8 (2006). ROC Analysis in Pattern Recognition, pp. 861–874. ISSN: 0167-8655. DOI: https://doi.org/10.1016/j.patrec.2005.10.010. URL: https://www.sciencedirect.com/science/article/pii/S016786550500303X.

[76] The Qt Company. *Qt*. 2021. URL: https://www.qt.io/.

[77] Nikkie Deelen. "Characterizing detector modules for the Upgrade of the Silicon Tracker of the Compact Muon Solenoid experiment". PhD thesis. 2019. URL: http://cds.cern.ch/record/2707148.

[78] Image Access. *CCD or CIS: The Technology Decision*. White paper. Image Access, 2013. URL: https://www.imageaccess.de/?page=WhitePapersCCDOrCIS&lang=en (visited on Apr. 12, 2021).

[79] Charles R. Harris et al. "Array programming with NumPy". In: *Nature* 585.7825 (Sept. 2020), pp. 357–362. DOI: 10.1038/s41586-020-2649-2. URL: https://doi.org/10.1038/s41586-020-2649-2.

[80] J. D. Hunter. "Matplotlib: A 2D graphics environment". In: *Computing in Science & Engineering* 9.3 (2007), pp. 90–95. DOI: 10.1109/MCSE.2007.55.

[81] Itseez. *Open Source Computer Vision Library*. https://github.com/itseez/opencv. 2015.

[82] Keyence Deutschland GmbH. *Digitales Mikroskop: VHX-900F*. 2021. URL: https://www.keyence.de/products/microscope/digital-microscope/vhx-900f/models/vhx-900f/.

[83] FormFactor. *Cascade PA200 BlueRay*. 2022. URL: https://www.formfactor.com/product/probe-systems/200-mm-systems/pa200-blueray/ (visited on Apr. 22, 2022).

[84] Tektronix. *Series 2400 Source Measure Unit Datasheet*. 2021. URL: https://de.tek.com/datasheet/series-2400-sourcemeter-instruments.

[85] Teledyne FLIR LLC. *Thermal Imaging, Night Vision and Infrared Camera Systems*. The model used in the course of this thesis is already outdated and the manufacturer has stopped the support. 2021. URL: https://www.flir.com/ (visited on Apr. 20, 2022).

[86] Totech. *SD+ Series: precision drying*. 2022. URL: https://superdry-totech.com/dry-cabinets-sd-plus-series/ (visited on Jan. 10, 2022).

[87] Sicco. *SICCO Maxi 1-Exsikkator, PMMA*. 2022. URL: https://www.sicco.de/produkte/exsikkatoren/exsikkatoren-zur-trocknunglagerung/119/sicco-maxi-1-exsikkator-pmma (visited on Jan. 10, 2022).

[88] Max Beckers. "Entwicklung eines verteilten Sensornetzwerks zur Reinraumüberwachung für die Produktion von CMS Silizium-Streifendetektormodulen". German. Bachelor Thesis. III. Physics Institut B, RWTH Aachen University, June 2021. URL: https://www.institut3b.physik.rwth-aachen.de/global/show_document.asp?id=aaaaaaaabcybfdu (visited on Jan. 18, 2022).

[89] Bosch Sensortec GmbH 2021. *Humidity Sensor BME280*. 2022. URL: https://www.bosch-sensortec.com/products/environmental-sensors/humidity-sensors-bme280/ (visited on Jan. 18, 2022).

[90] Piera Systems. *Intelligent Particle Sensors*. 2022. URL: https://pierasystems.com/intelligent-particle-sensors/ (visited on Jan. 18, 2022).

[91] OMRON Corporation. *D6T MEMS Thermal Sensors*. 2021. URL: https://components.omron.com/us-en/products/sensors/D6T (visited on Jan. 18, 2022).

[92] Grafana Labs. *Dashboard anything. Observe everything*. 2022. URL: https://grafana.com/grafana/ (visited on Jan. 18, 2022).

[93] InfluxData Inc. *Act in Time. Build on InfluxDB.* 2022. URL: https://www.influxdata.com/ (visited on Jan. 18, 2022).

[94] Oliver Pooth, Tim Ziemons. *Clean room plan.* 2021.

[95] Desco Europe. *222564*. 2022. URL: https://www.descoeurope.com/Europe-Catalogue/Footwear-and-Wrist-Strap-Testers/Footwear-and-Wrist-Strap-Testers/High-Speed-High-Accuracy-Wrist-Strap-and-Footwear-Tester/222564/ (visited on Mar. 17, 2022).

[96] Christian Dziwok. "Test systems for the Phase-2 Upgrade of the CMS Outer Tracker". Preliminary Title. PhD Thesis in preparation. RWTH Aachen University.

[97] Justus Braach. "Functional Tests of 2S Detector Modules for the CMS Phase 2 Outer Tracker Upgrade including the Development of an IR LED Array". MA thesis. Karlsruhe Institute of Technology (KIT), 2020.

[98] T. Bisanz et al. "EUTelescope: A modular reconstruction framework for beam telescope data". In: *Journal of Instrumentation* 15.09 (Sept. 2020), P09020–P09020. ISSN: 1748-0221. DOI: 10.1088/1748-0221/15/09/p09020. URL: http://dx.doi.org/10.1088/1748-0221/15/09/P09020.

[99] Deutsches Elektronen-Synchrotron DESY. *Test Beams at DESY*. 2021. URL: https://particle-physics.desy.de/test_beams_at_desy/.

[100] P. Ahlburg et al. "EUDAQ—a data acquisition software framework for common beam telescopes". In: *JINST* 15.01 (Jan. 2020), P01038–P01038. DOI: 10.1088/1748-0221/15/01/p01038. URL: https://doi.org/10.1088/1748-0221/15/01/p01038.

[101] Hendrik Jansen et al. "Performance of the EUDET-type beam telescopes". In: *EPJ Techniques and Instrumentation* 3.1 (Oct. 2016). ISSN: 2195-7045. DOI: 10.1140/epjti/s40485-016-0033-2. URL: http://dx.doi.org/10.1140/epjti/s40485-016-0033-2.

[102] C. Hu-Guo et al. "First reticule size MAPS with digital output and integrated zero suppression for the EUDET-JRA1 beam telescope". In: *Nuclear Instruments and Methods in Physics Research Section A: Accelerators, Spectrometers, Detectors and Associated Equipment* 623.1 (2010). 1st International Conference on Technology and Instrumentation in Particle Physics, pp. 480–482. ISSN: 0168-9002. DOI: https://doi.org/10.1016/j.nima.2010.03.043. URL: https://www.sciencedirect.com/science/article/pii/S0168900210006078.

[103] Lea Caminada et al. "ATLAS FE-I4 ASIC". In: *PoS* Vertex2012 (2013), p. 023. DOI: 10.22323/1.167.0023.

[104] M. Pesaresi et al. "The FC7 AMC for generic DAQ & control applications in CMS". In: *JINST* 10.03 (2015), p. C03036. DOI: 10.1088/1748-0221/10/03/C03036.

[105] NATIONAL INSTRUMENTS CORP. *FlexRIO Custom Instrumentation Flyer*. 2022. URL: https://www.ni.com/pdf/product-flyers/flexrio-custom-instrumentation.pdf (visited on Feb. 10, 2022).

[106] D. Cussans. *Description of the JRA1 Trigger Logic Unit (TLU), v0.2c*. 2009. URL: https://www.eudet.org/e26/e28/e182/e291/eudet-memo-2007-02.pdf (visited on Apr. 25, 2022).

[107] Mykyta Haranko. "Development of a test DAQ system for the CMS Phase-2 outer tracker upgrade". PhD thesis. 2019. URL: http://cds.cern.ch/record/2711873.

[108] Rene Brun et al. *root-project/root: v6.18/02*. Version v6-18-02. Aug. 2019. DOI: 10.5281/zenodo.3895860. URL: https://doi.org/10.5281/zenodo.3895860.

[109] Bosch Sensortec. *BME680 - Datasheet*. BST-BME680-DS001-06. 2021. URL: https://www.bosch-sensortec.com/media/boschsensortec/downloads/datasheets/bst-bme680-ds001.pdf (visited on Mar. 29, 2021).

[110] Deutsches Elektronen-Synchrotron DESY. *iLC Soft, Marlin*. 2021. URL: https://ilcsoft.desy.de/portal/software_packages/marlin/ (visited on Nov. 9, 2021).

[111] Frank Gaede et al. "LCIO - A persistency framework for linear collider simulation studies". In: *Talk from the 2003 Computing in High Energy and Nuclear Physics (CHEP03), https://arxiv.org/abs/physics/0306114* (2003).

[112] Deutsches Elektronen-Synchrotron DESY. *iLC Soft, LCIO*. 2021. URL: https://ilcsoft.desy.de/portal/software_packages/lcio/ (visited on Nov. 9, 2021).

[113] Deutsches Elektronen-Synchrotron DESY. *iLC Soft, Gear*. 2021. URL: https://ilcsoft.desy.de/portal/software_packages/gear/ (visited on Nov. 9, 2021).

[114] Eigen community. *Eigen is a C++ template library for linear algebra: matrices, vectors, numerical solvers, and related algorithms*. 2021. URL: https://eigen.tuxfamily.org/ (visited on Nov. 9, 2021).

[115] DESY. *Millepede-II*. 2021. URL: https://www.desy.de/~kleinwrt/MP2/doc/html/index.html (visited on Nov. 9, 2021).

[116] Volker Blobel, Claus Kleinwort, and Frank Meier. "Fast alignment of a complex tracking detector using advanced track models". In: *Computer Physics Communications* 182.9 (Sept. 2011), pp. 1760–1763. ISSN: 0010-4655. DOI: 10.1016/j.cpc.2011.03.017. URL: http://dx.doi.org/10.1016/j.cpc.2011.03.017.

[117] Eric W. Weisstein. *Euclidean Metric*. MathWorld: A Wolfram Web Resource. 2021. URL: https://mathworld.wolfram.com/EuclideanMetric.html (visited on Mar. 21, 2021).

[118] C. J. Clopper and Pearson E. S. "The use of confidence or fiducial limits illustrated in the case of the binomial". In: *Biometrika* 26.4 (Dec. 1934), pp. 404–413. ISSN: 0006-3444. DOI: 10.1093/biomet/26.4.404. eprint: https://academic.oup.com/biomet/article-pdf/26/4/404/823407/26-4-404.pdf. URL: https://doi.org/10.1093/biomet/26.4.404.

[119] *NIST Digital Library of Mathematical Functions*. http://dlmf.nist.gov/, Release 1.1.1 of 2021-03-15. F. W. J. Olver, A. B. Olde Daalhuis, D. W. Lozier, B. I. Schneider, R. F. Boisvert, C. W. Clark, B. R. Miller, B. V. Saunders, H. S. Cohl, and M. A. McClain, eds. URL: %5Curl%7Bhttp://dlmf.nist.gov/%7D.

[120] S. Spannagel and H. Jansen. *GBL Track Resolution Calculator v2.0*. 2016. DOI: 10.5281/zenodo.48795. URL: https://zenodo.org/record/48795 (visited on May 10, 2022).

[121] J. Andrea et al. "Beam Test Performance of Prototype Silicon Detectors for the Outer Tracker for the Phase-2 Upgrade of CMS". In: *CERN CDS* (July 2019). URL: http://cds.cern.ch/record/2702281.

[122] The CMS Collaboration. "The Phase-2 Upgrade of the CMS Tracker". In: *CERN CDS* CERN-LHCC-2017-009. CMS-TDR-014 (June 2017). URL: https://cds.cern.ch/record/2272264.

[123] C. D. Jones et al. "The New CMS Event Data Model and Framework". In: *Proceedings, CHEP 2006* 1 (2006). Ed. by S. Banerjee. URL: https://indico.cern.ch/event/408139/contributions/979800/attachments/815724/1117731/FrameworkPaper.pdf (visited on May 9, 2022).

[124] Christian Bierlich et al. *A comprehensive guide to the physics and usage of PYTHIA 8.3*. 2022. DOI: 10.48550/ARXIV.2203.11601. URL: https://arxiv.org/abs/2203.11601.

[125] The CMS Collaboration. "Extraction and validation of a new set of CMS pythia8 tunes from underlying-event measurements". In: *The European Physical Journal C* 80.1 (Jan. 2020). DOI: 10.1140/epjc/s10052-019-7499-4. URL: https://doi.org/10.1140%2Fepjc%2Fs10052-019-7499-4.

[126] The CMS Tracker Layout Modelling Group. *OT800_IT615 layout*. 2021. URL: https://cms-tklayout.web.cern.ch/cms-tklayout/layouts-work/recent-layouts/OT800_IT615/ (visited on Feb. 23, 2022).

[127] S. Agostinelli et al. "Geant4—a simulation toolkit". In: *Nuclear Instruments and Methods in Physics Research Section A: Accelerators, Spectrometers, Detectors and Associated Equipment* 506.3 (2003), pp. 250–303. ISSN: 0168-9002. DOI: https://doi.org/10.1016/S0168-9002(03)01368-8. URL: https://www.sciencedirect.com/science/article/pii/S0168900203013688.

List of Figures

2.1. Accelerator chain at CERN [11]. 4
2.2. Conceptional sketch of a slice through the CMS detector [16]. The sketch shows the path of different particles produced within the collision at the LHC and their interaction with the CMS detector. 6

3.1. The LHC and HL-LHC schedule [25]. 14
3.2. Transversal section of a quarter of the Phase-2 CMS tracker. The figure was created with Version *OT801_IT701* of *tkLayout* [36]. The black, orange and green lines show the mounting positions and orientations of different types of IT pixel modules. The blue and red lines present the OT PS and 2S modules, respectively. 17
3.3. Sketch of the stub mechanism. The sensor spacing and the strip pitch corresponds to the 2S modules. The shown stub mechanism is however also applicable for the PS modules. The particle trajectory is shown as black arrow. The seed layer (correlation layer) is shown on the bottom (top). The red squares symbolize the hit channels of the sensors. The correlation window is represented by the green colored squares. . . 19
3.4. Labeled sketch of the 2S module. The sketch shows the 4.0 mm version with a sixth cooling contact in an exploded view. 20
3.5. Sketch of the 2S sensor design. The sensor edges with the guard and bias ring are not shown. 20
3.6. Labeled sketch of the PS module. The sketch shows the PS module version with a sensor distance of 2.6 mm. 22
3.7. Photograph of a 2S module with 8CBC2 FEHs. The shown module is the first functional 2S module assembled in Aachen (referred to as M1801). The module is mounted into a carrier jig. 24
3.8. Photograph of an 8CBC3.1 module with CIC mezzanine cards. The module (referred to as M1804) is shown prepared for a beam test. 24

4.1. Sketch of the wire bonding process [56]. 28
4.2. Exemplary deformation curve (artificial). The scale of time and wire deformation are chosen at a realistic order of magnitude. 29

5.1. Overview of the 2S module assembly process. The silicon strip sensors are drawn in yellow. 33
5.2. The sensor part of the Kapton gluing jig. 34
5.3. The Kapton part of the Kapton gluing jig. 35

5.4. The pigtail holders [70]. In the photograph the pigtail holder for the bottom sensor pigtail is used. The pigtail holder for the top sensor pigtail (shown in the background) works similarly. 36
5.5. Photograph of the bottom sensor pigtail bonds in the assembly of the *M4002* module. 37
5.6. The sensor gluing process. These photographs have been taken during the assembly of the *M1801* module. 38
5.7. Photograph of the FEH gluing process using the hybrid gluing jig during the assembly of a dummy 2S module [58]. 39
5.8. Photograph of the wire bonding jig as used for the 2S module assembly at RWTH Aachen University. 40
5.9. Wire bonding preparation and pull testing jig. 41
5.10. Bonding program sketch. The red ellipses drawn into the last pair of bond pads indicate the position of remaining bond feet after removal of a broken wire. 43
5.11. Sketch of the 2S carrier jig and the dispensing program for wire bond encapsulation. 44
5.12. Exemplary wire deformation data. The blue line shows an expected wire deformation time dependence (modeled as an error function) in the case of an optimal bonding process. A non-optimal bonding process (related to for example bad support or contamination) is drawn in orange. The breakdown of the wire deformation slope during the bonding process is quantified as the bond quality index Ψ defined as the integrated area of the slope breakdown colored in green. 45
5.13. Corrected pull test results in the different areas of the prepared sample. The applied factor is 1.9 for both bonds, the start and the destination bond. 47
5.14. Sketch to define sensitivity, specificity and accuracy. 48
5.15. Sensitivity and specificity of the alert wires using $\hat{\Psi}$ with different alert thresholds $\hat{\Psi}_{\mathrm{min}}$ are presented within a ROC curve [75] on the left side. The distribution of J and S is shown on the right side. The red markers in both plots highlight the values at maximum S. 49
5.16. Summary of sensitivity and specificity of the analysis using different bond machine parameters. The combination of sensitivity and specificity achieving the maximized S is shown. 50
5.17. Conditional probabilities of alert wire detection. 51
5.18. Normalized S for different alert radii and bonding machine parameters. 51
5.19. GUI for the quick analysis of wire bonding data in the series production of 2S modules. 53
5.19. GUI for the quick analysis of wire bonding data in the series production of 2S modules. 54
5.20. Required time per wire measured for different sets of parameters. 56
5.21. Noise measurement of M1804 after the November 2019 beam test. The typical noise level of unconnected signal wires is approximately 2 Vcth units. 58
5.22. Photographs of the bondability tests on structures that have been potted with encapsulant material which is afterwards removed again. 58

5.23. The left plot shows pull test forces of wires that have been wire bonded on a clean surface compared with those of wires bonded after the encapsulant material Sylgard 186 has been applied and afterwards removed. The right plot presents the pull test forces measured after removal of the encapsulant and re-bonding of a dummy module. 59
5.24. Noise measurement of M1804 after removal of the encapsulant material and re-bonding on the module's left side. 60
5.25. Sketch of the 2S module with its AlCF bridges and Kapton strips. Important distances are defined for further description. The sketch presents the top sensor as well es the bottom sensor as there are only minor differences. 62
5.26. Data flow from the scanner image of the set of Kapton strips to a selection of usable parts for the module assembly. 64
5.27. The RGB spectrum of a scan image for the reception of Kapton strips. 65
5.28. Exemplary view of the GUI for the automated Kapton strip reception testing. 66
5.29. Photograph of a first version of the Kapton strip reception test jig. 68
5.30. Color spectrum of the scan image using a first version of a Kapton strip carrier jig. . 68
5.31. Widths and lengths of the analyzed Kapton strips in the preparation of the M1805 module assembly. The red colored area visualizes the dimensions of strips to be excluded from assembly. The green circle presents the nominal dimensions. 69
5.32. Fitmatch values of the analyzed Kapton strips in the preparation of the M1805 module assembly. The red dotted line shows the suggested threshold of 98 %. 70
5.33. Photograph of a thFZ240 sensor backside. The picture has been captured with a *Keyence VHX-900F* digital microscope [82]. 71
5.34. IV measurements of the thinned sensors performed at HEPHY and in Aachen. The measurements are not normalized to a constant temperature. 72
5.35. IV measurement of sensor 11 with the chuck at 50 °C. After reaching the set up compliance current of 7 µA the bias voltage is held at this level and a measurement is taken after each minute for approximately two hours. 72
5.36. Reproducibility study with sensor 11. IV curves are repeated several times without changing any measurement condition. Sensor 43 has shown a similar behavior. . . . 73
5.37. Bow of thin sensor with id 11 measured using the DSM. 74
5.38. M4001 top sensor IV measurements in the course of the module assembly. 75
5.39. Photos of the M4001 2S module taken with the IR camera and the microscope. . . . 76
5.40. Measurement of the voltage drop between pads and bias ring. 77
5.41. IV measurements taken at the M4001 top sensor before and after pulling the wire connected to the damaged strip. 77
5.42. Parallelization of steps during series production. Each column shows the workload of a day in series production. The red arrows indicate the propagation of assembly jigs. The bright blue and green highlighting of process frames indicates that either a gluing robot (blue) or the bonding machine (green) is occupied for this process. . . 79
5.43. Diagram of the traveling of a 2S module between different rooms during the series production. 81
5.44. Bar chart of the expected assembly time per step for four modules. 82

5.45. Sketch of a day in the 2S module series production. 84

5.46. Sketch of the clean room for module assembly and lab for module tests [94]. The red lines present the network infrastructure with the circles indicating the coarse position of the network socket. 86

6.1. Schematic of the particle beam generation at the DESY II Test Beam Facility [5]. The beam particle generation is shown for beam line 21. 90

6.2. The DATURA telescope. 92

6.3. Sketch of the data flow in the full DAQ chain. 94

6.4. Sketch to illustrate the hit / stub detect logic and the TDC phase. In the upper part two examples for analogue signals are shown as amplitude over time. The set up threshold is drawn as dashed horizontal line. The BX times are highlighted as dotted vertical lines. The time over threshold is shown as red rectangle. Below, the hit signal is shown for the different detect logics. The green vertical line marks the time of the external trigger. 95

6.5. CAD drawings of the DUT boxes used for the beam test campaigns of 2019 and 2020 at DESY. Both boxes are shown without the front and back plate for better illustration. The drawings were provided by the DESY CMS group who also took the responsibility to design and manufacture the boxes. 97

6.6. Number of clusters and tracks. 100

6.7. Sketch of the cluster to track linking technique. The yellow box represents the strip sensor. The dashed lines highlight the $y = \pm 25\,\text{mm}$ lines. The dotted line indicates the center of the module ($y = 0\,\text{mm}$). The star symbolizes the position of a hypothetical hit as measured with a 2S module. The crosses indicate different track projections which are candidates to be linked to the cluster. The green colored area indicates the tolerance zone of $\pm 300\,\mu\text{m}$ around $y = 0\,\text{mm}$. 101

6.8. Data flow of FABEL from EUTelescope output data to the output file for physics analysis. 102

6.9. Exemplary residual distribution for x coordinate alignment. 104

6.10. Example for the y coordinate alignment. The red distribution holds track y coordinates linked to clusters with $y_{\text{cluster}} > 0$, the blue distribution the ones linked to clusters with $y_{\text{cluster}} < 0$. 105

6.11. Alignment of rotation around the z axis. 106

6.12. Alignment of rotation around the y axis. 107

6.13. Alignment of the DUT z coordinates. The blue markers show the measured x coordinate residual at the differently aligned z coordinates. The orange line shows a polynomial fit of second order for the determination of the residual minimum z coordinate. 108

6.14. Residual distribution along the x coordinate of the M1804 module at the center position of the telescope. The blue markers represent the top sensor residual distribution, the red ones correspond to the bottom sensor. The distributions are normalized by the single strip hit probability of the intra-strip coordinate of the respective track. The dashed lines show the the fitted model function. The fit has been constrained to the region between $-45\,\mu m$ and $45\,\mu m$. 111
6.15. Distribution of track x coordinates of tracks passing the hit efficiency criteria and linked to a cluster with only a single strip hit, exemplarily shown for the M1804 bottom sensor. The track x coordinate is folded into a single strip with 0 mm being the center of the strip. The distribution is fitted with a Gaussian distribution, which is shown as red line. 111
6.16. Simulation of the energy dependence of the telescope track resolution at center position and DS position of the DATURA telescope. The simulation has been performed using the *GBL Track Resolution Calculator* [120] framework. The simulated resolution values of the top and the bottom sensor of the modules at the different positions are almost identical. 113
6.17. Distribution of displacement values in x of individually aligned runs for the AC-M1804 module. 114
6.18. Distribution of displacement values in y of individually aligned runs for the AC-M1804 module. 115
6.19. Hit efficiency of the M1804 module along the x axis (perpendicular to the strip direction). The top sensor is shown in blue, the bottom sensor is shown in red. The plotted error bars are pure statistical errors derived as Clopper-Pearson interval. . . 116
6.20. Hit efficiency of the M1804 module along the y axis (along the strip direction). The top sensor is shown in blue, the bottom sensor is shown in red. The plotted error bars are pure statistical errors derived as Clopper-Pearson interval. 117
6.21. Hit efficiency of the M1804 module along the x and y axes. The left (right) plot shows the hit efficiency at different positions of the top (bottom) sensor. The same color scale is applied both plots. 118
6.22. Stub efficiency as a function of the track y coordinate. The blue graph shows the stub efficiency as defined in Equation 6.2. The red graph shows the stub efficiency with an additional selection requiring the hits on the different sensors to be on the same sensor half. 119
6.23. Hit efficiency in dependence of the bias voltage for the KIT5 module. The top sensor hit efficiency is plotted in blue, the bottom sensor efficiency in red. The inserted top right side box shows a zoom into the high efficiency plateau. All shown uncertainties are pure statistical uncertainties. 120
6.24. Cluster size in dependence of the bias voltage for the KIT5 module measured during the beam test in November 2020. The cluster size is compared to the squared inverse capacitance which has been measured as part of the sensor QA in Karlsruhe. 121
6.25. Sketch showing the charge sharing between different strips. 122

6.26. Cluster size dependence on the incidence angle for different hit detection thresholds. The cluster size is shown at different hit detection thresholds: 525 Vcth units (green, triangles pointing down), 545 Vcth units (blue, circles) and 565 Vcth units (red, triangles pointing up). The individually applied fits are shown as dashed lines. The fit parameters are summarized in Table 6.4. 123

6.27. Stub efficiency in dependence on the test beam particle incidence angle. Two different stub efficiency definitions are compared: the standard definition as defined in Equation 6.2 and the standard definition with the bend cut. 125

6.28. Stub efficiency in dependence of the emulated transverse momentum. The emulated p_{T} has been calculated from the incidence angle using the geometric relation of Equation 6.13. 127

6.29. Simulated stub efficiency as a function of the emulated p_{T}. The simulation has been conducted with half strip resolution, strip resolution and with a more realistic resolution model. The stub window is set to ± 5 strips. 128

6.30. Results of a toy model simulation. The blue line shows the p_{T} resolution with the assumption of a half strip hit resolution, the green line represents the p_{T} resolution assuming strip hit resolution and the realistic resolution model is shown by the orange line. The red marker shows the p_{T} resolution measured at the beam test. . . 129

6.31. Sketch visualizing the origin of the stub insensitive area at the center of the 2S module. 131

6.32. Cluster size in y in dependence of the incidence angle along the strip axis. Only clusters fulfilling the cluster efficiency criteria and linked to a track with y coordinate from -1 to 1 mm are considered. The top sensor cluster size is shown in blue, the bottom sensor cluster size in red. 132

6.33. Effect of stub insensitivity in the center of the 2S modules for increased inclination angles. 132

6.34. Position maps of the OT modules. 134

6.35. Distributions of incidence angles and resulting stub sensitivities. 135

6.36. Number of modules in the path of particles traversing the Phase-2 CMS OT at different pseudorapitities η. The number of modules displayed is the average value of a sample of thousand randomly picked values of ϕ and η each. By selecting both coordinates randomly, systematic effects emerging from periodically mounted modules are avoided. 136

6.37. Distribution of the pseudorapidity of the tracks of charged particles. The η distribution of all charged particles is presented in blue. The particles hitting more than four tracker layers (both IT and OT) is shown in green. The vertical red dashed lines indicate the OT acceptance ($|\eta| \leq 2.4$). The distribution is accumulated over 3000 events. 137

6.38. Spectrum of transverse momentum p_{T}. The distribution includes particles with $|\eta| \leq 2.3$ and with more than four hit tracker layers (IT and OT). The p_{T} spectrum of all charged particles is presented by a black solid line. To study the stub turn-on effects, this spectrum is weighted by the stub efficiency with a turn-on at 2 GeV (3 GeV), simulated with stub noise effects ($\epsilon_{\text{stub noise}} = 2.5\,\%$) shown in turquoise (orange) and without shown in blue (red). Each of these distributions features a p_{T} resolution of 7.1 % (as measured at the beam test). The presented numbers are absolute numbers of entries accumulated over 3000 simulated events. A binning of 100 MeV is applied. 138

List of Tables

5.1. Overview of the assembled modules. 31
5.2. Summary of the relevant dimensions to specify dimensions for the reception of the Kapton strips for HV isolation. 63
5.3. Overview of jigs with minimum of required numbers and the footprint. For the minimum number of jigs required a daily completion of four modules is assumed. If a higher output shall be considered, the number scales linearly. 80

6.1. Overview of the three beam test campaigns to test the performance of 8CBC3 2S module prototypes. 89
6.2. Overview of the systematic uncertainties of the hit and stub efficiency for the nominal scenario. The uncertainty is given as the largest deviation from the nominal value. The uncertainty on the cluster efficiency is given as the largest deviation found for either the top or the bottom sensor. 109
6.3. Summary of parameters from convolution fit of the residual of the ACM1804 prototype 2S module. 112
6.4. Overview of the parameters obtained in the fit of the cluster size dependence on the incidence angle. 124
6.5. Overview of the systematic uncertainties of the hit and stub efficiency for an incidence angle of 16.2° which approximately corresponds to the average turn on angle at the used stub window setting. The uncertainty is given as the largest deviation from the nominal value. The uncertainty on the cluster efficiency is given as the largest deviation found for either the top or the bottom sensor. 130
6.6. Overview of the properties of the stub efficiency weighted p_{T} spectra. Only the region of $|\eta| \leq 2.3$ and tracks with more than four hit tracker layers are considered. . 139

A.1. Estimated time for the reception test of components for the module assembly. The "total time" column gives the estimated assembly time per day for the daily output of four modules. The reception test of the sensors can probably be skipped after pre-production, so that IV curves are not taken until performing the HV isolation test after Kapton and pigtail gluing. 163
A.2. Estimated time for Kapton and pigtail gluing. The "total time" column gives the estimated assembly time per day for the daily output of four modules. 163
A.3. Estimated time for HV wire bonding and encapsulation. The "total time" column gives the estimated assembly time per day for the daily output of four modules. . . . 164
A.4. Estimated time for the sensor gluing step. The "total time" column gives the estimated assembly time per day for the daily output of four modules. 164

A.5. Estimated time for the HV isolation and DSM test. The "total time" column gives the estimated assembly time per day for the daily output of four modules. 164
A.6. Estimated time for the hybrid gluing. The "total time" column gives the estimated assembly time per day for the daily output of four modules. 165
A.7. Estimated time for the wire bonding. The "total time" column gives the estimated assembly time per day for the daily output of four modules. The pull testing can probably be performed while another module is wire bonded. 165
A.8. Estimated time for the electrical readout test. The "total time" column gives the estimated assembly time per day for the daily output of four modules. 165
A.9. Estimated time for the wire bond encapsulation. The "total time" column gives the estimated assembly time per day for the daily output of four modules. 166

A. Detailed tables of assembly time estimation

Table A.1.: Estimated time for the reception test of components for the module assembly. The "total time" column gives the estimated assembly time per day for the daily output of four modules. The reception test of the sensors can probably be skipped after pre-production, so that IV curves are not taken until performing the HV isolation test after Kapton and pigtail gluing.

Work	**Time per module [min]**	**Total time [min]**
Sensor reception (2 per module), IV curve, optical inspection (photo)	20	80
FEH reception test (2 per module)	10	40
SEH reception test (1 per module)	10	40
Documentation	2	8

Table A.2.: Estimated time for Kapton and pigtail gluing. The "total time" column gives the estimated assembly time per day for the daily output of four modules.

Work	**Time per module [min]**	**Total time [min]**
Sensor check (2 per module), visual inspection	4	16
Kapton strips selection and cleaning (3 per sensor)	6	24
Visual check of pigtails	2	8
Mixing glue, filling in cartridge and cleaning tools		20
Kapton and pigtail gluing (programmed robot) incl. adjusting dispenser	5	20
Visual checks after curing	10	40
Documentation	2	8

Table A.3.: Estimated time for HV wire bonding and encapsulation. The "total time" column gives the estimated assembly time per day for the daily output of four modules.

Work	**Time per module [min]**	**Total time [min]**
Put on machine and start machine	6	24
Visual checks after bonding (2 sensors per module)	2	8
Mixing, filling and preparing Sylgard, cleaning of tools		20
Encapsulation of HV bonds	4	16
Visual checks of encapsulated bonds + manual corrections	4	16
Documentation	2	8

Table A.4.: Estimated time for the sensor gluing step. The "total time" column gives the estimated assembly time per day for the daily output of four modules.

Work	**Time per module [min]**	**Total time [min]**
Visual check and cleaning of bridges	8	32
Mixing Polytec TC 437, filling, preparation, cleaning of tools		20
Sensor 1 on jig, check positioning of sensor	2	8
Apply glue to bridges	12	48
Bare module assembly in jig	2	8
Sensor 2 on jig, check positioning of sensor	2	8
Put bare module on carrier	4	16
Documentation	2	8

Table A.5.: Estimated time for the HV isolation and DSM test. The "total time" column gives the estimated assembly time per day for the daily output of four modules.

Work	**Time per module [min]**	**Total time [min]**
Load module into machine	5	20
Programme	10	40
Data check	5	20
Documentation	2	8
Transport		5
HV isolation test	10	40
Edge inspection	4	16

Table A.6.: Estimated time for the hybrid gluing. The "total time" column gives the estimated assembly time per day for the daily output of four modules.

Work	**Time per module [min]**	**Total time [min]**
Visual check of hybrids, cleaning of gluing area	4	16
Mixing glue, filling, preparation		20
Positioning and gluing process (FEH and SEH)	15	60
Transfer from hybrid gluing to bond jig	2	8
Documentation	2	8

Table A.7.: Estimated time for the wire bonding. The "total time" column gives the estimated assembly time per day for the daily output of four modules. The pull testing can probably be performed while another module is wire bonded.

Work	**Time per module [min]**	**Total time [min]**
Modules on jigs, conveyer, adjust (top side)	3	12
Start machine, take modules out and process monitoring		15
Visual checks	10	40
Turn modules (bottom side) and fill machine	3	12
Start machine, take modules out and process monitoring		15
Visual checks	10	40
Pull tests (once per day)		30
Documentation	2	8
Moving the module safely from bond jig to module carrier	2	8

Table A.8.: Estimated time for the electrical readout test. The "total time" column gives the estimated assembly time per day for the daily output of four modules.

Work	**Time per module [min]**	**Total time [min]**
Connect modules	2	8
Start test program (incl. IV)		1
Disconnect modules	2	8
Data analysis and documentation	1	4

Table A.9.: Estimated time for the wire bond encapsulation. The "total time" column gives the estimated assembly time per day for the daily output of four modules.

Work	**Time per module [min]**	**Total time [min]**
Mixing, filling and preparing Sylgard		20
Carrier jigs positioning and preparation	1	4
Program preparation and executing	5	20
Manual corrections	1	4
Documentation	2	8
Carrier jigs positioning and preparation	1	4
Program preparation and executing	5	20
Manual corrections	1	4
Documentation	2	8

Acknowledgements

Ich möchte mich bei allen Menschen bedanken, die mir das Studium und die Promotion in dieser Form ermöglicht haben. Dabei möchte ich mich zunächst bei Oliver Pooth, Lutz Feld und Katja Klein bedanken. Ich habe mich in dieser institutsübergreifenden Gruppe sehr wohl gefühlt und konnte mich, wann auch immer ich Fragen hatte, offen an euch wenden. Katja gilt ein ganz besonderer Dank für die Kommentare und die vielen beantworteten Fragen kurz vor der Finalisierung dieser Arbeit. Ebenfalls möchte ich mich auch bei allen anderen Mitgliedern der Arbeitsgruppe bedanken, insbesondere bei Christian Dziwok mit dem ich über die gesamte Zeit das Büro geteilt und sehr gerne zusammen gearbeitet habe. Ich möchte mich auch bei den vielen anderen "Tanzsaalbewohnern" für die schöne Zeit außerhalb der eigentlichen Arbeitszeit bedanken. Explizit möchte ich mich auch bei den Werkstätten für die großartige Arbeit bedanken, ohne die vieles nicht möglich gewesen wäre. Besonders möchte ich mich bei Dieter Jahn, Eric Bock und Irfan Özen bedanken. Additionally, I would like to thank Suchandra Dutta for the nice discussions, her kind advice and the many answers to my questions in the context of CMSSW. Zuletzt möchte ich mich auch und ganz besonders bei meiner Frau Julia und dem Rest meiner Familie für die Unterstützung außerhalb der Universität bedanken.